Challenges in fractional dynamics and control theory

Dumitru Baleanu[1,2], Riccardo Caponetto[3] and JA Tenreiro Machado[4]

Fractional integro-differentiation (or, non-integer order integro-differentiation) is a mathematical framework that leads to efficient tools for modeling and control many of physical systems. Nevertheless, the overall area is commonly refereed as Fractional Calculus (FC) and become popular during the last years. In fact, FC can be used to describe in a solid and compact form systems characterized by long-range temporal or spatial dependence phenomena. Furthermore, the extension of classical and modern control theories to the new perspective, allows the development of algorithms applicable both integer and non-integer order systems.

The application of fractional calculus can have a considerable impact on everyday life namely in technology, social and health issues. Therefore, important challenges are still posed to the scientific community that motivate researchers to explore new features of fractional systems.

The special issue *Challenges in Fractional Dynamics and Control Theory* includes a selection of nine papers addressing topics that recently emerged in this area and is organized as follows.

Lopes and Machado (2015) contribute with the manuscript entitled *State space analysis of forest fires*. Burnt area, precipitation and atmospheric temperatures are interpreted as state variables of a complex system and the correlations between them are investigated. The study sheds light about a complex phenomenon that needs to be better understood in order to mitigate its devastating consequences, at both economical and environmental levels.

Balachandran et al. (2015) present the paper *Controllability of nonlinear implicit neutral fractional Volterra integrodifferential systems*. The control problem of non-linear neutral fractional Volterra integrodifferential systems with implicit fractional derivative is established. Sufficient conditions for controllability are obtained by means of the notions of condensing map and measure of noncompactness of a set.

Meerschaert, et al. (2015) have the study *Anisotropic fractional diffusion tensor imaging*. Traditional diffusion

tensor imaging (DTI) maps brain structure by fitting a diffusion model to the magnitude of the electrical signal acquired in magnetic resonance imaging (MRI). Fractional DTI employs anomalous diffusion models to obtain a better fit to real MRI data, which can exhibit anomalous diffusion in both time and space. The paper describes the challenge of developing and employing anisotropic fractional diffusion models for DTI.

Pinto and Carvalho (2015) develop the work *Fractional complex-order model for HIV infection with drug resistance during therapy*. They propose a fractional complex-order model for drug resistance in HIV infection. The fractional complex-order system reveals rich dynamics and variation of the value of the complex-order derivative sheds new light on the modeling of the intracellular delay.

Muresan et al. (2015) contribute with *Design and analysis of a multivariable fractional order controller for a non-minimum phase system*. Two control strategies for multivariable processes are proposed, based on a decentralised and a steady state decoupling approach. The designed controllers are fractional order PIs. The efficiency and robustness of the fractional algorithms is tested and validated using a non-minimum phase process.

Ventura et al. (2015) add the work *Fractional direct and inverse models of the dynamics of a human arm*. The paper presents a comparative study of both direct and inverse models of the human arm at the elbow joint.

[1]Department of Mathematics and Computer Science, Faculty of Arts and Sciences, Cankaya University, Ankara, Turkey
[2]Institute of Space Sciences, Magurele-Bucharest, Romania
[3]Dipartimento di Ingegneria, Elettrica, Elettronica e Informatica, Universita'degli Studi di Catania, Catania, Italy
[4]Institute of Engineering, Polytechnic of Porto, Department of Electrical Engineering, Porto, Portugal

Corresponding author:
JA Tenreiro Machado, Institute of Engineering, Polytechnic of Porto, Department of Electrical Engineering, Porto, Portugal.
Email: jtenreiromachado@gmail.com

Models of integer and fractional order are identified from the experiments. Likewise, for comparison purposes, neural networks models are also obtained. It is shown that fractional models are more adequate to describe human arm behavior, than the integer counterpart.

Zheng et al. (2015) have the contribution *Fractional-order modeling of permanent magnet synchronous motor speed servo system*. System identification experiments are performed on the electromagnetic part and the mechanical part of the permanent magnet synchronous motor speed servo system, respectively. Experiments in open-loop and closed-loop are performed and the advantages of the proposed fractional-order model is demonstrated.

Jafari, et al. (2015) present *On comparison between iterative methods for solving nonlinear optimal control problems*. In the manuscript are compared the Adomian decomposition, homotopy perturbation and modified variational iteration methods, for solving a type of nonlinear optimal control problem. It is proved that these methods are equivalent and that they use the same iterative formula to obtain the approximate/analytical solution.

Bhrawy (2015) adds *A highly accurate collocation algorithm for 1 + 1 and 2 + 1 fractional percolation equations*. The study addresses two spectral collocation methods for fractional percolation equations (FPEs). The proposed collocation scheme, both in temporal and spatial discretizations, is successfully extended to the numerical solution of two-dimensional FPEs. Several numerical examples with comparisons are reported to highlight the high accuracy of the proposed method.

The Guest Editors thank the preceding and present editors-in-chief, Professors Ali H Nayfeh and Mehdi Ahmadian, for their support in constructing this special issue with the latest results in the important area of Fractional Calculus.

References

Balachandran K, Divya S, Rivero M and Trujillo JJ (2015) Controllability of nonlinear implicit neutral fractional Volterra integrodifferential systems. *Journal of Vibration and Control*. Epub ahead of print doi: 10.1177/1077546314567182.

Bhrawy AH (2015) A highly accurate collocation algorithm for 1 + 1 and 2 + 1 fractional percolation equations. *Journal of Vibration and Control*. Epub ahead of print doi: 10.1177/1077546315597815.

Jafari H, Ghasempour S and Baleanu D (2015) On comparison between iterative methods for solving nonlinear optimal control problems. *Journal of Vibration and Control*. Epub ahead of print doi: 10.1177/1077546315590039.

Lopes AM and Machado JAT (2015) State space analysis of forest fires. *Journal of Vibration and Control*. Epub ahead of print doi: 10.1177/1077546314565687.

Meerschaert MM, Magin RL and Ye AQ (2015) Anisotropic fractional diffusion tensor imaging. *Journal of Vibration and Control*. Epub ahead of print doi: 10.1177/1077546314568696.

Muresan CI, Dulf EH, Copot C, De Keyser R and Ionescu C (2015) Design and analysis of a multivariable fractional order controller for a non-minimum phase system. *Journal of Vibration and Control*. Epub ahead of print doi: 10.1177/1077546315575433.

Pinto CMA and Carvalho ARM (2015) Fractional complex-order model for HIV infection with drug resistance during therapy. *Journal of Vibration and Control*. Epub ahead of print doi: 10.1177/1077546315574964.

Ventura A, Tejado I, Valério D and Martins J (2015) Fractional direct and inverse models of the dynamics of a human arm. *Journal of Vibration and Control*. Epub ahead of print doi: 10.1177/1077546315580471.

Zheng W, Luo Y, Chen Y and Pi Y (2015) Fractional-order modeling of permanent magnet synchronous motor speed servo system. *Journal of Vibration and Control*. Epub ahead of print doi: 10.1177/1077546315586504.

Article

State space analysis of forest fires

António M Lopes[1] and José A Tenreiro Machado[2]

Abstract

This paper studies forest fires from the perspective of dynamical systems. Burnt area, precipitation and atmospheric temperatures are interpreted as state variables of a complex system and the correlations between them are investigated by means of different mathematical tools. First, we use mutual information to reveal potential relationships in the data. Second, we adopt the state space portrait to characterize the system's behavior. Third, we compare the annual state space curves and we apply clustering and visualization tools to unveil long-range patterns. We use forest fire data for Portugal, covering the years 1980–2003. The territory is divided into two regions (North and South), characterized by different climates and vegetation. The adopted methodology represents a new viewpoint in the context of forest fires, shedding light on a complex phenomenon that needs to be better understood in order to mitigate its devastating consequences, at both economical and environmental levels.

1. Introduction

Forest fires (FFs) have a great impact on the environment and the economy (Logan et al., 2003; Rittmaster et al., 2006). Burnt areas correspond directly to flora and fauna losses, ecosystem damage and soil degradation (Smith et al., 2000; Certini, 2005). Long-term consequences are the modification of the water cycle, replacement of autochthonous vegetation by invasive species (Brooks et al., 2004), increase in carbon dioxide emissions (Page et al., 2002) and climate change (Flannigan et al., 2000) (e.g. global warming and extreme weather events). In fact, wildfires can be regarded as *positive feedback loops* acting on the climate complex system (CS), simultaneously potentiating and being potentiated by climate changes (Dale et al., 2001; Kirilenko and Sedjo, 2007).

FF propagation depends on many factors, such as weather conditions, terrain orography and type of vegetation. Moreover, the effectiveness of detection and suppression measures is fundamental in order to mitigate fire impact (Chandler et al., 1983). Fire size patterns and spatiotemporal distributions provide valuable information for deciding about preventive measures, helping in identifying possible hazards, and in planning strategies for prevention, detection and suppression (Tenreiro Machado and Lopes, 2014).

Standard statistical methods have proved to be inadequate for analyzing extreme fire events (Holmes et al., 2008) as they are not capable of capturing all characteristics underneath fire dynamics (Alvarado et al., 1998). FFs exhibit complex spatiotemporal correlations, characterized by long-range memory and absence of a characteristic length-scale (Malamud et al., 1998; Ricotta et al., 1999; Reed and McKelvey, 2002; Telesca et al., 2005; Song et al., 2006). Those features are explained by the self-organized critical (SOC) (Bak, 1990) and highly optimized tolerance (HOT) models, proposed to explain fire behavior (Grassberger and Kantz, 1991; Drossel and Schwabl, 1992; Carlson and Doyle, 1999; Moritz et al., 2005).

Ricotta et al. (1999) analyzed FF data for the region of Liguria (Italy), covering the years 1986–1993. They concluded that there is a power-law (PL) relationship between the frequency of occurrence of the event and

[1]Faculty of Engineering, University of Porto, Portugal
[2]Institute of Engineering, Polytechnic of Porto, Portugal

Received: 24 July 2014; accepted: 19 November 2014

Corresponding author:
António Lopes, Faculty of Engineering, University of Porto, Rua Dr. Roberto Frias, 4200-465 Porto, Portugal.
Email: aml@fe.up.pt

the burnt area (size). Malamud et al. (1998) analyzed FFs in the USA and Australia and showed that FFs exhibit a PL dependence frequency versus size, over many orders of magnitude. A simple fire model was proposed and it was concluded that actual FFs can be directly associated with the model. Deviations from PL behavior, observed in certain cases, were explained by Song et al. (2006). They examined the SOC and fractal characteristics of FFs in China and hinted at actual FF protection. Reed and McKelvey (2002) proposed empirical frequency–size distributions, derived from real data in six regions in North America, concluding that a simple PL distribution of sizes may be too simple to describe the distributions over their full range. They developed a stochastic model for the spread and extinguishment of FFs to examine the necessary conditions for PL behavior. FF time-scaling was addressed by Telesca et al. (2005), who characterized the temporal distribution of fires occurring in Gargano (Italy), known for its high density of fires. They concluded that the point process of fire events is a fractal process with a high degree of time-clusterization. Time-scales are of the order of a few days and the fire process tends to be less time-clustered with an increase in the burnt area. The time-scaling properties of yearly FF sequences occurring in the Reggio Calabria (Italy) region were studied by Lasaponara et al. (2005). Their results show that FFs exhibit a strong degree of time-clusterization.

The HOT conceptual framework, as an alternate to SOC, was used to explain the formation of scale-invariant patterns in CSs (Carlson and Doyle, 1999). It emphasizes that PL behavior results from optimization of tradeoffs between system yield and tolerance to risk, which drives the system to a specific spatial configuration. Moritz et al. (2005) studied historical fire catalogs and proposed a detailed fire simulation model. They concluded that both are in agreement with the HOT concept. Boer et al. (2008) showed that FF size distributions are closely related to distributions of weather events. Zheng et al. (2008) investigated the PL scaling behavior of FFs and weather parameters by means of a detrended fluctuation analysis method. They verified that temperature, relative humidity and precipitation data reveal characteristics similar to FFs. Their reported findings were shown to be useful for quantifying the underlying dynamics of FF and weather parameters, and for understanding the relationship between them.

In this paper we study FFs from the perspective of dynamical systems. Burnt area and weather variables, such as precipitation and atmospheric temperatures, are interpreted as state variables of a CS and the correlations between them are investigated on an annual basis using different mathematical tools. First, we propose the mutual information concept to unveil potential relationships in the data. Second, we adopt the state space portrait to characterize the system behavior. Third, we compare the state space curves and use clustering and visualization tools, namely hierarchical clustering and multidimensional scaling. Several long-range patterns emerge in FF time-lines. Our study focuses on data for Portugal (excluding Azores and Madeira), covering the time period from 1980–2003. We divide the Portuguese territory into two regions (North and South), as they present different climates and vegetation. The adopted methodology and tools represent a new viewpoint in the context of FF analysis, shedding light on a complex phenomenon that needs to be better understood in order to mitigate its severe consequences. The paper reveals the difficulties in forecasting future events based on a limited set of variables. However, it is clear that the emergence of clusters corresponds to complex dynamical effects. In fact, the emerging patterns resemble those of chaotic systems, leading to poor predictability. On the other hand, the study demonstrates that the results point towards measuring a richer set of environmental variables and the recording of longer time-series in order to establish a solid basis for computer data analysis systems.

Bearing these ideas in mind, this paper is organized as follows. Section 2 introduces some fundamental mathematical concepts. Section 3 describes the experimental dataset and characterizes the data using simple statistics. Section 4 analyzes the data by means of state space portrait and compares the state space curves using clustering and visualization tools. Finally, Section 5 presents the main conclusions.

2. Mathematical background

This section presents the mathematical tools used to process the data, namely mutual information (MI), state space portrait (SSP), hierarchical clustering (HC) and multidimensional scaling (MDS).

2.1. Mutual information

The MI statistical concept originated from the area of information theory. MI measures the statistical dependence between two random variables and can be interpreted as the amount of information that one variable 'contains' about the other (Shannon, 2001). Recently, MI has been used as an approach to analyze different CSs (Fraser and Swinney, 1986; Matsuda, 2000; Tenreiro Machado and Lopes, 2013). Mathematically, for two discrete random variables (X, Y), the MI, $I(X, Y)$ is given by

$$I(X, Y) = \sum_{y \in Y} \sum_{x \in X} p(x, y) \cdot \log\left(\frac{p(x, y)}{p(x) \cdot p(y)}\right) \quad (1)$$

where, $p(x)$ and $p(y)$ represent the marginal probability distribution functions of X and Y, respectively, and $p(x,y)$, is the joint probability distribution function. MI is always symmetric and nonnegative, that is, $I(X,Y) = I(Y, X) \geq 0$.

2.2. State space portrait

A n-dimensional dynamical system can be represented by a set of first-order differential equations governing n state variables, $x_1(t), x_2(t), \ldots, x_n(t)$, where t represents time. Such equations are obtained from the system input–output functional relationship (i.e. the system model), for a given set of state variables. Knowing the state variables at time $t = t_0$ and the system inputs for $t \geq t_0$, we can determine the system behavior for $t \geq t_0$. The state space consists of the set of all possible states, each one corresponding to a unique point. As t evolves, we get sequences of points describing trajectories in the state space. The set of trajectories is the SSP. For first-, second- and third-order systems, the SSP can be depicted on a map and the system behavior can be inferred from the corresponding graphical representation (Polderman and Willems, 1998).

2.3. Hierarchical clustering

Clustering analysis organizes data into groups (clusters) such that there is a high/low intra/inter-cluster similarity between objects. Clustering exposes the internal structures of the data, underlying rules and patterns. It has been adopted in data mining, machine learning, pattern recognition, image analysis and bioinformatics, among others (Hartigan, 1975).

There are two types of clustering: partitional and hierarchical. In partitional clustering, different partitions are created and then evaluated by means of some criterion (e.g. k-means (Jain, 2010)). In HC a hierarchy of object clusters is built. This is typically done by means of heuristic algorithms. In *agglomerative clustering* the algorithm starts with each object in its own cluster and, at each step, it finds the best (most similar) pair of clusters to merge into a new cluster. It iterates until all clusters are merged together. In *divisive clustering* the algorithm starts with all items in a single cluster, at each step, it chooses the best way to split the cluster into two and, recursively, operates on both new-formed clusters. The iterations stop when each object is in its own cluster.

Both in agglomerative and divisive clustering, the clusters are generated by evaluating the inter-cluster dissimilarity. A metric (i.e. a measure of the distance between pairs of objects) and a linkage criterion (i.e. the definition of the dissimilarity between clusters as a function of the pairwise distances between objects) are adopted to quantify the inter-cluster dissimilarity. Mathematically, for two clusters, U and V, a metric is used to measure the distance between objects, $d(x_U, x_V)$, $x_U \in V$ and $x_V \in V$. Based on that metric, the maximum, minimum, or average, linkage criterion is adopted, that is, respectively

$$d_{\max}(U, V) = \max_{x_U \in U, x_V \in V} d(x_U, x_V) \qquad (2)$$

$$d_{\min}(U, V) = \min_{x_U \in U, x_V \in V} d(x_U, x_V) \qquad (3)$$

$$d_{\mathrm{ave}}(U, V) = \frac{1}{\| U \| \| V \|} \sum_{x_U \in U, x_V \in V} d(x_U, x_V) \qquad (4)$$

The results of HC are usually presented in a dendrogram, where the similarity between two objects is represented by the height of their lowest common internal node.

2.4. Multidimensional scaling

MDS is a set of techniques for visualizing similarities/dissimilarities between objects in a dataset (Cox and Cox, 2000). MDS generates maps describing the objects' locus in the perspective that, if they are perceived to be similar/dissimilar to each other, then they are placed on the map close/distant to/from each other. MDS provides an intuitive and useful visual representation of complex relationships present among objects. In *metric MDS* the input is an $n \times n$ symmetric matrix, **M**, of object pairwise similarities/dissimilarities, where n denotes the number of objects in the dataset. The measure for quantifying similarities/dissimilarities depends of the researcher's choice and can be selected based on multiple criteria. MDS assigns a point to each object, rearranging the object's coordinates in a m-dimensional space. Using an optimization algorithm, it evaluates different configurations and outputs a coordinate matrix representing the configuration that best reproduces the observed similarities/dissimilarities. For $m = 2$ and $m = 3$ the results are easily represented in a graph, where the orientation of the axes is arbitrary. The distances between points are always the same, independently of any rotation or translation of the MDS map, and can be chosen in order to get a clearer visualization. Stress and Shepard plots are usually adopted for accessing MDS results. The stress is a function of the number of dimensions m. The corresponding diagram is a monotonic decreasing chart, which is useful to decide the 'best' dimension m, as a compromise between stress reduction and number of dimensions. The Shepard plot, maps the reproduced versus the observed similarities/dissimilarities. A narrow scatter around a $45°$ line indicates a good fit.

3. Brief description of the dataset

This section describes the dataset used in this study (i.e. FFs, precipitation and temperature) and complements the presentation with simple statistics.

We consider the Portuguese continental territory divided into the North (N) and South (S) regions as shown in Figure 1. These regions correspond to different climate, vegetation and orography conditions, which influence fire behavior. The time period of analysis is limited to years 1980–2003, which is imposed by the data available.

A catalog of FFs is compiled by the Portuguese Instituto da Conservação da Natureza e das Florestas (INCF), and is available online at http://www.icnf.pt/portal/florestas/dfci/inc/estatisticas. Each data record contains information about the date of the event, time

(with one-minute resolution), geographic location (expressed in latitude and longitude coordinates) and size (quantified by the burnt area, expressed in hectares). All occurrences are included, independently of their cause, namely natural factors, human negligence and human intent.

The data is pre-processed by calculating the daily burnt area in each region. Figure 2 shows the burnt area for regions N and S. We adopt a circular time-scale to represent the time evolution of fire within the period 1980–2003. The circular time evolves along an Archimedean spiral with its origin at the center of the circumferences defined by

$$\theta = 2\pi\left[\frac{t}{T} + (i - 1980)\right], \quad r = p + q\theta \qquad (5)$$

where (r,θ) denotes the radius and angle coordinates, respectively, $p = q = 1$, $i = 1980,\ldots,2003$ and t and T represent time and one year. The daily burnt area, B, expressed in logarithmic units, is related to the color of the marks. As can be seen, most events are depicted on the graph in the area corresponding to summer. Moreover, region N is more prone to fire than region S, which is justified by the availability of denser areas of forest and vegetation.

Data on precipitation was collected at the Instituto Português do Mar e da Atmosfera (IPMA) https://www.ipma.pt/en/. The database contains information of daily precipitation for Portugal, in a regular grid with $0.2° \times 0.2°$ resolution, for the period 1950–2003. The gridded data was obtained based on records from 806 meteorological stations, interpolating the original data using the Kriging method (Belo-Pereira et al., 2011).
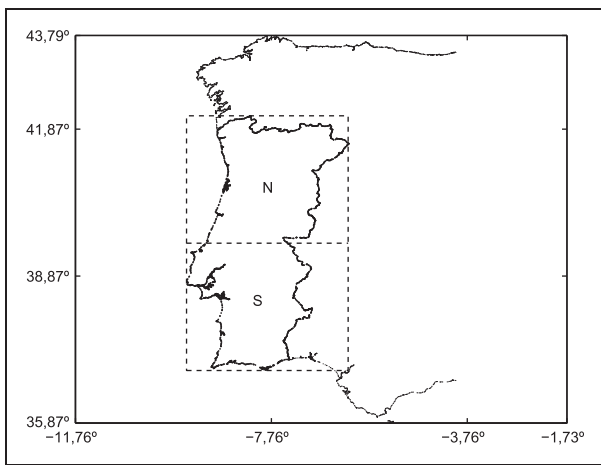

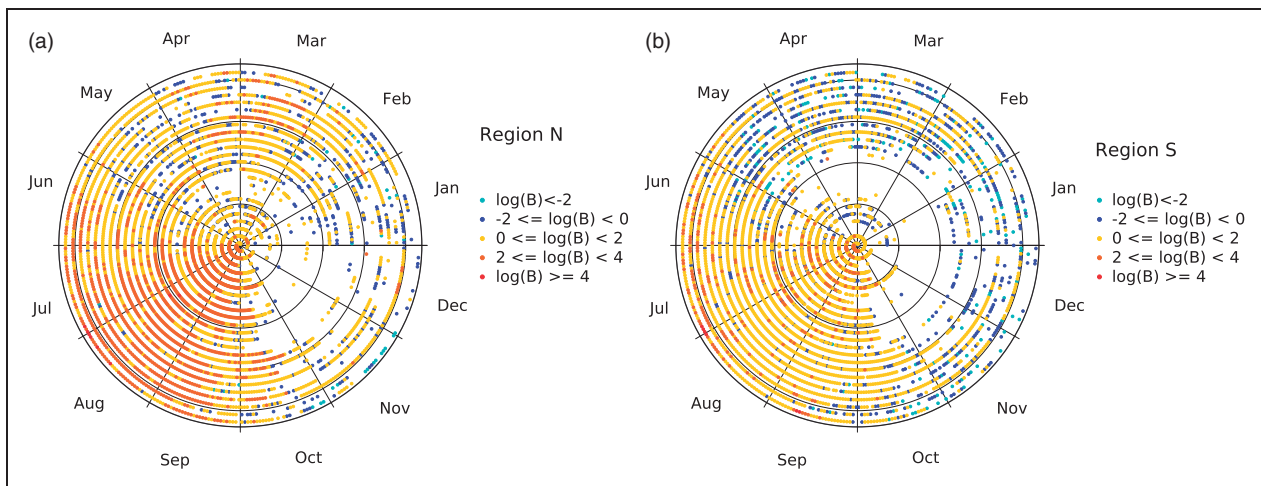**Figure 1.** Location of the two Portuguese regions studied.

Figure 2. Time evolution of the daily burnt area, during the period 1980–2003: (a) region N; (b) region S.
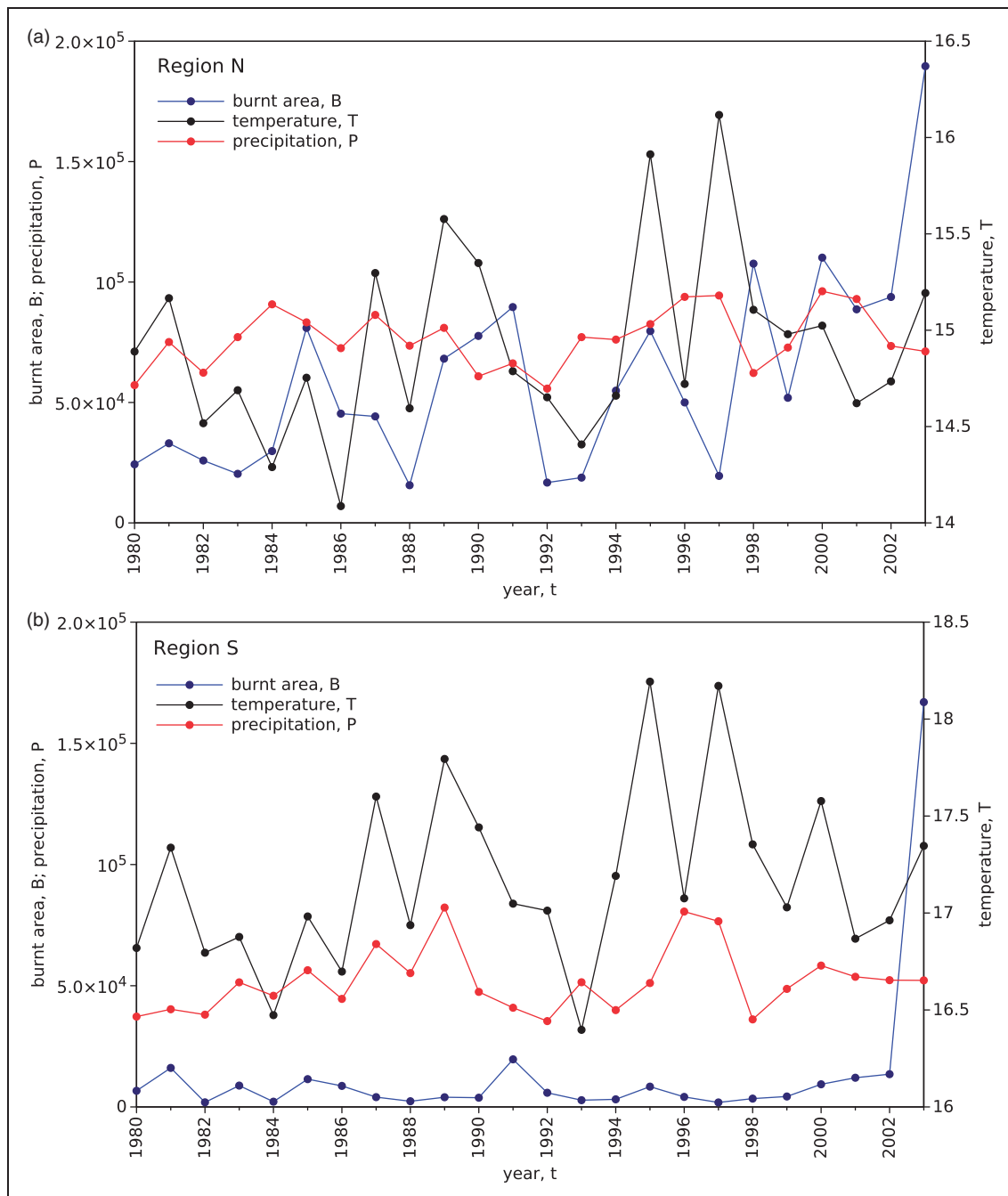
Figure 3. Evolution of the annual burnt area, mean temperature and precipitation, over the time period 1980–2003: (a) region N; (b) region S.

We pre-processed the gridded database, calculating the total daily precipitation for regions N and S in the period 1980–2003.

The source of temperature data was the National Aeronautics and Space Administration (NASA) website (http://data.giss.nasa.gov/gistemp/station_data/) Each data series consists of the average temperatures per month, expressed in Celsius degrees, of several worldwide meteorological stations. We use temperature time-series of Porto and Lisbon to represent the N and S regions of Portugal, respectively. This option is justifiable by the existence of accurate data for both cities and because Portugal is a small country, making the inclusion of other centers unnecessary. Thus, using
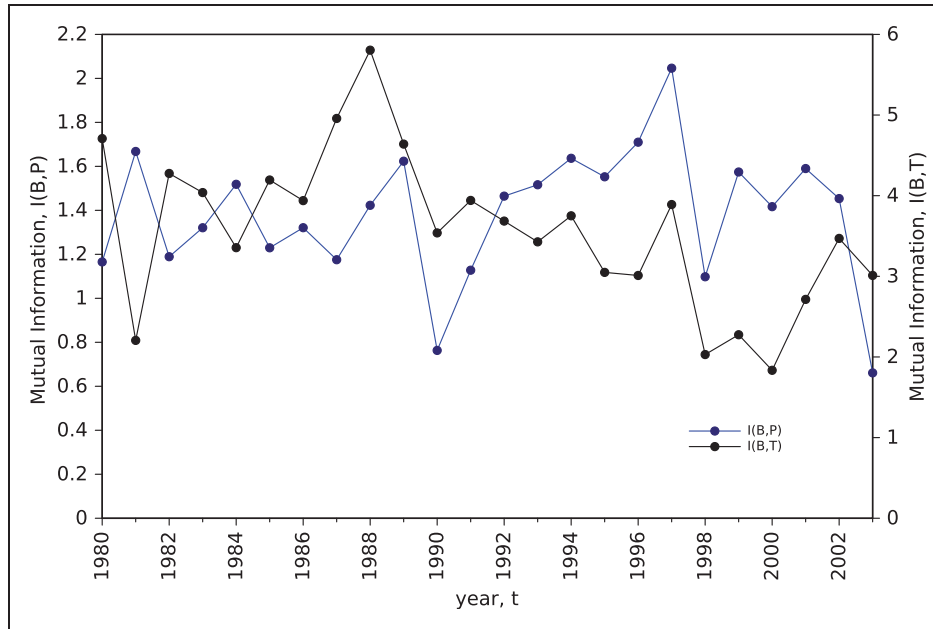
Figure 4. Evolution of the annual MI between burnt area and precipitation, *I*(*B*,P), and between burnt area and mean atmospheric temperature *I*(*B*,T), for region N, during the time period 1980–2003.
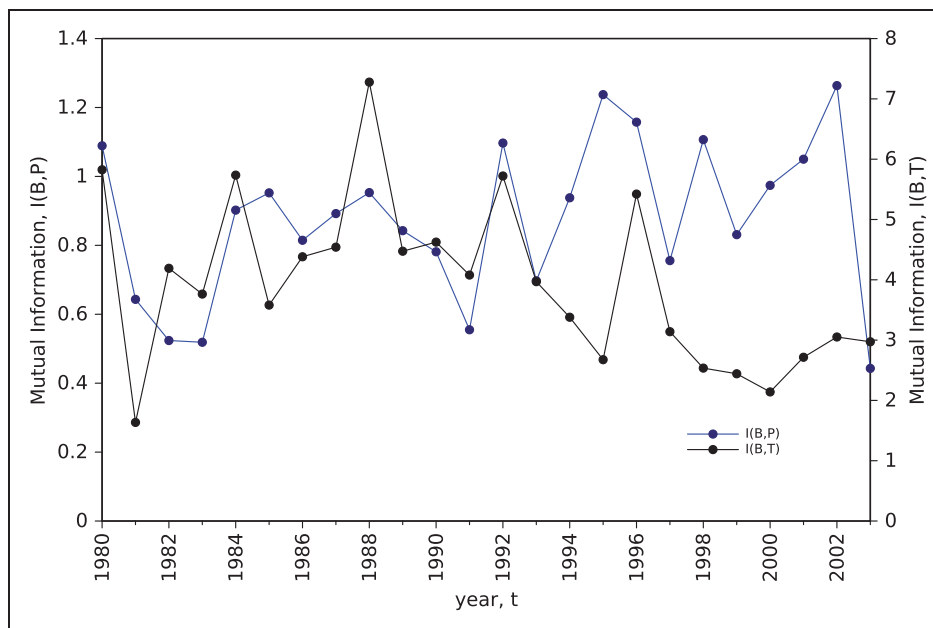

Figure 5. Evolution of the annual MI between burnt area and precipitation, *I*(*B*,P), and between burnt area and mean atmospheric temperature *I*(*B*,T), for region S, during the time period 1980–2003.

data from one place to characterize each region is a good approximation. We pre-processed the data, filling occasional gaps of one month (represented on the original dataset by the value 999.9) by temperature values calculated using linear interpolation between the two adjacent points. The distinct number of days of each month and the leap years were taken into account. The data was then interpolated linearly in order to get daily mean temperatures (Tenreiro Machado and Lopes, 2012; Lopes and Tenreiro Machado, 2014).

In Figure 3 we represent the evolution of the annual total burnt area, mean temperature and
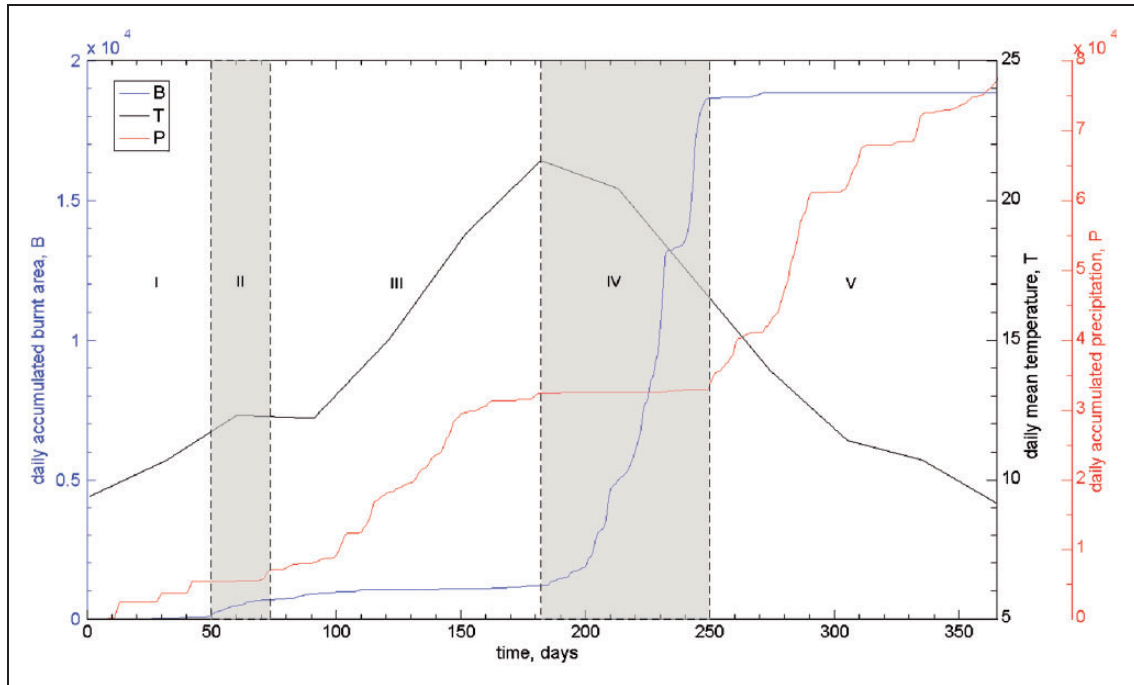
Figure 6. Time evolution of the variables $\tilde{X}_i^B(t)$, $\tilde{X}_i^P(t)$ and $x_i^T(t)$, for year $i = 1993$ and region N.
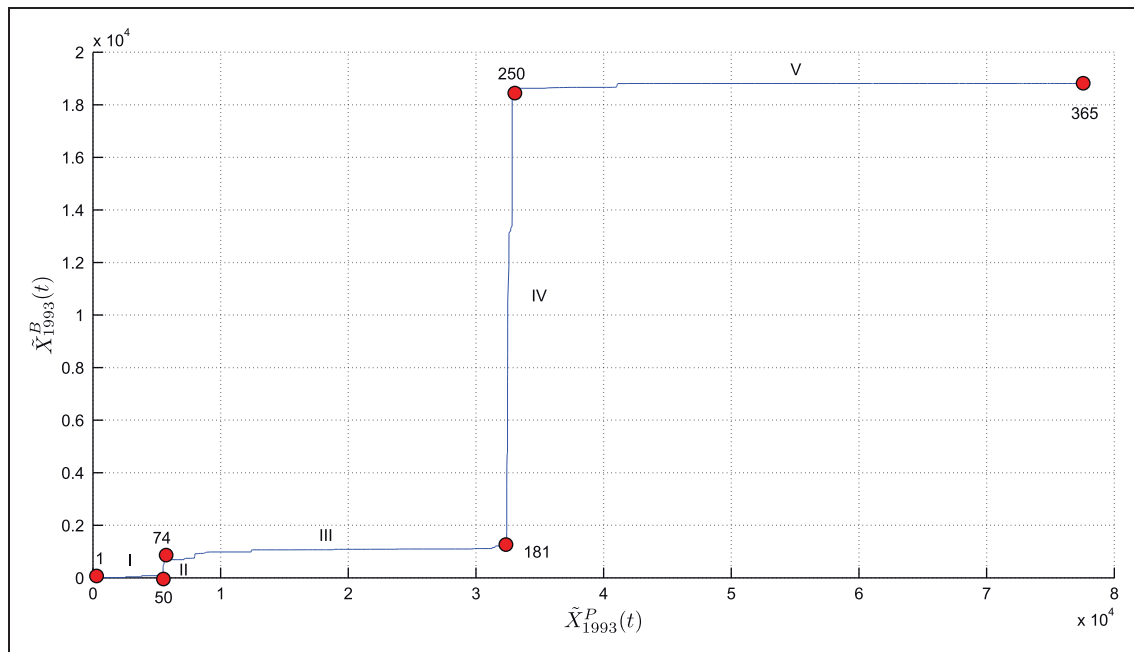
Figure 7. The SSP $\tilde{X}_i^B(t)$ vs. $\tilde{X}_i^P(t)$, for year $i = 1993$ and region N.

precipitation, for regions N and S, over the time period 1980–2003. It can be seen that there is a correlation between burnt area and both mean temperature and precipitation.

We verify that the previous simple statistics do not capture all the hidden relationships in the data. Therefore, in the next section, several complementary mathematical tools are adopted.

Figure 8. The SSP $\tilde{X}_i^B(t)$ vs. $x_i^T(t)$, for year $i = 1993$ and region N.
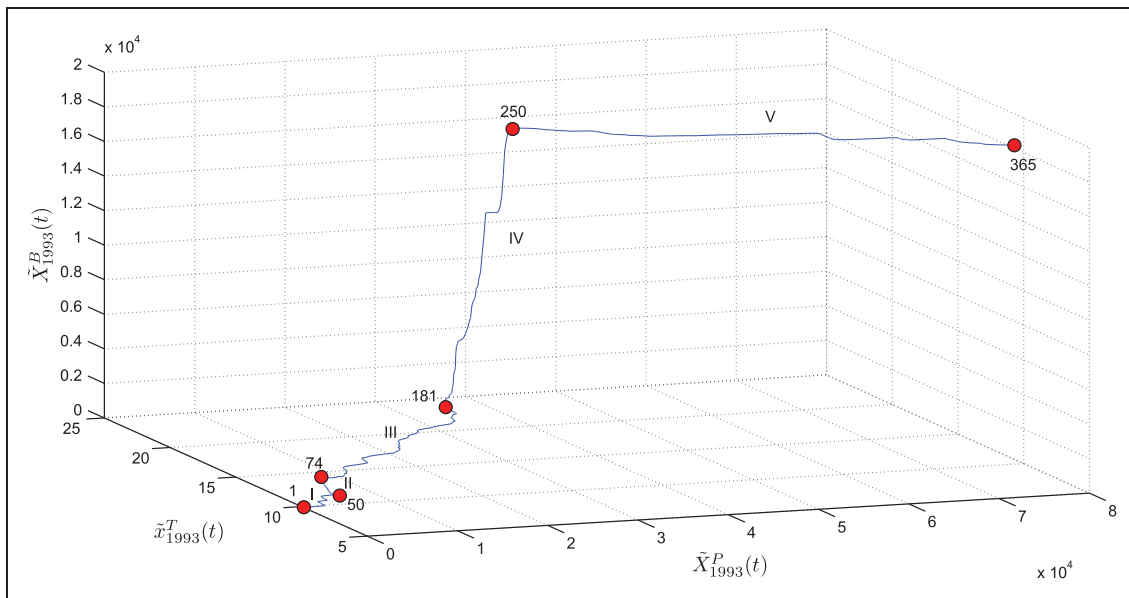
Figure 9. The SSP $\tilde{X}_i^B(t)$ vs. $\tilde{X}_i^P(t)$ vs. $x_i^T(t)$, for year $i = 1993$ and region N.

4. Data analysis and results
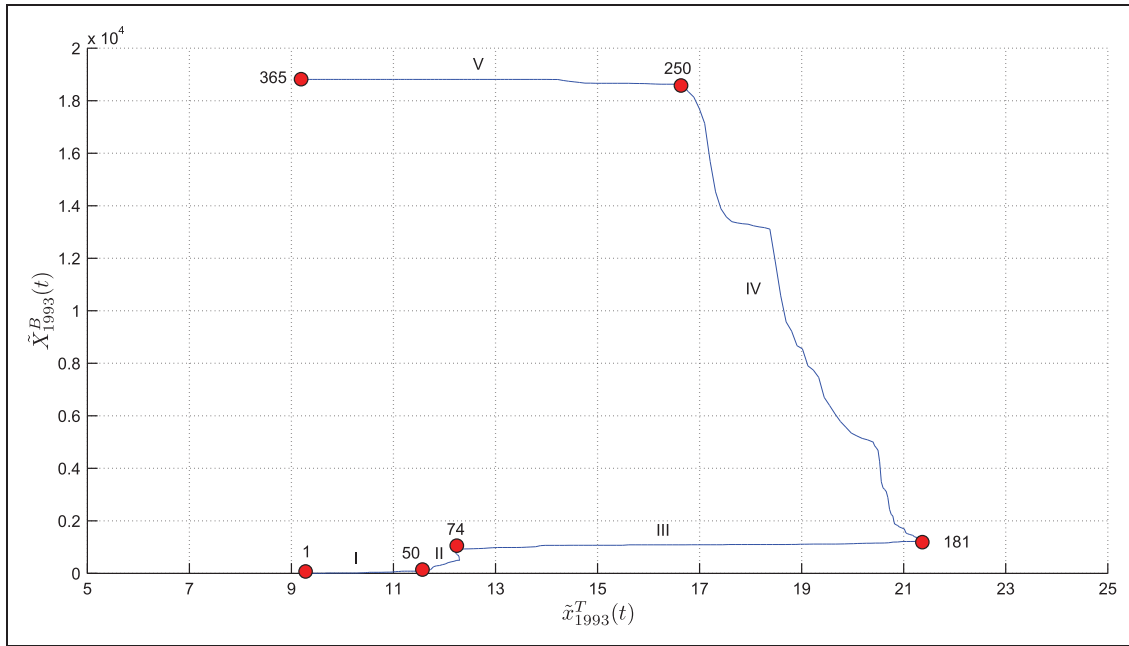
In this section, data comprising burnt area, precipitation and atmospheric temperatures are interpreted as state variables of a CS and correlations between the variables are investigated on an annual basis. In subsection 4.1, we use MI to analyze the relationships in the data. In Section 4.2, we adopt the SSP to characterize the system's behavior. Finally, in Section 4.3 we compare the state space curves by means of HC and MDS.

4.1. Mutual information analysis

To calculate the MI, we first generate the annual time-series of daily values

$$x_i^W(t) = \sum_{k=1}^{T} W_{i,k}\delta(t - t_{i,k}) \qquad (6)$$

leading to 24 time-series for each variable, where, $W = \{B, P, T\}$ denotes burnt area (B), precipitation

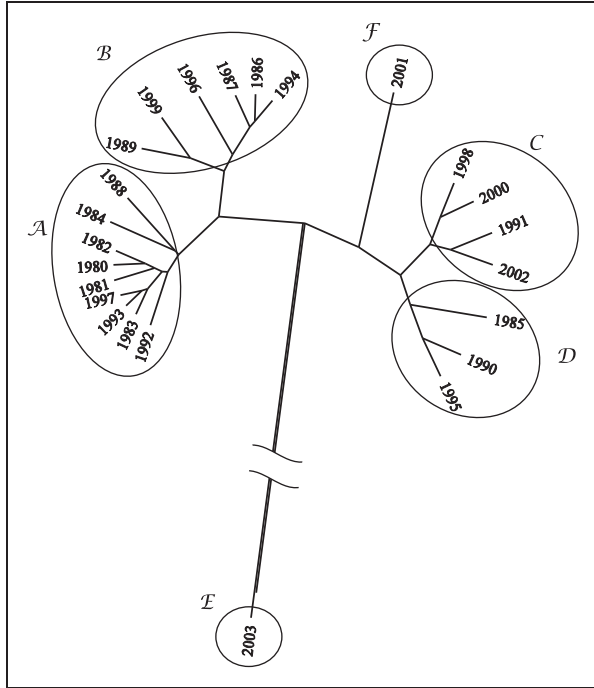**Figure 10.** Visualization tree generated by the HC algorithm, representing similarities between SSP annual curves, for region N.
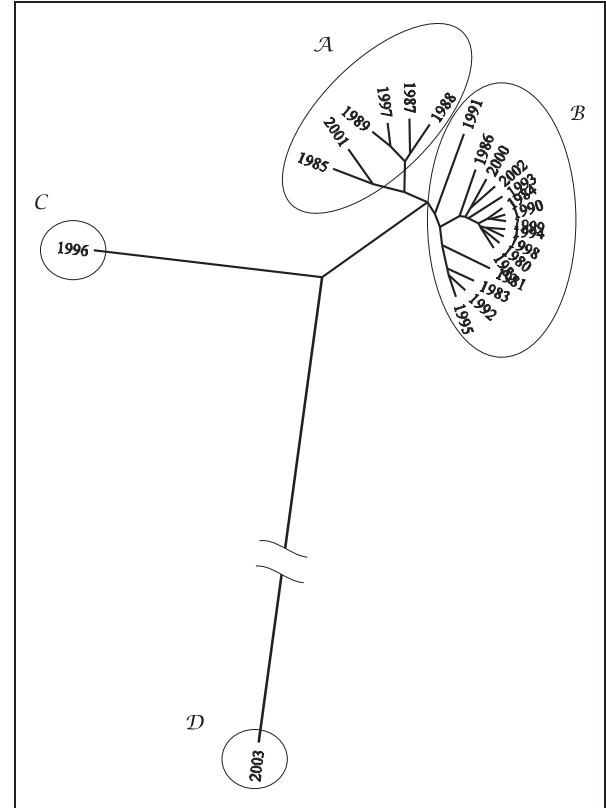

Figure 11. Visualization tree generated by the HC algorithm, representing similarities between SSP annual curves, for region S.

(P) and mean temperature (T), respectively. The variable $W_{i,k}$ represents daily values, $t_{i,k}$ are time-instants (i.e. days), T is the total number of days in one year, and $\delta(\cdot)$ corresponds to the Dirac delta function.

The annual MI between burnt area and precipitation, $I(B,P)$ and between burnt area and mean atmospheric temperature $I(B,T)$ were calculated, estimating the probabilities by means of the histograms of relative frequencies. For constructing the histograms, we adopt $N = 200$ bins.

Figures 4 and 5 represent the evolution of the annual MI between burnt area and precipitation, $I(B,P)$, and between burnt area and mean atmospheric temperature $I(B,T)$, for regions N and S, respectively. We can see that, for the two regions, $I(B,P)$ is lower than $I(B,T)$. For region N, $I(B,P)$ is somewhat 'noisy', but it stays almost constant over the period 1980–2003, with exception of the years {1990, 2003} and {1997}, where minimum and maximum values of MI are registered, respectively. With respect to $I(B,T)$, in the early years it is almost constant. In year {1988} it reaches a maximum value and, for more recent years, its trend is for decreasing. For region S, $I(B,P)$ is also 'noisy', but its trend reflects some increasing over time, except for years {1980, 2003}. The evolution of $I(B,T)$ shows a trend to increase during the first half and to decrease for the second half of the period of analysis.

4.2. State space analysis

To generate the SSP we first compute the annual time-series of accumulated burnt area, $\tilde{X}_i^B(t)$, and accumulated precipitation, $\tilde{X}_i^P(t)$, which are given by

$$\tilde{X}_i^Z(t) = \int_0^t x_i^Z(u)\mathrm{d}u, \ Z = \{B, P\} \qquad (7)$$

where, $0 \leq t \leq T$ and $t = 0$ corresponds to the first day of each year $i = 1980, \ldots, 2003$.

Second, we analyze the annual SSP generated by the three 'state' variables: accumulated burnt area, $\tilde{X}_i^B(t)$, accumulated precipitation, $\tilde{X}_i^P(t)$ and mean atmospheric temperature, $x_i^T(t)$, leading to 24 three-dimensional curves.

In this second analysis, to illustrate the methodology, we present the results for year 1993, in region N. Figure 6 depicts the time evolution of the variables, where we can see that the accumulated burnt area, $\tilde{X}_i^B(t)$, reveals five distinct regimes. Period I corresponds to $1 \leq t \leq 50$ days (i.e. from January up to mid-February), with negligible fire activity, low temperatures (below 11.7°C) and intermittent periods with
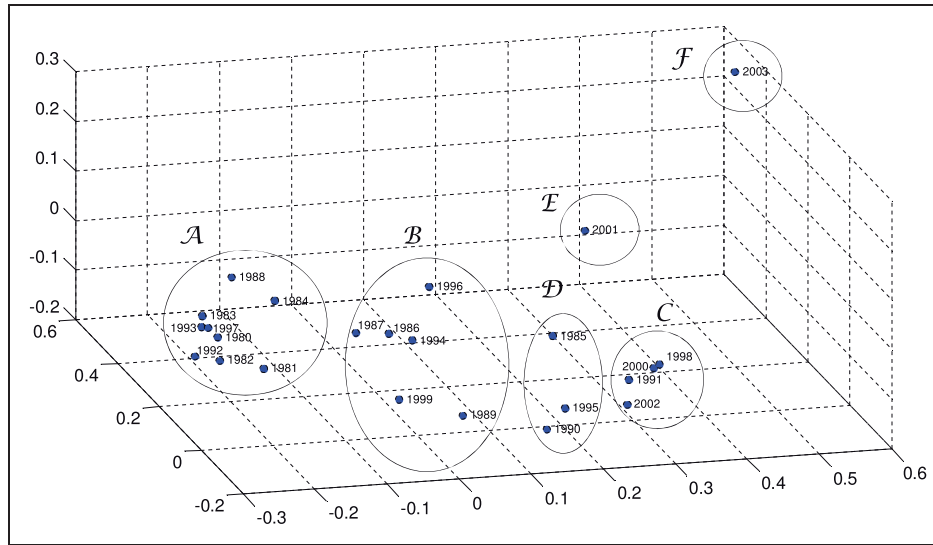
Figure 12. The MDS map for $k = 3$, representing similarities between SSP annual curves, for region N.
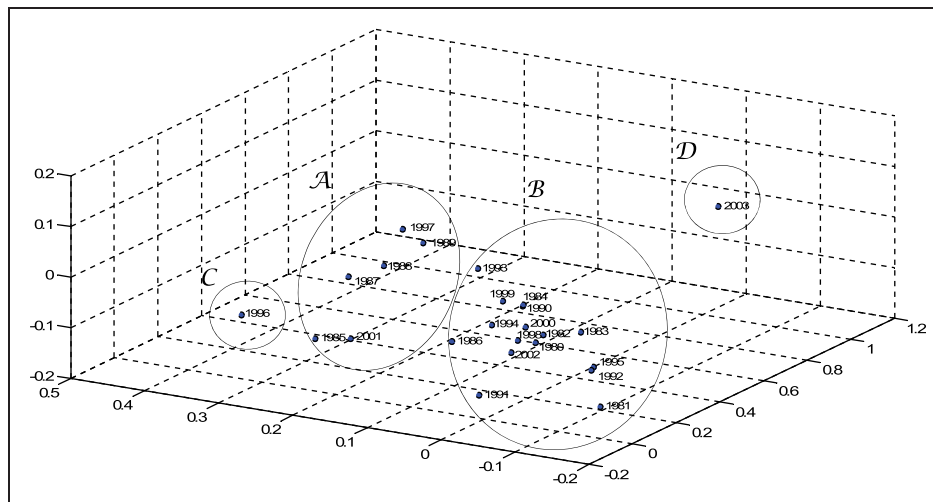

Figure 13. The MDS map for $k = 3$, representing similarities between SSP annual curves, for region S.

precipitation. Period II corresponds to $50 \leq t \leq 74$ days (i.e. from mid-February up to mid-March). Fire activity increases moderately, temperatures are in the interval [11.7°C,12.3°C] and precipitation is almost absent. In period III, $74 \leq t \leq 181$ days, (i.e. from mid-March up to end of June), fire activity is low, and temperatures increase up to the interval [12.3°C, 21.3°C] while precipitation is quite intense. Period IV, $181 \leq t \leq 250$ days, corresponds to the end of June up to the end of August. Fire activity goes up by a large increment. Temperatures stay above 16.5°C and precipitation is negligible. Finally, in period V, $250 \leq t \leq 365$ days (from the end of August up to the end of the year), fire activity is again negligible, temperatures

decrease continuously and precipitation remains present.

The relationships between $\tilde{X}_i^B(t)$, $\tilde{X}_i^P(t)$ and $x_i^T(t)$ ($i = 1993$) are presented in Figures 7, 8 and 9, corresponding to the SSP $\tilde{X}_i^B(t)$ vs. $\tilde{X}_i^P(t)$, $\tilde{X}_i^B(t)$ vs. $x_i^T(t)$ and $\tilde{X}_i^B(t)$ vs. $\tilde{X}_i^P(t)$ vs. $x_i^T(t)$, respectively.

4.3. Clustering analysis and visualization

In this subsection clustering and visualization algorithm are adopted to compare the annual SSP curves and to unveil relationships in the data.

To compare all SSPs we calculate a 24×24 dissimilarity matrix $\mathbf{M} = [e_{ij}]$, based on the Euclidean

distance e_{ij} $(i,j = 1980, \ldots, 2003)$, between the SSP curves

$$e_{ij} = \sqrt{(x_i - x_j)^2 + (y_i - y_j)^2 + (z_i - z_j)^2} \qquad (8)$$

where, (x_i,y_i,z_i) and (x_j,y_j,z_j) represent the coordinates of the SSP curve pairs (i,j), respectively.

Two visualization trees are generated using HC, corresponding to regions N and S (Figures 10 and 11, respectively). The successive (agglomerative) clustering and average-linkage methods are adopted. The software PHYLIP is used for generating the graphs (http://evolution.genetics.washington.edu/phylip.html). For region N, we can note the emergence of six clusters: $\mathcal{A} = \{1980, 1981, 1982, 1983, 1984, 1988, 1992, 1993, 1997\}$, $\mathcal{B} = \{1986, 1987, 1989, 1994, 1996, 1999\}$, $C = \{1991, 1998, 2000, 2002\}$, $\mathcal{D} = \{1985, 1990, 1995\}$, $\mathcal{E} = \{2003\}$ and $\mathcal{F} = \{2001\}$. For region S, we identify four clusters: $\mathcal{A} = \{1985, 1987, 1988, 1989, 1997, 2001\}$, $\mathcal{B} = \{1980, 1981, 1982, 1983, 1984, 1986, 1990, 1991, 1992, 1993, 1994, 1995, 1998, 1999, 2000, 2002\}$, $C = \{1996\}$ and $\mathcal{D} = \{2003\}$.

As an alternative to HC and visualization trees we adopt MDS, feeding the algorithm with matrix $\mathbf{M}$. The MDS maps for $m = 3$ are depicted in Figures 12 and 13, corresponding to regions N and S, respectively. As said previously, a shorter (larger) distance between two points on a map means that the corresponding objects are more similar (distinct). The clusters identified previously are also depicted. We can say that both visualization trees and MDS maps allow good interpretation of the results. However, MDS maps have an advantage when dealing with a large number of objects, being more intuitive.

5. Conclusions

In this paper we proposed analyzing FFs from the perspective of dynamical systems. We used daily data for Portugal (excluding the Atlantic islands Azores and Madeira), covering the time period from 1980–2003. In the adopted methodology, burnt area, precipitation and atmospheric temperatures were interpreted as state variables of a CS and the correlations between them were investigated. First, we used the MI concept to unveil potential relationships in the data. Second, we considered the SSP to characterize the system's behavior. Third, we compared the annual state space curves and adopted HC and MDS techniques to unveil existing patterns. Both tools identified the same clusters and exposed similarities between groups of consecutive years. The proposed analysis and findings can further contribute to better understand FF behavior and reveal hidden features not captured by standard tools.

References

Alvarado E, Sandberg DV and Pickford SG (1998) Modeling large forest fires as extreme events. Northwest Science 72: 66–75.

Bak P (1990) Self-organized criticality. *Physica A: Statistical Mechanics and its Applications* 163(1): 403–409.

Belo-Pereira M, Dutra E and Viterbo P (2011) Evaluation of global precipitation data sets over the Iberian Peninsula. *Journal of Geophysical Research: Atmospheres* 116: D20101.

Boer MM, Sadler RJ, Bradstock RA, Gill AM and Grierson PF (2008) Spatial scale invariance of southern Australian forest fires mirrors the scaling behaviour of fire-driving weather events. *Landscape Ecology* 23(8): 899–913.

Brooks ML, D'Antonio CM, Richardson DM, et al. (2004) Effects of invasive alien plants on fire regimes. *BioScience* 54(7): 677–688.

Carlson JM and Doyle J (1999) Highly optimized tolerance: A mechanism for power laws in designed systems. *Physical Review E* 60(2): 1412.

Certini G (2005) Effects of fire on properties of forest soils: a review. *Oecologia* 143(1): 1–10.

Chandler C, Cheney P, Thomas P, et al. (1983) *Fire in Forestry*. New York: John Wiley & Sons.

Cox TF and Cox MA (2000) *Multidimensional Scaling*. Boca Raton: CRC Press.

Dale VH, Joyce LA, McNulty S, et al. (2001) Climate change and forest disturbances: Climate change can affect forests by altering the frequency, intensity, duration, and timing of fire, drought, introduced species, insect and pathogen outbreaks, hurricanes, windstorms, ice storms, or landslides. *BioScience* 51(9): 723–734.

Drossel B and Schwabl F (1992) Self-organized critical forest-fire model. *Physical Review Letters* 69(11): 1629.

Flannigan M, Stocks BJ and Wotton B (2000) Climate change and forest fires. *Science of the Total Environment* 262(3): 221–229.

Fraser AM and Swinney HL (1986) Independent coordinates for strange attractors from mutual information. *Physical Review A* 33(2): 1134.

Grassberger P and Kantz H (1991) On a forest fire model with supposed self-organized criticality. *Journal of Statistical Physics* 63(3–4): 685–700.

Hartigan JA (1975) *Clustering Algorithms*. New York: John Wiley & Sons.

Holmes TP, Huggett RJ Jr and Westerling AL (2008) Statistical analysis of large wildfires. In: *The Economics of Forest Disturbances*. Netherlands: Springer, pp. 59–77.

Jain AK (2010) Data clustering: 50 years beyond K-means. *Pattern Recognition Letters* 31(8): 651–666.

Kirilenko AP and Sedjo RA (2007) Climate change impacts on forestry. *Proceedings of the National Academy of Sciences of the United States of America* 104(50): 19697–19702.

Lasaponara R, Santulli A and Telesca L (2005) Time-clustering analysis of forest-fire sequences in southern Italy. *Chaos, Solitons & Fractals* 24(1): 139–149.

Logan JA, Regniere J and Powell JA (2003) Assessing the impacts of global warming on forest pest dynamics. *Frontiers in Ecology and the Environment* 1(3): 130–137.

Lopes AM and Tenreiro Machado JA (2014) Analysis of temperature time-series: Embedding dynamics into the MDS method. *Communications in Nonlinear Science and Numerical Simulation* 19(4): 851–871.

Malamud BD, Morein G and Turcotte DL (1998) Forest fires: An example of self-organized critical behavior. *Science* 281(5384): 1840–1842.

Matsuda H (2000) Physical nature of higher-order mutual information: Intrinsic correlations and frustration. *Physical Review E* 62(3): 3096.

Moritz MA, Morais ME, Summerell LA, Carlson J and Doyle J (2005) Wildfires, complexity, and highly optimized tolerance. *Proceedings of the National Academy of Sciences of the United States of America* 102(50): 17912–17917.

Page SE, Siegert F, Rieley JO, et al. (2002) The amount of carbon released from peat and forest fires in Indonesia during 1997. *Nature* 420(6911): 61–65.

Polderman JW and Willems JC (1998) *Introduction to Mathematical Systems Theory: A Behavioral Approach.* New York: Springer.

Reed WJ and McKelvey KS (2002) Power-law behaviour and parametric models for the size-distribution of forest fires. *Ecological Modelling* 150(3): 239–254.

Ricotta C, Avena G and Marchetti M (1999) The flaming sandpile: self-organized criticality and wildfires. *Ecological Modelling* 119(1): 73–77.

Rittmaster R, Adamowicz W, Amiro B and Pelletier R (2006) Economic analysis of health effects from forest fires. *Canadian Journal of Forest Research* 36(4): 868–877.

Shannon CE (2001) A mathematical theory of communication. *Mobile Computing and Communications Review* 5(1): 3–55.

Smith JK, Lyon LJ, Huff M, et al. (2000) *Wildland fire in ecosystems. Effects of fire on fauna.* Report no. RMRS-GTR-42. Rocky Mountain Research Station: USDA Forest Service.

Song W, Wang J, Satoh K and Fan W (2006) Three types of power-law distribution of forest fires in Japan. *Ecological Modelling* 196(3): 527–532.

Telesca L, Amatulli G, Lasaponara R, Lovallo M and Santulli A (2005) Time-scaling properties in forest-fire sequences observed in Gargano area (southern Italy). *Ecological Modelling* 185(2): 531–544.

Tenreiro Machado JA and Lopes AM (2012) Dynamical analysis of the global warming. *Mathematical Problems in Engineering* 2012: 971641.

Tenreiro Machado JA and Lopes AM (2013) Analysis and visualization of seismic data using mutual information. *Entropy* 15(9): 3892–3909.

Tenreiro Machado JA and Lopes AM (2014) Analysis of forest fires by means of pseudo phase plane and multidimensional scaling methods. *Mathematical Problems in Engineering* 2014: 575872.

Zheng H, Song W and Wang J (2008) Detrended fluctuation analysis of forest fires and related weather parameters. *Physica A: Statistical Mechanics and its Applications* 387(8): 2091–2099.

Article

Controllability of nonlinear implicit neutral fractional Volterra integrodifferential systems

K Balachandran[1], S Divya[1], M Rivero[2] and JJ Trujillo[3]

Abstract

In this paper, the control problem of nonlinear neutral fractional Volterra integrodifferential systems with implicit fractional derivative is established. Such kind of problems involve a number of problems on complex media. Sufficient conditions for controllability are obtained through the notions of a condensing map and measure of noncompactness of a set. A example to check the main results included in this paper is included.

1. Introduction

In recent years, fractional differential equations have been emerging as a new branch of applied mathematics which have been used to model many practical systems in science and engineering (Ahmed and Elgazzar, 2007; Bagley and Torvik, 1983; El-Sayed, 1996; Metzler and Klafter, 2000).

Indeed fractional differential equations can be considered as a complementary tool to model classical linear or nonlinear differential equations of the dynamics of complex processes on complex media. Moreover, Bonilla et al. (2007) have shown some fractional models involving Riemann–Liouville fractional derivative can contain solutions impossible for the classical differential models. The theory of fractional differential equations has been investigated extensively by many authors (see, for example, Hernandez et al., 2010; Kilbas et al., 2006; Lakshmikantham, 2008; Miller and Ross, 1993; Oldham and Spanier, 1974; Podlubny, 1999). Various types of models are reformulated and articulated in terms of fractional differential equations and so the physical meaning will be integrated in the mathematical models more practically.

Controllability, observability and stabilizability are the qualitative properties on fractional dynamical systems which are the latest issues that are dealt with by many researchers. The fractional control theory is a generalization of the classical control theory.

Any control system is said to be controllable if every state corresponding to this process can be affected or controlled in respective time by some control signals. Controllability results for linear and nonlinear integer order dynamical systems in finite-dimensional spaces have been discussed by many authors (Balachandran and Dauer, 1987; Klamka, 1993, 2008). Recently Balachandran and Kokila (2012a); Balachandran et al. (2012c) established the controllability results for linear and nonlinear fractional dynamical systems using Schauder's fixed point theorem and extended the results for the same systems with multiple time-varying delays in control as well as distributed delays in control variables in Balachandran et al. (2012b,d).

It is well known that the neutral differential equation is a very special class of ordinary differential equation and it arises in compartmental models in which the system can be divided into separate compartments,

[1]Department of Mathematics, Bharathiar University, Coimbatore, India
[2]Departamento de Matemática, Estadítica e I.O., Universidad de La Laguna, Tenerife, Spain
[3]Departamento de Análisis Matemático, Universidad de La Laguna, Tenerife, Spain

Corresponding author:
JJ Trujillo, Departamento de Análisis Matemático, Universidad de La Laguna, 38271 La Laguna, Tenerife, Spain.
Email: jtrujill@ullmat.es

marking the pathways of material flow between compartments and the possible outflow into the inflow from the environment of the system (Gyori and Wu, 1991). These models are frequently used in theoretical epidemiology, physiology and population dynamics to describe the evolution of systems. These equations can be remodeled as neutral fractional differential equations or neutral fractional Volterra integrodifferential equations. The main aim of this present article is to study the controllability for such fractional systems.

The problem of controllability of linear neutral systems has been investigated by Banks and Kent (1972) and Jacobs and Langenhop (1976). The motivation for neutral systems and their importance in other fields can be found in Hale (1972). Chukwu (1987) considered the Euclidean controllability of a neutral system with nonlinear base. Onwuatu (1984) discussed the problem for nonlinear systems of neutral functional differential equations with limited controls. Gahl (1978) derived a set of sufficient conditions for the controllability of nonlinear neutral systems through a fixed-point method. Balachandran and Balasubramaniam (1994) established sufficient conditions for the controllability of nonlinear neutral Volterra integrodifferential systems. Anichini et al. (1986) studied the problem through the notions of condensing map and measure of non-compactness of a set. They used the fixed-point theorem due to Sadovskii. Balachandran and Kokila (2013b) derived a set of sufficient conditions for the controllability of nonlinear implicit fractional dynamical systems through the notion of measure of non-compactness of a set and Darbo's fixed point theorem and extended the results for fractional integrodifferential systems with prescribed controls (Balachandran and Kokila, 2013a). In this paper we study the controllability of nonlinear neutral fractional Volterra integrodifferential systems with implicit derivative by suitably adopting the technique of Anichini et al. (1986).

2. Preliminaries

In this section, we present some definitions and preliminary facts that will be used in the paper (Kexue and Jigen, 2011; Kilbas et al., 2006; Miller and Ross, 1993; Podlubny, 1999).

Let α, $\beta > 0$ with $n - 1 < \alpha < n$, $n - 1 < \beta < n$ and $n \in \mathbb{N}$, D is the usual differential operator. Let $\mathbb{R}^m$ be the m-dimensional Euclidean space, $\mathbb{R}_+ = [0, \infty)$ and suppose $f \in L_1(\mathbb{R}_+)$. The Riemann–Liouville fractional integral operator is defined by

$$(I_{0+}^\alpha f)(t) = \frac{1}{\Gamma(\alpha)} \int_0^t (t-s)^{\alpha-1} f(s) \mathrm{d}s$$
$$(D_{0+}^\alpha f)(t) = D^n (I_{a+}^{n-\alpha} f)(t)$$

and the Caputo fractional derivative is defined by

$$^C D_{0+}^\alpha f(t) = (I_{0+}^{n-\alpha} D^n f)(t), \quad (0 < \alpha < 1)$$

and, in particular, $I_{0+}^\alpha {}^C D_{0+}^\alpha f(t) = f(t) - f(0)$.

The following is a well-known relation, for a finite interval $[a, b]$,

$$^C D_{0+}^\alpha f(t) = D_{0+}^\alpha f(t) - \sum_{k=0}^{n-1} \frac{t^{k-\alpha}}{\Gamma(k-\alpha+1)} f^{(k)}(0^+),$$
$$(n = \Re(\alpha) + 1)$$

The Laplace transform of the Caputo fractional derivative is

$$\mathcal{L}\{^C D_{0+}^\alpha f(t)\}(s) = s^\alpha F(s) - \sum_{k=0}^{n-1} f^k(0^+) s^{\alpha-k-1}$$

The Riemann–Liouville fractional derivatives have singularity at zero and the fractional differential equations in the Riemann–Liouville sense require initial conditions of special form lacking physical interpretation. To overcome this difficulty Caputo introduced a new definition of fractional derivative but in general, both the Riemann–Liouville and the Caputo fractional operators possess neither semigroup nor commutative properties, which are inherent to the derivatives on integer order. Due to this fact, the concept of sequential fractional derivatives are discussed in Kilbas et al. (2006).

For $n \in \mathbb{N}$ the sequential fractional derivative for a suitable function f is defined by

$$f^{(k\alpha)} := (D^{k\alpha} f)(t) = (D^\alpha D^{(k-1)\alpha} f)(t)$$

where $k = 1, \ldots, n$, $(D^\alpha f)(t) = f(t)$ and D^α is any fractional differential operator, here we take it as $^C D^\alpha$.

Next we give the definition of Mittag–Leffler function as $E_{\alpha,\beta}(z) = \sum_{k=0}^\infty \frac{z^k}{\Gamma(\alpha k + \beta)}$, for $\alpha, \beta > 0$.

The Laplace transform of $E_{\alpha,\beta}(z)$ is $\mathcal{L}\{t^{\beta-1} E_{\alpha,\beta}(\pm a t^\alpha)\}(s) = \frac{s^{\alpha-\beta}}{s^\alpha \mp a}$, for $Re(s) > |a|^{\frac{1}{\alpha}}$ and $Re(\beta) > 0$. In particular, for $\beta = 1$,

$$E_{\alpha,1}(az^\alpha) = E_\alpha(az^\alpha) = \sum_{k=0}^\infty \frac{a^k z^{\alpha k}}{\Gamma(\alpha k + 1)}, \quad a, z \in \mathbb{C}$$

have the interesting property $^C D^\alpha E_\alpha(az^\alpha) = a E_\alpha(az^\alpha)$ and $\mathcal{L}\{E_\alpha(\pm a t^\alpha)\}(s) = \frac{s^{\alpha-1}}{s^\alpha \mp a}$.

For brevity, we take I_{0+}^α as I^α and $^C D_{0+}^\alpha$ as $^C D^\alpha$. In the following, we obtain the solution representation of various forms of integrodifferential equations.

First, consider the following linear fractional integrodifferential equation

$$\left.\begin{array}{c} {}^{C}D^{\alpha}x(t) = Ax(t) + \int_0^t H(t-s)x(s)\mathrm{d}s + f(t), \\ (0 < \alpha < 1),\ t \in [0, t_1] := J \\ x(0) = x_0 \end{array}\right\} \quad (1)$$

where the state vector $x(t) \in \mathbb{R}^n$, A is an $n \times n$ matrix, $H(t)$ is an $n \times n$ continuous matrix and $f(t)$ is a continuous function. By the Laplace transformation approach, we have the solution as (Balachandran and Kokila, 2013a; Kexue and Jigen, 2011)

$$x(t) = R_{\alpha}(t) + \int_0^t (t-s)^{\alpha-1} R_{\alpha,\alpha}(t-s)f(s)\mathrm{d}s$$

where $R_{\alpha}(t)$ is an $n \times n$ matrix satisfying the condition stated in (Balachandran and Kokila, 2013a) and $R_{\alpha,\alpha}(\theta) = \theta^{1-\alpha} D I^{\alpha} R_{\alpha}(\theta)$.

Next consider the linear neutral fractional Volterra integrodifferential equation of the form

$$\left.\begin{array}{c} {}^{C}D^{\alpha}\left[x(t) - \int_0^t C(t-s)x(s)\mathrm{d}s\right] \\ = Ax(t) + \int_0^t H(t-s)x(s)\mathrm{d}s \\ x(0) = x_0, \quad 0 < \alpha < 1,\ t \in J \end{array}\right\}$$

where the state vector $x(t) \in \mathbb{R}^n$, A is an $n \times n$ matrix, $C(t)$ and $H(t)$ are continuous $n \times n$ matrices. By the Laplace transformation approach, we have the solution as

$$\left.\begin{array}{c} \mathcal{L}^{-1}\{X(s)\}(t) = \mathcal{L}^{-1}\left\{\frac{s^{\alpha-1}}{(s^{\alpha}(I-\mathcal{L}(C))-A-\mathcal{L}(H))}\right\}(t)x_0 \\ x(t) = Z_{\alpha}(t)x_0 \end{array}\right\}$$

where $Z_{\alpha}(t)$ is an $n \times n$ solution matrix satisfying the following conditions:

a. $Z_{\alpha}(0) = I$;
b. ${}^{C}D^{\alpha}\left[Z_{\alpha}(t) - \int_0^t C(t-s)Z_{\alpha}(s)\mathrm{d}s\right] = AZ_{\alpha}(t) + \int_0^t H \times (t-s)Z_{\alpha}(s)\mathrm{d}s$;
c. $\mathcal{L}\{Z_{\alpha}(t)\}(s) = \int_0^t e^{-st}Z_{\alpha}(t)\mathrm{d}t := s^{\alpha-1}(s^{\alpha}(I-\mathcal{L}(C)) - A - \mathcal{L}(H))^{-1}$.

For the fractional integrodifferential system

$$\left.\begin{array}{c} {}^{C}D^{\alpha}\left[x(t) - \int_0^t C(t-s)x(s)\mathrm{d}s\right] \\ = Ax(t) + \int_0^t H(t-s)x(s)\mathrm{d}s + Bu(t) \\ x(0) = x_0, \quad t \in J,\ 0 < \alpha < 1 \end{array}\right\} \quad (2)$$

the solution is given by

$$\begin{aligned} x(t) &= \mathcal{L}^{-1}\left\{\frac{s^{\alpha-1}}{(s^{\alpha}(I-C(s))-A-H(s))}\right\}(t)x_0 \\ &\quad + \mathcal{L}^{-1}\left\{\frac{1}{(s^{\alpha}(I-C(s))-A-H(s))}\right\}(t)L^{-1}\{BU(s)\}(t) \\ &= Z_{\alpha}(t)x_0 + \int_0^t (t-s)^{\alpha-1}Z_{\alpha,\alpha}(t-s)Bu(s) \end{aligned}$$

where $Z_{\alpha,\alpha}(\theta) = \theta^{1-\alpha} D I^{\alpha} Z_{\alpha}(\theta)$.

Next we summarize some facts concerning condensing maps; for definitions and results about the measure of non-compactness and related topics, the reader can refer to the papers Anichini et al. (1986) and Sadovskii (1972).

Definition 2.1. Let X be a subset of a Banach space. An operator $T : X \to X$ is called condensing if, for any bounded subset $E \subset X$ with $\mu(E) \neq 0$, we get $\mu(T(E)) < \mu(E)$, where $\mu(E)$ denotes the measure of non-compactness of the set E, whose properties are given in Dacka (1980).

Let $C_n(J)$ denote the Banach space of continuous $\mathbb{R}^n-$ valued functions on the interval J. For $x \in C_n(J)$ and $h > 0$, let

$$\theta(x, h) = \sup\{|x(t) - x(s)| : t, s \in J \text{ and } |t - s| \leq h\} \quad (3)$$

and write $\theta(E, h) = \sup_{x \in E} \theta(x, h)$ so that $\theta(E, .)$ is the modulus of continuity of a bounded set E and let Ω be the set of functions $\omega : \mathbb{R}^+ \to \mathbb{R}^+$ that are right continuous and nondecreasing such that $\omega(r) < r$, for $r > 0$.

Lemma 2.1 (Sadovskii, 1972). Let $X \subset C_n(J)$ and let β and γ be functions defined on $[0, t_1]$ such that $\lim_{s \to 0} \beta(s) = \lim_{s \to 0} \gamma(s) = 0$. If a mapping $T : X \to C_n(J)$ exists such that it maps bounded sets into bounded sets and is such that

$$\theta(T(x), h) < \omega(\theta(x, \beta(h))) + \gamma(h)$$

with $\omega \in \Omega$, $x \in X$ and for all $h \in [0, t_1]$, then T is a condensing mapping.

Lemma 2.2 (Anichini et al., 1986; Sadovskii, 1972). Let $X \subset C_n(I)$, $I = [0, 1]$ and $S \subset X$ be a bounded closed convex set. Let $P : I \times S \to X$ be a continuous operator such that, for any $\lambda \in I$, the map $P(\lambda, .) : S \to X$ is condensing. If $x \neq P(\lambda, x)$ for any $\lambda \in I$ and any $x \in \partial S$ (the boundary of S), then $P(1, .)$ has a fixed point.

Finally it is possible to show that, for any bounded and equicontinuous set E in $C_n^{\alpha}(I)$, the following relation holds:

$$\mu_{C_n^{\alpha}}(E) \equiv \mu_1(E) \equiv \mu({}^{C}D^{\alpha}E) \equiv \mu_{C_n}({}^{C}D^{\alpha}E)$$

where ${}^{C}D^{\alpha}E = \{{}^{C}D^{\alpha}x : x \in E\}$.

3. Controllability results

Similar to the conventional controllability concept we define the controllability of fractional dynamical systems as follows.

Definition 3.1. System (2) is said to be controllable on J if, for every $x_0,\ x_1 \in \mathbb{R}^n$, there exists a control $u(t)$ such that the solution $x(t)$ of the system (2) satisfies the condition $x(0) = x_0$ and $x(t_1) = x_1$.

Define the controllability matrix

$$G(0, t_1) = \int_0^{t_1} (t_1 - s)^{\alpha-1} [Z_{\alpha,\alpha}(t_1 - s)B][Z_{\alpha,\alpha}(t_1 - s)B]^* \, \mathrm{d}s$$

where the star denotes the matrix transpose. It is proved that the linear system (2) is controllable on J if and only if the controllability matrix $G(0, t_1)$ is positive definite, for some $t_1 > 0$ (Balachandran and Kokila, 2013a).

Consider the nonlinear neutral fractional Volterra integrodifferential system of the form

$$\left.\begin{aligned}
{}^C D^\alpha &\left[x(t) - \int_0^t C(t-s)x(s)\mathrm{d}s - g(t) \right] \\
&= Ax(t) + \int_0^t H(t-s)x(s)\mathrm{d}s + Bu(t) \\
&\quad + f(t, x(t), {}^C D^\alpha x(t), u(t)) \\
&\qquad\qquad x(0) = x_0
\end{aligned}\right\} \quad (4)$$

where $t \in J$, $0 < \alpha < 1$, $x \in \mathbb{R}^n$, A, B are respectively $n \times n$, $n \times m$ matrices and the control function $u \in \mathbb{R}^m$; $C(t)$ and $H(t)$ are $n \times n$ continuous matrix valued functions; f and g are respectively continuous and continuously differentiable n-vector functions.

The solution of (4) is given by (Balachandran and Kokila, 2013a)

$$\begin{aligned}
x(t) &= Z_\alpha(t)x_0 + \int_0^t (t-s)^{\alpha-1} Z_{\alpha,\alpha}(t-s)[Bu(s) \\
&\quad + f(s, x(s), {}^C D^\alpha x(s), u(s))]\mathrm{d}s + \frac{1}{\Gamma(1-\alpha)} \\
&\quad \times \int_0^t \int_0^s (t-s)^{\alpha-1}(s-\tau)^{-\alpha} Z_{\alpha,\alpha}(t-s) g'(\tau)\mathrm{d}\tau\mathrm{d}s
\end{aligned} \quad (5)$$

Now we prove the main result of the paper.

Theorem 3.1. Suppose that the following conditions hold.

(i) The symmetric matrix $G(0, t_1)$ is nonsingular for some $t_1 > 0$.

(ii) There exists a continuous nondecreasing function $\omega : \mathbb{R}^+ \to \mathbb{R}^+$ with $\omega(r) < r$ such that

$$|f(t, x, y, u) - f(t, x, z, u)| < \omega(|y - z|);$$
$$\forall\, (t, x, y, u) \in J \times \mathbb{R}^{2n} \times \mathbb{R}^m$$

(iii) $\lim_{|x| \to \infty} \frac{f(t,x,y,u)}{|x|} = 0$. Then the system (4) is controllable on J.

Proof. Define the nonlinear transformation

$$T: \ C_m(J) \times C_n^\alpha(J) \to C_m(J) \times C_n^\alpha(J)$$

by

$$T(u, x)(t) = (T_1\, (u, x)(t),\, T_2\, (u, x)(t))$$

where the pair of operators T_1 and T_2 is defined as

$$\begin{aligned}
T_1(u, x)(t) &= B^* Z_{\alpha,\alpha}^*(t_1 - t) G^{-1}\bigg[x_1 - Z_\alpha(t_1)x_0 \\
&\quad \times \int_0^{t_1} (t_1 - s)^{\alpha-1} Z_{\alpha,\alpha}(t_1 - s) f(s, x(s), \\
&\qquad {}^C D^\alpha x(s), u(s))\mathrm{d}s \\
&\quad - \frac{1}{\Gamma(1-\alpha)} \int_0^{t_1} \int_0^s (t_1 - s)^{\alpha-1}(s-\tau)^{-\alpha} \\
&\qquad \times Z_{\alpha,\alpha}(t_1 - s) g'(\tau)\mathrm{d}\tau\mathrm{d}s \bigg]
\end{aligned}$$

$$\begin{aligned}
T_2(u, x)(t) &= Z_\alpha(t)x_0 + \int_0^t (t-s)^{\alpha-1} Z_{\alpha,\alpha}(t-s) \\
&\quad \times BT_1(u, x)(s)\mathrm{d}s + \int_0^t (t-s)^{\alpha-1} Z_{\alpha,\alpha}(t-s) \\
&\quad \times f(s, x(s), {}^C D^\alpha x(s), T_1(u, x)(s))\mathrm{d}s \\
&\quad + \frac{1}{\Gamma(1-\alpha)} \int_0^t \int_0^s (t-s)^{\alpha-1}(s-\tau)^{-\alpha} \\
&\quad \times Z_{\alpha,\alpha}(t-s) g'(\tau)\mathrm{d}\tau\mathrm{d}s
\end{aligned}$$

Since all of the functions involved in the definition of the operator T are continuous, T is continuous. $\eta^0 = (u^0, x^0) \in C_m(J) \times C_n^\alpha(J)$ and $\eta = (u, x) \in [C_m(J) \times C_n^\alpha(J)]\backslash(0, 0)$.

Then the equation $\eta^0 = \eta - \lambda T(\eta)$, where $\lambda \in [0, 1]$, can be written equivalently as

$$u = u^0 + \lambda T_1(u, x) \quad (6)$$

$$x = x^0 + \lambda T_2(u, x) \quad (7)$$

The condition (iii) says that, for any $\epsilon > 0$, there exists $R > 0$ such that if $|x| > R$ then $|f(t, x, y, u)| < \epsilon|x|$. Then (6) gives

$$\|u\| \le |u^0| + k_1 + a_1 a_2^2 a_3 \epsilon t_1^\alpha \alpha^{-1}|x| \qquad (8)$$

and from (7), by applying Gronwall's inequality, we have

$$\|x\| \le [|x^0| + a_4 x_0 + a_1 a_2 t_1^\alpha \alpha^{-1}(k_1 + a_1 a_2^2 a_3 \epsilon|x|t_1^\alpha \alpha^{-1}$$
$$+ a_2 a_5 \Gamma(\alpha)t_1^\alpha)]\exp(t_1^\alpha \alpha^{-1} a_2 \epsilon) \qquad (9)$$

where

$$a_1 = \|B\|; \quad a_2 = \sup\|Z_{\alpha,\alpha}(t_1 - s)\|$$
$$a_3 = \|G^{-1}(0, t_1)\|; \quad a_4 = \|Z_\alpha(t_1)\|$$
$$a_5 = \sup\|g'(t)\|; \quad a_6 = |x_0 - g(0)|$$
$$a_7 = \sup\|g(t)\|; \quad a_8 = \sup\|{}^C D^\alpha g(t)\|$$
$$k_1 = a_1 a_2 a_3[|x_1| + a_4 x_0 + a_2 a_5 \Gamma(\alpha)t_1]$$

Note that

$${}^C D^\alpha\left[T_2(u, x)(t) - \int_0^t C(t - s)T_2(u, x)(s)\mathrm{d}s - g(t)\right]$$
$$= AT_2(u, x)(t) + \int_0^t H(t - s)T_2(u, x)(s)\mathrm{d}s$$
$$+ BT_1(u, x)(t) + f(t, x(t), {}^C D^\alpha x(t), T_1(u, x)(t))$$

Applying Gronwall's inequality, we have

$$\|T_2(u, x)(t)\|$$
$$\le \left[a_6 + a_7 + \frac{a_1\|T_1(u, x)(t)\|t_1^\alpha}{\Gamma(\alpha + 1)} + \frac{\epsilon|x|t_1^\alpha}{\Gamma(\alpha + 1)}\right]\exp(A_0),$$
$$(10)$$

where

$$A_0 = \int_0^{t_1}\left|\frac{(t_1 - s)^{\alpha-1}A}{\Gamma(\alpha)} + C(t_1 - s)\right.$$
$$\left. + \frac{1}{\Gamma(\alpha + 1)}\int_0^{t_1}(t_1 - s)^\alpha H(\eta - s)\mathrm{d}\eta\right|\mathrm{d}s$$

Taking the Caputo derivative with respect to t, we obtain, from (7),

$${}^C D^\alpha x(t) = {}^C D^\alpha x^0(t) + \lambda^C D^\alpha(T_2(u, x)(t))$$

and using Leibnitz's rule gives

$$\left|{}^C D^\alpha x(t)\right| \le \left|{}^C D^\alpha x^0\right| + a\|T_2(u, x)(t)\| + a_1\|T_1(u, x)(t)\|$$
$$+ \epsilon|x| + a_7$$

where

$$a = \|A\| + \frac{\sup\|\dot{C}(t)\|t_1^{2-\alpha}}{\Gamma(3 - \alpha)} + \frac{|C(0)|t_1^{1-\alpha}}{\Gamma(2 - \alpha)} + \sup\|H(t)\|t_1$$
$$(11)$$

Thus, from (9), we have

$$\left|{}^C D^\alpha x(t)\right| \le \left|{}^C D^\alpha x^0\right| + k_2 + |x|\left[a_1^2 a_2^2 a_3 \epsilon t_1^\alpha \alpha^{-1}(at_1^\alpha \exp(A_0)\right.$$
$$\left. + 1) + \frac{a\epsilon|x|t_1^\alpha \exp(A_0)}{\Gamma(\alpha + 1)} + \epsilon\right]$$

where

$$k_2 = k_1\left[a_1\left(\frac{at_1^\alpha \exp(A_0)}{\Gamma(\alpha + 1)} + 1\right) + a(a_6 + a_7)\exp(A_0) + a_8\right]$$

From (8), (9) and (11), we have respectively

$$\|u\| - a_1 a_2^2 a_3 \epsilon|x|t_1^\alpha \alpha^{-1} \le |u^0| + k_1$$
$$\|x\|[\exp(-t_1^\alpha \alpha^{-1} a_2 \epsilon) - a_1^2 a_2^3 a_3 \epsilon t_1^{2\alpha} \alpha^{-2}] \le k_3 + |x^0|$$

where

$$k_3 = a_4 x_0 + a_1 a_2 t_1^\alpha \alpha^{-1} k_1 + a_2 a_5 \Gamma(\alpha)t_1$$

and

$$\left|{}^C D^\alpha x(t)\right| - |x|[a_1^2 a_2^2 a_3 \epsilon t_1^\alpha \alpha^{-1}(at_1^\alpha \exp(A_0) + 1)$$
$$+ \frac{1}{\Gamma(\alpha + 1)}a\epsilon t_1^\alpha \exp(A_0) + \epsilon] \le k_2 + |{}^C D^\alpha x^0|$$

Taking the sum of all of the above quantities, we have

$$\|u\| - k\|x\| + \left|{}^C D^\alpha x(t)\right|$$
$$\le |u^0| + |x^0| + |{}^C D^\alpha x^0| + k_1 + k_2 + k_3$$

where

$$k = a_1 a_2^2 \epsilon t_1^\alpha \alpha^{-1} - \exp(-a_2 \epsilon t_1^\alpha \alpha^{-1}) + a_1^2 a_2^2 a_3 \epsilon t_1^\alpha \alpha^{-1}$$
$$(at_1^\alpha \exp(A_0) + 1) + a_1^2 a_2^3 a_3 \epsilon t_1^{2\alpha} \alpha^{-2} + \epsilon]$$

Then, for appropriate positive constants, k_4, k_5 and k_6, we can write

$$\|u\| - [\epsilon k_4 - \exp(-\epsilon k_5)]\|x\| + \|CD^\alpha x(t)\|$$
$$\le |u^0| + |x^0| + |{}^C D^\alpha x^0| + k_6$$

Now we divide by $\|u\| + \|x\| + |^C D^\alpha x(t)|$ and by the arbitrariness of ϵ, we get the existence of a sufficiently large ball $S \subset C_m(J) \times C_n^\alpha(J)$ such that

$$\eta - \lambda T(\eta) > 0 \quad \text{for } \eta = (u, x) \in \partial S$$

In the next step we want to show that T is a condensing map. To this aim, we note that $T_1 : C_m(J) \to C_m(J)$ is a compact operator(from the Ascoli–Arzela theorem) and then, if E is a bounded set, $\mu(T_1(E)) = 0$. Then it will be enough to show that T_2 is a condensing operator. To do this, we use the modulus of continuity argument and the fact that

$$\mu_1(T_2(E)) = \mu(^C D^\alpha T_2(E)) = \frac{1}{2}\theta_0(^C D^\alpha T_2(E))$$

We consider the modulus of continuity of $^C D^\alpha T_2(u, x)(.)$:

$$
\begin{aligned}
&|^C D^\alpha T_2([u, x](t)) - {}^C D^\alpha T_2([u, x](s))| \\
&\leq |AT_2([u, x])(t) - AT_2([u, x])(s)| + |BT_1([u, x])(t) \\
&\quad - BT_1([u, x])(s)| + \left| \int_0^t H(t - s)T_2([u, x](\eta))d\eta \right. \\
&\quad \left. - \int_0^s H(s - \eta)T_2([u, x](\eta))d\eta \right| + |f(t, x(t), \\
&\quad {}^C D^\alpha x(t), u(t)) - f(s, x(s), {}^C D^\alpha x(s), u(s))| \\
&\quad + |^C D^\alpha g(t) - {}^C D^\alpha g(s)| + \left| \frac{1}{\Gamma(1 - \alpha)} \int_0^t (t - s)^{-\alpha} \right. \\
&\quad \times \int_0^s \dot{C}(s - \tau)T_2[(u, x)](\tau)d\tau ds - \frac{1}{\Gamma(1 - \alpha)} \\
&\quad \left. \times \int_0^s (s - \tau)^{-\alpha} \int_0^\tau \dot{C}(\tau - \sigma)T_2[(u, x)](\sigma)d\sigma d\tau \right| \\
&\quad + |C(0)T_2[(u, x)](t) - C(0)T_2[(u, x)](s)| \qquad (12)
\end{aligned}
$$

For the first and last three terms of the right-hand side of (12), we give the upper estimate as $\beta_0(|t - s|)$; and for fourth term $\omega(|^C D^\alpha x(t) - {}^C D^\alpha x(s)|) + \beta_1(|t - s|)$, with $\lim_{h\to 0}\beta_i(h) = 0$. Hence,

$$\theta(^C D^\alpha T_2([u, x](t)), h) \leq \omega(\theta(^C D^\alpha E, h)) + \beta(h)$$

where $\beta = \beta_0 + \beta_1$. Therefore, by Lemma 2.1, we get $\theta_0(^C D^\alpha T_2(E)) < \theta_0(^C D^\alpha E)$. Hence, from

$$
\begin{aligned}
2\mu(T_2(E)) &= 2\mu(^C D^\alpha T_2(E)) = \theta_0(^C D^\alpha T_2(E)) \\
&< \theta_0(^C D^\alpha E) = 2\mu(^C D^\alpha E) = 2\mu_1(E)
\end{aligned}
$$

it follows that $\mu_1(T(E)) < \mu_1(E)$. Then the existence of the fixed point for operator T follows from Lemma 2.2;

that is, there exist functions $u \in C_m(J)$ and $x \in C_n^\alpha(J)$ such that $T(u, x) = (u, x)$ that is

$$u(t) = T_1(u, x)(t), \quad x(t) = T_2(u, x)(t)$$

These functions are the required solutions. Further it is easy to verify that the function $x(.)$ given above of the system (4) satisfies $x(t_1) = x_1$ for every $x(0) \in \mathbb{R}^n$. Hence, the system (4) is controllable.

4. Example

Consider the nonlinear neutral fractional Volterra integrodifferential system involving the fractional derivative (4) with $\alpha = 1/2$

$$x(t) = \begin{pmatrix} x_1(t) \\ x_2(t) \end{pmatrix}, \quad A = \begin{pmatrix} 1 & 1 \\ -2 & 1 \end{pmatrix}, \quad B = \begin{pmatrix} 1 & 0 \\ 1 & 1 \end{pmatrix},$$

$$g(t) = \begin{pmatrix} 0 \\ t\sin t \end{pmatrix}$$

$$f(t, x(t), {}^C D^{1/2}x(t), u(t)) = \begin{pmatrix} 0 \\ \dfrac{x^2}{\sqrt{1 + u^2}} + \tan^{-1}[^C D^{1/2}x(t)] \end{pmatrix}$$

and

$$C(t) = \frac{1}{\sqrt{\pi}}\begin{pmatrix} 4t^{-1/2} & -t^{-1/2} \\ 2t^{-1/2} & 3t^{-1/2} \end{pmatrix}, \quad H(t) = \frac{1}{\sqrt{\pi}}\begin{pmatrix} t^{-1/2} & 0 \\ 0 & t^{-1/2} \end{pmatrix}$$

are defined and continuous on $(0, t_1]$.

The initial condition is given by $x(0) = \begin{pmatrix} 0 \\ 1 \end{pmatrix}$.

For the linear part of the above system the solution is given by

$$x(t) = Z_{1/2}(t)x(0) \qquad (13)$$

where

$$Z_{1/2}(t) = \begin{pmatrix} P_1(t) & 0 \\ 0 & P_2(t) \end{pmatrix}$$

with

$$
\begin{aligned}
P_1(t) &= \frac{5 + \sqrt{29}}{2\sqrt{29}} E_{1/2}((5 + \sqrt{29})t^{1/2}) \\
&\quad - \frac{5 - \sqrt{29}}{2\sqrt{29}} E_{1/2}((5 - \sqrt{29})t^{1/2})
\end{aligned}
$$

$$P_2(t) = \frac{1 + \sqrt{2}}{2\sqrt{2}} E_{1/2}((1 + \sqrt{2})t^{1/2})$$
$$- \frac{1 - \sqrt{2}}{2\sqrt{2}} E_{1/2}((1 - \sqrt{2})t^{1/2})$$

where $Z_{1/2}(t)$ is the resolvent matrix and satisfies the conditions (a), (b) and (c) for $\alpha = 1/2$.

The solution of the nonlinear system takes the following form

$$x(t) = Z_{1/2}(t)x_0 + \int_0^t (t - s)^{-1/2} Z_{1/2,1/2}(t - s)$$
$$\times [Bu(s) + f(s, x(s), {}^C D^{1/2} x(s), u(s))]\mathrm{d}s$$
$$+ \frac{1}{\Gamma(1/2)} \int_0^t \int_0^s (t - s)^{\frac{1}{2} - 1} (s - \tau)^{-1/2}$$
$$\times Z_{1/2,1/2}(t - s) g'(\tau)\mathrm{d}\tau\mathrm{d}s \qquad (14)$$

where

$$Z_{1/2,1/2}(t) = \begin{pmatrix} Q_1(t) & 0 \\ 0 & Q_2(t) \end{pmatrix}$$

with

$$Q_1(t) = \left[\frac{5 + \sqrt{29}}{2\sqrt{29}} E_{1/2,1/2}((5 + \sqrt{29})t^{1/2}) \right.$$
$$\left. - \frac{5 - \sqrt{29}}{2\sqrt{29}} E_{1/2,1/2}((5 - \sqrt{29})t^{1/2}) \right]$$
$$Q_2(t) = \left[\frac{1 + \sqrt{2}}{2\sqrt{2}} E_{1/2,1/2}((1 + \sqrt{2})t^{1/2}) \right.$$
$$\left. - \frac{1 - \sqrt{2}}{2\sqrt{2}} E_{1/2,1/2}((1 - \sqrt{2})t^{1/2}) \right]$$

By simple matrix calculation, we see that the controllability Grammian matrix

$$G = \int_0^{t_1} (t_1 - s)^{-1/2} [Z_{1/2,1/2}(t_1 - s)B][Z_{1/2,1/2}(t_1 - s)B]^* \mathrm{d}s$$
$$= \int_0^{t_1} (t_1 - s)^{-1/2} \begin{pmatrix} Q_1^2 & Q_1 Q_2 \\ Q_2 Q_2 & 2Q_2^2 \end{pmatrix} \mathrm{d}s$$

is positive definite for any $t_1 > 0$. Further

$$|f(t, x, y, u) - f(t, x, \bar{y}, u)|$$
$$= \tan^{-1} y - \tan^{-1} \bar{y}|$$
$$< \tan^{-1} |y - \bar{y}|, \quad \text{if } y \neq \bar{y}$$

and

$$\lim_{|x| \to \infty} \frac{|f(t, x, y, u)|}{|x|} = 0$$

So the hypotheses of Theorem 3.1. are satisfied. Hence, the system is controllable.

Funding

References

Ahmed E and Elgazzar AS (2007) On fractional order differential equations model for nonlocal epidemics. *Physica A* 379(2): 607–614.

Anichini G, Conti G and Zecca P (1986) A note on controllability of certain nonlinear systems. *Note di Matematica* 6(1): 99–111.

Bagley RL and Torvik PJ (1983) A theoretical basis for the application of fractional calculus to viscoelasticity. *Journal of Rheology* 27(3): 201–210.

Balachandran K and Balasubramaniam P (1994) Controllability of nonlinear neutral Volterra integrodifferential systems. *Journal of the Australian Mathematical Society* 36(1): 107–116.

Balachandran K and Dauer JP (1987) Controllability of nonlinear systems via fixed point theorems. *Journal of Optimization Theory and Applications* 53(3): 345–352.

Balachandran K and Kokila J (2012a) On the controllability of fractional dynamical systems. *International Journal of Applied Mathematics and Computer Science* 22(3): 523–531.

Balachandran K and Kokila J (2013a) Constrained controllability of fractional dynamical systems. *Numerical Functional Analysis and Optimization* 34(11): 1187–1205.

Balachandran K and Kokila J (2013b) Controllability of nonlinear implicit fractional dynamical systems. *IMA Journal of Applied Mathematics* 79(3): 562–570.

Balachandran K, Kokila J and Trujillo JJ (2012b) Relative controllability of fractional dynamical systems with multiple delays in control. *Computers and Mathematics with Applications* 64(10): 3037–3045.

Balachandran K, Park JY and Trujillo JJ (2012c) Controllability of nonlinear fractional dynamical systems. *Nonlinear Analysis: Theory, Methods and Applications* 75(4): 1919–1926.

Balachandran K, Zhou Y and Kokila J (2012d) Relative controllability of fractional dynamical systems with delays in control. *Communications in Nonlinear Science and Numerical Simulation* 17(9): 3508–3520.

Banks HT and Kent GA (1972) Control of functional differential equations of retarded and neutral type to target sets in function space. *SIAM Journal of Control* 10(4): 562–593.

Bonilla B, Rivero M, Rodríguez-Germaá L and Trujillo JJ (2007) Fractional differential equations as alternative

models to nonlinear differential equations. *Applied Mathematics and Computation* 187(1): 79–88.

Chukwu EN (1987) On the Euclidean controllability of a neutral system with nonlinear base. *Nonlinear Analysis: Theory, Methods and Applications* 11(1): 115–123.

Dacka C (1980) On the controllability of a class of nonlinear systems. *IEEE Transaction on Automatic Control* 25(2): 263–266.

El-Sayed AMA (1996) Fractional-order diffusion-wave equation. *International Journal of Theoretical Physics* 35(2): 311–322.

Gahl RD (1978) Controllability of nonlinear systems of neutral type. *Journal of Mathematical Analysis and Applications* 63(1): 33–42.

Gyori I and Wu J (1991) A neutral equation arising form compartmental systems with pipes. *Journal of Dynamics and Differential Equations* 3(2): 289–311.

Hale JK (1972) *Theory of Functional Differential Equations*. New York: Springer-Verlag.

Hernández E, O'Regan D and Balachandran K (2010) On recent developments in the theory of abstract differential equations with fractional derivatives. *Nonlinear Analysis: Theory, Methods and Applications* 73(10): 3462–3471.

Jacobs MQ and Langenhop CE (1976) Criteria for function space controllability of linear neutral systems. *SIAM Journal on Control and Optimization* 14(6): 1009–1048.

Kexue L and Jigen P (2011) Laplace transform and fractional differential equations. *Applied Mathematics Letters* 24(12): 2013–2019.

Kilbas AA, Srivastava HM and Trujillo JJ (2006) *Theory and Applications of Fractional Differential Equations*. Amsterdam: Elsevier.

Klamka J (1993) *Controllability of Dynamical Systems*. Dordrecht: Kluwer Academic.

Klamka J (2008) Constrained controllability of semi linear systems with delayed controls. *Bulletin of the Polish Academy of Sciences: Technical Sciences* 56(4): 333–337.

Lakshmikantham V (2008) Theory of fractional functional differential equations. *Nonlinear Analysis: Theory, Methods and Applications* 69(10): 3337–3343.

Metzler R and Klafter J (2000) The random walk's guide to anomalous diffusion: a fractional dynamics approach. *Physics Reports* 339(1): 1–77.

Miller KS and Ross B (1993) *An Introduction to the Fractional Calculus and Fractional Differential Equations*. New York: Wiley.

Oldham KB and Spanier J (1974) *The Fractional Calculus*. London: Academic Press.

Onwuatu JU (1984) On the null controllability in function space of nonlinear systems of neutral functional differential equations with limited controls. *Journal of Optimization Theory and Applications* 42(3): 327–420.

Podlubny I (1999) *Fractional Differential Equations*. New York: Academic Press.

Sadovskii JB (1972) Linear compact and condensing operator. *Russian Mathematical Surveys* 27: 85–165.

Anisotropic fractional diffusion tensor imaging

Mark M Meerschaert[1], Richard L Magin[2] and Allen Q Ye[2]

Abstract
Traditional diffusion tensor imaging (DTI) maps brain structure by fitting a diffusion model to the magnitude of the electrical signal acquired in magnetic resonance imaging (MRI). Fractional DTI employs anomalous diffusion models to obtain a better fit to real MRI data, which can exhibit anomalous diffusion in both time and space. In this paper, we describe the challenge of developing and employing anisotropic fractional diffusion models for DTI. Since anisotropy is clearly present in the three-dimensional MRI signal response, such models hold great promise for improving brain imaging. We then propose some candidate models, based on stochastic theory.

1. Introduction

The structural complexity of the human brain is manifest at each level of functional organization: synapses, axons, neurons, cortical layers, fiber tracts, and cerebral convolutions (gyri and sulci) (Schaltenbrand and Wahren, 1998). Magnetic resonance imaging (MRI) in general, and diffusion tensor imaging (DTI) in particular, exhibit contrast that reflects tissue heterogeneity and anisotropy in both the white and the gray matter (Mori, 2006). The overall goal of these imaging modalities is to provide spatial maps of structural features that correspond to the specific neural networks that provide the basis for sensory awareness, memory, cognition and coordinated movement (Le Bihan, 1995). Disruption of these neural pathways is a hallmark of trauma, stroke, tumors and degenerative disease. Although MRI and DTI are useful clinical tools for diagnosis and treatment monitoring, their typical voxel resolution ($1 \, \text{mm}^3$) is orders of magnitude above that of a single cell ($10 \, \mu\text{m}^3$) (Johansen-Berg and Behrens, 2009). Therefore there is a need to probe sub-voxel structure to improve both the sensitivity and the specificity of diagnosis. Since water movement within the voxel leads to MR signal attenuation that reflects collisions with molecules, membranes, and axonal fibers (Haacke et al., 1999) we anticipate that stochastic models of diffusion

(isotropic, anisotropic, restricted, hindered, Gaussian, nonGaussian) can be used to encode sub-millimeter structure.

2. Fractional DTI

The connection between diffusion and magnetic resonance for water protons is described by the Bloch–Torrey equation (Torrey, 1956; Haacke et al., 1999; Callaghan, 2011). Solving the Bloch–Torrey equation for an anisotropic material, such as brain white matter (WM), provides the basis for DTI (Le Bihan, 1995). In standard DTI, a pair of trapezoidal gradient pulses is added to the MR imaging sequence (Mori, 2006). The acquired diffusion-weighted (DW) signal S decays in a manner dependent upon the diffusion gradient strength, G, gradient duration, δ, and the time interval, Δ, between gradient pulses. The resultant

[1]Department of Statistics and Probability, Michigan State University, East Lansing, MI, USA
[2]Department of Bioengineering, University of Illinois at Chicago, IL, USA

Received: 2 July 2014; accepted: 16 September 2014

Corresponding author:
Mark M Meerschaert, Department of Statistics and Probability, Michigan State University, East Lansing, MI 48824, USA.
Email: mcubed@stt.msu.edu

decay can be modeled (Haacke et al., 1999) by the equation

$$S = S_0 \exp(-(\gamma G \delta)^2 \boldsymbol{g} \cdot \mathbf{D}\boldsymbol{g} \cdot (\Delta - \delta/3)) \qquad (2.1)$$

where S_0 is the initial signal intensity, γ is the gyromagnetic ratio (42.57 MHz/T for water protons), $\mathbf{D}$ is a symmetric positive-definite matrix that defines the diffusion tensor, $\boldsymbol{G} = G\boldsymbol{g}$ where $\boldsymbol{g}$ is a unit vector that points in the direction of the applied magnetic field gradient $\boldsymbol{G}$. The eigenvector corresponding to the largest eigenvalue of the matrix $\mathbf{D}$ points in the direction of WM fibers, since the water is maximally dispersed in this direction. A single parameter b describes the overall diffusion sensitivity of a sequence, and for a pair of identical rectangular gradient pulses (height G and width δ) we find $b = (\gamma G \delta)^2(\Delta - \delta/3)$ (Haacke et al., 1999). Then (2.1) reduces to

$$S(b, \boldsymbol{g}) = S_0 \exp(-b\boldsymbol{g} \cdot \mathbf{D}\boldsymbol{g}) \qquad (2.2)$$

If the gradient pulses are of short duration (Callaghan, 2011), one can view (2.2) as the Fourier transform of the solution to a traditional diffusion equation, and this observation provides the essential link between MRI and diffusion: let $p(\boldsymbol{x}, t)$ be the probability density of a diffusing particle, which solves the diffusion equation

$$\partial_t p(\boldsymbol{x}, t) = \nabla \cdot \mathbf{D}\nabla p(\boldsymbol{x}, t) \qquad (2.3)$$

with a point source initial condition $p(\boldsymbol{x}, 0) = \delta(\boldsymbol{x})$. Given a suitable function $f(\boldsymbol{x})$, define its Fourier transform $\hat{f}(\boldsymbol{k}) = \int e^{-i\boldsymbol{k}\cdot\boldsymbol{x}} f(\boldsymbol{x}) \, d\boldsymbol{x}$, and recall that $(i\boldsymbol{k})\hat{f}(\boldsymbol{k})$ is the Fourier transform of $\nabla f(\boldsymbol{x})$ (Meerschaert and Sikorskii, 2012, p. 150). Take Fourier transforms in (2.3) to get the ordinary differential equation $\partial_t \hat{p}(\boldsymbol{k}, t) = (i\boldsymbol{k}) \cdot \mathbf{D}(i\boldsymbol{k})\hat{p}(\boldsymbol{k}, t)$ with initial condition $\hat{p}(\boldsymbol{k}, 0) \equiv 1$. Obviously the solution to this simple differential equation is $\hat{p}(\boldsymbol{k}, t) = \exp(-t\boldsymbol{k} \cdot \mathbf{D}\boldsymbol{k})$, which is the same form as (2.2) with $b = t\|\boldsymbol{k}\|^2$ and $\boldsymbol{g} = \boldsymbol{k}/\|\boldsymbol{k}\|$.

Since $\mathbf{D}$ is symmetric and positive definite, there is an orthonormal basis of eigenvectors $\boldsymbol{v}_1, \ldots, \boldsymbol{v}_d$ with corresponding eigenvalues a_i such that $\mathbf{D}\boldsymbol{v}_i = a_i\boldsymbol{v}_i$ for $1 \le i \le d$. For any $\boldsymbol{k} \in \mathbb{R}^d$ we can write $\boldsymbol{k} = \sum_{j=1}^{d} k_j\boldsymbol{v}_j$ where $k_j = \boldsymbol{k} \cdot \boldsymbol{v}_j$. Then $\boldsymbol{v}_i \cdot \mathbf{D}\boldsymbol{v}_j = 0$ if $j \ne i$ and $\boldsymbol{v}_i \cdot \mathbf{D}\boldsymbol{v}_i = a_i$. It follows easily that

$$\hat{p}(\boldsymbol{k}, t) = \exp\left[-t \sum_{i=1}^{d} a_i k_i^2\right] \qquad (2.4)$$

The level sets of the function $\boldsymbol{k} \mapsto \hat{p}(\boldsymbol{k}, t)$ are ellipsoids $a_1 k_1^2 + \cdots + a_d k_d^2 = C$ whose principal axes are the eigenvectors $\boldsymbol{v}_1, \ldots, \boldsymbol{v}_d$. The level sets are widest in the
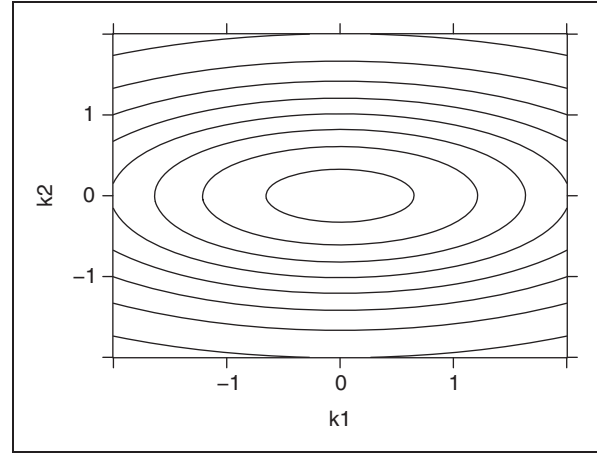

Figure 1. Level sets of the Fourier solution (2.4) to the traditional diffusion equation in $d = 2$ dimensions with diffusion tensor (2.5) at $b = 1$.

direction of the eigenvector with the smallest eigenvalue. Figure 1 shows the level sets of this function at time $t = 1$ in the case where

$$\mathbf{D} = \begin{pmatrix} 1/2 & 0 \\ 0 & 2 \end{pmatrix} \qquad (2.5)$$

in $d = 2$ dimensions. In this case, the eigenvectors of $\mathbf{D}$ are the coordinate axes, which give the major and minor axes of the elliptical level sets. As t increases, the level sets spread out at the rate $t^{1/2}$, which is the hallmark of traditional diffusion. This spreading rate can easily be verified by noting that $\hat{p}(\boldsymbol{k}, t) = (t^{1/2}\boldsymbol{k}, 1)$. This solution exhibits *mild isotropy*, in which the solution spreading rate is radially symmetric, but the level sets are not. For complete details, see Meerschaert and Sikorskii (2012, Section 6.1).

In many applications (Metzler and Klafter, 2000, 2004; Mainardi, 2010; Meerschaert and Sikorskii, 2012), a diffusing front spreads at a different rate than the $t^{1/2}$ predicted by the traditional diffusion equation. This can be captured by introducing fractional derivatives into the diffusion model. For simplicity, let us focus on the isotropic diffusion model where $\mathbf{D} = D\mathbf{I}$ for some positive constant D, and where $\mathbf{I}$ is the $d \times d$ identity matrix. Then the diffusion equation (2.3) reduces to $\partial_t p(\boldsymbol{x}, t) = D\Delta p(\boldsymbol{x}, t)$, and its point source solution has Fourier transform $(\boldsymbol{k}, t) = \exp(-Dt\|\boldsymbol{k}\|^2)$ where $\|\boldsymbol{k}\|^2 = \boldsymbol{k} \cdot \boldsymbol{k}$. The level sets of the solution $p(\boldsymbol{x}, t)$ are circles in two dimensions, or spheres in three dimensions.

The fractional Laplacian is an isotropic space-fractional derivative, defined so that $\Delta^{\alpha/2} f(\boldsymbol{x})$ has Fourier transform $-\|\boldsymbol{k}\|^\alpha \hat{f}(\boldsymbol{k})$ with $0 < \alpha < 2$.

This reduces to the traditional Laplacian when $\alpha = 2$. The isotropic space-fractional diffusion equation

$$\partial_t p(\mathbf{x}, t) = D\Delta^{\alpha/2} p(\mathbf{x}, t) \qquad (2.6)$$

has Fourier transform $\partial_t \hat{p}(\mathbf{k}, t) = -\mathbf{D}\|\mathbf{k}\|^\alpha(\mathbf{k}, t)$, whose point source solution is $\hat{p}(\mathbf{k}, t) = \exp(-Dt\|\mathbf{k}\|^\alpha)$. Since $(\mathbf{k}, t) = \hat{p}(t^{1/\alpha}\mathbf{k}, 1)$, solutions spread like $t^{1/\alpha}$ in this model, a phenomenon called superdiffusion. This model is also isotropic, which follows from the fact that $\hat{p}(\mathbf{k}, t)$ only depends on $\|\mathbf{k}\|$.

3. Fractional Bloch–Torrey equation

The traditional Bloch–Torrey equation

$$\partial_t S = -(i\gamma\, \mathbf{x} \cdot \mathbf{G})S + \nabla \cdot \mathbf{D}\nabla S \qquad (3.1)$$

describes magnetization $S(\mathbf{x}, t)$ in a time-varying gradient $\mathbf{G}(t)$. Assume a solution $S = S_0 A e^{-i\mathbf{x}\cdot\mathbf{L}}$ where $S_0 > 0$ is a constant, and A, $\mathbf{L}$ are functions of t with

$$\mathbf{L} := \gamma \int_0^t \mathbf{G}(\tau)\mathrm{d}\tau$$

Substitute the solution into (3.1) to see that

$$\frac{A'}{A}S - (i\mathbf{x} \cdot \gamma\mathbf{G})S = -i\gamma(\mathbf{x} \cdot \mathbf{G})S + \nabla \cdot \mathbf{D}\nabla S$$

Compute $\nabla \cdot \mathbf{D}\nabla S = \mathbf{L} \cdot \mathbf{D}\mathbf{L}S$: then it follows that the solution with $A(0) = 1$ satisfies

$$A(t) = \exp\left[-\int_0^t \mathbf{L}(\tau) \cdot \mathbf{D}\mathbf{L}(\tau)\,\mathrm{d}\tau\right]$$

for any $t > 0$. For a specified signal, it is then straightforward to compute the solution to the Bloch–Torrey equation (3.1). The Stejskal–Tanner pulse sequence consists of two rectangular functions of length δ separated by time Δ, with amplitude G and direction $\mathbf{g}$. Then one can easily compute the solution (2.1), which reduces to (2.2) with $b = (\gamma G\delta)^2(\Delta - \delta/3)$.

The simplest space-fractional Bloch–Torrey equation

$$\partial_t S = -(i\gamma\mathbf{x} \cdot \mathbf{G})S + D_0\Delta^{\alpha/2}S \qquad (3.2)$$

can be solved by a similar method. Assume the solution $S = S_0 A e^{-i\mathbf{x}\cdot\mathbf{L}}$ as before, and compute

$$\frac{A'}{A}S = D_0\Delta^{\alpha/2}S$$

Next compute the fractional Laplacian of the solution using Fourier transforms. It follows from the Fourier

inversion formula $f(x) = (2\pi)^{-d}\int e^{i\mathbf{k}\cdot\mathbf{x}}(\mathbf{k})\mathrm{d}\mathbf{k}$ that the function $f(\mathbf{x}) = e^{-i\mathbf{a}\cdot\mathbf{x}}$ has the Fourier transform $\hat{f}(\mathbf{k}) = (2\pi)^d\delta(\mathbf{k} + \mathbf{a})$ using the Dirac delta function. Then $D_0\Delta^{\alpha/2}S$ is the inverse Fourier transform of $-D_0\|\mathbf{k}\|^\alpha\hat{S}(\mathbf{k}, t)$, which is evidently $-D_0\|\mathbf{L}\|^\alpha S$. Hence we have

$$A(t) = \exp\left[-D_0\int_0^t \|\mathbf{L}(\tau)\|^\alpha\,\mathrm{d}\tau\right]$$

in this case. For a Stejskal–Tanner pulse sequence, the solution reduces to

$$S = S_0\exp\left[-D_0(\gamma G\delta)^\alpha\left(\Delta - \frac{\alpha - 1}{\alpha + 1}\delta\right)\right] \qquad (3.3)$$

where $\delta > 0$ is a constant; see Magin et al. (2008) for more details. If we take $D = D_0\Delta - D_0(\alpha - 1)\delta/(\alpha + 1)$ and $b = \gamma G\delta$, this reduces to the *stretched exponential* form

$$S = S_0\exp(-b^\alpha D) \qquad (3.4)$$

where $0 < \alpha < 2$.

4. The need for anisotropic fractional DTI models

In MRI experiments, it is often observed (Bennett et al., 2003; Hall and Barrick, 2008; Ingo et al., 2014) that the acquired DW signal S follows the stretched exponential model (3.4) for high b values. In applications to brain imaging, it is also found that the parameter α varies with direction: an indication of anisotropy (Hall and Barrick, 2012). For example, in one experiment (Ingo et al., 2014), formalin-fixed brains from normal, adult rats were soaked in Fluorinert to reduce magnetic susceptibility and imaged ex vivo in a Bruker 750 MHz spectrometer (17.6 T, 89 mm bore). A pulsed gradient stimulated echo diffusion sequence was used with pulse repetition time of 2 s, echo time of 28 ms, in-plane resolution of 190 μm and slice thickness of 1 mm. The signal S was acquired in six different vector directions $\mathbf{g}_1 = (0, 0, 1)^T$, $\mathbf{g}_2 = (0.89,\ 0,\ 0.45)^T$, $\mathbf{g}_3 = (0.28,\ 0.09,\ 0.45)^T$, $\mathbf{g}_4 = (-0.72,\ -0.53,\ 0.45)^T$, $\mathbf{g}_5 = (0.28,\ -0.85,\ 0.45)^T$, and $\mathbf{g}_6 = (-0.72,\ -0.53,\ 0.45)^T$ with 10 different b values ranging up to a maximum value of 26,190 s/mm^2. In this experiment, Δ (17.5 ms) and δ (3.5 ms) were kept constant and G was scaled to increase with the b value. Under these conditions, the short-pulse condition $\delta \ll \Delta$ holds.

Next, we validate the stretched exponential model (3.4) using linear regression. Taking logs in the
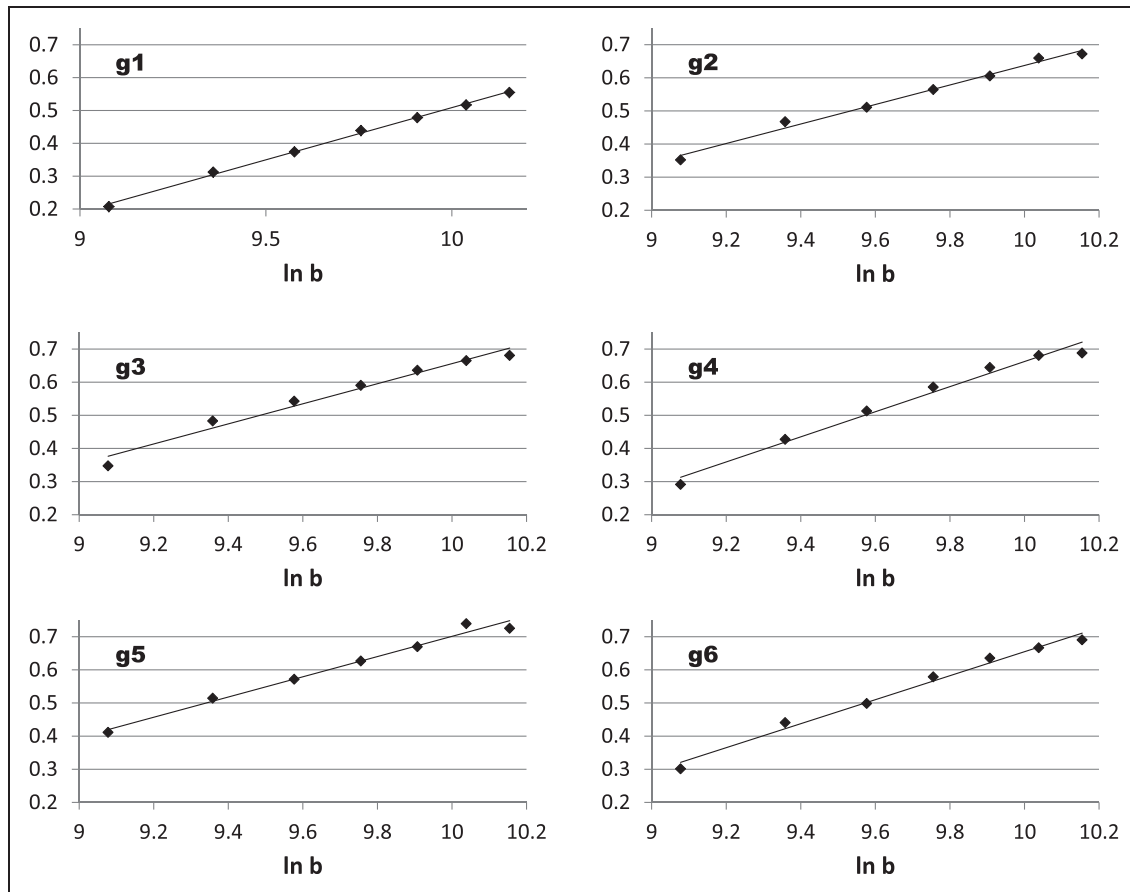
Figure 2. Plot of s versus ln b in six different directions, to validate the stretched exponential model (4.1).

model yields $\ln(S/S_0) = -Db^{\alpha}$, and taking logs again produces

$$s := \ln(-\ln(S/S_0)) = \ln D + \alpha \ln b \qquad (4.1)$$

Hence, a plot of s versus $\ln b$ should produce a straight line with slope α. Figure 2 shows this plot for each of the directions $g_1, \ldots, g_6$ along with the best-fitting straight line model, found using simple linear regression. It is apparent from these graphs that the relation between the acquired signals S and b follows the stretched exponential model (3.4).

To illustrate the anisotropic nature of DTI, we compare the slopes α from the straight line fit of s versus $\ln b$ for each direction $j = 1, 2, \ldots, 6$. The results are summarized in Table 1. It is clear that the power law slope depends on direction. For example, the slope for direction 4 (corresponding to direction vector g_4) is $\alpha = 0.379 \pm 0.023$ which is significantly different from the $\alpha = 0.294$ value in direction 2. To obtain a formal confidence interval for these α values, one can use the standard t-interval from linear regression theory. Since the sample size is $n = 7$, the 95% confidence interval is $\alpha \pm 2.571$ SE where α is the estimate in the first row of

Table 1. Best-fit α values via linear regression on the data in Figure 2 for six different directions, demonstrating anisotropy.

Direction	1	2	3	4	5	6
α	0.318	0.294	0.303	0.379	0.305	0.362
Standard error	0.007	0.014	0.022	0.023	0.018	0.018

Table 1, SE is the standard error in the second row of Table 1, and 2.571 is the 97.5th percentile of the standard t distribution with $n - 2 = 5$ degrees of freedom. For example, we are 95% confident that the correct α value for direction 1 lies in the interval (0.300, 0.336).

Previous work has shown α to be a biomarker that reflects tissue heterogeneity (Bennett et al., 2003; Ozarslan and Mareci, 2003; Hall and Barrick, 2008; Magin et al., 2008; Zhou et al., 2010; Palombo et al., 2011; Ingo et al., 2014; Magin et al., 2014). In particular, the stretched exponential parameter α exhibits a lower value in more tortuous porous materials, and more heterogeneous tissue. Since the heterogeneity parameter α also varies with direction, it would be advantageous to include anisotropy in the fractional DTI model, to capture this effect.

5. Anisotropic fractional diffusion models for DTI

In the previous section, we demonstrated that the anisotropy parameter α in a DTI model can vary with direction. An open challenge in MRI theory is to develop a suitable anisotropic model for fractional diffusion that captures this anisotropy, and can be fit to data acquired within the constraints of a clinical MR scan. The scan generates multidimensional data that must be quickly and accurately presented to the radiologist for analysis. Fractional order models are attractive because they capture tissue complexity in a small set of parameters. Within the continuous time random walk (CTRW) paradigm, for example, the random motion of water is hindered or restricted by tissue heterogeneity that alters the waiting times and jump increments in a manner simply expressed by power laws (Metzler and Klafter, 2000, 2004; Meerschaert and Sikorskii, 2012). In the remainder of this paper, we survey existing anisotropic models for fractional DTI, and also discuss some potential new models.

5.1. Anisotropic fractional diffusion

A recent paper of Hanyga and Magin (2014) proposed a new space-fractional diffusion model that seems well-suited for applications to DTI. The model is

$$\partial_t p(\boldsymbol{x}, t) = \mathbf{Q} p(\boldsymbol{x}, t) \qquad (5.1)$$

where the anisotropic fractional derivative operator $\mathbf{Q}$ is defined in terms of Fourier transforms. Define

$$\hat{Q}(\mathbf{k}) = -\int_{\mathbf{y} \in \Omega} |\mathbf{y} \cdot \mathbf{k}|^{\alpha(\mathbf{y})} m(d\mathbf{y}) \qquad (5.2)$$

where $\Omega = \{\mathbf{y} \in \mathbb{R}^d : \|\mathbf{y}\| = 1\}$ is the unit sphere in d-dimensional Euclidean space, $m(d\mathbf{y})$ is a finite Borel measure on the sphere, and $\alpha(\mathbf{y})$ is a symmetric function $\alpha(\mathbf{y}) = \alpha(-\mathbf{y})$ on the sphere that takes values in the interval $(0, 2)$. Then one defines $\mathbf{Q} f(x)$ to be the function with Fourier transform $\hat{Q}(\mathbf{k}) \hat{f}(\boldsymbol{k})$. Hanyga and Magin (2014) continue to prove that solutions to (5.1) remain nonnegative for a nonnegative initial condition $p(\boldsymbol{x}, 0) = f(\boldsymbol{x}) \geq 0$. Next we provide an alternative proof of this fact, by showing that the solutions to (5.1) are the probability densities of a *Lévy process* (Sato, 1999; Meerschaert and Sikorskii, 2012, Section 4.3).

Proposition 5.1. There exists a Lévy process $\mathbf{X}(t)$ that satisfies

$$\hat{p}(\mathbf{k}, t) = \mathbb{E}[e^{-i\mathbf{k} \cdot \mathbf{X}(t)}] = e^{t\hat{Q}(\mathbf{k})} \qquad (5.3)$$

for all $\mathbf{k} \in \mathbb{R}^d$ and all $t \geq 0$, for any symmetric index function $\alpha \colon \Omega \to (0, 2)$ and any finite Borel measure $m(d\mathbf{y})$ on the unit sphere.

Proof. Any Lévy process $\{\mathbf{X}(t) : t \geq 0\}$ is determined by the distribution of $\mathbf{X} := \mathbf{X}(1)$, which can be specified using the Lévy representation (Meerschaert and Scheffler, 2001, Theorem 3.1.11): a random vector $\mathbf{X}$ on $\mathbb{R}^d$ is infinitely divisible if and only if we can write $\mathrm{E}[e^{-i\mathbf{k} \cdot \mathbf{X}}] = \exp(\hat{Q}(\mathbf{k}))$, where

$$\hat{Q}(\mathbf{k}) = -i\mathbf{a} \cdot \mathbf{k} + \frac{1}{2} \mathbf{k} \cdot \mathbf{A} \, \mathbf{k}$$
$$- \int_{\mathbf{x} \neq 0} \left(e^{i\mathbf{k} \cdot \mathbf{x}} - 1 - \frac{i\mathbf{k} \cdot \mathbf{x}}{1 + \|\mathbf{x}\|^2} \right) \phi(d\mathbf{x}) \qquad (5.4)$$

for $\mathbf{a} \in \mathbb{R}^d$, $\mathbf{A}$ a nonnegative definite $d \times d$ matrix, and ϕ a σ-finite Borel measure on $\mathbb{R}^d \backslash \{0\}$ such that

$$\int_{\mathbf{x} \neq 0} \min\{1, \|\mathbf{x}\|^2\} \phi(d\mathbf{x}) < \infty \qquad (5.5)$$

The triple $[a, \mathbf{A}, \phi]$ is unique. Next we note that, in the one-dimensional case $d = 1$, there exists an infinitely divisible random variable X such that $\mathbb{E}[e^{-ikX}] = \exp(-|k|^\alpha)$ for any $0 < \alpha < 2$, and in this case, it follows from Meerschaert and Scheffler (2001, Lemma 7.3.10) (for $0 < \alpha < 1$), Meerschaert and Scheffler (2001, Lemma 7.3.11) (for $1 < \alpha < 2$), and Meerschaert and Scheffler (2001, Lemma 7.3.12) (for $\alpha = 1$) that this random variable has Lévy representation $[0, 0, \phi_\alpha]$ where

$$\phi_\alpha(dx) = \frac{C_\alpha}{2} \alpha |x|^{-\alpha-1} dx \qquad (5.6)$$

with

$$C_\alpha = \frac{1 - \alpha}{\Gamma(2 - \alpha) \cos(\pi\alpha/2)} \quad \text{for } 0 < \alpha < 1 \text{ or } 1 < \alpha < 2 \qquad (5.7)$$

and $C_1 = 2/\pi$. Then we have

$$|k|^\alpha = \int_{x \neq 0} \left(e^{ikx} - 1 - \frac{ikx}{1 + x^2} \right) \phi_\alpha(dx) \qquad (5.8)$$

for each $0 < \alpha < 2$. Next, define an infinitely divisible random vector $\mathbf{X}$ on $\mathbb{R}^d$ (e.g. let $d = 3$) by specifying its Lévy representation $[0, 0, \phi]$ where $\mathbf{x} = r\mathbf{y}$ in polar coordinates $r > 0$ and $\|\mathbf{y}\| = 1$, and

$$\phi(d\mathbf{x}) = \phi(dr, d\mathbf{y}) = C_{\alpha(\mathbf{y})} \alpha(\mathbf{y}) r^{-\alpha(\mathbf{y})-1} dr \, \bar{m}(d\mathbf{y}) \qquad (5.9)$$

where $m(d\mathbf{y}) = [m(d\mathbf{y}) + m(-d\mathbf{y})]/2$ is the symmetrized version of the measure $m(d\mathbf{y})$. Then the random

vector **X** has Lévy representation $\mathbb{E}[e^{-i\mathbf{k}\cdot\mathbf{X}}] = \exp(\hat{Q}(\mathbf{k}))$, where

$$-\hat{Q}(\mathbf{k}) = \int_{\mathbf{y}\in\Omega}\int_0^\infty \left(e^{ir\mathbf{k}\cdot\mathbf{y}} - 1 - \frac{ir\mathbf{k}\cdot\mathbf{y}}{1 + r^2(\mathbf{k}\cdot\mathbf{y})^2}\right)$$
$$\times C_{\alpha(\mathbf{y})}\alpha(\mathbf{y})r^{-\alpha(\mathbf{y})-1}\,dr\,\bar{m}(d\mathbf{y})$$

$$= \int_{\mathbf{y}\in\Omega}\int_0^\infty \left(e^{ir\mathbf{k}\cdot\mathbf{y}} - 1 - \frac{ir\mathbf{k}\cdot\mathbf{y}}{1 + r^2(\mathbf{k}\cdot\mathbf{y})^2}\right)$$
$$\times \frac{C_{\alpha(\mathbf{y})}}{2}\alpha(\mathbf{y})r^{-\alpha(\mathbf{y})-1}\,dr\,m(d\mathbf{y})$$
$$+ \int_{\mathbf{y}\in\Omega}\int_0^\infty \left(e^{ir\mathbf{k}\cdot\mathbf{y}} - 1 - \frac{ir\mathbf{k}\cdot\mathbf{y}}{1 + r^2(\mathbf{k}\cdot\mathbf{y})^2}\right)$$
$$\times \frac{C_{\alpha(\mathbf{y})}}{2}\alpha(\mathbf{y})r^{-\alpha(\mathbf{y})-1}\,dr\,m(-d\mathbf{y})$$

$$= \int_{\mathbf{y}\in\Omega}\int_0^\infty \left(e^{ir\mathbf{k}\cdot\mathbf{y}} - 1 - \frac{ir\mathbf{k}\cdot\mathbf{y}}{1 + r^2(\mathbf{k}\cdot\mathbf{y})^2}\right)$$
$$\times \frac{C_{\alpha(\mathbf{y})}}{2}\alpha(\mathbf{y})r^{-\alpha(\mathbf{y})-1}\,dr\,m(d\mathbf{y})$$
$$+ \int_{\mathbf{y}\in\Omega}\int_0^\infty \left(e^{-ir\mathbf{k}\cdot\mathbf{y}} - 1 - \frac{-ir\mathbf{k}\cdot\mathbf{y}}{1 + r^2(\mathbf{k}\cdot\mathbf{y})^2}\right)$$
$$\times \frac{C_{\alpha(\mathbf{y})}}{2}\alpha(\mathbf{y})r^{-\alpha(\mathbf{y})-1}\,dr\,m(d\mathbf{y})$$

$$= \int_{\mathbf{y}\in\Omega}\int_0^\infty \left(e^{ir\mathbf{k}\cdot\mathbf{y}} - 1 - \frac{ir\mathbf{k}\cdot\mathbf{y}}{1 + r^2(\mathbf{k}\cdot\mathbf{y})^2}\right)$$
$$\times \frac{C_{\alpha(\mathbf{y})}}{2}\alpha(\mathbf{y})r^{-\alpha(\mathbf{y})-1}\,dr\,m(d\mathbf{y})$$
$$+ \int_{\mathbf{y}\in\Omega}\int_{-\infty}^0 \left(e^{ir\mathbf{k}\cdot\mathbf{y}} - 1 - \frac{ir\mathbf{k}\cdot\mathbf{y}}{1 + r^2(\mathbf{k}\cdot\mathbf{y})^2}\right)$$
$$\times \frac{C_{\alpha(\mathbf{y})}}{2}\alpha(\mathbf{y})|r|^{-\alpha(\mathbf{y})-1}\,dr\,m(d\mathbf{y})$$

$$= \int_{\mathbf{y}\in\Omega}\int_{r\neq 0} \left(e^{ir(\mathbf{k}\cdot\mathbf{y})} - 1 - \frac{ir(\mathbf{k}\cdot\mathbf{y})}{1 + r^2}\right)$$
$$\times \frac{C_{\alpha(\mathbf{y})}}{2}\alpha(\mathbf{y})|r|^{-\alpha(\mathbf{y})-1}\,dr\,m(d\mathbf{y})$$
$$+ \int_{\mathbf{y}\in\Omega}\int_{r\neq 0} \left(\frac{ir(\mathbf{k}\cdot\mathbf{y})}{1 + r^2} - \frac{ir(\mathbf{k}\cdot\mathbf{y})}{1 + r^2(\mathbf{k}\cdot\mathbf{y})^2}\right)$$
$$\times \frac{C_{\alpha(\mathbf{y})}}{2}\alpha(\mathbf{y})|r|^{-\alpha(\mathbf{y})-1}\,dr\,m(d\mathbf{y})$$

$$= \int_{\mathbf{y}\in\Omega}|\mathbf{k}\cdot\mathbf{y}|^{\alpha(\mathbf{y})}\,m(d\mathbf{y}) \tag{5.10}$$

in view of (5.8), since the integral in the next to last line equals zero by symmetry. This shows that (5.3) holds. Since C_α is a bounded continuous function on the interval $0 < \alpha < 2$, it follows easily that (5.5) holds, so (5.9) is a Lévy measure. □

We say that a random vector **X** is full if it is not supported on a lower-dimensional hyperplane, that is,

if there is no unit vector $\mathbf{y}\in\Omega$ such that $\mathbf{X}\cdot\mathbf{y} = 0$ with probability one.

Proposition 5.2. If $\int_{\mathbf{y}\in\Omega}|\mathbf{y}\cdot\mathbf{w}|^{\alpha(\mathbf{y})}m(d\mathbf{y}) > 0$ for every $\mathbf{w}\in\Omega$, and $\alpha(\mathbf{y}) \geq \alpha_0 > 0$ for all $\mathbf{y}\in\Omega$, then the infinitely divisible random variable $X(t)$ in Proposition 5.1 is full, and has a density $p(\mathbf{x}, t)$ with respect to Lebesgue measure for any $t > 0$.

Proof. Define $\hat{p}(\mathbf{k}, t) = e^{t\hat{Q}(\mathbf{k})}$ for all $\mathbf{k}\in\mathbb{R}^d$ and all $t \geq 0$. The Fourier inversion theorem (Meerschaert and Scheffler, 2001, Theorem 1.3.7) implies that

$$p(\mathbf{x}, t) = (2\pi)^{-d}\int e^{i\mathbf{k}\cdot\mathbf{x}}\hat{p}(\mathbf{k}, t)\,d\mathbf{k} \tag{5.11}$$

is the function with Fourier transform $\hat{p}(\mathbf{k}, t)$, so long as the integral $\int|\hat{p}(\mathbf{k}, t)|d\mathbf{k} < \infty$. Since $\hat{Q}(\mathbf{k}) \leq 0$ for any $\mathbf{k}\in\mathbb{R}^d$, it follows that $0 \leq \hat{p}(\mathbf{k}, t) \leq 1$ for all $\mathbf{k}\in\mathbb{R}^d$ and all $t \geq 0$. Hence it suffices to check that $\int_{\|\mathbf{k}\|\geq 1}|\hat{p}(\mathbf{k}, t)|d\mathbf{k} < \infty$. Adopt the polar coordinates $\mathbf{k} = \rho\mathbf{w}$ where $\rho > 0$ and $\|\mathbf{w}\| = 1$. Since $\alpha(\mathbf{y}) \geq \alpha_0 > 0$ for all $\mathbf{y}\in\Omega$, we have

$$-\hat{Q}(\mathbf{k}) = \int_{\mathbf{y}\in\Omega}\rho^{\alpha(\mathbf{y})}|\mathbf{y}\cdot\mathbf{w}|^{\alpha(\mathbf{y})}m(d\mathbf{y}) \geq \rho^{\alpha_0}\int_{\mathbf{y}\in\Omega}|\mathbf{y}\cdot\mathbf{w}|^{\alpha(\mathbf{y})}m(d\mathbf{y})$$

for all $\|\mathbf{k}\| \geq 1$. It follows from the Dominated Convergence Theorem (Rudin, 1976, Theorem 11.32) that $g(\mathbf{w}) := \int_{\mathbf{y}\in\Omega}|\mathbf{y}\cdot\mathbf{w}|^{\alpha(\mathbf{y})}m(d\mathbf{y})$ is a continuous function on the compact set Ω, and since $g(\mathbf{w}) > 0$ by assumption, it follows that $g(\mathbf{w}) \geq g_0 > 0$ for all $\mathbf{w}\in\Omega$. Then $-\hat{Q}(k) \geq g_0\rho^{\alpha_0}$ for all $\|\mathbf{k}\| \geq 1$. Then we have

$$\int_{\|\mathbf{k}\|\geq 1}|\hat{p}(\mathbf{k}, t)|\,d\mathbf{k} \leq \int_{\mathbf{w}\in\Omega}\int_0^\infty e^{-g_0\rho^{\alpha_0}}\,\mathrm{d}\rho\,m(d\mathbf{w}) \leq C_0 m(\Omega)$$

where $C_0 = \int_0^\infty e^{-g_0\rho^{\alpha_0}}\,\mathrm{d}\rho < \infty$. This shows that (5.11) holds. If $\mathbf{X}(t)$ were not full, then we would have $\mathbf{X}(t)\cdot\mathbf{w} = 0$ for some unit vector $\mathbf{w}$, and then we would have $\mathbb{E}(e^{-i\mathbf{w}\cdot\mathbf{X}(t)}) = e^{t\hat{Q}(\mathbf{w})} = 1$, hence $\hat{Q}(\mathbf{w}) = 0$. But this contradicts $-\hat{Q}(\mathbf{k}) \geq g_0\rho^{\alpha_0}$, and so $\mathbf{X}(t)$ is full for every $t > 0$. □

Remark 5.3. Since $p(\mathbf{x}, t)$ is a probability density for any $t > 0$, it follows that $p(\mathbf{x}, t) \geq 0$ for all $\mathbf{x}\in\mathbb{R}^d$ and all $t > 0$. With some additional work, it should be possible to show that $p(\mathbf{x}, t) > 0$ for all $\mathbf{x}\in\mathbb{R}^d$ and all $t > 0$.

Remark 5.4. It should not be hard to extend these arguments to the asymmetric case

$$\hat{Q}(\mathbf{k}) = \int_{\mathbf{y}\in\Omega}(\mathbf{y}\cdot i\mathbf{k})^{\alpha(\mathbf{y})}m(d\mathbf{y}) \tag{5.12}$$

which reduces to the case (5.2) if the measure $m(d\mathbf{y})$ is symmetric, that is, $m(d\mathbf{y}) = m(-d\mathbf{y})$. One just has to be a bit careful about the centering constants.

Remark 5.5. A variety of *stable-like* processes have been considered in the literature, but the process constructed in Proposition 5.1 seems new. Bass (1988) considers a stable-like process in one dimension with jump intensity

$$\phi(x, dy) = \frac{C_\alpha(x)}{2} \alpha |y|^{-\alpha(x)-1} dy$$

which behaves locally like an α-stable process whose index varies in space. Bass and Tang (2009) consider a d-dimensional stable-like process with jump intensity $\phi(\mathbf{x}, d\mathbf{y}) = A(\mathbf{x},\mathbf{y})\|\mathbf{y}\|^{-\alpha-d}d\mathbf{y}$ where $A(\mathbf{x},\mathbf{y}) > 0$ is bounded away from zero and infinity. That model exhibits mild anisotropy, as opposed to the strong anisotropy in the Hanyga model. It would certainly be interesting to explore the mathematical properties of the Lévy process in Proposition 5.1 in more detail.

5.2. Anisotropic fractional Bloch–Torrey equation

Here we propose a new anisotropic fractional Bloch–Torrey equation

$$\partial_t S = -(i\gamma \mathbf{x} \cdot \mathbf{G})S + D_0 \mathbf{Q} S \qquad (5.13)$$

which can be solved by the method introduced in Section 3. Assume the same solution form $S = S_0 A e^{-i\mathbf{x} \cdot \mathbf{L}}$ as before, and compute

$$\frac{A'}{A} S = D_0 \mathbf{Q}$$

Next compute $\hat{Q}S$ using Fourier transforms. Recall that the function $f(\mathbf{x}) = e^{-i\mathbf{a} \cdot \mathbf{x}}$ has Fourier transform $\hat{f}(\mathbf{k}) = (2\pi)^d \delta(\mathbf{k} + \mathbf{a})$. Then note that $D_0 \hat{Q} S$ has Fourier transform

$$D_0 \hat{Q}(\mathbf{k})\hat{S}(\mathbf{k}, t) = -D_0 \int_{\mathbf{y} \in \Omega} |\mathbf{y} \cdot \mathbf{k}|^{\alpha(\mathbf{y})} m(d\mathbf{y}) \, \hat{S}(\mathbf{k}, t)$$

Inverting as in Section 3, it follows that

$$A(t) = \exp\left[-D_0 \int_0^t \int_{\mathbf{y} \in \Omega} |\mathbf{y} \cdot \mathbf{L}(\tau)|^{\alpha(\mathbf{y})} m(d\mathbf{y}) \, d\tau \right]$$

in this case. For a Stejskal–Tanner pulse sequence, the solution reduces to

$$S = S_0 \exp\left[-D_0 \int_{\mathbf{y} \in \Omega} |\gamma \mathbf{G}\delta \cdot \mathbf{y}|^{\alpha(\mathbf{y})} \left(\Delta - \frac{\alpha(\mathbf{y}) - 1}{\alpha(\mathbf{y}) + 1}\delta \right) m(d\mathbf{y}) \right] \qquad (5.14)$$

If the mixing measure $m(d\mathbf{y})$ is concentrated on d point masses on an arbitrary set of coordinate axes $\mathbf{v}_1, \ldots, \mathbf{v}_d$ which need not be orthogonal, this reduces to a model recently proposed and tested by GadElkarim et al. (2013). That model has the solution

$$S = S_0 \exp\left[-\sum_{j=1}^d D_j |\gamma \mathbf{G}\delta \cdot \mathbf{v}_j|^{\alpha_j} \left(\Delta - \frac{\alpha_j - 1}{\alpha_j + 1}\delta \right) \right] \qquad (5.15)$$

where $D_j = D_0 m(\mathbf{v}_j)$, which agrees with GadElkarim et al. (2013, equation (20)) up to an obvious change in notation.

Remark 5.6. In practical applications, an open challenge is to fit the model (5.14) to MRI data as in Figure 2. The statistical problem is under-specified, since there are an infinite number of choices for $\alpha(\mathbf{y})$ and $m(d\mathbf{y}) = M(\mathbf{y})d\mathbf{y}$ that will agree with any finite data set. One reasonable approach is to fit the simplest functions $\alpha(\mathbf{y})$ and $M(\mathbf{y})$ using spherical harmonics in $d = 3$ dimensions. For example, the data in Figure 2 can be fit using six spherical harmonics. The resulting functions $\alpha(\mathbf{y})$ and $M(\mathbf{y})$ will agree exactly with the measured values of $\alpha(\mathbf{y})$ and the corresponding weights $M(\mathbf{y})$ obtained from the regression lines in Figure 2, and smoothly interpolate in between.

6. Time-fractional models for DTI

Here we explore the challenge of developing effective time-fractional models for DTI. These models can be useful if the data exhibit a power law decay in S as a function of b.

Anomalous subdiffusion can be modeled using a fractional derivative in time. Given a function $f(t)$ with Laplace transform $\tilde{f}(s) = \int_0^\infty e^{-st} f(t)dt$, recall that $s\tilde{f}(s) - f(0)$ is the Laplace transform of the first derivative $f'(s)$. The Caputo fractional derivative $\partial_t^\beta f(t)$ is defined for $0 < \beta < 1$ as the function with Laplace transform $s^\beta(s) - s^{\beta-1}f(0)$, extending the traditional form. Take Fourier and then Laplace transforms in the space-time fractional diffusion equation

$$\partial_t^\beta p(\mathbf{x}, t) = D\Delta^{\alpha/2} p(\mathbf{x}, t) \qquad (6.1)$$

with point source initial condition $\hat{p}(\mathbf{k}, t) \equiv 0$ to get $s^\beta \bar{p}(\mathbf{k}, s) - s^{\beta-1} = -\mathbf{D}\|\mathbf{k}\|^\alpha \bar{p}(\mathbf{k}, s)$, where $\bar{p}(\mathbf{k}, s)$ is the Laplace transform of $\hat{p}(\mathbf{k}, t)$. Solve to obtain

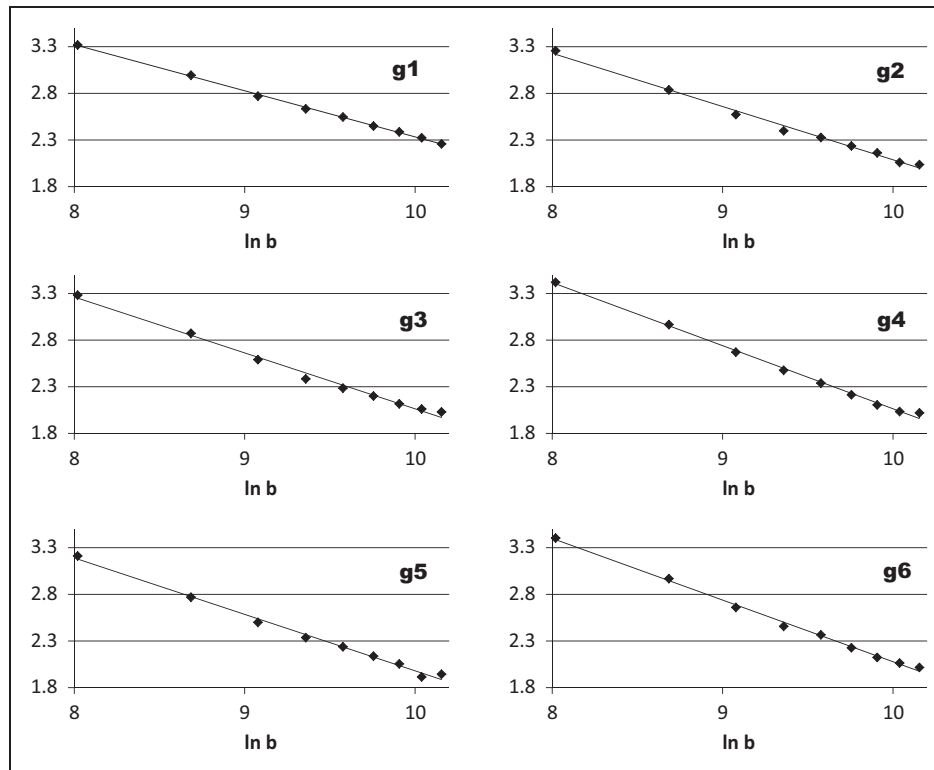$$\bar{p}(\mathbf{k}, s) = \frac{s^{\beta-1}}{s^\beta + D\|\mathbf{k}\|^\alpha}$$

Figure 3. Plot of ln S versus ln b in six different directions, to validate the power law model $S \approx Cb^{-\beta}$.

and then use the fact that $\tilde{g}(s) := s^{\beta-1}/(s^\beta + c)$ is the Laplace transform of $g(t) = E_\beta(-ct^\beta)$, where the Mittag-Leffler function

$$E_\beta(x) := \sum_{n=0}^{\infty} \frac{x^n}{\Gamma(1 + \beta n)}$$

for $\beta > 0$ (Mainardi, 2010, p. 223). It follows that $\hat{p}(\boldsymbol{k}, t) = E_\beta(-t^\beta D \|\boldsymbol{k}\|^\alpha)$ is the Fourier transform of the solution to the isotropic time-fractional diffusion equation (6.1). Since $\hat{p}(\boldsymbol{k}, t) = \hat{p}(t^{\beta/\alpha} \boldsymbol{k}, 1)$, solutions spread at the subdiffusive rate $t^{\beta/2}$ in this model when $\alpha = 2$. This model is isotropic, since $\hat{p}(\boldsymbol{k}, t)$ only depends on $\|\boldsymbol{k}\|$. Recalling the asymptotic property

$$E_\beta(x) \sim \frac{x^{-1}}{\Gamma(1 - \beta)} \quad \text{as } x \to \infty \quad (6.2)$$

(Mainardi, 2010, p. 215) we can see that $\hat{p}(\boldsymbol{k}, t)$ then falls off like $t^{-\beta}$ for large values of t.

Figure 3 shows a log–log plot of S versus b for the data from Figure 2, for all six directions. The straight line behavior in Figure 3 shows that a time-fractional model is a reasonable alternative to the stretched exponential, since a power law $S \approx Cb^{-\beta}$ also gives a good fit to the data. This is indicated by a straight line on the log–log plot with slope $-\beta$, since $\ln S \approx \ln C - \beta \ln b$.

Table 2. Best-fit β values via linear regression on the data in Figure 3 for six different directions, demonstrating anisotropy.

Direction	1	2	3	4	5	6
β	0.494	0.571	0.599	0.676	0.605	0.661
Standard error	0.006	0.017	0.020	0.014	0.018	0.014

The β estimates and standard errors are listed in Table 2.

Again, it is clear that the data exhibit significant anisotropy, since the β values vary significantly with direction. For example, the value for direction 1 (corresponding to direction vector $\boldsymbol{g}_1$) is $\beta = 0.494 \pm 0.006$ which is significantly different from the $\beta = 0.571$ value in direction 2. Since the sample size is $n = 9$, the 95% confidence interval is $\beta \pm 2.365\,\mathrm{SE}$ using the 97.5th percentile of the standard t distribution with $n - 2 = 7$ degrees of freedom. For example, we are 95% confident that the correct β value for direction 1 lies in the interval (0.480, 0.508).

6.1. Time-fractional Hanyga diffusion

The paper of Hanyga and Magin (2014) also proposed a time-fractional version of their anisotropic fractional

diffusion model. Define the pseudo-differential operator **Q** on the space $C_0(\mathbb{R}^d)$ of smooth functions with compact support (i.e. $f(\mathbf{x}) = 0$ for all $\|\mathbf{x}\| \geq M$ for some $M > 0$) such that $\mathbf{Q}f(\mathbf{x})$ has Fourier transform $\hat{Q}(\mathbf{k})\hat{f}(\mathbf{k})$, where $\hat{Q}(\mathbf{k})$ is defined by (5.2). This operator can then be extended to larger spaces of functions, or even distributions (i.e. generalized functions). Since $\hat{p}(\mathbf{k}, t) = e^{t\hat{Q}(\mathbf{k})}$, it is obvious that this Fourier transform solves the ordinary differential equation

$$\frac{d}{dt}\hat{p}(\mathbf{k}, t) = \hat{Q}(\mathbf{k})\hat{p}(\mathbf{k}, t); \quad \hat{p}(\mathbf{k}, 0) \equiv 1 \qquad (6.3)$$

Inverting the Fourier transform shows that the probability densities $p(\mathbf{x}, t)$ of the stochastic process $\mathbf{X}(t)$ from Proposition 5.1 solve the pseudo-differential equation

$$\frac{\partial}{\partial t}p(\mathbf{x}, t) = \mathbf{Q}p(\mathbf{x}, t); \quad p(\mathbf{x}, 0) = \delta(\mathbf{x}) \qquad (6.4)$$

The equation (6.4) is also called a Cauchy problem (Arendt et al., 2001). In fact, if we define the semigroup

$$T_t f(\mathbf{x}) = \int f(\mathbf{x} - \mathbf{y})\, p(\mathbf{y}, t)\, d\mathbf{y}$$

on the space $L^1(\mathbb{R}^d)$ of integrable functions $f: \mathbb{R}^d \to \mathbb{R}$, then $\hat{Q}$ is the generator of that semigroup (Baeumer and Meerschaert, 2001, Theorem 2.2), and $T_t f(\mathbf{x})$ solves the Cauchy problem

$$\partial_t p(\mathbf{x}, t) = \mathbf{Q}p(\mathbf{x}, t); \quad p(\mathbf{x}, 0) = f(\mathbf{x}) \qquad (6.5)$$

for any $f \in Dom(\hat{Q})$, the domain of the generator. It follows from Baeumer and Meerschaert (2001, Proposition 2.1) that this semigroup T_t is strongly continuous and uniformly bounded, and that we can write the generator explicitly in the form

$$\mathbf{Q}f(\mathbf{x}) = \int_{\mathbf{y} \neq 0} \left(f(\mathbf{x} - \mathbf{y}) - f(\mathbf{x}) + \frac{\mathbf{y} \cdot \nabla f(\mathbf{x})}{1 + \|\mathbf{y}\|^2} \right) \phi(d\mathbf{y})$$

for any $f \in W^{2,1}(\mathbb{R}^d)$, the Sobolev space of functions in $L^1(\mathbb{R}^d)$ whose first and second partial derivatives are all in $L^1(\mathbb{R}^d)$.

Given any $0 < \beta < 1$, define the Riemann–Liouville fractional derivative

$$\mathbb{D}_t^\beta g(t) = \frac{1}{\Gamma(1 - \beta)} \frac{d}{dt} \int_0^\infty g(t - s)s^{-\beta}\mathrm{d}s$$

Then it follows from Baeumer and Meerschaert (2001, Theorem 3.1) that the function

$$q(\mathbf{x}, t) = \int_0^\infty p(\mathbf{x}, (t/u)^\beta)\, g_\beta(u)\, du \qquad (6.6)$$

solves the fractional Cauchy problem

$$\mathbb{D}_t^\beta q(\mathbf{x}, t) = \mathbf{Q}q(\mathbf{x}, t) + \frac{t^{-\beta}}{\Gamma(1 - \beta)}f(\mathbf{x}) \qquad (6.7)$$

whenever $p(\mathbf{x}, t)$ solves the Cauchy problem (6.5). Here $g_\beta(u)$ is the probability density function of the standard β-stable subordinator, most simply characterized in terms of its Laplace transform

$$\int_0^\infty e^{-st}g_\beta(t)\, dt = e^{-s^\beta} \qquad (6.8)$$

for all $s > 0$, for any $0 < \beta < 1$. A simple change of variable in the formula (6.6) reveals that

$$q(\mathbf{x}, t) = \int_0^\infty p(\mathbf{x}, u)h(u, t)\, \mathrm{d}u \qquad (6.9)$$

where

$$h(u, t) = \frac{t}{\beta}u^{-1-1/\beta}g_\beta(tu^{-1/\beta}) \qquad (6.10)$$

and this leads to a stochastic solution: let $\mathbf{D}(t)$ be the standard β-stable subordinator, a strictly increasing infinitely divisible Lévy process such that $\mathbf{D} = \mathbf{D}(1)$ has the probability density function $g_\beta(t)$. Define the inverse stable process (first passage time)

$$E_t = \inf\{u > 0 : D(u) > t\} \qquad (6.11)$$

and apply Corollary 3.1 from Meerschaert and Scheffler (2004) to see that the function $h(u,t)$ in (6.10) is the probability density function of the stochastic process E_t for each $t > 0$. Then it follows by a standard conditioning argument that the solution $q(\mathbf{x}, t)$ to the fractional Cauchy problem (6.7) with the point source initial condition $f(\mathbf{x}) = \delta(\mathbf{x})$ is also the probability density function of the time-changed process $\mathbf{X}(E_t)$, where E_t is independent from $\mathbf{X}(t)$. For a general initial condition $f(\mathbf{x})$ that is a probability density function, the solution $q(\mathbf{x}, t)$ to the fractional Cauchy problem (6.7) with initial condition $f(\mathbf{x})$ is the probability density function of $\mathbf{X}_0 + \mathbf{X}(E_t)$, where the initial particle location $\mathbf{X}_0$ has probability density function $f(\mathbf{x})$. See Meerschaert and Scheffler (2008, Theorem 4.1 and Remark 4.6) for more details and extensions. Freely available R code to compute the function $h(u,t)$ is available (Meerschaert and Sikorskii, 2012, Example 5.13) so that the solution (6.9) to the fractional Cauchy problem can be explicitly computed by numerically integrating the formula (6.9), once the probability density function $p(\mathbf{x}, t)$ has been computed.

The Caputo and Riemann–Liouville fractional derivatives are related by

$$\partial_t^\beta g(t) = \mathbb{D}_t^\beta g(t) - \frac{t^{-\beta}}{\Gamma(1-\beta)} g(0)$$

Then clearly one can also write the fractional Cauchy problem in a more compact form:

$$\partial_t^\beta q(\mathbf{x}, t) = \mathbf{Q} q(\mathbf{x}, t) \tag{6.12}$$

This extends the results of Hanyga (2002) for the case where $\beta(\mathbf{y})$ is a constant.

6.2. Time-fractional Bloch–Torrey equation

Let $\hat{Q}$ be the generator of some C_0 semigroup (Arendt et al., 2001). The time-fractional Bloch–Torrey equation has been written in the literature as

$$\partial_t^\beta S = -(i\gamma \mathbf{x} \cdot \mathbf{G}) S + D_0 \mathbf{Q} S \tag{6.13}$$

but this form is not dimensionally correct, since the time units of $\partial_t^\beta S$ are different to the units of the term $\partial_t S$ and, more importantly, the reaction term $-(i\gamma \mathbf{x} \cdot \mathbf{G}) S$.

Using an idea from Baeumer et al. (2005), we can write a dimensionally correct version of the time-fractional Bloch–Torrey equation as

$$\partial_t S = -(i\gamma\, \mathbf{x} \cdot \mathbf{G}) S + \nabla \cdot \mathbf{D} \nabla \partial_t^{1-\beta} S$$

Equivalently, we can write

$$\partial_t^\beta S = -i\gamma\, \mathbf{x} \cdot \mathbb{I}_t^{1-\beta}[\mathbf{G}S] + \nabla \cdot \mathbf{D} \nabla S$$

where $\mathbb{I}^{1-\beta}$ is the Riemann–Liouville fractional integral defined by

$$\mathbb{I}^\gamma g(t) := \frac{1}{\Gamma(\gamma)} \int_0^\infty g(t-u) u^{\gamma-1}\, du$$

An alternative form is proposed by Haynga and Seredyńska (2012, equation (17)). An open challenge in the theory of DTI is to derive an analytical solution for a physically correct time-fractional Bloch–Torrey equation, suitable for clinical applications.

7. Space-variable fractional DTI models

In clinical practice, the parameters of the (fractional) Bloch–Torrey equation vary with location. Indeed, three-dimensional maps of the parameters are an important outcome of fractional DTI modeling; see for example GadElkarim et al. (2013). An open

challenge is to develop the mathematical foundations of space-variable fractional DTI models. One promising approach is to use the theory of pseudo-differential operators (Schilling, 1998; Jacob, 2001). We can consider the Cauchy problem

$$\frac{\partial}{\partial t} p(\mathbf{x}, t) = \mathbf{Q} p(\mathbf{x}, t); \quad p(\mathbf{x}, 0) = p_0(\mathbf{x}) \tag{7.1}$$

where the pseudo-differential operator $\mathbf{Q}$ is defined in terms of the equation

$$\mathbf{Q} f(\mathbf{x}) = \int_{\mathbf{y} \neq 0} \left(f(\mathbf{x} - \mathbf{y}) - f(\mathbf{x}) + \frac{\mathbf{y} \cdot \nabla f(\mathbf{x})}{1 + \|\mathbf{y}\|^2} \right) \phi(\mathbf{x}, d\mathbf{y})$$

Here the Lévy measure is generalized to a jump intensity $\phi(\mathbf{x}, d\mathbf{y})$ that varies in space. Then, for example, one can consider the Hanyga diffusion model where (5.2) is replaced by

$$\hat{Q}(\mathbf{x}, \mathbf{k}) = -\int_{\mathbf{y} \in \Omega} |\mathbf{y} \cdot \mathbf{k}|^{\alpha(\mathbf{x}, \mathbf{y})} m(\mathbf{x}, d\mathbf{y}) \tag{7.2}$$

The extension to time-fractional forms follows along the same lines as in Section 6, using the general theory of time-fractional Cauchy problems.

References

Arendt W, Batty CJK, Hieber M, et al. (2001) *Vector-Valued Laplace Transforms and Cauchy Problems*, 2nd edn. Basel, Switzerland: Birkhäuser.

Baeumer B and Meerschaert MM (2001) Stochastic solutions for fractional Cauchy problems. *Fractional Calculus and Applied Analysis* 4: 481–500.

Baeumer B, Meerschaert MM and Kurita S (2005) Inhomogeneous fractional diffusion equations. *Fractional Calculus and Applied Analysis* 8: 371–386.

Bass RF (1988) Occupation time densities for stable-like processes and other pure jump Markov processes. *Stochastic Processes and their Applications* 29: 65–83.

Bass RF and Tang H (2009) The martingale problem for a class of stable-like processes. *Stochastic Processes and their Applications* 119: 1144–1167.

Bennett EM, Schmainda KM, Bennett RT, et al. (2003) Characterization of continuously distributed cortical water diffusion rates with a stretched-exponential model. *Magnetic Resonance in Medicine* 50: 727–734.

Callaghan PT (2011) *Translational Dynamics and Magnetic Resonance: Principles of Pulsed Gradient Spin Echo NMR*. Oxford: Oxford University Press.

GadElkarim JJ, Magin RL, Meerschaert MM, et al. (2013) Directional behavior of anomalous diffusion expressed through a multi-dimensional fractionalization of the Bloch-Torrey equation. *IEEE Journal on Emerging and Selected Topics in Circuits and Systems* 3: 432–441.

Haacke EM, Brown RW, Thompson MR, et al. (1999) *Magnetic Resonance Imaging: Physical Principles and Sequence Design*. New York, NY: Wiley-Liss.

Hall MG and Barrick TR (2008) From diffusion-weighted MRI to anomalous diffusion imaging. *Magnetic Resonance in Medicine* 59: 447–455.

Hall MG and Barrick TR (2012) Two-step anomalous diffusion tensor imaging. *NMR Biomedicine* 25(2): 286–294.

Hanyga A (2002) Multi-dimensional solutions of space-time-fractional diffusion equations. *Proceedings of the Royal Society of London A* 458(2018): 429–450.

Hanyga A and Magin RL (2014) A new anisotropic fractional model of diffusion model in a bio-tissue for applications in diffusion tensor imaging. *Proceedings of the Royal Society of London A* 470: 20140319.

Hanyga A and Seredyńska M (2012) Anisotropy in high-resolution diffusion-weighted MRI and anomalous diffusion. *Journal of Magnetic Resonance* 220: 85–93.

Ingo C, Magin RL, Colon-Perez L, et al. (2014) On random walks and entropy in diffusion-weighted magnetic resonance imaging studies of neural tissue. *Magnetic Resonance in Medicine* 71: 617–627.

Jacob N (2001) *Pseudo Differential Operators and Markov Processes*. Vol. I, London: Imperial College Press.

Johansen-Berg H and Behrens TE (2009) *Diffusion MRI: From Quantitative Measurement to In Vivo Neuroanatomy*. London: Elsevier.

Le Bihan H (1995) *Diffusion and Perfusion Magnetic Resonance Imaging: Applications to Functional MRI*. New York, NY: Raven Press.

Magin RL, Abdullah O, Baleanu D, et al. (2008) Anomalous diffusion expressed through fractional order differential operators in the Bloch–Torrey equation. *Journal of Magnetic Resonance* 190(2): 255–270.

Magin RL, Ingo C, Colon-Perez L, et al. (2014) Characterization of anomalous diffusion in porous biological tissues using fractional order derivatives and entropy. *Microporous and Mesoporous Materials* 71: 617–627.

Mainardi F (2010) *Fractional Calculus and Waves in Linear Viscoelasticity: An Introduction to Mathematical Models*. Singapore: World Scientific.

Meerschaert MM and Scheffler HP (2001) *Limit Distributions for Sums of Independent Random Vectors: Heavy Tails in Theory and Practice*. Wiley: New York.

Meerschaert MM and Scheffler HP (2004) Limit theorems for continuous-time random walks with infinite mean waiting times. *Journal of Applied Probability* 41: 623–638.

Meerschaert MM and Scheffler HP (2008) Triangular array limits for continuous time random walks. *Stochastic Processes and their Applications* 118: 1606–1633.

Meerschaert MM and Sikorskii A (2012) *Stochastic Models for Fractional Calculus*. Berlin: De Gruyter.

Metzler R and Klafter J (2000) The random walk's guide to anomalous diffusion: A fractional dynamics approach. *Physics Reports* 339: 1–77.

Metzler R and Klafter J (2004) The restaurant at the end of the random walk: Recent developments in the description of anomalous transport by fractional dynamics. *Journal of Physics A* 37: R161–R208.

Mori S (2006) *Introduction to Diffusion Tensor Imaging*. Amsterdam: Elsevier.

Özarslan E and Mareci TH (2003) Generalized diffusion tensor imaging and analytical relationships between diffusion tensor imaging and high angular resolution diffusion imaging. *Magnetic Resonance in Medicine* 50: 955–965.

Palombo M, Gabrielli A, De Santis S, et al. (2011) Spatio-temporal anomalous diffusion in heterogeneous media by nuclear magnetic resonance. *The Journal of Chemical Physics* 135(3): 034504.

Rudin W (1976) *Principles of Mathematical Analysis*, 3rd edn. New York, NY: McGraw-Hill.

Sato KI (1999) *Lévy Processes and Infinitely Divisible Distributions*. Cambridge: Cambridge University Press.

Schaltenbrand G and Wahren H (1998) *Atlas for Stereotaxy of the Human Brain*, 2nd edn. Stuttgart, Germany: Thieme.

Schilling RL (1998) Growth and Hölder conditions for the sample paths of Feller processes. *Probability Theory and Related Fields* 112: 565–611.

Torrey HC (1956) Bloch equations with diffusion terms. *Physical Review* 104: 563–565.

Zhou XJ, Gao Q, Abdullah O, et al. (2010) Studies of anomalous diffusion in the human brain using fractional order calculus. *Magnetic Resonance in Medicine* 63: 562–569.

Fractional complex-order model for HIV infection with drug resistance during therapy

Carla MA Pinto[1,2] and Ana RM Carvalho[3]

Abstract

We propose a fractional complex-order model for drug resistance in HIV infection. We consider three distinct growth rates for the CD4^{+} T helper cells. We simulate the model for different values of the fractional derivative of complex order $D^{\alpha \pm j\beta}$, where $\alpha, \beta \in R^+$, and for distinct growth rates. The fractional derivative of complex order is a generalization of the integer-order derivative where $\alpha = 1$ and $\beta = 0$. The fractional complex-order system reveals rich dynamics and variation of the value of the complex-order derivative sheds new light on the modeling of the intracellular delay. Additionally, fractional patterns are characterized by time responses with faster transients and slower evolutions towards the steady state.

1. Introduction

The human immunodeficiency virus (HIV) is a retrovirus that impairs the immune response system. It targets the CD4^{+} helper T cells by, for example, the gp120 binding to CD4 and CXCR4 receptors. This ability of the HIV virus results in its vast replication during the acute phase. The next typical stage of the HIV infection is the chronic phase, where the viral load lowers and approaches a quasi-steady state. This is mainly due to the balance between virus production and clearance rates (Wei et al., 1995). The AIDS phase follows the chronic phase, where the number of CD4^{+} T cells declines steadily and the viral load increases (Ho et al., 1995).

The treatment for HIV/AIDS relies on antiretroviral drugs that suppress the HIV viral load below the limit of detection. The major five drug classes to fight HIV/AIDS are the reverse transcriptase inhibitors (RTI), the protease inhibitors (PI), the fusion/entry inhibitors (FEI), the integrase inhibitors (II), and the multidrug inhibitors (MI). The RTI interfere with the reverse transcription, preventing the HIV enzyme reverse transcriptase from converting HIV RNA into HIV DNA. The PI prevent the production of infectious viral particles by the HIV protease enzyme. The FEI interfere with the ability of the virus to bond to the cell membrane. The II block the introduction of virus genetic material into the host cell. Finally, the MI combine distinct drugs of the above classes in order to avoid virus strains becoming resistant to specific antiretroviral drugs. The latter is known as highly antiretroviral therapy (HAART).

Antiretroviral therapy (ART) (and HAART) may not be effective for certain patients. There is evidence of virus persistence during treatment, and of viral load rebounds shortly after ART interruption (Montaner et al., 1998; Harrigan et al., 1999). The existent virus reservoirs, in the form of latently infected CD4^{+} T cells, and infected macrophages and dendritic cells, are responsible for this phenomenon and make the eradication of the virus extremely complex. The effectiveness of ART may also be reduced by the appearance of drug resistance. Drug resistance is associated with high virus replication and mutation rates, poor adherence to therapy, and poor absorption and pharmacokinetics (Wahl and Nowak, 2000).

[1]School of Engineering, Polytechnic of Porto, Portugal
[2]Centro de Matemática da Universidade do Porto, Portugal
[3]Department of Mathematics, Faculty of Sciences, University of Porto, Portugal

Corresponding author:
Carla MA Pinto, School of Engineering, Polytechnic of Porto and Center for Mathematics of the University of Porto, Rua Dr António Bernardino de Almeida, 431, 4200-072 Porto, Portugal.
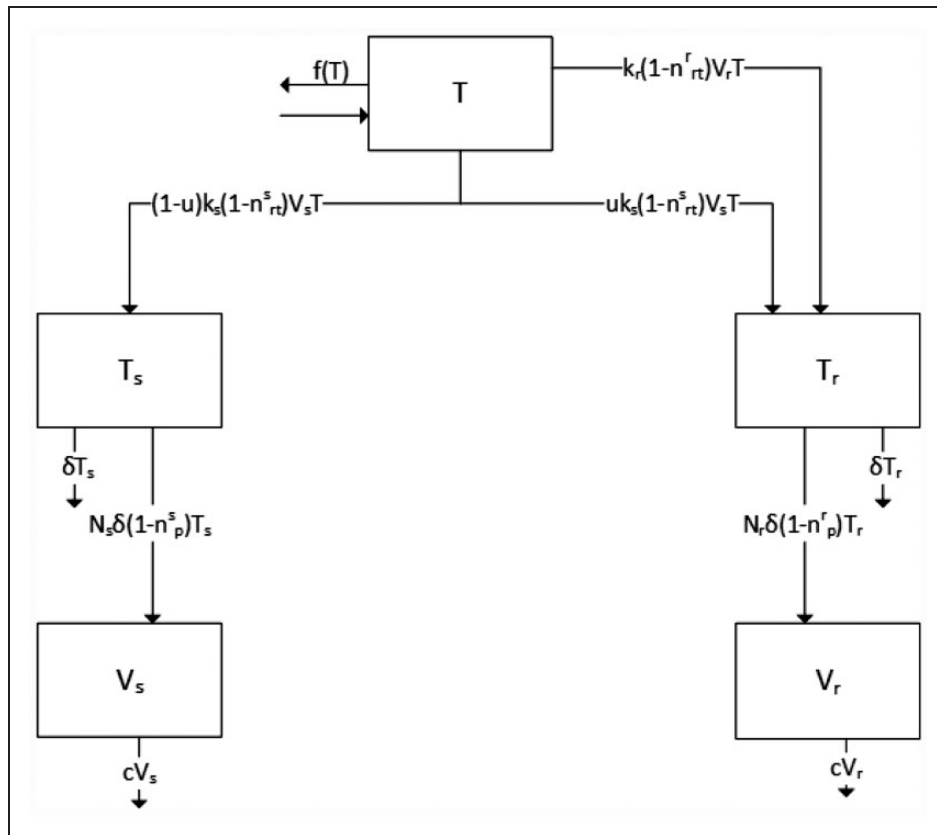Email: cap@isep.ipp.pt

Figure 1. Schematic diagram of model (4).

In the last two or three decades there has been a major breakthrough in the modeling of HIV epidemics (Pinto and Carvalho, 2014) and the efficiency of ART regimens. Ouifki and Witten (2009) proposed a model for HIV-1 infection that included RTI and three intracellular delays. Authors observed that introducing delays promoted the appearance of Hopf bifurcations, translated in the model as periodic orbits around the endemic equilibrium. These solutions were consistent with the viral blips seen in HIV patient data. In Pitchaimani et al. (2013), the authors studied a model for HIV-1 infection with PI therapy and three delays. They showed that the delays reduced the number of infected cells and viruses at the HIV endemic equilibrium, thus lowering the critical efficacy of the PI regimen. Wang et al. (2014) proposed a model for drug resistance that includes intracellular delay and a general form of target cell density, during ART. The authors obtained sustained oscillations, promoted by variation of the T cells' growth rate, in a biologically reasonable parameter space. This finding suggested the viral strains rapidly turn over and any successful ART regimen should take this into consideration.

In this paper, we propose a fractional complex-order model for drug resistance in HIV infection. We consider three distinct growth rates of the CD4$^+$ T helper cells.

Table 1. Parameters used in the numerical simulations of model (4).

Parameter	Value	Reference
λ	75	Luo et al. (2012)
d	0.1	Althaus and Boer (2011)
r	0.03	Wang et al. (2014)
T_{max}	1500	Wang et al. (2014)
k_s	2.4×10^{-5}	Luo et al. (2012)
k_r	2×10^{-5}	Luo et al. (2012)
u	3×10^{-5}	Sanjuán et al. (2010), Wang et al. (2014)
δ	1	Althaus and Boer (2011)
N_s	4800	Luo et al. (2012)
N_r	4000	Luo et al. (2012)
c	23	Althaus and Boer (2011)
n_{rt}^s	0.4	Wang et al. (2014)
n_{rt}^r	0.2	Wang et al. (2014)
n_p^s	0.1	Wang et al. (2014)
n_p^r	0.1	Wang et al. (2014)

We numerically simulate the model for different values of the order of the fractional complex derivative $D^{\alpha \pm j\beta}$. Bearing these ideas in mind, the paper is organized as follows. In Section 2, we describe the fractional model.
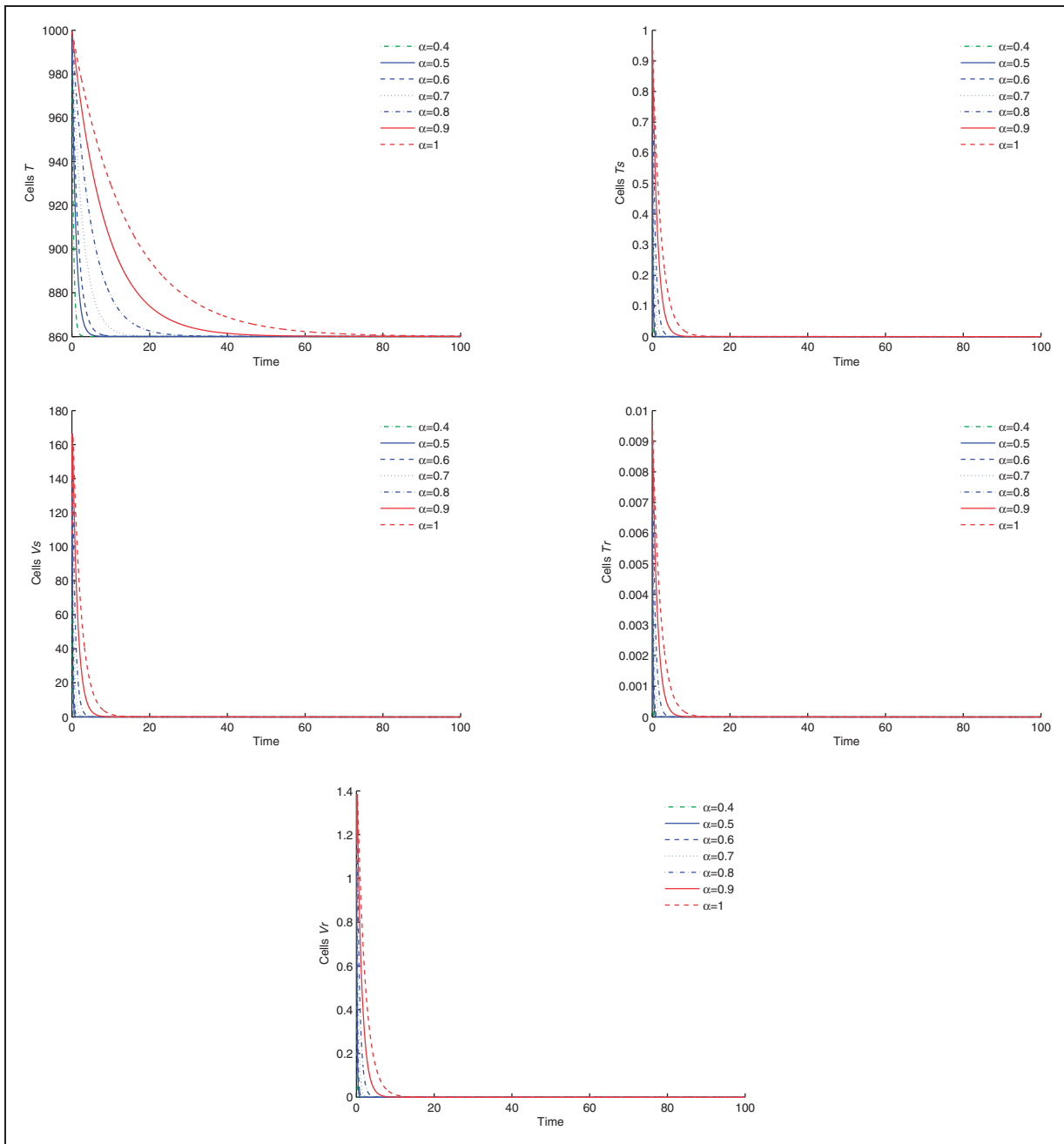
Figure 2. Disease-free equilibrium of the model (4) for the parameter values of Table 1 except for $k_s = 2.4 \times 10^{-6}$, $k_r = 2.0 \times 10^{-6}$, given initial conditions, and growth rate $f_1(t)$.

In Section 3, we analyze several simulations of the model, for distinct values of the order of the fractional derivative, and for distinct growth rates. We discuss implications of the results. Finally, we state the main conclusions and highlight future research.

1.1. Fractional calculus: brief summary

In the last few decades, fractional calculus, that is, non-integer-order calculus, has been widely studied by mathematicians and engineers (Oldham and Spanier, 1974; Miller and Ross, 1993; Samko et al., 1993; Tarasov, 2010). The fractional-order derivative is a generalization of the integer-order derivative. The models including fractional derivatives have been applied in a variety of research areas, such as in fluid mechanics (Momani and Odibat, 2006), electrochemistry (Oldham, 2010), engineering (Makris and Constantinou, 1993; Mainardi, 1996; Pinto and Machado, 2001; Baleanu, 2009; Machado, 2009; Pinto

Figure 3. Drug-sensitive endemic equilibrium of the model (4) for the parameter values given in Table 1, except for $u = 3 \times 10^{-8}$ and $N_r = 2300$, given initial conditions, and growth rate $f_1(t)$.

and Machado, 2012; Golmankhaneh et al., 2013), physics (Caputo and Mainardi, 1971; Nigmatullin and Baleanu, 2010).

There are three important and well-studied definitions for a fractional-order derivative, namely, the Riemann–Liouville, the Grünwald–Letnikov (GL), and the Caputo formulas (Oldham and Spanier, 1974;

Miller and Ross, 1993). In our work, we consider the GL derivative, given by equation (1):

$$
{}_a^{\mathrm{GL}} D_t^\alpha f(t) = \lim_{h \to 0} \frac{1}{h^\alpha} \sum_{k=0}^{\left[\frac{t-a}{h}\right]} (-1)^k \binom{\alpha}{k} f(t - kh),
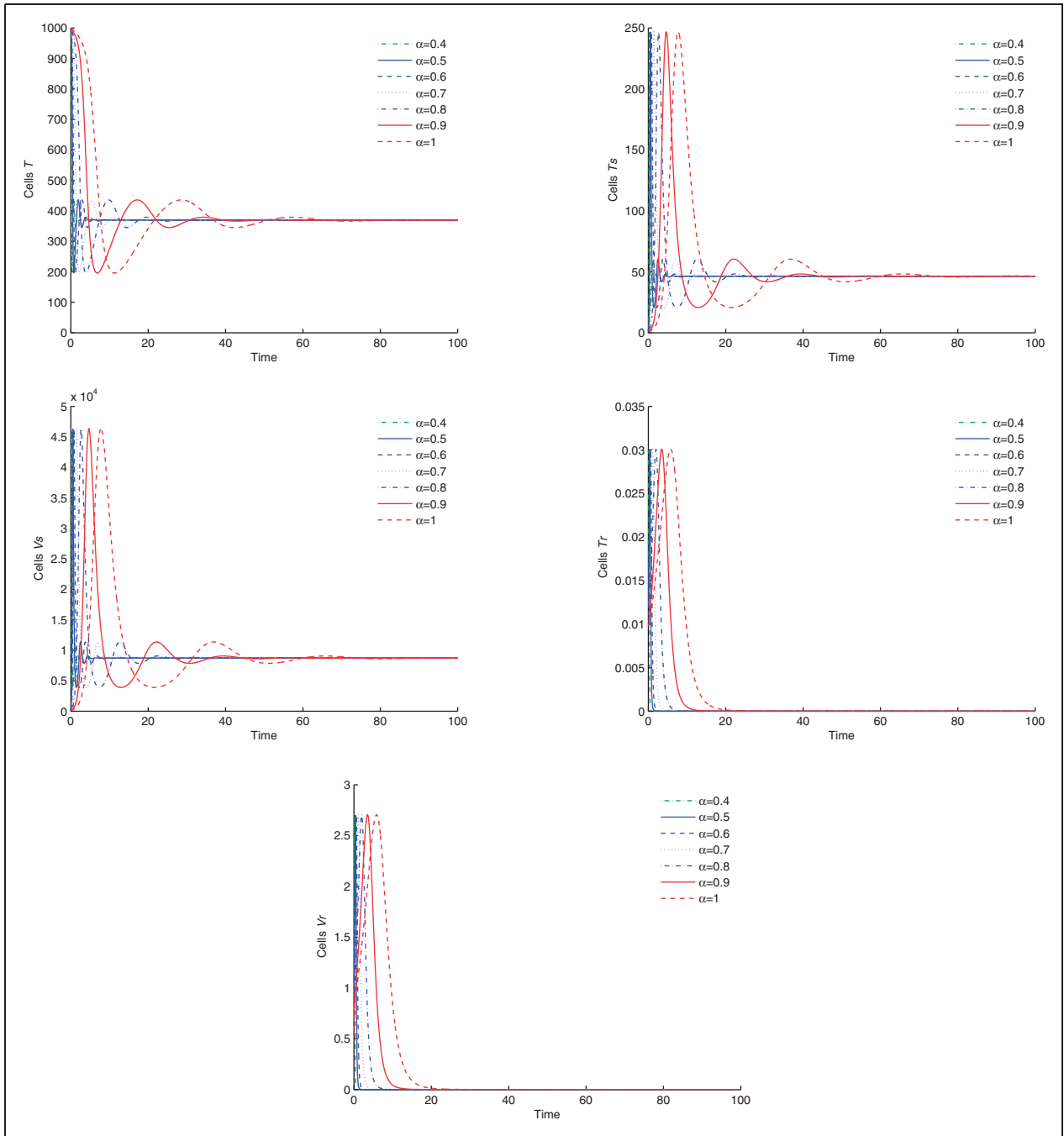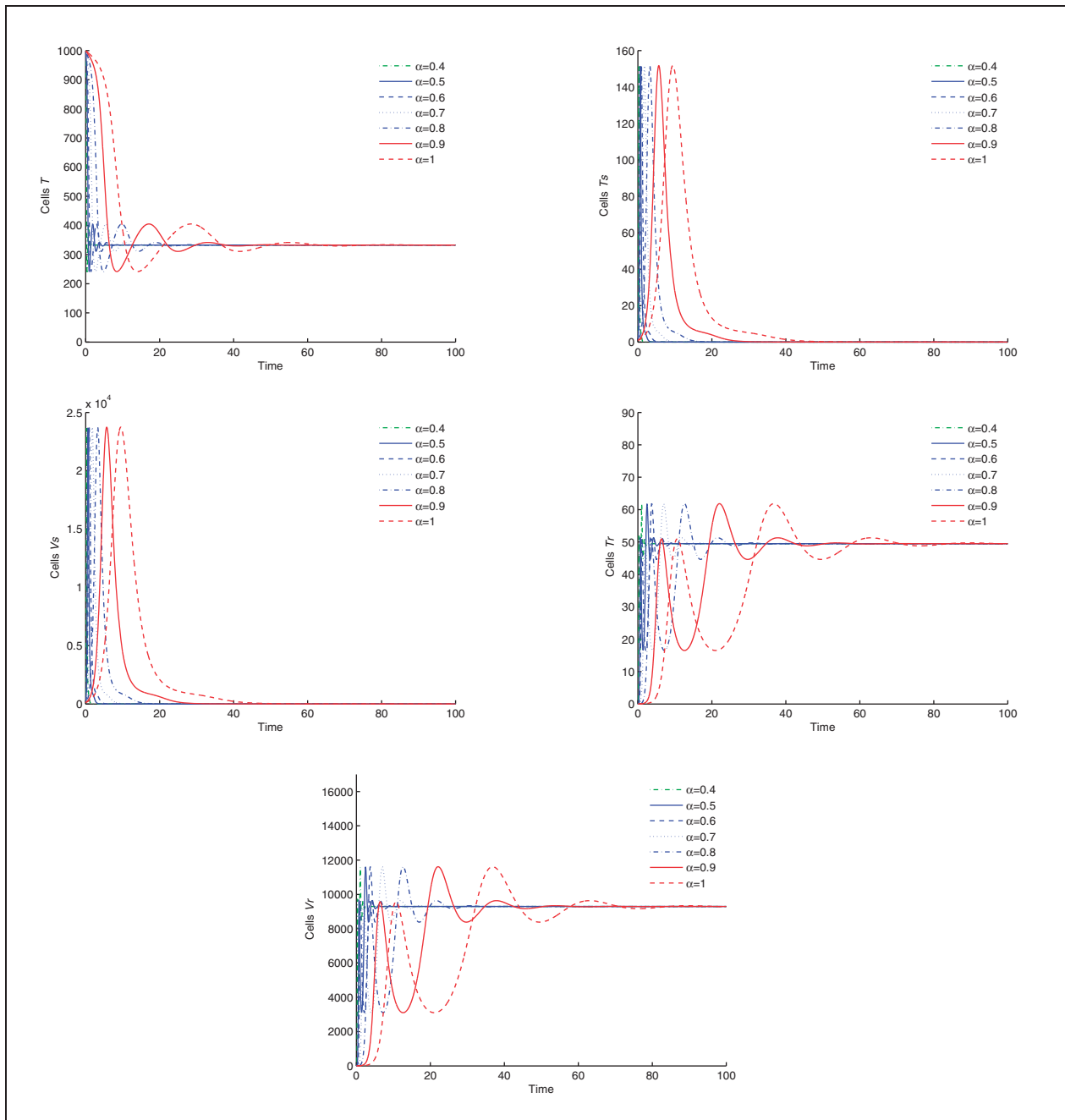$$
$$
t > a, \alpha > 0 \tag{1}
$$

Figure 4. Drug resistance endemic equilibrium of the model (4) for the parameter values given in Table 1, except $N_s = 4000$ and $N_r = 4800$, given initial conditions, and growth rate $f_1(t)$.

where $[x]$ means the integer part of x, and h represents the time step increment.

The fractional derivatives capture the history of the variable, or, in other words, have memory, contrary to integer-order derivatives, which are local operators. This characteristic makes them an important tool in the modeling of memory-intense and delay systems.

The most often adopted generalization of the fractional derivative operator consists in $\alpha \in \mathbf{R}$.

The fractional derivative of complex order $\alpha \pm J\beta \in \mathbf{C}$, when applied to a system of equations, results in complex-valued outcomes. The latter restricts a practical application. In order to overcome this difficulty, Hartley et al. (2005) and Barbosa et al. (2008) proposed the association of two complex-order derivatives. One of these associations is the sum of two complex conjugate derivatives $D^{\alpha \pm J\beta}$, given in equation (2). Other combinations and approximation
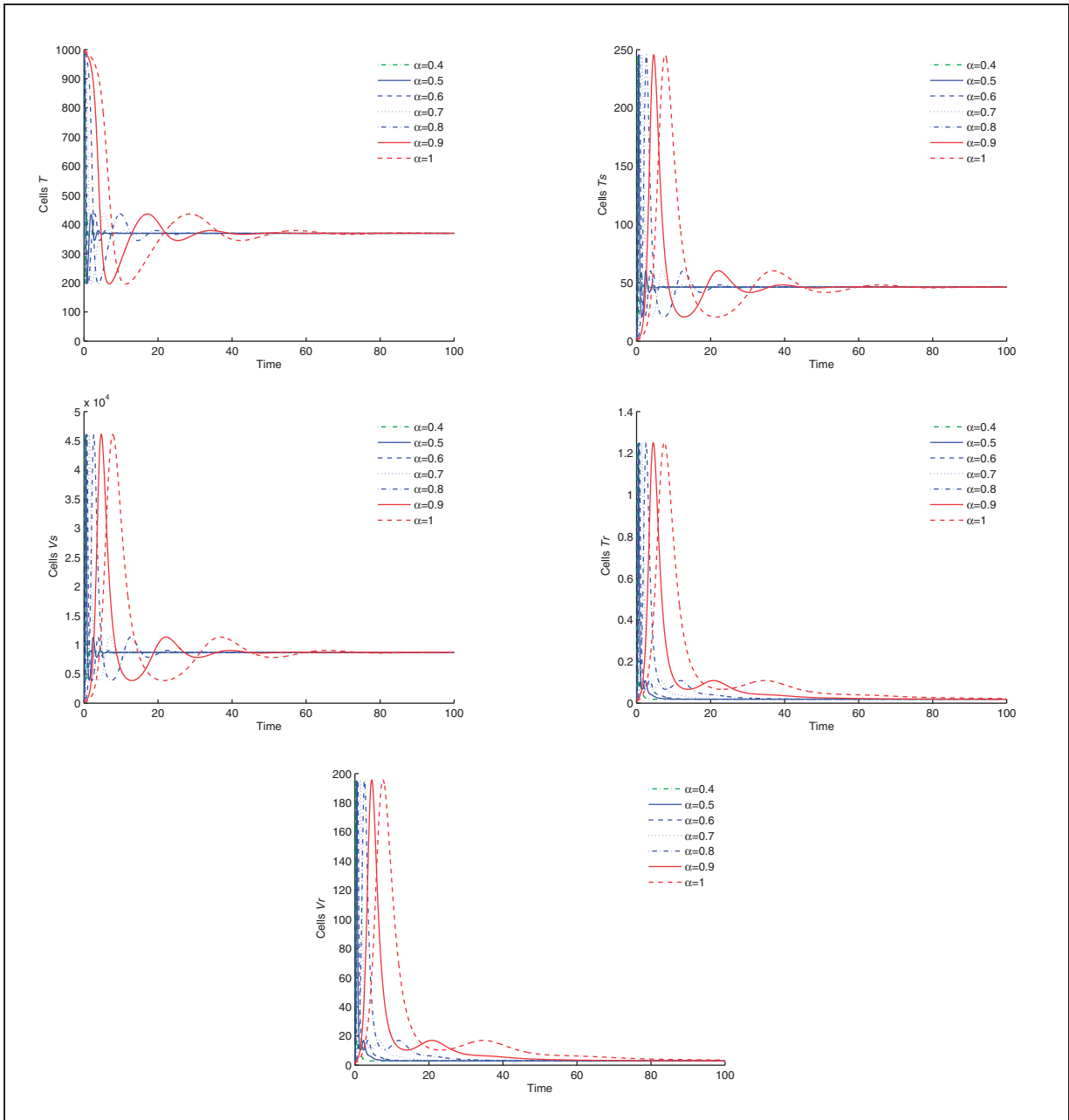
Figure 5. Endemic equilibrium of the model (4) for given parameter values in Table 1, given initial conditions, and growth rate $f_1(t)$.

methods are possible. In this paper, we will use expression (2):

$$Z\left\{\frac{1}{2}\left[D^{\alpha-j\beta}x(t)+D^{\alpha+j\beta}x(t)\right]\right\}$$
$$\approx\frac{1}{T^\alpha}\left\{\sin\left[\beta\ln\left(\frac{1}{T}\right)\right]\left[\beta z^{-1}+\frac{1}{2}\beta(1-2\alpha)z^{-2}+\cdots\right]\right.$$
$$\left.+\cos\left[\beta\ln\left(\frac{1}{T}\right)\right]\left[-1+\alpha z^{-1}-\frac{1}{2}\beta(\alpha^2-\alpha-\beta^2+\cdots)\right]\right\}X(z)$$

$$(2)$$

2. Description of model

The model describes the dynamics of the populations of uninfected CD4$^+$ T cells T, drug-sensitive infected CD4$^+$ T cells T_s, drug-resistant infected CD4$^+$ T cells T_r, drug-sensitive infectious viruses V_s, and drug-resistant infectious viruses V_r.

The epidemiology of the disease is as follows. The uninfected CD4$^+$ T cells, T, are produced at a rate λ and die at a rate d. These cells, when in contact with
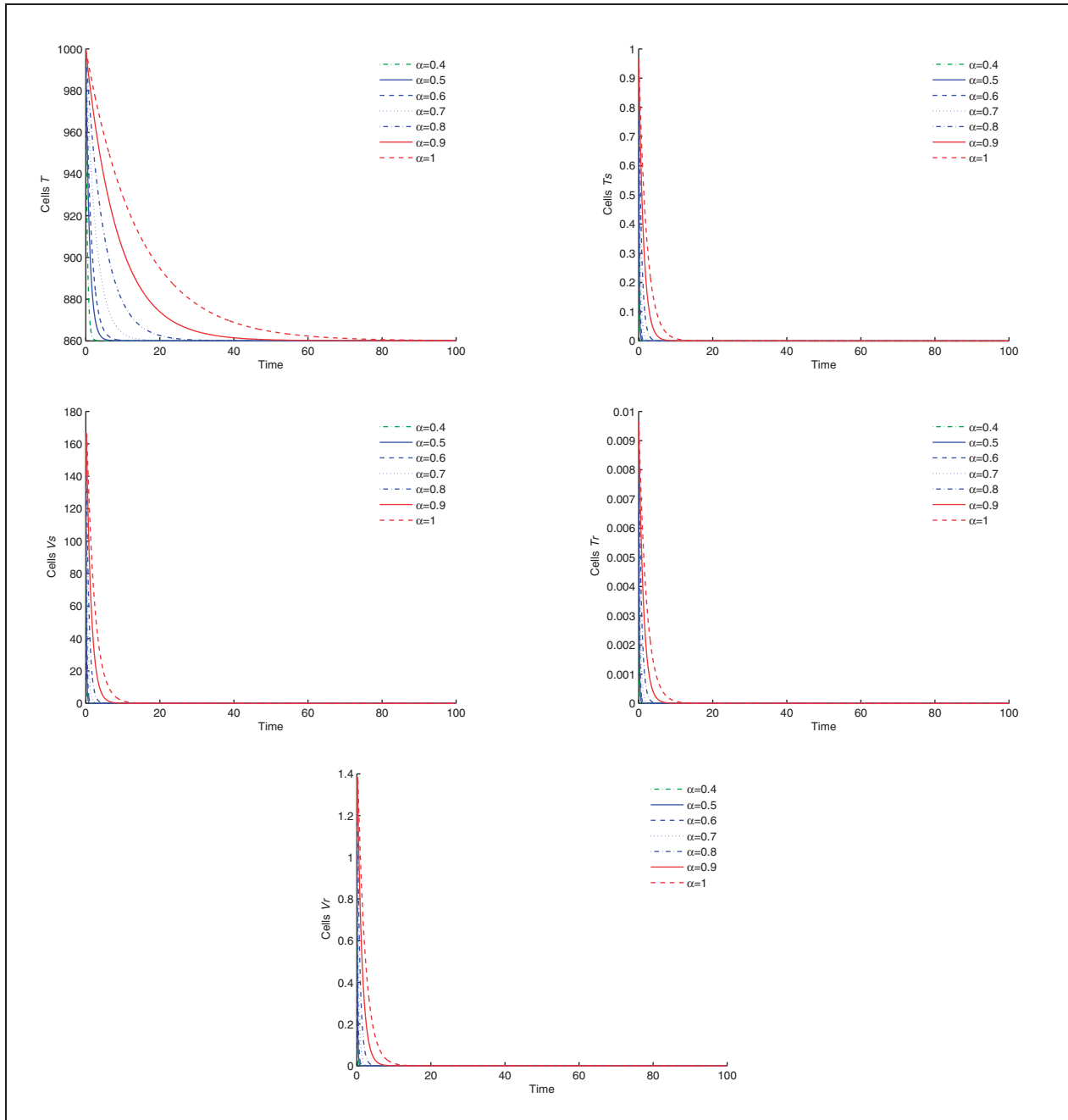
Figure 6. Disease-free equilibrium of the model (4) for the parameter values of Table 1, except $k_s = 2.4 \times 10^{-6}$ and $k_r = 2.0 \times 10^{-6}$, given initial conditions, and the growth rate $f_2(t)$.

HIV, get infected, at a rate k_s, by drug-sensitive viruses and move to the T_s class. Moreover, T cells may be infected, at a rate k_r, by drug-resistant viruses and move to the T_r class.

The proportions of T_s and T_r cells that, after contact with the virus, are not eliminated by RTI are $1 - n_{rt}^s$ and $1 - n_{rt}^r$, respectively. Parameters n_{rt}^s and n_{rt}^r represent the efficacy rates of RTI for wild type and mutants, respectively.

Throughout the infection, a proportion u, $0 < u < 1$, of T_s cells can become resistant to the antiretroviral drugs and move to the class T_r.

The infected CD4$^+$ T cells die at a rate δ and the viruses are cleared at a rate c. The V_s and V_r particles are produced by the corresponding infected CD4$^+$ T cell populations, with bursting sizes of drug-sensitive strain, N_s, and of drug-resistant strain, N_r. The proportions of virus particles that are not eliminated by PI are
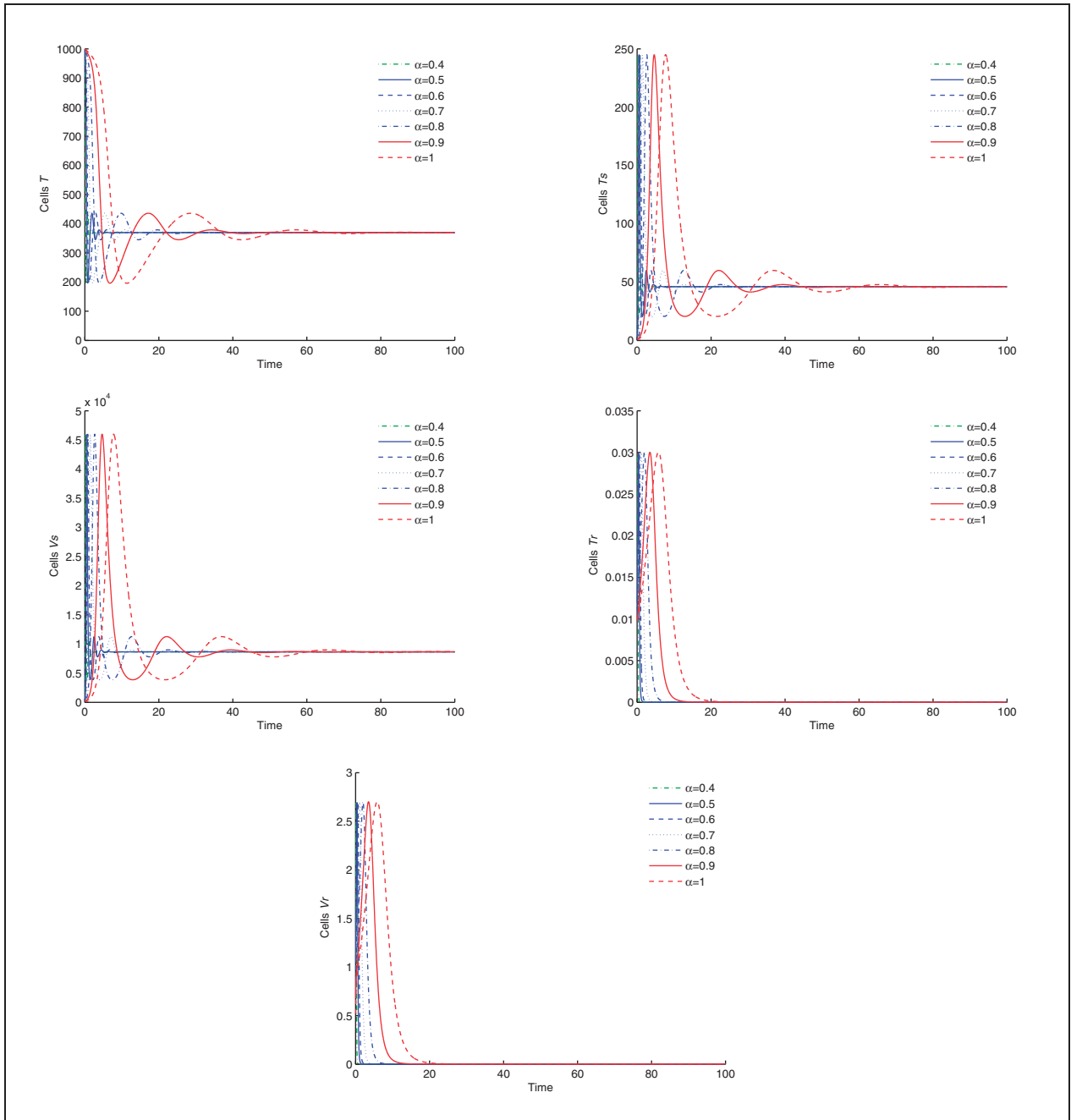
Figure 7. Drug-sensitive endemic equilibrium of the model (4) for the parameter values given in Table 1, except $u = 3 \times 10^{-8}$, and $N_r = 2300$, given initial conditions, and growth rate $f_2(t)$.

$1 - n_p^s$ and $1 - n_p^r$, where n_p^s is the efficacy of PI for wild-type strain, and n_p^r is the efficacy of PI for mutants.

We will consider three distinct growth rates for the uninfected target cells T, namely (Xiao et al., 2013)

$$f(T) = \begin{cases} f_1(T) & = \lambda - \mathrm{d}T + r\left(1 - \dfrac{T}{T_{max}}\right) \\ f_2(T) & = \lambda - \mathrm{d}T + r\left(1 - \dfrac{T + T_s + T_r}{T_{max}}\right) \\ f_3(T) & = \lambda - \mathrm{d}T \end{cases} \quad (3)$$

where λ and d are as above. When $f = f_1$, the healthy T cells are assumed to proliferate exponentially at a rate r until they reach the carrying capacity T_{max}, in the absence of the virus or infected T cells.

The following nonlinear system of ordinary differential equations describes the dynamics of the fractional model of complex order:

$$\begin{aligned} \tfrac{1}{2}\left(D^{\alpha+J\beta} + D^{\alpha-J\beta}\right)T(t) &= f(T) - k_s(1 - \overline{n_{rt}^s})V_s(t)T(t) - k_r(1 - n_{rt}^r)V_r(t)T(t) \\ \tfrac{1}{2}\left(D^{\alpha+J\beta} + D^{\alpha-J\beta}\right)T_s(t) &= (1 - u)k_s(1 - n_{rt}^s)V_s(t)T(t) - \delta T_s(t) \\ \tfrac{1}{2}\left(D^{\alpha+J\beta} + D^{\alpha-J\beta}\right)V_s(t) &= N_s\delta(1 - n_p^s)T_s(t) - cV_s(t) \\ \tfrac{1}{2}\left(D^{\alpha+J\beta} + D^{\alpha-J\beta}\right)T_r(t) &= uk_s(1 - n_{rt}^s)V_s(t)T(t) + k_r(1 - n_{rt}^r)V_r(t)T(t) - \delta T_r(t) \\ \tfrac{1}{2}\left(D^{\alpha+J\beta} + D^{\alpha-J\beta}\right)V_r(t) &= N_r\delta(1 - n_p^r)T_r(t) - cV_r(r) \end{aligned} \quad (4)$$

The schematic diagram of the proposed model can be seen in Figure 1.

3. Numerical results

In this section we present the numerical results for model (4). The parameters used in the simulations are given in Table 1 and the initial conditions are set to $T(0) = 1000$, $T_s(0) = 1$ and $V_s(0) = T_r(0) = V_r(0) = 0.01$.

We simulate the model (4) for different values of the complex-order fractional derivative $D^{\alpha \pm J\beta}$. We fix $\beta = 0.8$ and vary $\alpha \in \{0.4, 0, 5, 0.6, 0.7, 0.8, 0.9, 1.0\}$. We also distinguish the three functions $f(T)$ for the growth rate of the uninfected CD4+ helper T cells.

We adopt the Power Series Expansion (PSE) method for the approximation of the complex-order derivative in the discrete-time numerical integration. Several experiments demonstrated that a slight adaption to the standard approach based on a simple truncation of the series is required. The latter corresponds to a diminishing of the gain (Machado, 2009) and, consequently, leads to difficulties in the promotion of periodic orbits. Therefore, in order to overcome this limitation, we decided to include a gain adjustment factor corresponding to the sum of the missing truncated series coefficients.

3.1. Growth rate f₁

We consider $f(T) = \lambda - \mathrm{d}T + pT(1 - \frac{T}{T_{max}})$, fix $\beta = 0.8$ and vary $\alpha \in \{0.4, 0.5, 0.6, 0.7, 0.8, 0.9, 1.0\}$.

In Figure 2, we observe that the model (4) asymptotically approaches the disease-free equilibrium for growth rate $f_1(t)$.

In Figure 3, the dynamics of the variables of system (4) for the drug-sensitive endemic equilibrium for growth rate $f_1(t)$ is shown.

The dynamics corresponding to the drug-resistant endemic equilibrium of system (4) for growth rate $f_1(t)$ can be seen in Figure 4.

Figure 5 depicts the dynamics of the endemic equilibrium of the model (4) for the growth rate $f_1(t)$.

3.2. Growth rate f₂

In this section we simulate the model for the growth rate $f_2(t) = \lambda - \mathrm{d}T + p\left(1 - \frac{T+T_s+T_r}{T_{max}}\right)$, fix $\beta = 0.8$ and $\alpha \in \{0.4, 0.5, 0.6, 0.7, 0.8, 0.9, 1.0\}$.

In Figure 6, we observe that the model (4) asymptotically approaches the disease-free equilibrium, for the growth rate $f_2(t)$.

In Figure 7, the dynamics of the variables of system (4) for the drug-sensitive endemic equilibrium, for the growth rate $f_2(t)$, is shown.

The dynamics corresponding to the drug-resistant endemic equilibrium of system (4) can be seen in Figure 8, for the growth rate $f_2(t)$.

Figure 9 depicts the dynamics of the endemic equilibrium of the model (4), for the growth rate $f_2(t)$.

3.3. Growth rate f₃

In this section we simulate the model (4) for $f(t) = f_3(t) = \lambda - dT$, fix $\beta = 0.8$ and vary $\alpha \in \{0.4, 0.5, 0.6, 0.7, 0.8, 0.9, 1.0\}$.

In Figure 10, we observe that the model (4) asymptotically approaches the disease-free equilibrium, for the growth rate $f_3(t)$.

In Figure 11, the dynamics of the variables of system (4) for the drug-sensitive endemic equilibrium is shown. The growth rate of the helper T cells is $f_3(t)$.

The dynamics corresponding to the drug-resistant endemic equilibrium of system (4) can be seen in Figure 12, for the growth rate $f_3(t)$.

Figure 13 depicts the dynamics of the endemic equilibrium of the model (4), for the growth rate $f_3(t)$.

Figure 8. Drug resistance endemic equilibrium of the model (4) for the parameter values given in Table 1, except for $N_s = 4000$ and $N_r = 4800$, given initial conditions, and growth rate $f_2(t)$.

Figure 9. Endemic equilibrium of the model (4) for given parameter values in Table 1, given initial conditions, and growth rate $f_2(t)$.
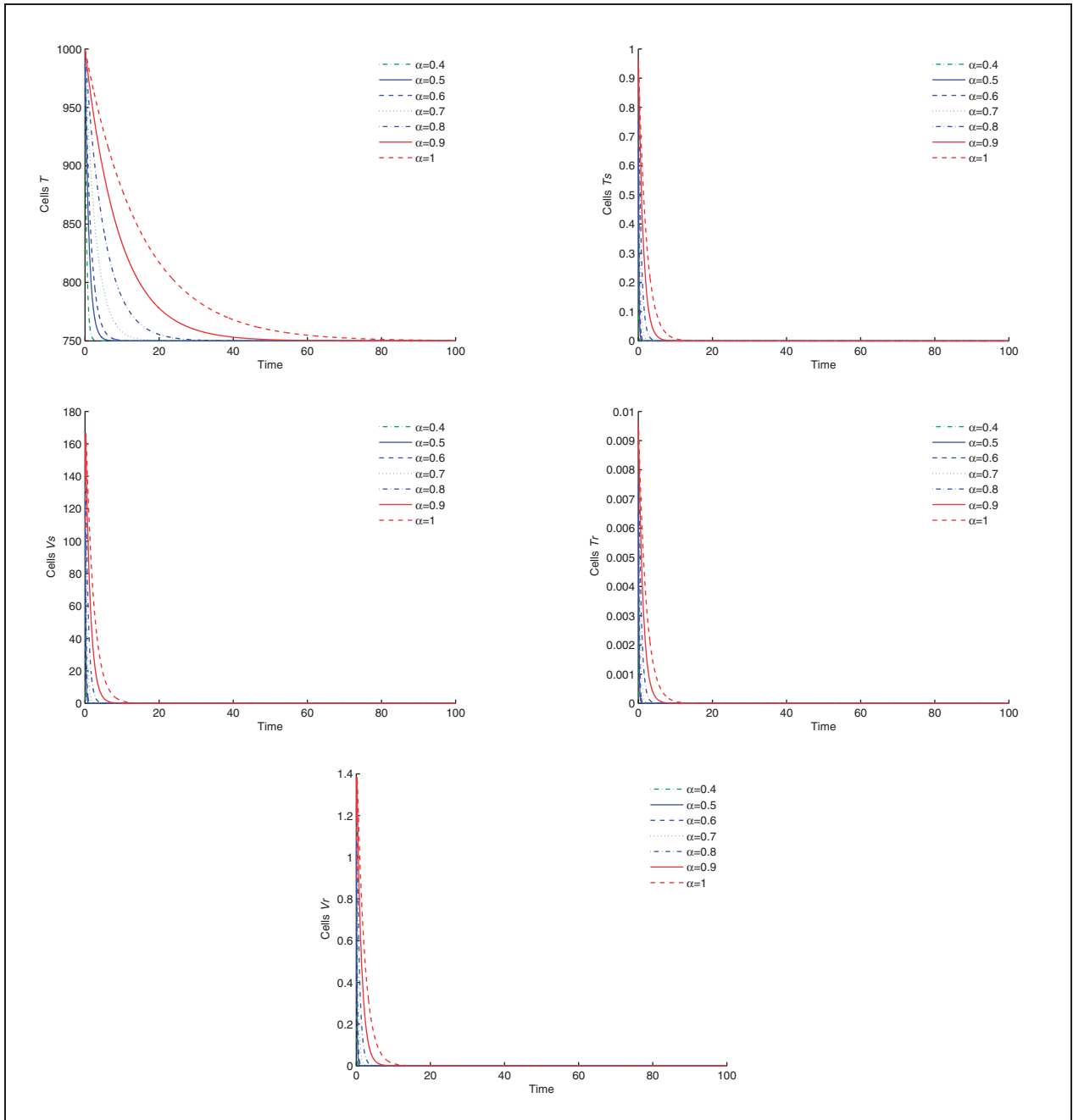
Figure 10. Disease-free equilibrium of the model (4) for parameter values of Table 1 except $k_s = 2.4 \times 10^{-6}$ and $k_r = 2.0 \times 10^{-6}$, given initial conditions, and the growth rate $f_3(t)$.

Figure 11. Drug-sensitive endemic equilibrium of the model (4) for the parameter values given in Table 1, except for $u = 3 \times 10^{-8}$ and $N_r = 2300$, given initial conditions, and growth rate $f_3(t)$.
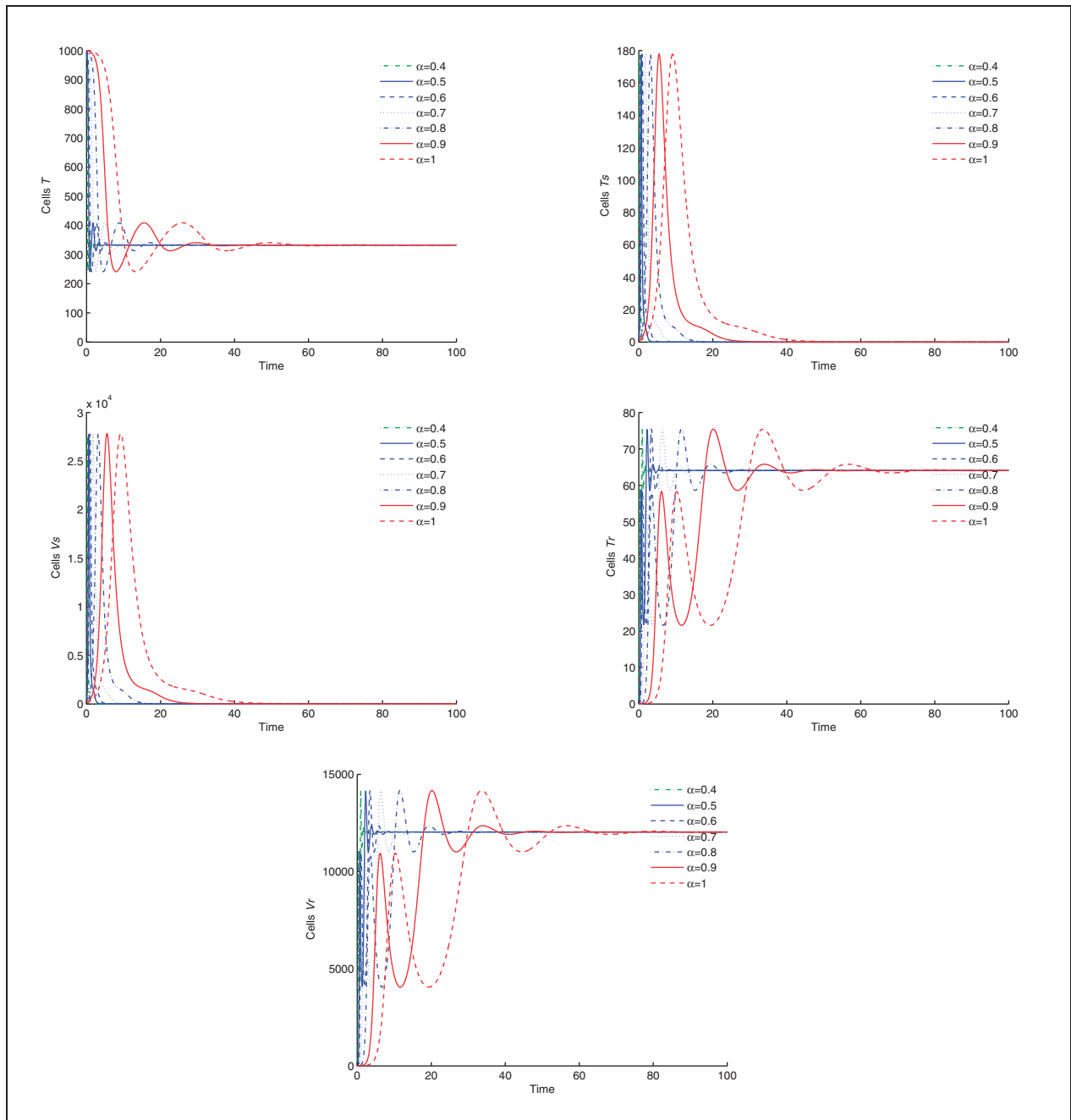
Figure 12. Drug resistance endemic equilibrium of the model (4) for the parameter values given in Table 1, except for $N_s = 4000$ and $N_r = 4800$, given initial conditions, for the growth rate $f_3(t)$.
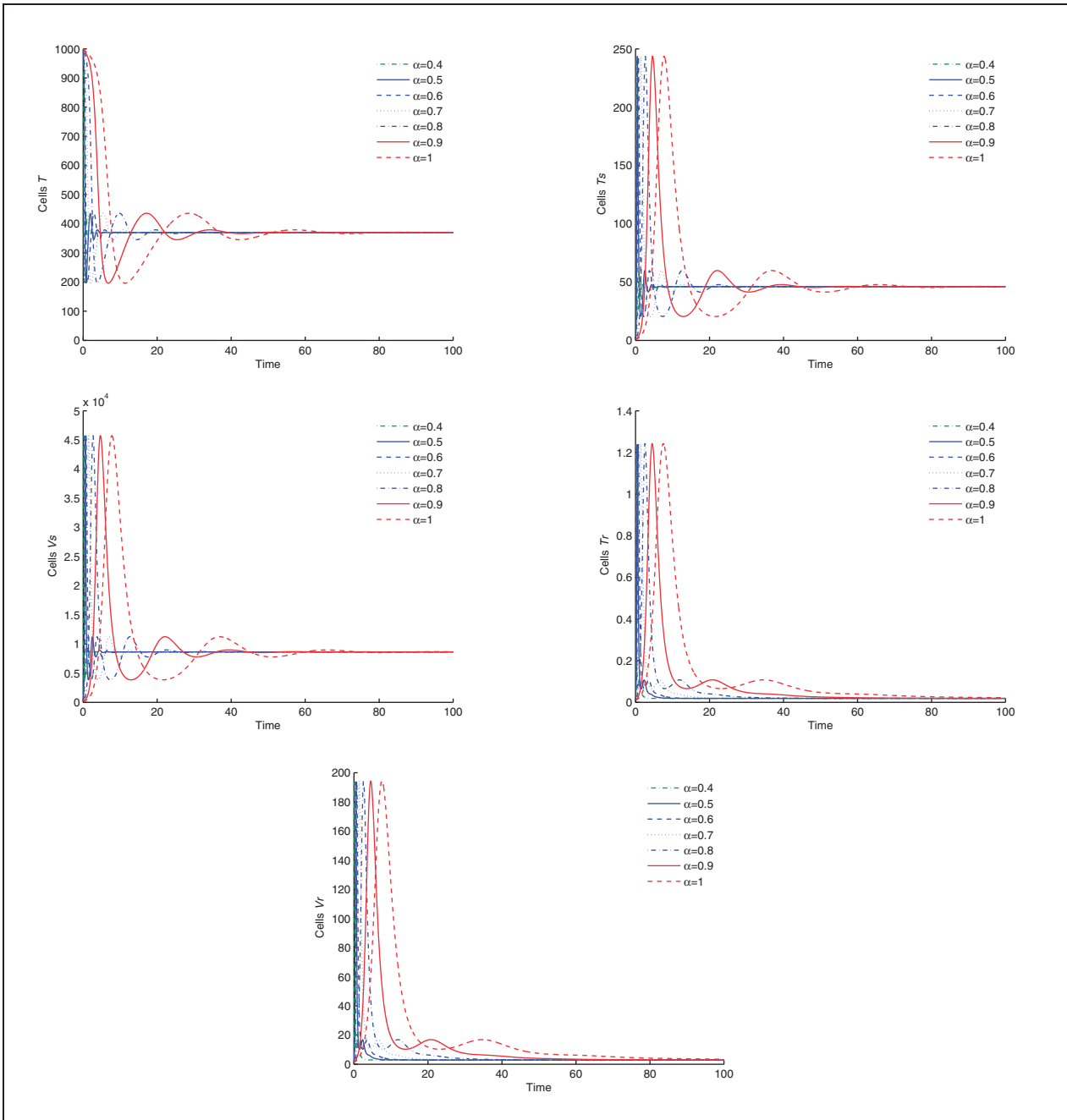
Figure 13. Endemic equilibrium of the model (4) for the given parameter values in Table 1, given initial conditions, for the growth rate $f_3(t)$.
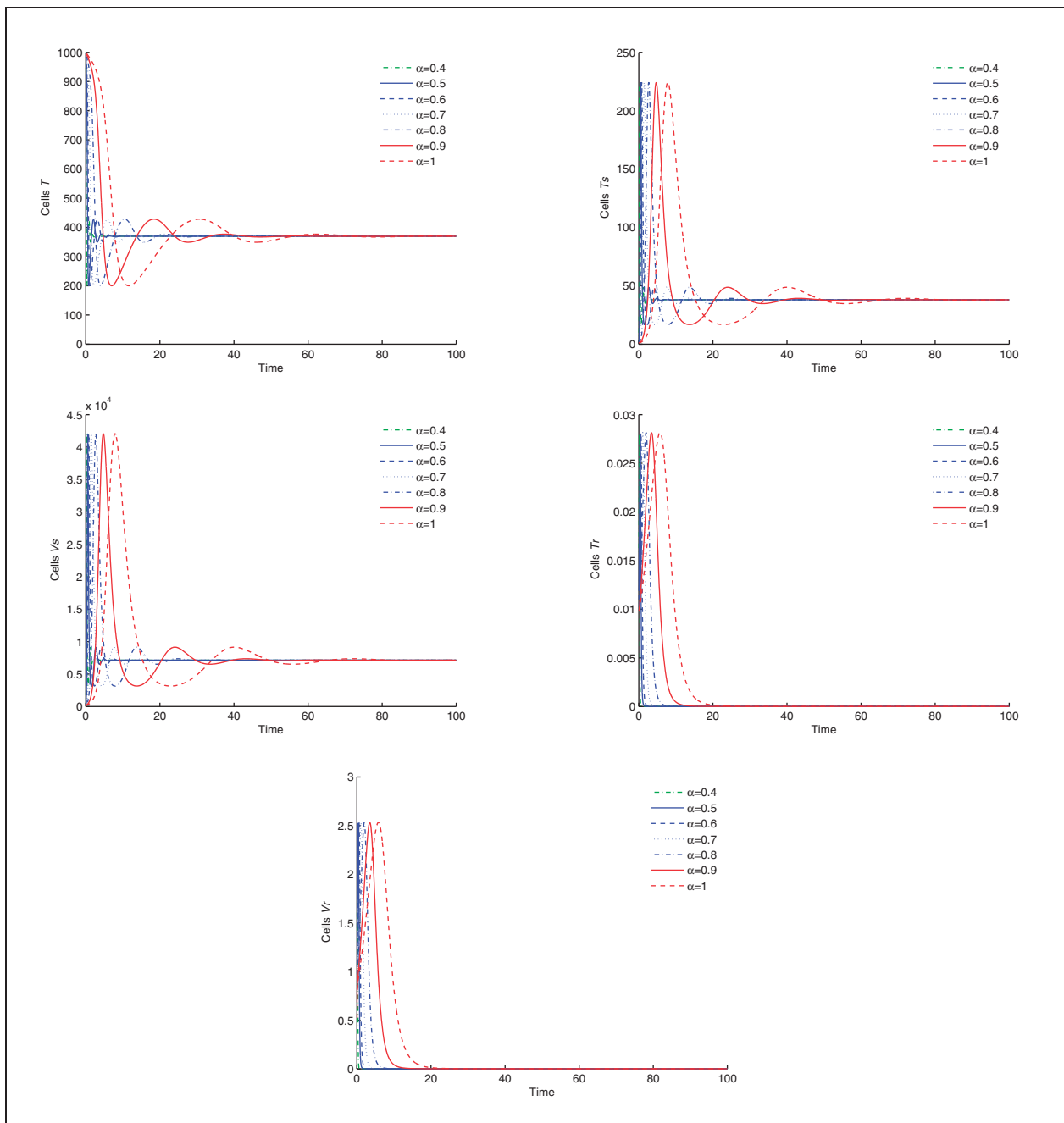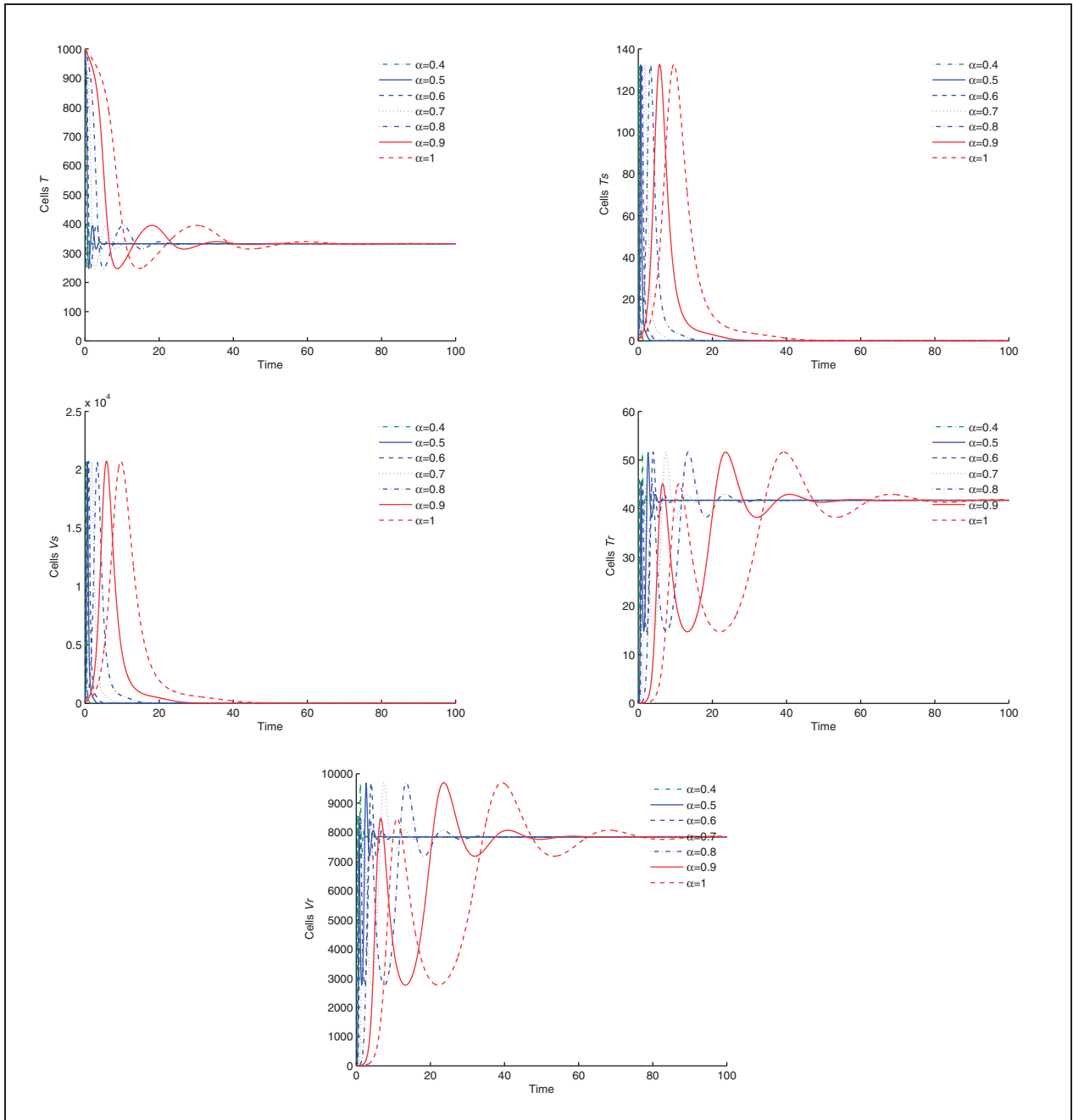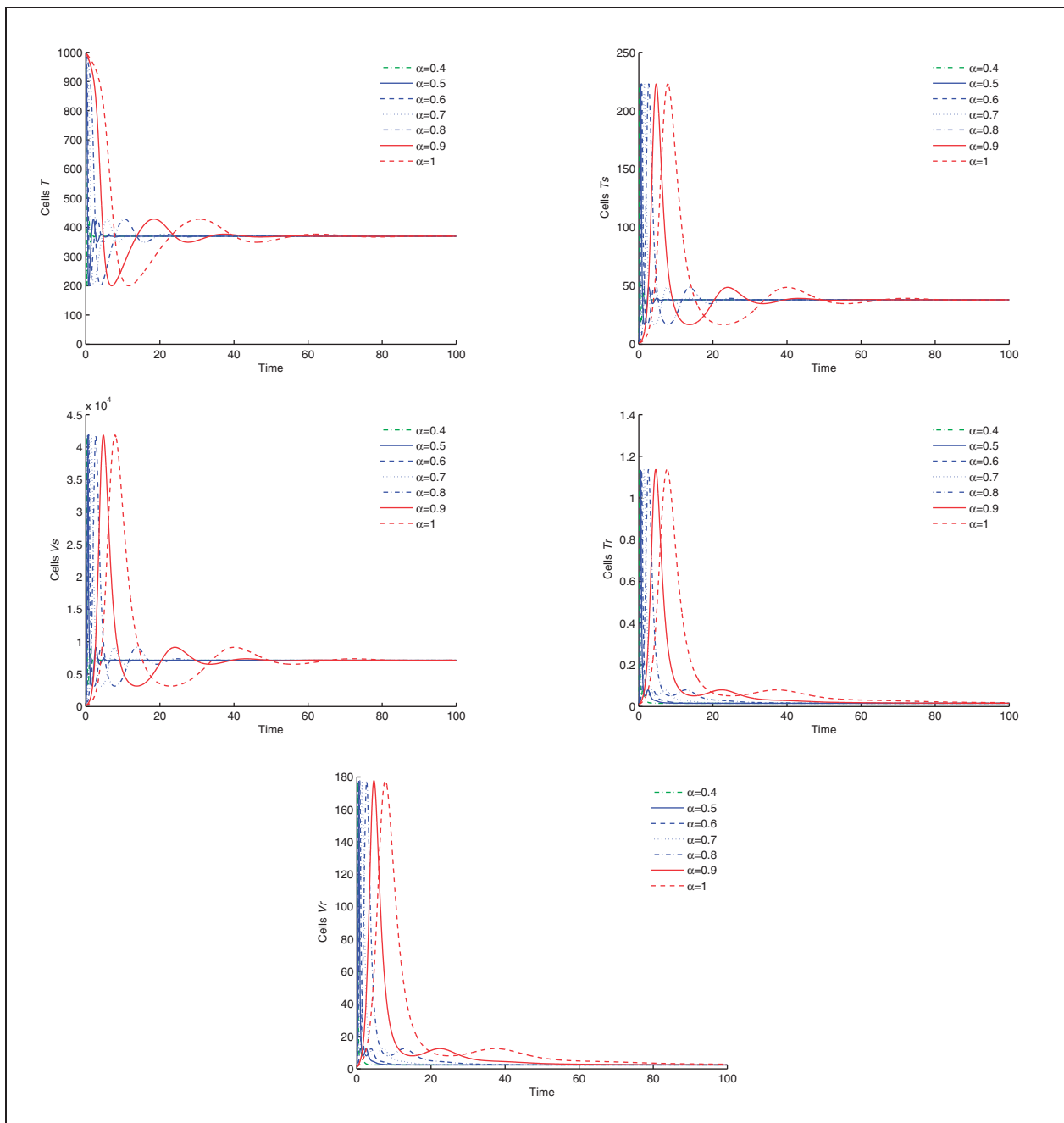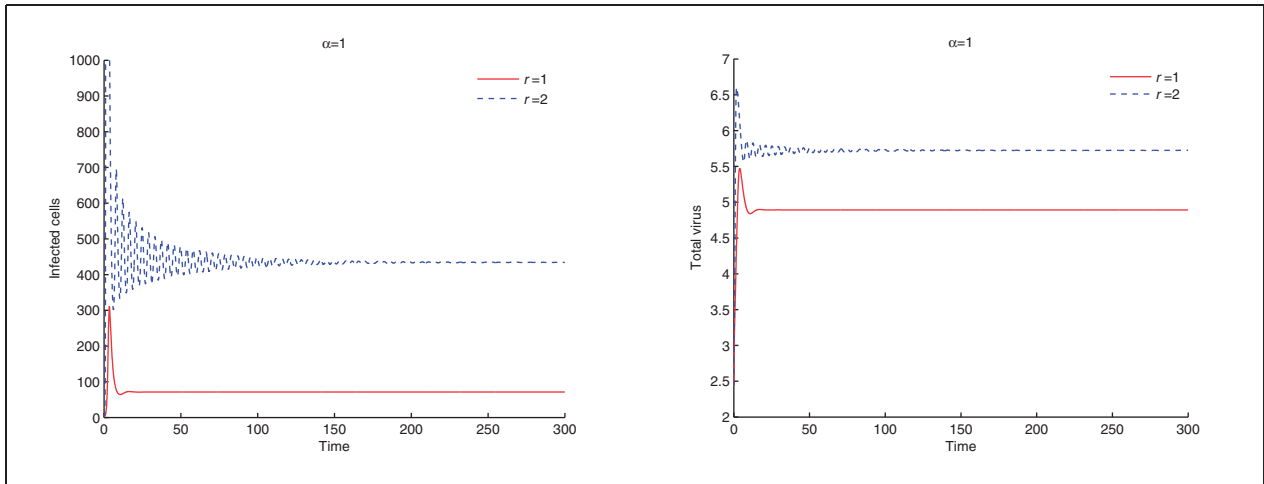
Figure 14. Dynamics of variables of model (4) for variation of the proliferation rate r, $\alpha = 1.0$, given the parameter values in Table 1 and initial conditions, for the growth rate $f_1(t)$.
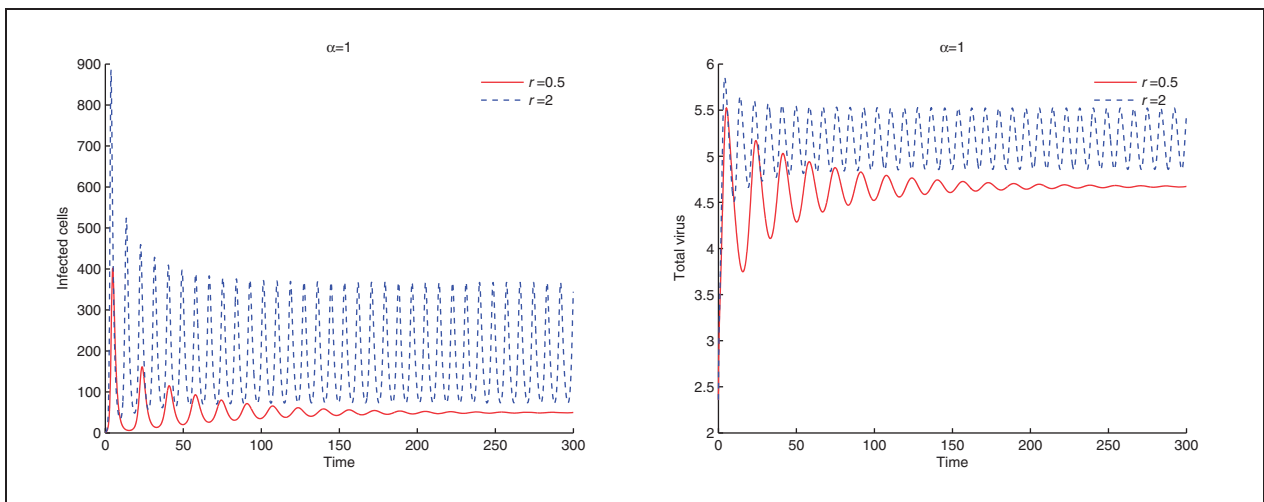
Figure 15. Dynamics of variables of model (4) for variation of the proliferation rate r, $\alpha = 1.0$, given the parameter values in Table 1, except $\lambda = 10$, $n_{rt}^s = 0.6$, $n_{rt}^r = 0.5$, $n_p^s = 0.3$, and $n_p^r = 0.2$, and initial conditions, for the growth rate $f_1(t)$.

In all figures, we observe faster transients for decreasing values of α. Moreover, we verify that for $\alpha = 1.0$ we have the slowest evolution to the steady state, while $\alpha = 0.4$ yields the fastest transient. This property of complex-order fractional systems is similar to the patterns seen for distinct values of the delays in integer-order models (Wang et al., 2014). Those patterns reveal that the delay prolongs the time to peak for every oscillation and decreases the amplitude of the oscillations (Wang et al., 2014). We conjecture that varying α may thus promote patterns similar to varying the delay in integer-order systems.

3.4. Variation of the proliferation rate r

In this section we vary the proliferation rate r for the growth functions $f_i(t)$, $i = 1, 2, 3$. We fix $\beta = 0.8$ and vary

$\alpha \in \{0.4, 0.7, 1.0\}$. We observe that increasing the proliferation rate r affects the stability of the dynamical patterns of the model. Moreover, we observe that increasing r leads to an endemic state (see Figures 14 and 15). Thus, the stability of the endemic equilibrium depends on the target cell density, leading to sustained oscillations, the so-called blips, as r increases (Wang et al., 2014) (Figure 15). We only show the figures concerning $\alpha = 1$ and $f(t) = f_1(t)$ since analogous behavior is seen for $\alpha = 0.4$ and $\alpha = 0.7$, and for the other growth rates.

4. Conclusions

In this paper we propose a fractional complex-order model for drug resistance during HIV therapy, that includes three distinct growth rates for the CD4$^+$

T cells. We simulate the model for different values of the fractional complex-order derivative and for distinct rates. We observe that the variation of the complex-order fractional derivative may be compared to the variation of the delay in integer-order systems, in biologically meaning intervals. This happens for all growth rates. We also observe the appearance of sustained oscillations (blips) as the proliferation rate increases. Future work will focus on the inclusion of cytotoxic T lymphocytes (CTLs) cells in the model, since it is believed that they play a major role in the prevention of HIV virus replication. CTLs are activated by the HIV virus and kill infected (virus-specific and nonspecific) CD4$^+$ T cells. Additionally, we will include a term concerning cell-to-cell transmission of the virus. It is known that HIV infects not only CD4$^+$ T cells but also monocytes/macrophages. These cells travel throughout the host circulatory and lymphatic systems. T cells and macrophages interaction may help the HIV to spread from cell to cell. We will study the effect of this on the dynamics of the model.

Funding

References

Althaus C and Boer RD (2011) Implications of CTL-mediated killing of HIV-infected cells during the non-productive stage of infection. *PLoS ONE* 6(2): e16468.

Baleanu D (2009) About fractional quantization and fractional variational principles. *Communications in Nonlinear Science and Numerical Simulations* 14(6): 2520–2523.

Barbosa R, Machado JT and Silva M (2008) Discretization of complex-order algorithms for control applications. *Journal of Vibration and Control* 14(9–10): 1349–1361.

Caputo M and Mainardi F (1971) A new dissipation model based on memory mechanism. *Pure and Applied Geophysics* 91(8): 134–147.

Golmankhaneh A, Arefi R and Baleanu D (2013) Synchronization in a nonidentical fractional order of a proposed modified system. *Journal of Vibration and Control* Epub ahead of print 24 July 2013. DOI: 10.1177/1077546313494953.

Harrigan P, Whaley M and Montaner J (1999) Rate of HIV-1 RNA rebound upon stopping antiretroviral therapy. *AIDS* 13: 59–62.

Hartley T, Lorenzo C and Adams J. (2005) Conjugated-order differintegrals. In: *Proceedings of the ASME international design engineering technical conferences and computers and information in engineering conference*.

Ho D, Neumann A, Perelson A, et al. (1995) Rapid turnover of plasma virions and CD4 lymphocytes in HIV-1 infection. *Nature* 373: 123–126.

Luo R, Piovoso M, Martinez-Picado J, et al. (2012) HIV model parameter estimates from interruption trial data including drug efficacy and reservoir dynamics. *PLoS ONE* 7(7): e40198.

Machado JT (2009) Fractional derivatives: Probability interpretation and frequency response of rational approximations. *Communications in Nonlinear Science and Numerical Simulations* 14(9–10): 3492–3497.

Mainardi F (1996) Fractional relaxation-oscillation and fractional diffusion-wave phenomena. *Chaos, Solitons and Fractals* 7: 1461–1477.

Makris N and Constantinou M (1993) Models of viscoelasticity with complex-order derivatives. *Journal of Engineering Mechanics* 119(7): 1453–1464.

Miller K and Ross B (1993) *An Introduction to the Fractional Calculus and Fractional Differential Equations*. New York, NY: John Wiley and Sons.

Momani S and Odibat Z (2006) Analytical approach to linear fractional partial differential equations arising in fluid mechanics. *Physics Letters A* 355(4–5): 271–279.

Montaner J, Harris M, Mo T, et al. (1998) Rebound of plasma viral load following prolonged suppression with combination therapy. *AIDS* 12: 1398–1399.

Nigmatullin R and Baleanu D (2010) Is it possible to derive Newtonian equations of motion with memory? *International Journal of Theoretical Physics* 49: 701–708.

Oldham K (2010) Fractional differential equations in electrochemistry. *Advances in Engineering Software* 41(1): 9–12.

Oldham K and Spanier J (1974) *The Fractional Calculus: Theory and Application of Differentiation and Integration to Arbitrary Order*. New York, NY: Academic Press.

Ouifki R and Witten G (2009) Stability analysis of a model for HIV infection with RTI and three intracellular delays. *BioSystems* 95: 1–6.

Pinto C and Carvalho A (2014) Mathematical model for HIV dynamics in HIV-specific helper cells. *Communications in Nonlinear Science and Numerical Simulation* 19(3): 693–701.

Pinto C and Machado JT (2001) Complex order van der Pol oscillator. *Nonlinear Dynamics* 65(3): 247–254.

Pinto C and Machado JT (2012) Complex-order forced van der Pol oscillator. *Journal of Vibration and Control* 18(14): 2201–2209.

Pitchaimani M, Monica C and Divya M (2013) Stability analysis for HIV infection delay model with protease inhibitor. *BioSystems* 114: 118–124.

Samko S, Kilbas A and Marichev O (1993) *Fractional Integrals and Derivatives: Theory and Applications*. London: Gordon and Breach Science Publishers.

Sanjuán R, Nebot M, Chirico N, et al. (2010) Viral mutation rates. *Journal of Virology* 84(19): 9733–9748.

Tarasov V (2010) *Fractional Dynamics: Applications of Fractional Calculus to Dynamics of Particles, Fields and Media*. New York, NY: Springer.

Wahl L and Nowak M (2000) Adherence and drug resistance: Predictions for therapy outcome. *Proceedings of Biological Sciences* 267: 835–843.

Wang Y, Brauer F, Wu J, et al. (2014) A delay-dependent model with HIV drug resistance during therapy. *Journal of Mathematical Analysis and Applications* 414: 514–531.

Wei X, Ghosh S, Taylor M, et al. (1995) Viral dynamics in human immune deficiency virus type 1 infection. *Nature* 373: 117–122.

Xiao Y, Miao H, Tang S, et al. (2013) Modeling antiretroviral drug responses for HIV-1 infected patients using differential equation models. *Advanced Drug Delivery Reviews* 65: 940–953.

Design and analysis of a multivariable fractional order controller for a non-minimum phase system

Cristina I Muresan[1], Eva H Dulf[1], Cosmin Copot[2], Robin De Keyser[2] and Clara Ionescu[1]

Abstract

Two control strategies for multivariable processes are proposed that are based on a decentralised and a steady state decoupling approach. The designed controllers are fractional order PIs. The efficiency and robustness of the proposed strategies is tested and validated using a non-minimum phase process. Previous research for the same non-minimum phase process has proven that simple decentralised or decoupling techniques do not yield satisfactorily results and a multivariable IMC controller has been proposed as an alternative solution. The simulation results presented in this paper, as well as the experimental results, show that the proposed fractional order multivariable control strategies ensure an improved closed loop performance and disturbance rejection, as well as increased robustness to modelling uncertainties, as compared to traditional multivariable IMC controllers.

1. Introduction

The large majority of chemical processes are multivariable in nature, exhibiting some strong couplings and occasionally a non-minimum phase character that makes the control design problem a challenging task (Bequette, 2003; Kantera et al., 2002). In general, for such chemical processes, the objective of a control system is to maintain several controlled variables at independent set points. Despite the coupling problems associated with multivariable systems, a non-minimum phase system is even more difficult to control. None of the techniques that are based upon model inversion can be used since such an inversion leads to an unstable closed loop system. Multivariable controllers have been previously designed for such systems. However, centralized controller design for multiple-input-multiple-output (MIMO) systems is associated with possible problems concerning the complex computations, maintenance due to the size and a high risk of failure even though it provides better performance. Simplified algorithms are generally preferred as an alternative solution. In contrast to the centralised

multivariable control, decentralised control is widely preferred in practice and industrial applications especially because of its main advantage that allows for an easy implementation and tuning, if a sufficient number of sensors and actuators exist. It is also highly reliable and flexible. If properly tuned, it can lead to excellent closed loop results.

Nevertheless, for highly interacting processes, a decoupling control is usually preferred instead of a decentralized algorithm. Decoupling is a procedure that reduces multivariable interactions (Astrom et al., 2002) and sets the premises for an improved design of the decentralized control. The mathematical procedure to decouple a MIMO system consists in a

[1]Technical University of Cluj-Napoca, Romania
[2]University of Ghent, Ghent, Belgium

Corresponding author:
Eva H Dulf, Technical University of Cluj-Napoca, Department of Automation, Memorandumului street, no. 28, 400114 Cluj-Napoca, Romania.
Email: eva.dulf@aut.utcluj.ro

transformation of the original transfer function matrix of the process into a diagonal one. This is achieved by using an additional controller, also called a decoupler, which is designed in order to compensate for process interactions. Then, for the resulting pseudo-plant, consisting of the original model of the multivariable process and the decoupler, single-input-single-output (SISO) techniques can directly be used in designing the controllers.

The quadruple tank process is the case study considered in this paper. These particular processes have been the focus of numerous papers, since they exhibit elegantly complex dynamics of interest in both control and research education. They have been widely used in chemical engineering laboratories to illustrate the performance limitations for multivariable systems due to strong interactions, right-half plane transmission zeros and model uncertainties (Suja and Thyagarajan, 2008). The most extensively employed method for controlling the quadruple tank system has been the classical PID (Proportional plus Integral plus Derivative), either in a decentralised or a decoupling approach (Ramadevi and Vijayan, 2014). The choice for traditional PID controllers has been based upon their general acceptance in both academic and industrial domains, with more than 95% of the control loops in process control industry being of PI/PID type. For example, a recent paper compares the decentralised and decoupling techniques, while the tuning of the PI controllers is performed in several ways, ranging from direct synthesis, sequential relay with ZN settings, to more advanced methods such as the Internal Model Control (IMC) (Ramadevi and Vijayan, 2014). A robust decentralized PID controller is also the selected option for dealing with nonlinearities, non-minimum phase characteristics and modeling uncertainties (Rosinov and Markech, 2008). The properties and control have been analysed in a decentralised approach for similar quadruple tank processes that exhibit also multiple dead times, with the experimental results portraying some of the control difficulties related to the presence of non-minimum phase zeros (Shneiderman and Palmor, 2010). The performance of PID controllers, in various control configurations, has been analysed over a quadruple tank process, considering the shifting of the system configuration from minimum to non-minimum phase (Govinda Kumar et al., 2014).

To enhance the closed loop performance and to reduce the interaction effects, a partial decoupling method for MIMO systems has also been proposed and implemented for the non-minimum phase quadruple tank system (Garelli et al., 2006a, 2006b). For example, an approach to design auto tuned decentralized PI controller using ideal decouplers and adaptive techniques have been developed (Vijula and Devarajan, 2014). The initial multivariable non-minimum phase quadruple tank system is transformed into two single-input-single-output systems, while the controller's parameters are adjusted using the Model Reference Adaptive reference Control. The proposed controller can adjust the controller parameters in response to changes in plant uncertainties and disturbances based on the specified reference model and prevent the system from interaction between process variables.

Other more advanced methods have also been employed for the quadruple tank process, such as fuzzy control algorithms implemented in a decentralised version (Suja and Thyagarajan, 2008). The results obtained prove that the closed loop performance is improved when compared to the traditional decentralised PI control. Fuzzy logic has also been used to tune a combined state-feedback sliding-mode controller for quadruple tank system (Mirakhorli and Farrokhi, 2011). The simulation results showed that the proposed version achieved better closed loop performance than the stand alone versions of state-feedback controller or sliding-mode controller. Sliding mode control has been designed and tested on an experimental setup, providing increased robustness and excellent set point tracking (Pani Biswas et al., 2009). Neural networks have also been used to effectively tackle the problems concerned with multivariable non-minimum phase systems, such as the neural network based disturbance observer, proposed as a solution to overcome the limitations of traditional disturbance observers (Li et al., 2014).

For the particular setup considered in this paper, the quadruple tank system from Quanser, decentralised, decoupling and multivariable IMC strategies have been previously proposed (Maxim et al., 2013). However, the experimental results obtained showed the necessity of more complex control algorithms, when stringent performance is envisaged and coupling, as well as RHP zeros need to be tackled efficiently. For this particular process, both decentralized and decoupling controls achieved poor performance for disturbance rejection tests, which motivated the application of the more advanced IMC control and even a possible future work regarding model predictive control.

The purpose of this paper is to design a simple control algorithm that is based on combining fractional order controllers with a decentralised as well as decoupling approach that allow for a SISO interpretation of the controller tuning, but that can also achieve improved performance compared to the multivariable IMC control (MIMO IMC). The fractional order PID

(FOPID) controller was proposed as a generalization of the traditional integer order PID controller. The use of fractional order controllers is expected to enhance the performance of the closed loop system and increase the robustness of the system (Podlubny, 1999; Oustaloup, 1991; Li et al., 2010), being used in a wide area of applications (Gutiérrez et al., 2010). Several fractional order techniques have been proposed in literature for controlling multivariable processes, such as the extension of the CRONE algorithm (Gruel et al., 2009), MIMO-QFT robust synthesis methodology combined with CRONE control (Yousfi et al., 2012), sliding mode control based on the selection of a special fractional-order sliding variable (Pisano et al., 2010). Different methods for tuning multivariable fractional PID have been developed, such as an approach to consider the tuning formulated as an H∞ problem with a controller structure constraint (Chenikher et al., 2012), the Linear Matrix Inequalities (LMI) approach (Song et al., 2011), as well as a genetic algorithm for determining the gains and orders of the fractional order PID controllers (Moradi, 2014). Contrary to these multivariable fractional order control algorithms, the present paper proposes simpler approaches, also based on robust fractional order control algorithms that enable the use of SISO control techniques for multivariable processes. Thus, the main contribution of the paper resides in the tuning of simple fractional order controllers, in both decentralised and decoupling approach, for a specific non-minimum phase system, the quadruple tank system, as well as the implementation, the experimental testing and analysis of the final control algorithms.

The paper is structured as follows. The first section contains the alternative designs of the multivariable fractional order controllers, including a decentralised as well as a decoupling approach. Then, the controller designs are applied to the specific case study, the non-minimum phase water tanks system. The third section presents the experimental results, while the main conclusions are stated in the final section of the paper.

2. Alternative designs of a fractional order controller for multivariable processes

The two alternative designs for the fractional order controller proposed in this paper consist in a decentralised, as well as a steady state decoupling approach.

2.1. Decentralised approach

The decentralised approach in controlling MIMO systems consists in a proper selection of the input-output pairings, with the purpose of dividing the initial control problem into several SISO control loops, while aiming to reduce the amount of interaction. The first step in the decentralised approach consists in a Relative Gain Array (RGA) analysis of the multivariable process that allows for a proper pairing of the input-output signals (Bristol, 1966; Moaveni and Khaki-Sedigh, 2007). The next step consists in the design of the individual fractional order PI controllers for each input-output pairing by neglecting the effect of the interaction loop. The transfer function of the fractional order PI controller, proposed in this paper, is given as

$$H_{FO-PI}(s) = k_p \left(1 + \frac{k_i}{s^{\mu}} \right) \tag{1}$$

with μ the fractional order. To tune the fractional order PI controller, three performance specifications are imposed: a) a certain gain crossover frequency – ω_{gc}, b) a phase margin – φ_m – of the open loop system, denoted $H_d(s)$ and c) a robustness condition to gain variations. Considering that the open loop transfer function is written as

$$H_d(s) = H_{FO-PI}(s)H_P(s) \tag{2}$$

where $H_p(s)$ is the process transfer function, the tuning of the controller is done based on the following set of equations (Muresan et al., 2013; Monje et al., 2010; Muresan, 2014)

$$\left| \frac{1}{K+jL} \right|_{\omega_{gc}} \left| k_p \left[1 + k_i \omega_{gc}^{-\mu} \left(\cos \frac{\pi \mu}{2} - j \sin \frac{\pi \mu}{2} \right) \right] \right| = 1 \tag{3}$$

$$\frac{k_i \sin\left(\frac{\pi \cdot \mu}{2}\right)}{\omega_{gc}^{\mu} + k_i \cos\left(\frac{\pi \cdot \mu}{2}\right)} = tg\left(\pi - \varphi_m - a\tan\left(\frac{L}{K}\right) \right) \tag{4}$$

$$\frac{\mu k_i \omega_{gc}^{-\mu-1} \sin \frac{\pi \mu}{2}}{1 + 2k_i \omega_{gc}^{-\mu} \cos \frac{\pi \mu}{2} + k_i^2 \omega_{gc}^{-2\mu}} - \frac{\dot{L}K - L\dot{K}}{L^2 + K^2} = 0 \tag{5}$$

where K is the real part and L is its imaginary part of the process $H_P(j\omega_{gc})$. To simplify the computation of the fractional order PI controller parameters, the values for k_i and μ are determined graphically using equations (4) and (5) (Muresan et al., 2013; Monje et al., 2010; Muresan, 2014), while k_p is then computed using equation (3).

2.2. Decoupling approach

In case of a highly coupled MIMO system, the decentralised approach may result in poor closed loop

performance due to the multiple input-output inter-actions. A decoupling solution could then be used instead. In this paper, a steady state decoupling is employed. Given the $n \times n$ MIMO system

$$G_p(s) = \begin{pmatrix} H_{p11}(s) & H_{p12}(s) & \dots & H_{p1n}(s) \\ H_{p21}(s) & H_{p22}(s) & \dots & H_{p2n}(s) \\ \dots & \dots & \dots & \dots \\ H_{pn1}(s) & H_{pn2}(s) & \dots & H_{pnn}(s) \end{pmatrix} \quad (6)$$

the steady state decoupler is the inverse of the process transfer function gain matrix in equation (6), denoted as $G_m^{\#}$. The steady state decoupled process is then computed as

$$G_D(s) = G_m^{\#} \begin{pmatrix} H_{p11}(s) & H_{p12}(s) & \dots & H_{p1n}(s) \\ H_{p21}(s) & H_{p22}(s) & \dots & H_{p2n}(s) \\ \dots & \dots & \dots & \dots \\ H_{pn1}(s) & H_{pn2}(s) & \dots & H_{pnn}(s) \end{pmatrix} \quad (7)$$

The tuning of the fractional order PI controllers is then performed for each diagonal element in the decoupled process $G_D(s)$ using the same tuning procedure based on equations (3)–(5). The final multivariable FO-PI controller is computed as

$$G_C(s) = G_m^{\#} \begin{pmatrix} H_{FO-PI_1}(s) & 0 & \dots & 0 \\ 0 & H_{FO-PI_2}(s) & \dots & 0 \\ \dots & \dots & \dots & 0 \\ 0 & 0 & \dots & H_{FO-PI_n}(s) \end{pmatrix} \quad (8)$$

3. Case study. control strategies for non-minimum phase quadruple tank system

The schematic representation of the quadruple water tanks system is given in Figure 1. The system is a multi-variable one, with two inputs, the voltages applied to the two pumps, denoted as $V_{p1}(t)$ and $V_{p2}(t)$, and two outputs, the water levels of the lower tanks, Tank2 and Tank4, denoted as $L_2(t)$ and $L_4(t)$, respectively. There is a strong coupling effect between the inputs and the outputs. Such a coupling may be observed in Tank2 which has two inputs: the flow from Pump1 ($V_{p1}(t)$) through Out2, marked with dashed red line, and the flow from Pump2 ($V_{p2}(t)$) through Out1, denoted with green continuous line, that is the output flow from Tank1).
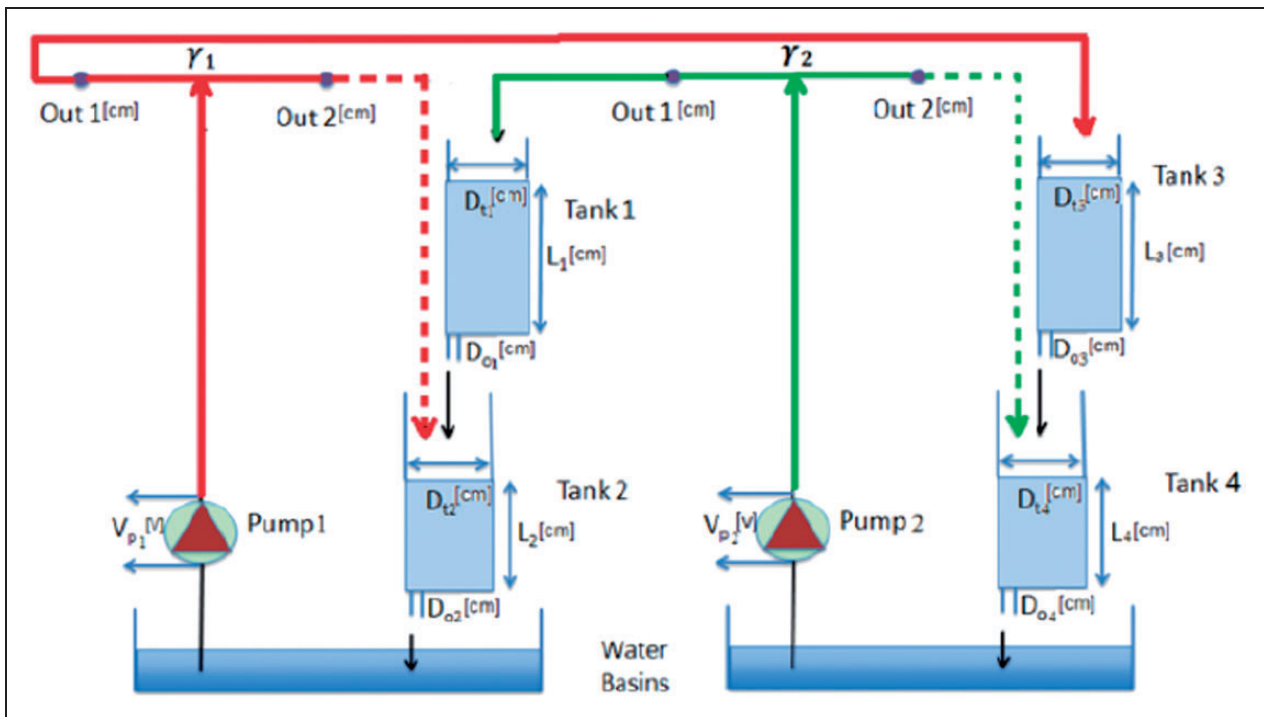

Figure 1. Schematic diagram of the quadruple water tanks system.

Hence, the controlled level in Tank2 (L_2) is influenced by the two inputs.

By a simple adjustment of the percentage of water flow from each input, one can change the system for having minimum phase or non-minimum phase dynamics (Maxim et al., 2013). The configuration used in this paper and indicated in Figure 1 is a non-minimum phase one, with a greater flow coming from Pump2, via Tank1, into Tank2, in comparison with the flow coming directly from Pump1. This is due to the fact that the outlet diameter Out1 is bigger than the diameter Out2, while the outgoing orifices from each tank Do1, Do2, Do3 and Do4 have the same diameter. A similar situation occurs in the case of Tank4. Then, the dominant flow in Tank2 and Tank4 comes from the manner in which the physical coupling is implemented via the choice of the setup (Johansson, 2000; Johansson et al., 1999).

The model transfer function matrix has been previously determined experimentally to be (Maxim et al., 2013)

$$G(s) = \begin{bmatrix} \dfrac{1.64}{18.43s + 1} & \dfrac{2.49}{178.8s^2 + 26.74s + 1} \\ \dfrac{2.56}{172.2s^2 + 27.6s + 1} & \dfrac{1.28}{15.92s + 1} \end{bmatrix} \tag{9}$$

The transmission zeros for the quadruple water tanks system are: $z_1 = -0.26$; $z_2 = 0.07$; $z_3 = -0.06$; $z_4 = -0.05$. Due to the positive zero $z_2 = 0.07$, the system is non-minimum phase.

A simple RGA analysis shows that for the configuration previously described the following RGA values are obtained (Maxim et al., 2013)

$$\Lambda = \begin{bmatrix} -0.49 & 1.49 \\ 1.49 & -0.49 \end{bmatrix} \tag{10}$$

According to equation (10), 1-2/2-1 pairing is selected and two FO-PI controllers are then computed. The following performance specifications are imposed for the two loops: $\omega_{gc1} = 0.03$, $\varphi_{m1} = 70°$ and $\omega_{gc2} = 0.03$, $\varphi_{m2} = 70°$. The resulting fractional order PI controllers, to be used in the decentralised approach are

$$\begin{cases} H_{FO-PI_1}(s) = 0.3\left(1 + \dfrac{0.024}{s^{1.16}}\right) \\ H_{FO-PI_2}(s) = 0.29\left(1 + \dfrac{0.025}{s^{1.16}}\right) \end{cases} \tag{11}$$

To tune the fractional order controllers for the decoupling control strategy, the decoupler was first computed as

$$G_m^{\#} = \begin{pmatrix} -0.3 & 0.58 \\ 0.6 & -0.38 \end{pmatrix} \tag{12}$$

Similar performance specifications were imposed to design the fractional order controllers for the decoupling strategy, $\omega_{gc1} = 0.02$, $\varphi_{m1} = 70°$ and $\omega_{gc2} = 0.02$, $\varphi_{m2} = 70°$, in order to obtain similar closed loop performance in terms of overshoot and settling time. The two fractional order controllers are

$$H_{FO-PI_1}(s) = 0.53\left(1 + \dfrac{0.022}{s^{1.16}}\right) \tag{13}$$

$$H_{FO-PI_2}(s) = 0.6\left(1 + \dfrac{0.018}{s^{1.17}}\right) \tag{14}$$

with the final multivariable FO-PI controller determined using equation (8).

To compare the results, a multivariable IMC strategy has been designed according to (Maxim et al., 2013), to yield similar closed loop performance in terms of settling time, as compared to the decentralised and decoupling fractional order control algorithms given by equations (11) and (13)–(14), respectively. The closed loop simulation results, considering step changes in the reference signals for the levels L_2 and L_4, are given in Figures 2 and 3.

Since the simplified model in equation (9) was obtained by linearizing a nonlinear model around the operating point of 10 cm (Maxim et al., 2013), the results in Figures 2 and 3 are regarded as nominal operating conditions. The decentralised and decoupling fractional order control strategies ensure no overshoot and 150 seconds settling time. The 150 seconds settling
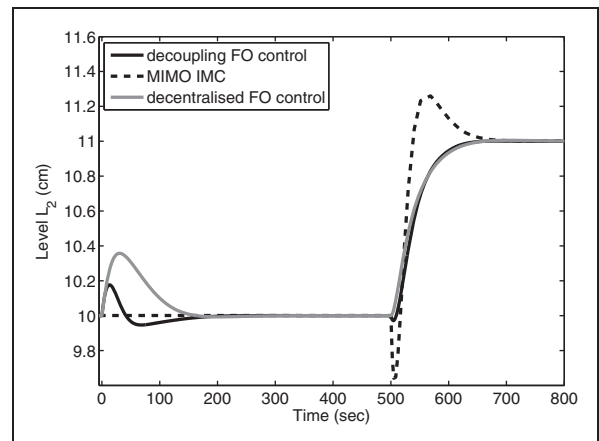

Figure 2. Comparative nominal closed loop simulation results considering a step change in the reference signal for L_2.
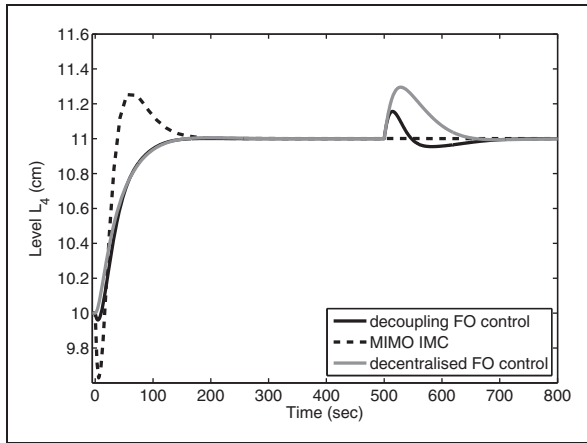
Figure 3. Comparative nominal closed loop simulation results considering a step change in the reference signal for L_4.
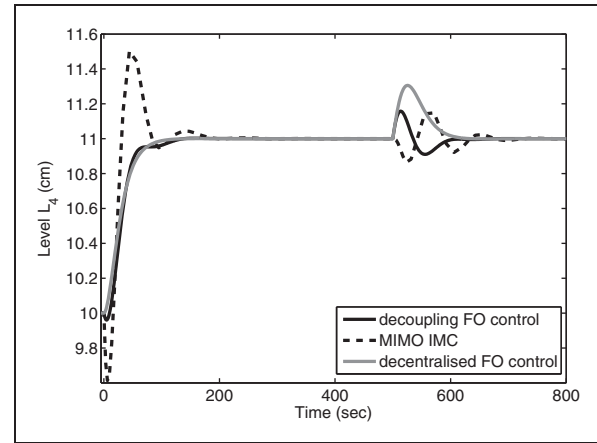

Figure 5. Comparative robust closed loop simulation results considering a step change in the reference signal for L_4.

The closed loop comparative robustness simulation results are indicated in Figures 4 and 5. As noted from the two figures, for the fractional order control strategies, the 30% change in the modeling parameters do not affect significantly the closed loop performance results, with no overshoot and a smaller settling time below 120 seconds for both outputs.

Considering the performance criteria of 150 seconds maximum settling time, both the decentralised and the decoupling FO controllers meet this requirement. The robustness of the decentralized and decoupling control strategies are almost identical in terms of reference tracking. On the other hand, the MIMO IMC results show a degradation of the closed loop performance, with a slight increase in the settling time of 170 seconds, but a significant increase of the overshoot accounting to 50%. The maximum amplitudes of the interaction responses show that the MIMO IMC and the decoupling FO controllers have similar performance, with the decentralised FO controllers behaving the poorest. The settling time is however 50% larger with the MIMO IMC (150 seconds) compared to the decentralised and decoupling FO controllers. Overall, the proposed fractional order decentralised and decoupling strategies offer an increased robustness as compared to the previously proposed MIMO IMC algorithm.

Previous results (Maxim et al., 2013) showed that poor disturbance rejection performance was achieved when using classical integer order PID controllers in a decentralised or decoupling approach, which justified the application of the more advanced MIMO IMC control. Figures 6 and 7 present the disturbance rejection tests, considering the nominal conditions, while Figures 8 and 9 present the same disturbance rejection tests in the case of the modeling errors in equation (15). The simulation results show that the MIMO IMC and the decoupling fractional order controller are

Figure 4. Comparative robust closed loop simulation results considering a step change in the reference signal for L_2.

time will be further considered as a performance criteria. The MIMO IMC algorithm ensures the same settling time, but with an overshoot of 25%. It must be noted here that zero overshoot for the MIMO IMC strategy is possible to be obtained at the expense of a major increase in the settling time. In terms of interaction, the MIMO IMC offers the best results, however this is valid under the assumption of a perfect model. Among the fractional order control strategies, the decoupling approach provides better interaction responses than the decentralised control algorithm.

To test the robustness of the designed controller, similar step changes in the reference signals were considered, but with a variation of 30% of the gains and time constants of the process in equation (9)

$$G(s) = \begin{bmatrix} \dfrac{2.14}{23.96s+1} & \dfrac{3.24}{232s^2+26.74s+1} \\ \dfrac{3.33}{230s^2+27.6s+1} & \dfrac{1.66}{21s+1} \end{bmatrix} \quad (15)$$

Figure 6. Comparative disturbance rejection tests considering nominal conditions and a step change in the reference signal for L₂.

Figure 7. Comparative disturbance rejection tests considering nominal conditions and a step change in the reference signal for L₄.
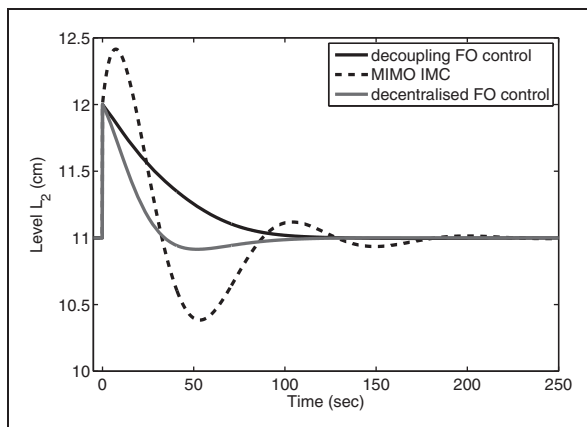
Figure 8. Comparative disturbance rejection tests considering modelling errors and a step change in the reference signal for L₂.

Figure 9. Comparative disturbance rejection tests considering modelling errors and a step change in the reference signal for L₄.

outperformed in terms of settling times by the decentralised fractional order controller. Also, the MIMO IMC is more oscillating with increased amplitudes compared to the decoupling fractional order controller.

To evaluate the disturbance rejection tests, the following performance index was used

$$J = \sum_{t=0}^{\infty} (r_i(t) - y_i(t))^2, \quad \text{with } i = 1, 2 \qquad (16)$$

where r_i is the setpoint for the corresponding output signal y_i (either tank levels L_2 or L_4).

The computed values are given in Table 1 and show that the proposed fractional order control strategies outperform the MIMO IMC in terms of disturbance rejection, both under nominal as well as modelling errors.

4. Experimental results

The two fractional order control strategies described above have been tested on the coupled tanks system by Quanser. Figures 10 and 11 show the comparative closed loop tests for both the decentralised and the decoupling fractional order control strategies. The case study considered here consists in a step change for the L_2 reference from 9 cm to 11 cm, thus near the linearization point. The L_4 reference signal is kept at 10 cm.

In terms of interaction, the decoupling fractional order control strategy performs better than the decentralised fractional order control algorithm. Using the same performance index as in equation (16) for the interaction responses yields a value of $J = 9.14$ for the decoupled version, while for the decentralised control strategy, $J = 21.26$. This suggests that the decoupled control algorithm ensures a 50% reduction of the interaction responses.

Table 1. Performance index for the disturbance rejection tests.

Control strategy	Output y1		Output y2	
	Nominal	Modelling errors	Nominal	Modelling errors
Decentralised fractional order control	J = 10.35	J = 9.37	J = 11.35	J = 10.03
Decoupling fractional order control	J = 23.6	J = 19.57	J = 23.6	J = 19.3
MIMO IMC	J = 34.23	J = 43.72	J = 34.22	J = 43.31

previous section, with a slight increase in the overshoot of 2%.

5. Conclusions

This paper presented two alternative solutions for controlling non-minimum phase systems and significant coupling. The previous traditional decentralised and decoupling strategies applied for the presented case study, the quadruple tank system, have shown the necessity for an advanced control solution, such as the MIMO IMC. The alternative solutions proposed in this paper consist in decentralised and decoupling fractional order control strategies. The simulation results prove that the proposed multivariable fractional order control algorithms outperform the MIMO IMC solution previously proposed, in terms of closed loop performance, disturbance rejection, both under nominal conditions, as well as modelling errors.

The experimental results considering the decoupled and decentralised fractional order control strategies are in good agreement with the closed loop simulation results. The settling time and the overshoot obtained on the experimental quadruple tank system meet the performance criteria specified for the simulated closed loop system. The decoupled fractional order control algorithm achieves similar performance in terms of reference tracking when compared to the decentralised fractional order control strategy. The most important contribution of the decoupled fractional order control algorithm is the 50% reduction in the interaction response, compared to the decentralised approach.

Further research includes the design of advanced fractional order controllers, based on combining advanced control algorithms with fractional calculus, implementation and testing of the new solutions compared to the decentralised and decoupling fractional order controllers presented in this paper.

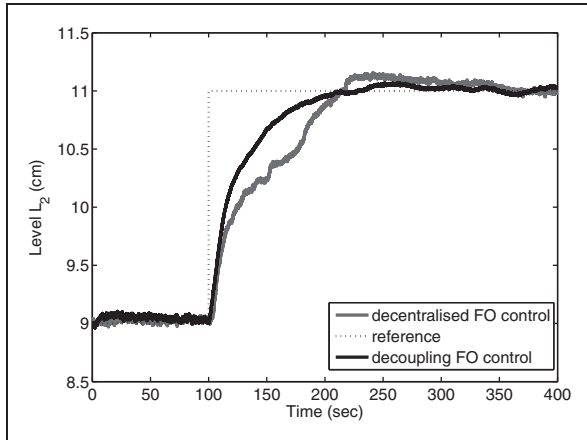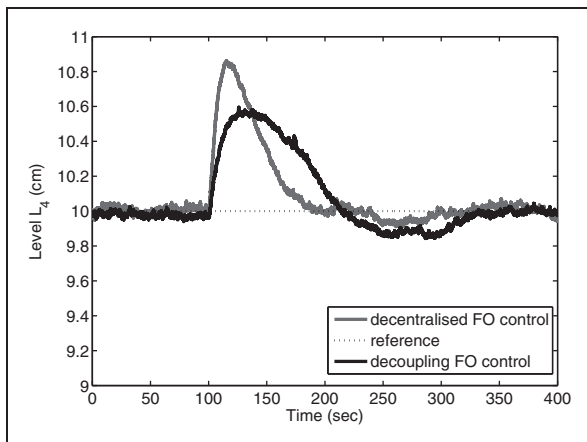**Figure 10.** Comparative closed loop experimental results for reference tracking.

Figure 11. Comparative closed loop experimental results for interaction response.

In terms of reference tracking, the experimental results in Figure 10 show that the two fractional order control strategies achieve similar performance. The settling time in both cases is 150 seconds, as obtained in the simulation results presented in the

References

Astrom KJ, Johansson AH and Wang QG (2002) Design of decoupled PI controllers for two by two system. *IEE Proceedings on Control Theory and Applications* 149: 74–81.

Bequette W (2003) *Process Control: Modeling, Design and Simulation*. New Jersey: Prentice Hall Professional.

Bristol E (1966) On a new measure of interaction for multivariable process control. *IEEE Transactions on Automatic Control* 11: 133–134.

Chenikher S, Abdelmalek S and Sedraoui M (2012) Control of uncertainly multi-variable system with fractional PID. *Proceedings of the 16th IEEE Mediterranean Electrotechnical Conference* 1: 1079–1082.

Garelli F, Mantz RJ and Battista HD (2006a) Partial decoupling of non-minimum phase processes with bounds on the remaining coupling. *Chemical Engineering Science* 61: 7706–7716.

Garelli F, Mantz RJ and Battista HD (2006b) Limiting interactions in decentralized control of MIMO system. *Journal of Process Control* 16: 473–483.

Govinda Kumar E, Mithunchakravarthi B and Dhivya N (2014) Enhancement of PID Controller Performance for a Quadruple Tank Process with Minimum and Non-Minimum Phase Behaviors. *Procedia Technology* 14: 480–489.

Gruel DN, Lanusse P and Oustaloup A (2009) Robust control design for multivariable plants with time-delays. *Chemical Engineering Journal* 146: 414–427.

Gutiérrez RE, Rosário JM and Machado JT (2010) Fractional order calculus: basic concepts and engineering applications. *Mathematical Problems in Engineering* article ID:375858.

Johansson KJ (2000) The quadruple-tank process. A multivariable laboratory process with an adjustable zero. *IEEE Transactions on Control Systems Technology* 8: 456–465.

Johansson KJ, Horh A, Wijk O, et al. (1999) Teaching multivariable control using the quadruple-tank process. *Proceedings of the 38th IEEE Conference on Decision and Control* 1: 807–812.

Kantera JM, Soroushb M and Seidera WD (2002) Nonlinear feedback control of multivariable non-minimum-phase processes. *Journal of Process Control* 12: 667–686.

Li HS, Luo Y and Chen YQ (2010) A fractional order proportional and derivative (FOPD) motion controller: tuning rule and experiments. *IEEE Transactions on Control Systems Technology* 18: 516–520.

Li J, Li S, Chen X, et al. (2014) RBFNDOB-based neural network inverse control for non-minimum phase MIMO system with disturbances. *ISA Transactions* 53: 983–993.

Maxim A, Ionescu CM, Copot C, et al. (2013) Multivariable model-based control strategies for level control in a quadruple tank process. *Proceedings of the 17th International Conference on System Theory, Control and Computing Joint Conference* 1: 343–348.

Mirakhorli E and Farrokhi M (2011) Sliding-mode state-feedback control of non-minimum phase quadruple tank system using fuzzy logic. *Proceedings of the 18th IFAC World Congress* 1: 13546–13551.

Moaveni B and Khaki-Sedigh A (2007) Input-output pairing for nonlinear multivariable systems. *Journal of Applied Science* 7: 3492–3498.

Monje CA, Chen Y, Vinagre BM, et al. (2010) *Fractional order Systems and Controls: Fundamentals and Applications*. London: Springer-Verlag.

Moradi M (2014) A genetic-multivariable fractional order PID control to multi-input multi-output processes. *Journal of Process Control* 24: 336–343.

Muresan CI, Folea S, Mois G, DUlf EH, et al. (2013) Development and implementation of an FPGA based fractional order controller for a DC motor. *Mechatronics* 23: 798–804.

Muresan CI (2014) Fractional Calculus: From Simple Control Solutions to Complex Implementation Issues. In: Machado JAT, Baleanu D and Luo A (eds) *Discontinuity and Complexity in Nonlinear Physical Systems, Nonlinear Systems and Complexity*. Cham, Switzerland: Springer, pp. 113–134.

Oustaloup A (1991) *La Commande CRONE: Commande Robuste d'Ordre Non Entier*. Paris: Hermes.

Pani Biswas P, Rishi S, Subhabrata R, Amar NS, et al. (2009) Sliding mode control of quadruple tank process. *Mechatronics* 19: 548–561.

Pisano A, Rapaic MR, Jelicic ZD, Usai E, et al. (2010) Sliding mode control approaches to the robust regulation of linear multivariable fractional-order dynamics. *International Journal of Robust and Nonlinear Control* 20: 2045–2056.

Podlubny I (1999) Fractional-order systems and PIλDμ- controllers. *IEEE Transactions on Automatic Control* 44: 208–214.

Ramadevi C and Vijayan V (2014) Design of decoupled PI controller for quadruple tank system. *International Journal of Science and Research* 3: 318–323.

Rosinov D and Markech M (2008) Robust control of quadruple – tank process. *ICIC Express Letters* 2: 231–238.

Shneiderman D and Palmor ZJ (2010) Properties and control of the quadruple-tank process with multivariable dead-times. *Journal of Process Control* 20: 18–28.

Song X, Chen YQ, Tejado I, Vinagre BM, et al. (2011) Multivariable fractional order PID controller design via LMI approach. *Proceedings of the 18th IFAC World Congress* 1: 13960–13965.

Suja MMR and Thyagarajan T (2008) Design of decentralized fuzzy controllers for quadruple tank process. *International Journal of Computer Science and Network Security* 8: 163–168.

Yousfi N, Melchior P, Rekik C, et al. (2012) Comparison between H∞ and CRONE control combined with QFT approach to control multivariable systems in path tracking design. *International Journal of Computer Applications* 45: 1–9.

Vijula DA and Devarajan N (2014) Design of Decentralised PI Controller using Model Reference Adaptive Control for Quadruple Tank Process. *International Journal of Engineering and Technology* 5: 5057–5066.

Article

Fractional direct and inverse models of the dynamics of a human arm

André Ventura[1], Inés Tejado[2], Duarte Valério[1] and
Jorge Martins[1]

Abstract
When developing control architectures for physical human–robot interaction, it is often necessary to use a model of the human operator. This paper presents a comparative study of both direct and inverse models of the human arm at the elbow joint, relating the force at the hand with the arm angle and vice versa. Specifically, models of integer and fractional (commensurable and non-commensurable) nature are identified from the experiments. Likewise, for comparison purposes, neural networks models are also obtained. Taking into account their parameter variability, it is shown that fractional models are more adequate to describe human arm behaviour; they are simpler, more exact and with less parameter uncertainty.

1. Introduction

Controlling a robotic arm so that it will behave as much as possible as a human arm seems to be a good solution for surgical robots (Garbey et al., 2014; Park et al., 2006). If properly designed, such robots can achieve performances with an accuracy that represent a valuable assistance even to the most seasoned surgeons. However, to attain this goal, the surgeon has to be comfortable working with the robot and, consequently, dynamic models for the human arm are needed to replicate its behaviour (Fu and Cavusoglu, 2012; Potkonjak et al., 2001; Taïx et al., 2013). A robot that feels more like another person's arm has shown to be a better companion than a robot with some other type of behaviour.

In the literature, third-order linear models are a usual proposal for this system (see e.g. Fu and Cavusoglu, 2012), whose structure is shown in Figure 1. Experimental data can be reasonably fitted, and there is furthermore a very reasonable rationale argument in its favour. More accurate results can be obtained with more complicated identification techniques and structures (Adewusi et al., 2012; Mobasser and Hashtrudi-Zaad, 2006; Nagarsheth et al., 2008; Venture et al., 2006). Whether this pays off or whether the simpler linear option is better because it is good enough depends, of course, on the intended use.

In a previous paper (Tejado et al., 2013), we found fractional order linear models for the human arm, obtained from experimental data with the measured force at the hand as model input and the measured arm angle as output, and compared them with the above mentioned third-order models. There are several reasons to expect this type of non-integer models, because the dynamics of muscles of several animal species (including humans) have been modelled using fractional derivatives (Djordjevic et al., 2003; Sommacal et al., 2007b,a, 2008), and because muscles show visco-elastic behaviour, that can also be modelled using fractional derivatives (Magin, 2004; Mainardi, 2010). In their turn, fractional derivatives are expectable here given the fractal nature of muscular tissue.

In the current paper, we present both direct and inverse (i.e. using now the measured arm angle as

[1]IDMEC, Instituto Superior Técnico, Universidade de Lisboa, Portugal
[2]Industrial Engineering School, University of Extremadura, Spain

Corresponding author:
Duarte Valério, IDMEC, Instituto Superior Técnico, Universidade de Lisboa, Av. Rovisco Pais 1, Pav. Eng. Mec. III gab. 3.10, Lisboa, 1049-001, Portugal.
Email: duarte.valerio@tecnico.ulisboa.pt
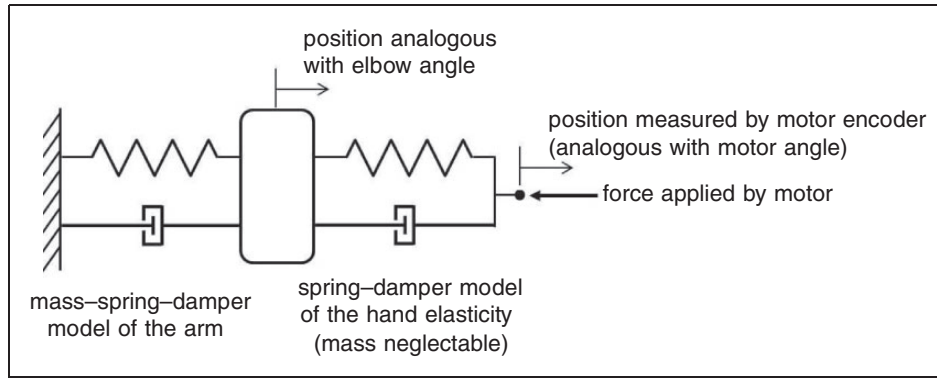
Figure 1. Third-order translation analog to elbow dynamics.

model input and the measured force at the hand as output) models for the human arm, using the same data from Tejado et al. (2013), comparing fractional and third-order (integer) linear models with neural networks (NNs). NNs provide nonlinear models that often obtain excellent performances (Haykin, 1999; Jang et al., 1997; Nørgaard et al., 2003) and have been used to model different kinds of muscles (see e.g. Bhowmick et al., 2013; Cheron et al., 2003; Jailani et al., 2012; Rosen et al., 1999; Simunic, 2003). Hence the pertinency of the comparison with fractional models, to see whether they can stand the test. Parameter variability is checked and held as an important indicator of model suitability. Preliminary results of this work can be found in Ventura et al. (2015).

The contents of the paper are as follows. In Section 2, the types of models considered for the human arm are described. Section 3 briefly explains how data was obtained. Then, Section 4 presents a comparative study of the obtained models based on parameter variability. Lastly, Section 5 offers comments and conclusions.

2. Types of models

This section describes which models, of a different nature, were used to find the transfer functions

$$G_{arm, direct}(s) = \frac{\theta(s)}{F_{measured}(s)} \tag{1}$$

$$G_{arm, inverse}(s) = \frac{F_{measured}(s)}{\theta(s)} \tag{2}$$

where θ and $F_{measured}$ are the measured arm angle and force at the hand, respectively.

2.1. Third-order integer linear models

These have already been mentioned above, together with the reasoning behind their choice in Figure 1.

The identification methods were the same described below for fractional transfer functions, restricting differentiation orders to natural numbers.

2.2. Fractional linear models

From the definition of derivative

$$\frac{\mathrm{d}f(t)}{\mathrm{d}t} = \lim_{h \to 0} \frac{f(t) - f(t-h)}{h} \tag{3}$$

it can be shown, by mathematical induction, that

$$\frac{\mathrm{d}^n f(t)}{\mathrm{d}t^n} = \lim_{h \to 0} \frac{\sum_{k=0}^{n} (-1)^k \binom{n}{k} f(t-kh)}{h^n} \tag{4}$$

By allowing combinations of a things, b at a time, defined for $a, b \in \mathbb{N}$ as $\binom{a}{b} = \frac{a!}{b!(a-b)!}$, to be generalized to $a, b \in \mathbb{C}$ using function Gamma as

$$
\binom{a}{b}
$$

$$
= \begin{cases}
\frac{\Gamma(a+1)}{\Gamma(b+1)\Gamma(a-b+1)}, & \text{if } a, b, a-b \notin \mathbb{Z}^- \\
\frac{(-1)^b \Gamma(b-a)}{\Gamma(b+1)\Gamma(-a)}, & \text{if } a \in \mathbb{Z}^- \wedge b \in \mathbb{Z}_0^+ \\
0, & \text{if } [(b \in \mathbb{Z}^- \vee b-a \in \mathbb{N}) \wedge a \notin \mathbb{Z}^-] \\
& \vee (a, b \in \mathbb{Z}^- \wedge |a| > |b|)
\end{cases}
\tag{5}
$$

expression (4) can be used to define derivatives of an arbitrary order $\alpha \in \mathbb{C}$, usually denoted as D^α:

$$_c D_t^\alpha f(t) = \lim_{h \to 0^+} \frac{\sum_{k=0}^{\lfloor \frac{t-c}{h} \rfloor} (-1)^k \binom{\alpha}{k} f(t-kh)}{h^\alpha} \tag{6}$$

The upper limit of the summation was chosen so that, when $\alpha = -1, -2, -3, \ldots$, equation (6) reduces to a

Riemann integral calculated from c to t. Actually terminals c and t are needed for all orders α save the usual integer derivatives, $\alpha = 1, 2, 3, \ldots$

Definition (6) above, the Grünwald–Letnikoff definition of fractional derivatives, is one of the several possible. Whatever the case, however, if initial conditions are zero, $\mathscr{L}\left[{}_0 D_t^\alpha f(t)\right] = s^\alpha F(s)$, and that is how, from a differential equation with fractional derivatives, fractional transfer functions arise. Those in which all orders share a least common multiple (the commensurability order) are called commensurate. Commensurate transfer functions with a commensurability order of 1 are integer transfer functions.

The sketch above of how fractional derivatives can be introduced is developed, for interested readers, in several books and papers, among which we mention Valério and Sá da Costa (2012), Valério and Sá da Costa (2011), Podlubny (1999), Miller and Ross (1993), Samko et al. (1993), Magin (2004), and Baleanu et al. (2012).

To identify a fractional transfer function from the measured data, rather than using a method to do this directly from a time response (Malti et al., 2008; Valério and Sá da Costa, 2012), a frequency response was estimated first (using Welch's method on the filtered output), and then Levy's method was applied, as this leads to less noisy results. Levy's method fits to frequency response $G(j\omega_p)$, $p = 1, \ldots, f$ a commensurable fractional model with a frequency response given by

$$\hat{G}(j\omega_p) = \frac{\sum_{k=0}^{m} b_k (j\omega_p)^{k\alpha}}{1 + \sum_{k=1}^{n} a_k (j\omega_p)^{k\alpha}} = \frac{N(j\omega_p)}{D(j\omega_p)} \quad (7)$$

minimizing $(G(j\omega)D(j\omega) - N(j\omega))^2$ (which is easier than the more obvious alternative of minimizing $|G(j\omega) - \frac{N(j\omega)}{D(j\omega)}|^2$, which leads to a nonlinear problem). Commensurable orders of fractional models were found sweeping the $\alpha \in [0, 2]$ range (outside which no transfer function is stable) with a 0.1 step, and keeping the α for which results are better, using a heuristic which is better described below in Section 4 after performance indexes are introduced. For more details on identification procedures of transfer functions for this plant, see Tejado et al. (2013). Levy's method for fractional transfer functions is covered in Valério et al. (2008).

The rationale for the use of these models was given in Section 1. Fractional models can often describe complex dynamic behaviours with fewer parameters than an integer order model (Magin, 2004; Podlubny, 1999; Valério and Sá da Costa, 2012), as a fractional derivative can more easily be fitted to data. While fractional models can be simulated using a variety of numerical schemes (see e.g. Bhrawry et al., 2014; Bhrawy et al.,

2015; Diethelm et al., 2006), integer order transfer functions providing an approximated dynamical behaviour are often employed (Valério and Sá da Costa, 2011, 2012). Such approximations of fractional models may have a larger number of zeros and poles than the integer models that could also be used, but in any case fractional derivatives are instrumental in providing the way to actually place zeros and poles in the desired locus.

2.3. Neural networks

A NN is a nonlinear modelling tool inspired on the way human brain processes information. The human brain is composed by a network of neurons interconnected by dendrites that communicate with each other using electrochemical signals at synapses. These connections are strengthened or weakened depending on their activation frequency. Likewise, an artificial NN is composed by neurons and weighted connections.

There are many kinds of NN configurations, the major distinction being between feedforward and feedback or recursive configurations. In both, neurons are arranged in layers (the last one being the output layer, and all others the hidden layers), that feed one another; but whereas in feedforward networks information flows always from left to right, in feedback networks information is fed back from one or more layers through which it had already passed. Figure 2 shows a particular architecture of a feedback NN called neural network auto-regressive with exogenous inputs (NNARX) model. Notice how the model dynamics appears through the delay operator z^{-1} to make use of past values of both the input and the output of the system. Maximum input and output delays, denoted as m and n, respectively, determine the memory the model has of the input and output signals. In particular, n defines the model order, which, for a linear system, would coincide with the number of model poles, which, together with their location on the complex plane, strongly affect the model's behaviour. Even though a NN is not linear, a number of poles very different from the real memory of the physical system to be identified will likewise result in a weak model.

As input, each neuron i in layer n receives a signal $y_{n,i}$ that is a linear combination of every output signal of the neurons in the previous layer $n - 1$

$$y_{n,i} = b_{n,i} + \sum_{i=1}^{N_{n-1}} w_{n-1,i} x_{n-1,i} \quad (8)$$

where $x_{n-1,i}$ is the ith input of the neuron coming from the previous layer, $w_{n-1,i}$ is a weight associated with that input, N_{n-1} is the number of such inputs, and $b_{n,i}$
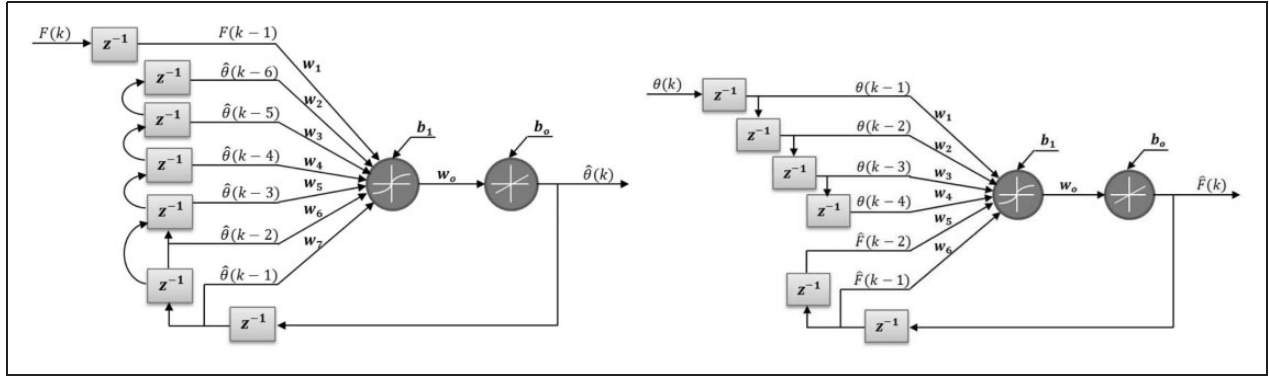
Figure 2. Neural network auto-regressive with exogenous inputs (NNARX) models. Left: Direct model, with one input and one output, one hidden layer, $n = 6$ output delays and $m = 1$ input delays. Right: inverse model, with one input and one output, one hidden layer, $n = 2$ output delays and $m = 4$ input delays.

is a bias. Obviously, layer number 0 (which does not exist) corresponds to the NN's inputs themselves. The neuron's output $x_{n,i}$ is determined by its transfer function $f_{n,i}$, usually known as an activation function. Activation functions may be transfer functions, but if the NN already includes a dynamic elsewhere activation functions will probably be static; the hyperbolic tangent sigmoid function is commonly used:

$$x_{n,i} = f_{n,i}(y_{n,i}) = \frac{1 - e^{-y_{n,i}}}{1 + e^{-y_{n,i}}} \quad (9)$$

NNs employed below use the activation function $x_{n,i} = f_{n,i}(y_{n,i}) = y_{n,i}$ in the output layer; in other words, their output is a biased linear combination of all of the inputs. For more details on NN architecture, see the references in Section 1.

In order to have a NN as a satisfactory nonlinear mapping between input and output data, optimal weights must be assigned to the synapses, or connections, through the training process. Offline training of a NN is, in fact, an optimization process in which the weights $w_{n,i}$ and bias factors $b_{n,i}$ are iteratively updated in order to minimize the mean squared error (MSE) between the model output signals and the output data. Instead of using data batches to train the NN, online training updates the network parameters recursively using online measured data. In any case, the result of this optimization, or training, process is a NN that is a black box model of the plant under study. Numbers of delays m and n are to be identified along with the weights and bias of the NN.

For the system at stake, NNARX models were trained using the Levenberg–Marquardt backpropagation algorithm, chosen for speed and accuracy. It is, actually, a local minimization method, therefore it is not guaranteed that a global optimal set of networks parameters is achieved. Because of this and the fact that

the algorithm initialization has a random basis, the probability of two networks having equal final weights and biases is very low, even when trained with the same data. The data, after being resampled at 500 Hz (the robot's communication frequency), was then actually split into three parts: 60% for training, 20% for validation, and 20% for testing. The best results were consistently obtained for NNs with four input delays, two output delays and a single neuron in the hidden layer: this was thus the configuration chosen. Indeed, architectures with more than one neuron in the hidden layer were tested, showing insignificantly better or weaker overall results, depending on the number of input and output delays. As to the number of input and output delays, it was determined as discussed in Section 4. That is why only networks with a single neuron in the hidden layer are considered in this work. More details on NN training can be found in Mandic and Chambers (2001) and Marquardt (1963).

3. Experiments

As mentioned previously, the experimental data used in this paper is that of Tejado et al. (2013); refer to this paper for further details.

Nine female and nine male volunteers, with ages ranging from 25 to 66, without any known musculo-skeletal injuries of the higher limbs, kneeled or sat holding a horizontal robotic arm and tried to keep it steady, while it moved randomly. The robotic arm was moved by a Kollmorgen direct drive D061M-23-1310 motor, able to produce $5.3\,\text{N}\cdot\text{m}$ continuous torque and $16.9\,\text{N}\cdot\text{m}$ peak torque, in current control mode. The rotation range was limited to $\pm 0.9\,\text{rad}$ for safety reasons. The measured angle was obtained from an encoder with a resolution of 65,535 pulses/revolution. At the end of the aluminium horizontal robotic arm there was a handle for the volunteers to grab, a JR3
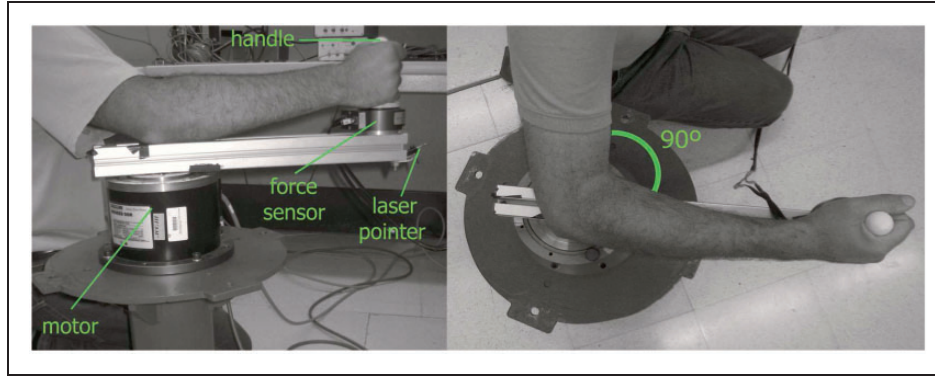
Figure 3. Picture of the robotic arm used to obtain experimental data of human arm dynamics.

12-degree-of-freedom DSP-based force sensor, and a laser pointer which should be kept inside a target. Data was recorded with a 2 kHz sampling frequency. A picture of the experimental set-up is shown in Figure 3.

Experiments, which lasted 40 s to avoid fatigue, are grouped into three types.

- Type I. Oscillations in both directions around the zero-point.
- Type II. Oscillations only in the positive side of the zero-point (flexion of the elbow).
- Type III. Oscillations only in the negative side of the zero-point (extension of the elbow).

The oscillations were random to avoid anticipatory reflexes, which would interfere with the modelling of the arm dynamics. So the forces generated by the motor were a sum of sinusoids with frequencies in the [0.12, 15] Hz range (chosen because the bandwidth for the human arm is approximated to 10 Hz), limited to not exceed 4 N. Eight volunteers of either sex performed two experiments of type I, one experiment of type II, and one experiment of type III (68 data sets in total). The two other volunteers performed 16 additional experiments: six of type I, seven of type II, and seven of type III. The force measured by the mentioned sensor was practically identical to the force input.

4. Results

Results were assessed with the following four performance indexes: MSE, mean absolute deviation (MAD), maximum deviation (MD) and variance accounted for (VAF), defined as

$$MSE = \frac{\sum_{j=1}^{N} \left(y_j - \hat{y}_j\right)^2}{N} \qquad (10)$$

$$MAD = \frac{\sum_{j=1}^{N} \left|y_j - \hat{y}_j\right|}{N} \qquad (11)$$

$$MD = \max_{N} \left|y_j - \hat{y}_j\right| \qquad (12)$$

$$VAF = 1 - \frac{\sigma^2(\mathbf{y} - \hat{\mathbf{y}})}{\sigma^2(\mathbf{y})} \qquad (13)$$

The meaning of the variables for frequency and time responses is given in Table 1. With three series to compare (gain, phase, time response) and four indexes, there are in all 12 values to assess a model's performance.

4.1. Direct models

In Tejado et al. (2013), we have shown that fractional models are better than integer order models, inasmuch as they achieve a performance which is similar or even slightly better, with one parameter less, and with clearly less parameter uncertainty. For this paper, NN models were further obtained. Model parameters are given in Tables 2–4 and their performances are shown in Table 5 (best results are shown in bold).

4.2. Inverse models

Since integer direct models have two zeros and three poles, inverse models with three poles and three zeros were considered, as they ought to be causal.

In the case of fractional order models, the same principle as above was applied. Since in Tejado et al. (2013) fractional order direct models have one zero and two poles, causal inverse models with two zeros and two poles were considered. But this time there is the commensurability factor. So, in a first stage, the best commensurable order was found sweeping this factor in the [0.1,1.9] range with a 0.1 step, keeping the model's dynamical structure (two zeros and two poles).

Table 1. Variables in equations (10)–(13).

| Variables | Frequency response | | Time response |
	Gain	Phase	
y	Gain curve estimated from measured data for a certain frequency vector	Phase curve estimated from measured data for a certain frequency vector	Time series of measured input data
ŷ	Gain curve estimated from measured input and identified inverse model for the same frequency vector of **y**	Phase curve estimated from measured input and identified inverse model for the same frequency vector of **y**	Time series of inverse model output
N	Length of the frequency vector, that must be the same for **y** and **ŷ**		Length of the time series

Table 2. Parameters for integer order direct models of the human arm (three poles, one zero).

| Input | | Zeros | | | Poles$_{2,3}$ | | |
		Re	Im	Polei	Re	Im	Gain
All	Nominal	−21.28	±111.38	−128.63	−15.11	±30.79	0.1
	Min	−30.8	90.8	−1684.2	−25	−21.9	−0.6
	Max	−4.66	112.04	512.44	−6.27	43.09	1.52
	Mean	−16.79	99.64	−189.9	−14.1	31.60	0.16
	Std	8.54	6.36	411.81	4.99	5.11	0.39
Type I	Nominal	−19.1034	±96.96	−76.59	−16.43	±35.13	0.08
	Min	−34.87	89.37	−268.32	−23.33	25.24	0.04
	Max	−6.48	107.86	−30.37	−7.47	53.57	0.28
	Mean	−19.30	95.78	−98.28	−15.06	36.83	0.1
	Std	8.83	5.8	76.63	4.09	6.91	0.06
Type II	Nominal	−17.16	±101.91	−170.71	−12.6	±27.61	0.13
	Min	−35.36	82.09	−645.08	−20.56	22.22	−13.15
	Max	−2.5	123.7	7653.4	−6	45.2	0.4
	Mean	−18.71	100.87	355.36	−11.6	29.75	−0.67
	Std	11.0	12.6	1850.2	4.1	6	3.1
Type III	Nominal	−10.61	±103.19	−455.59	−11.16	±28.42	0.323
	Min	−33.81	90.6	−887.12	−22.77	21.27	−0.477
	Max	27.16	164.08	393.36	−4.36	37.03	0.574
	Mean	−13.62	104.35	−152.8	−11.02	29.77	0.102
	Std	14.35	16.5	247.21	4.79	4.27	0.207

The output of this process is a set of 19 models to compare using the 12 aforementioned performance indexes. The following heuristic, essentially a multi-criteria optimization algorithm, was used to choose the commensurate order.

1. Initialize $P = 12$ lists with a length $L = 1$.

2. Select the best L models according to each performance index.
3. Model by model, check for its presence in any of the P lists with length L and compute a histogram that shows the number of presences of every model in all of the lists.
4. If one model is found to be present in every single list, that is the best choice and the heuristic stops.

Table 3. Parameters for fractional order direct models of the human arm (two poles, one zero).

Input		Zero	Poles		Gain	α
			Re	Im		
All	Nominal	−525.73	−164.45,−143.08	0	0.32	1.4
	Min	−521.50	−159.01	0	0.13	1.3
	Max	−360.51	−74.39	93.42	0.34	1.4
	Mean	−451.9	−121.82	52.29	0.24	1.37
	Std	49.19	22.67	22.11	0.07	0.05
Type I	Nominal	−502.75	−149.75	±48.24	0.27	1.4
	Min	−555.85	−168.87	19.69	0.07	1.2
	Max	−374.90	−60.87	101.95	0.34	1.4
	Mean	−474.40	−119.07	60.98	0.22	1.36
	Std	55.50	31.73	21.85	0.08	0.06
Type II	Nominal	−432.93	−127.45	±35.21	0.29	1.4
	Min	−528.22	−269.18	0	0.12	1.3
	Max	−290.58	−51.58	96.82	0.55	1.4
	Mean	−432.52	−118.67	45.13	0.26	1.37
	Std	63.07	46.43	28.04	0.1	0.05
Type III	Nominal	−418.47	−124.64	±52.1	0.29	1.4
	Min	−516.15	−216.62	0	0.06	1.2
	Max	−240.87	−33.18	94.75	0.37	1.4
	Mean	−417.47	−114.14	53.88	0.25	1.37
	Std	82.02	48.02	26.26	0.09	0.06

Table 4. Parameters for neural network direct models of the human arm.

Input		w_1	w_2	w_3	w_4	w_5	w_6	w_7	w_0	b_1	b_0
All	Nominal	−0.0018	6.286	−0.299	−4.298	−4.977	−3.721	0.522	−0.149	0.013	0.002
	Min	−0.194	−17.830	−14.502	−13.374	−14.321	−12.572	−5.281	−0.940	−1.037	−0.623
	Max	0.498	112.829	95.083	77.390	58.761	40.518	23.497	1.043	0.685	0.281
	Mean	0.006	1.107	0.864	0.626	0.478	0.185	0.044	−0.103	−0.019	−0.0001
	Std	0.077	13.483	11.195	9.264	7.235	5.130	2.812	0.517	0.288	0.123
Type I	Nominal	0.0008	−1.821	−0.192	0.977	1.342	2.399	0.495	0.304	−0.045	0.014
	Min	−0.037	−8.957	−7.390	−13.374	−13.760	−10.783	−1.180	−0.940	−0.382	−0.258
	Max	0.031	9.450	4.653	3.6262	2.901	1.909	1.044	0.928	0.397	0.140
	Mean	−0.002	0.092	−0.409	−0.545	−0.585	−0.538	−0.258	−0.230	−0.001	0.009
	Std	0.010	2.697	1.870	2.822	2.857	2.124	0.592	0.537	0.154	0.073
Type II	Nominal	−0.0002	1.020	−0.262	−0.752	−0.146	−0.517	−0.654	−0.749	−0.019	−0.014
	Min	0.498	112.830	95.083	77.390	58.761	40.518	23.497	1.043	0.685	0.281
	Max	−0.058	−2.721	−8.449	−13.241	−14.321	−12.572	−5.281	−0.711	−1.037	−0.623
	Mean	0.035	5.269	4.037	2.947	920	1.050	1.050	−0.051	0.013	0.013
	Std	0.121	22.394	18.839	15.403	831	8.281	4.798	0.526	0.361	0.164
Type III	Nominal	0.0002	−0.628	−0.279	0.257	311	0.142	0.318	0.886	−0.135	0.119
	Min	0.052	0.671	3.179	8.683	277	10.053	2.025	0.768	0.463	0.189
	Max	−0.194	−17.830	−14.502	−10.377	−7.519	−5.328	−2.768	−0.780	−0.849	−0.849
	Mean	−0.017	−2.368	−1.089	−0.471	0.263	0.177	−0.127	0.014	−0.082	−0.029
	Std	0.055	5.570	4.282	3.812	3.396	2.793	0.971	0.458	0.334	0.125

Table 5. Performance comparison between identified direct models of the human arm in Tables 2, 3 and 4 (best results are shown in bold).

| Model | | Frequency response | | | | | | | | Time response | | | |
| | | Magnitude (dB) | | | | Phase (°) | | | | | | | |
		MSE	MAS	MD	VAF	MSE	MAS	MD	VAF	MSE	MAS	MD	VAF
All	Int.	**13.78**	**2.78**	7.76	**92.73**	273.25	11.11	38.03	94.31	6.38	4.73	13.8	49.58
	Frac.	15.13	2.98	**7.61**	92.20	**260.77**	**10.84**	**37.17**	**94.63**	6.21	4.64	13.8	49.86
	NN	32.95	4.41	21.63	80.32	754.47	21.41	93.67	87.52	**1.74**	**2.96**	**1.51**	**52.19**
Type I	Int.	**9.38**	**2.29**	6.94	92.91	225.37	10.18	35.30	**95.405**	7.22	5.31	13.8	58.03
	Frac.	9.66	2.35	**6.61**	**93.04**	**220.53**	**9.67**	**34.46**	95.401	7.15	5.25	13.8	53.74
	NN	32.13	4.37	18.63	78.82	771.37	23.09	74.69	87.65	**2.58**	**3.71**	**1.88**	**58.35**
Type II	Int.	11.32	**2.61**	8.48	91.08	332.83	12.13	45.60	93.46	5.23	4.01	12.00	46.62
	Frac.	**11.27**	2.62	**7.80**	**92.18**	**313.96**	**10.81**	**45.40**	**93.75**	5.14	3.82	12.10	46.96
	NN	30.09	4.04	25.24	83.55	732.83	17.80	115.69	87.03	**1.35**	**2.58**	**1.41**	**48.61**
Type III	Int.	10.42	2.64	7.27	92.36	252.75	12.55	32.77	95.04	5.13	3.85	13.60	47.18
	Frac.	**9.61**	**2.53**	**5.97**	**94.26**	**232.37**	**10.89**	**32.29**	**95.26**	5.11	3.84	13.60	45.66
	NN	32.35	4.46	20.68	81.19	669.88	20.71	94.00	87.34	**0.96**	**2.31**	**1.10**	**48.49**

5. Otherwise, increment the value of L by one and repeat from step 2.

It may happen that more than one model comes to appear in all P lists at the same time. In that case, either may be selected as convenient. With this heuristic a good value for the commensurability order may be obtained, but a 0.1 step may be a little too rough, so a second stage search was performed. In this stage, the best model was found by sweeping the commensurable order, with a 0.01 step, in a range defined by a neighbourhood, with a 0.1 radius, centred on the best commensurability value (or values) obtained on the first stage. From this sweeping process, another set of models arises and is, consequently, compared, again, using the same heuristic. Therefore, this second stage is basically a refined search around the best solution (or solutions) of the first stage.

In the case of NNARX models, training algorithms are rather blind when it comes to the best values of m and n. Models with an unrealistically large (and unnecessary) number of input and output delays may still provide good results. So we might assume, initially, an unrealistically large number of input and output delays and analyze the corresponding weights, comparing them to decide whether m and n should be decremented, until none of the weights is lower than a certain threshold value. But in this case it is possible to use prior knowledge of the system to be identified, assume a maximum value for the number of input and output delays and try every dynamical structural combination within that maximum number of delays; from this process, results a set of models that should be compared, keeping the best one. It was shown that linear inverse models are of second or third order, so a maximum of six input and output delays was considered, to give some margin for possible additional nonlinear dynamics to be identified in measured data. With this maximum value, one obtains a set of 36 NNs to compare and a heuristic similar to the one described above for fractional plants was employed. The only difference here is that, as mentioned previously, very complex networks can have slightly better results, but at the cost of a lower computational efficiency. Therefore, to the 12 values of performance indexes mentioned above, two more were added: m and n themselves, thus providing for a NN which is a compromise between model performance and model complexity.

Model parameters are given in Tables 6–9 and their performances are shown in Table 10 (again, best results are in bold). This time, models with fixed commensurable orders were obtained, to ascertain that parameter uncertainty does not get unacceptable in that case.

5. Discussion and conclusions

Performance results for direct models show that while NNs outperform both integer and fractional models in what time responses are concerned, they do so at the expense of a poorer fit to frequency data and more parameters. Performance results for inverse models show that integer models often get better results in

Table 6. Parameters for integer order inverse models of the human arm (three poles, three zeros).

Input		Zero 1	Zeros 2 and 3 Re	Im	Pole 1	Poles 2 and 3 Re	Im	Gain
All	Nominal	−10.23	−46.01	±50.80	290.76	−10.62	±91.88	−1987.74
	Min	−195.80	−21.93	19.40	−5492.62	−68.51	68.35	−548521.81
	Max	−13.59	−4.58	52.08	3610.01	−12.03	141.33	167096.50
	Mean	−40.12	−14.62	34.69	31297.12	−38.96	88.41	−68294.69
	Std	33.07	3.95	8.10		11.02	11.49	606890.65
Type I	Nominal	−19.41	−45.03	±44.93	285.29	−10.71	±92.69	−1918.72
	Min	−85.48	−20.64	22.48	−5283.10	−64.53	71.33	−5485421.81
	Max	−16.63	−6.81	52.08	28320.12	−16.99	141.33	136220.47
	Mean	−31.84	−14.66	37.78	8801.50	−39.92	90.80	−168159.62
	Std	17.92	3.49	7.36	50096.81	11.65	13.7	971051.06
Type II	Nominal	−5.98	−47.20	±51.68	281.92	−11.52	±91.71	−2086.99
	Min	−89.23	−21.93	19.40	−5492.62	−53.64	68.35	−140316.66
	Max	−13.59	−5.93	50.97	5941.93	−14.55	118.41	167096.50
	Mean	−39.11	−14.93	32.71	239.05	−38.60	86.26	−3261.17
	Std	25.27	4.36	8.91	2026.21	9.27	9.76	52659.83
Type III	Nominal	−6.86	−45.92	±53.78	307.94	−9.84	±91.26	−1957.36
	Min	−195.80	−21.70	21.87	−1625.27	−68.51	70.37	−28421.13
	Max	−16.38	−4.58	45.95	1924.50	−12.03	107.97	39359.73
	Mean	−52.83	−14.20	32.72	344.26	−38.03	87.61	−5695.89
	Std	50.50	4.19	6.98	919.21	12.32	9.71	17730.88

Table 7. Parameters for fractional order inverse models of the human arm (two poles, two zeros).

Input		Zero 1 Re	Im	Zero 2 Re	Im	Pole 1 Re	Im	Pole 2 Re	Im	Gain	α
All	Nominal	−61.66	0	−605.19	0	−936.36	596.35	−936.36	−596.35	1550.49	1.52
	Min	−326.45	0	−1198.46	−79.61	−1487.65	0	−6879.69	−400.75	913.90	0.75
	Max	1.09	79.61	1.09	0	15.52	400.75	15.52	0	19017.54	1.76
	Mean	−58.54	27.27	−172.15	−27.27	−333.26	122.29	−1202.18	−122.29	4020.08	1.21
	Std	68.18	19.53	327.16	19.53	404.38	119.72	2072.98	119.72	3164.83	0.29
Type I	Nominal	−82.77	0	−525.77	0	−841.90	585.45	−841.90	−585.45	1586.60	1.50
	Min	−326.45	0	−1198.46	−79.61	−1487.65	0	−5956.06	−400.75	932.94	0.89
	Max	−3.17	79.61	−3.17	0	13.57	400.75	13.57	0	10984.09	1.75
	Mean	−66.89	35.18	−142.20	−35.18	−335.79	173.16	−955.22	−173.16	3764.06	1.22
	Std	83.04	19.68	317.58	19.68	411.73	122.19	1876.72	122.19	2695.34	0.24
Type II	Nominal	−75.48	0	−936.27	0	−1509.90	563.76	−1509.90	−563.76	1800.96	1.60
	Min	−260.51	0	−1162.86	−45.60	−1386.18	0	−6660.02	−372.50	964.40	0.83
	Max	−0.10	45.60	−0.10	0	13.89	372.50	13.89	0	19017.54	1.76
	Mean	−63.43	17.53	−264.01	−17.53	−402.17	78.78	−1686.46	−78.78	4042.19	1.24
	Std	74.06	15.20	414.17	15.20	482.59	100.34	2535.12	100.34	3676.66	0.33

(continued)

Table 7. Continued

Input		Zero 1		Zero 2		Pole 1		Pole 2		Gain	α
		Re	Im	Re	Im	Re	Im	Re	Im		
Type III	Nominal	−85.15	0	−961.72	0	−1419.68	638.44	−1419.68	−638.44	1433.38	1.60
	Min	−164.54	0	−955.11	−62.12	−1115.75	0	−6879.69	−352.91	913.90	0.75
	Max	1.09	62.12	1.09	0	15.52	352.91	15.52	0	14211.15	1.74
	Mean	−49.13	26.51	−122.28	−26.51	−277.93	109.15	−1053.38	−109.15	4079.69	1.17
	Std	49.27	19.29	238.80	19.29	315.93	118.80	1827.26	118.80	3287.26	0.28

Table 8. Parameters for fractional order inverse models of the human arm with a fixed commensurable order (two poles, two zeros).

Input		Zero 1		Zero 2		Pole 1		Pole 2		Gain	α
		Re	Im	Re	Im	Re	Im	Re	Im		
All	Nominal	−61.66	0	−605.19	0	−936.36	596.35	−936.36	−596.35	1550.49	1.52
	Min	−217.88	0	−595.98	0	−1534.79	0	−16268.49	−496.61	926.97	
	Max	−61.81	0	−214.40	0	−548.98	496.61	−898.58	0	24899.36	
	Mean	−129.15	0	−396.41	0	−812.03	42.51	−3619.24	−42.51	7060.07	
	Std	33.94	0	82.49	0	200.36	124.14	1918.81	124.14	3503.82	
Type I	Nominal	−82.77	0	−525.77	0	−841.90	585.45	−841.90	−585.45	1586.60	1.50
	Min	−231.73	0	−527.07	−25.46	−1375.17	0	−4315.26	−520.87	1399.31	
	Max	−72.91	25.46	−214.43	0	−568.47	520.87	−955.78	0	12031.24	
	Mean	−146.47	1.17	−350.22	−1.17	−828.92	51.95	−2730.80	−51.95	6091.86	
	Std	38.70	4.91	79.68	4.91	188.65	141.46	1001.68	141.46	2415.18	
Type II	Nominal	−75.48	0	−936.27	0	−1509.90	563.76	−1509.90	−563.76	1800.96	1.60
	Min	−201.48	0	−932.18	0	−1504.23	0	−8588.36	−275.20	1347.41	
	Max	−77.91	0	−429.35	0	−710.95	275.20	−1486.08	0	13369.12	
	Mean	−138.33	0	−633.01	0	−975.81	10.19	−5197.77	−10.19	6760.52	
	Std	34.41	0	123.87	0	220.37	52.96	1542.85	52.96	2612.39	
Type III	Nominal	−85.15	0	−961.72	0	−1419.68	638.44	−1419.68	−638.44	1433.38	1.60
	Min	−197.11	0	−890.80	0	−1579.94	0	−18499.77	−454.14	917.06	
	Max	−104.83	0	−425.34	0	−703.79	454.14	−1361.17	0	18691.05	
	Mean	−150.72	0	−629.74	0	−990.39	19.75	−5515.16	−19.75	6467.75	
	Std	29.20	0	121.94	0	228.89	94.70	3291.45	94.70	9914.50	

what the gain of the transfer function is concerned, but not the phase, or above all the time response; NN models, even though nonlinear, do not consistently perform better, and, when they do, only slightly.

Since we are dealing with different performance indexes, it is necessary to try to make a global comparison. For this purpose all indexes have been normalized between 0 (attributed to the poorest value) and 1 (attributed to the best value). Results were then averaged. This composite index is shown in Table 11. It can be seen that fractional models achieve, globally

speaking, the best performance, both for direct and inverse models. NNs are a close runner up for inverse models, but fractional models are linear and continuous, which NNs are not. This last characteristic means that fractional models will work for any sampling time (while NNs will not). Linear models are a close runner up for direct models, but fractional models use one parameter less, and are thus the simplest possible.

Finally, there is no clear interpretation of what a fractional derivative means, geometrically, physically or statistically, although attempts at that have been

Table 9. Parameters for neural network inverse models of the human arm.

Input		w_1	w_2	w_3	w_4	w_5	w_6	w_0	b_1	b_1
All	Nominal	417.700	−1191.466	1136.109	−362.158	−0.083	0.167	11.471	−0.015	0.170
	Min	−527.180	−262.133	−1490.932	−390.051	−1.106	−2.639	−172.050	−1.847	−11.301
	Max	469.371	1534.079	361.952	483.919	2.355	1.420	123.258	0.991	11.051
	Mean	−5.227	23.800	−20.645	3.023	0.037	−0.029	0.923	−0.048	−0.273
	Std	123.701	187.432	183.509	106.781	0.463	0.482	33.056	0.381	2.716
Type I	Nominal	−146.102	421.829	−407.494	131.713	0.028	−0.056	−33.879	−0.021	−0.710
	Min	−527.180	−142.773	−1490.932	−98.539	−0.448	−0.380	−172.050	−0.244	−4.726
	Max	164.011	1534.079	167.815	483.919	0.677	1.168	123.258	0.344	4.317
	Mean	−15.094	48.261	−60.754	25.110	0.053	0.001	−0.318	0.006	−0.572
	Std	124.270	277.454	268.187	105.808	0.233	0.272	49.704	0.121	1.763
Type II	Nominal	1694.113	−4923.864	4780.281	−1550.272	−0.226	0.469	4.013	−0.374	1.541
	Min	−400.669	−101.294	−96.134	−351.761	−0.859	−0.646	−30.484	−0.761	−6.142
	Max	85.682	388.599	361.952	144.209	0.700	0.563	45.276	0.682	4.273
	Mean	−12.376	7.666	0.119	5.344	0.014	0.006	4.509	−0.021	0.996
	Std	100.264	90.42	86.57	88.64	0.328	0.268	15.331	0.327	1.776
Type III	Nominal	43.708	−107.075	84.611	−21.186	−0.031	0.061	91.667	0.044	−1.455
	Min	−242.838	−262.133	−272.991	−390.051	−1.105	−2.639	−35.145	−1.847	−11.301
	Max	469.371	232.262	249.388	259.889	2.355	1.420	33.354	0.991	11.051
	Mean	16.893	8.709	10.786	−30.432	0.043	−0.110	−1.560	−0.154	−1.348
	Std	148.262	98.906	99.409	122.611	0.766	0.810	15.486	0.609	3.968

Table 10. Performance comparison between identified inverse models of the human arm in Tables 6, 7 and 9 (best results are shown in bold).

Model		Frequency response								Time response			
		Magnitude (dB)				Phase (°)							
		MSE	MAS	MD	VAF	MSE	MAS	MD	VAF	MSE	MAS	MD	VAF
All	Int.	**15.410**	**2.903**	**11.994**	**92.545**	1007.274	28.486	69.760	74.125	0.272	0.371	1.819	41.508
	Frac.	21.632	3.455	14.352	88.903	628.689	18.032	**58.400**	86.449	**0.266**	**0.354**	**1.658**	47.888
	NN	23.028	3.807	18.378	90.812	**559.089**	**16.279**	101.135	**87.496**	1.616	1.096	2.335	**57.827**
Type I	Int.	**12.294**	**2.587**	**11.398**	**92.703**	764.852	24.454	62.375	82.033	0.421	0.490	2.440	51.515
	Frac.	18.769	3.274	12.803	89.150	**404.851**	**14.437**	**42.690**	**90.971**	0.423	0.477	2.284	55.144
	NN	25.354	4.094	14.948	90.574	467.089	16.026	76.924	88.489	**0.286**	**0.415**	**2.001**	**63.803**
Type II	Int.	**15.315**	**2.842**	**12.230**	**93.656**	1146.667	30.209	69.054	68.563	0.143	0.280	1.408	39.239
	Frac.	23.264	3.483	17.098	88.926	**624.472**	**17.813**	**59.324**	**85.727**	0.136	0.269	1.267	45.956
	NN	22.443	3.908	14.337	93.456	920.851	17.971	157.716	81.771	**0.086**	**0.227**	**1.086**	**57.492**
Type III	Int.	**16.032**	**3.089**	**10.971**	93.165	1318.925	31.813	80.725	65.715	0.126	0.271	1.363	31.355
	Frac.	21.802	3.507	14.387	89.999	687.664	19.075	**67.334**	**84.818**	0.096	**0.239**	1.143	45.007
	NN	24.498	4.129	12.308	**93.450**	647.907	**17.872**	128.764	84.132	0.098	0.250	**1.041**	**54.529**

Table 11. Performance indexes of Tables 5 and 10, normalized between 0 and 1, and averaged (best results are shown in bold).

Type or domain	Direct models			Inverse models		
	Integer	Fractional	Neural network	Integer	Fractional	Neural network
All types	0.657	**0.663**	0.333	0.622	**0.685**	0.377
Type I	**0.736**	0.668	0.333	0.370	0.538	**0.566**
Type II	0.630	**0.693**	0.333	0.408	0.462	**0.651**
Type III	0.663	**0.668**	0.333	0.392	0.671	**0.682**
Gain	0.966	**0.982**	0	**0.995**	0.261	0.260
Phase	0.956	**0.999**	0	0.178	**0.967**	0.659
Time response	0.092	0.038	**1**	0.172	0.601	**0.788**
Global	0.671	**0.673**	0.333	0.448	**0.598**	0.569
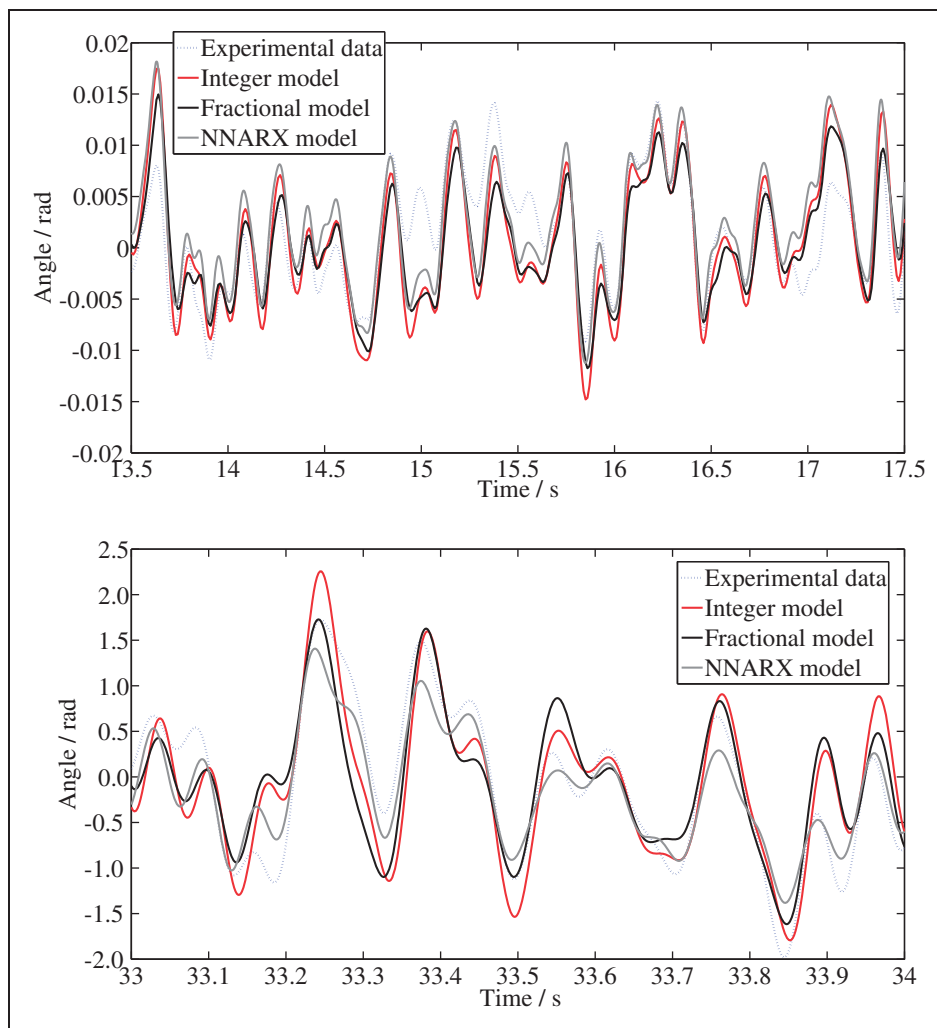
Figure 4. Part of the responses of the several models, compared with experimental data: top, direct models; bottom, inverse models.
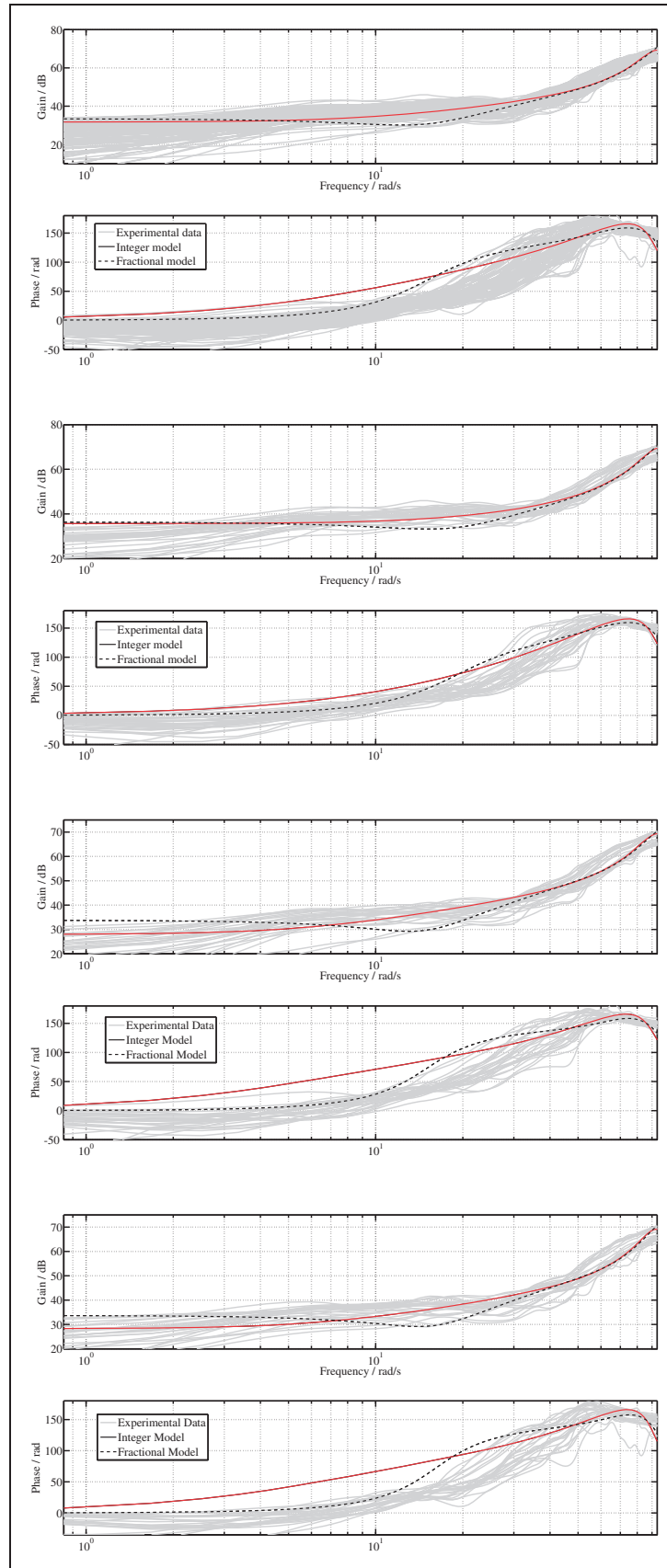
Figure 5. Frequency responses of the inverse linear models, compared with experimental data; from top to bottom: all types of inputs, inputs of type I, inputs of type II, and inputs of type III.

published (see e.g. Machado (2003), Podlubny (2002), and a short review by Valério and Sá da Costa (2012)). But still the fractional model is not the worst off: NNs too lack a clear interpretation, and the integer model includes a third-order derivative, which, unlike first- and second-order ones, also lacks a clear interpretation.

So again we conclude that the dynamic behaviour we are dealing with is best described by fractional transfer functions (just as was seen in Tejado et al. (2013) for direct models only). Figure 4 shows some seconds of the responses obtained with the different models, compared with experimental data, for both the direct and the inverse plant. Figure 5 shows the same for the frequency responses of inverse linear models; a similar figure for direct models is found in Tejado et al. (2013).

Funding

References

Adewusi S, Rakheja S and Marcotte P (2012) Biomechanical models of the human hand-arm to simulate distributed biodynamic responses for different postures. *International Journal of Industrial Ergonomics* 42(2): 249–260.

Baleanu D, Diethelm K, Scalas E and Trujillo JJ (2012) *Fractional Calculus: Models and Numerical Methods*. Singapore: World Scientific.

Bhowmick S, Bag R, Hossain SM, Ghosh S, Mazumder S and Gupta SD (2013) Modelling and control of a robotic arm using artificial neural network. *IOSR Journal of Computer Engineering* 15(2): 42–49.

Bhrawry AH, Doha E, Baleanu D and Ezz-Eldien S (2014) A spectral tau algorithm based on Jacobi operational matrix for numerical solution of time fractional diffusion-wave equations. *Journal of Computational Physics* DOI: 10.1016/j.jcp.2014.03.039.

Bhrawy AH, Abdelkawy MA, Zaky MA and Baleanu D (2015) Numerical simulation of time variable fractional order mobile–immobile advection–dispersion model. *Romanian Reports in Physics* 67(3): A5.

Cheron G, Leurs F, Bengoetxea A, Draye JP, Destrée M and Dan B (2003) A dynamic recurrent neural network for multiple muscles electromyographic mapping to elevation angles of the lower limb in human locomotion. *Journal of Neuroscience Methods* 129: 95–104.

Diethelm K, Ford JM, Ford NJ and Weilbeer M (2006) Pitfalls in fast numerical solvers for fractional differential equations. *Journal of Computational and Applied Mathematics* 186(2): 482–503.

Djordjevic VD, Jaric J, Fabry B, Fredberg JJ and Stamenovic D (2003) Fractional derivatives embody essential features of cell rheological behavior. *Annals of Biomedical Engineering* 31: 692–699.

Fu MJ and Cavusoglu MC (2012) Human-arm-and-hand-dynamic model with variability analyses for a stylus-based haptic interface. *IEEE Transactions on Systems, Man, and Cybernetics, Part B: Cybernetics* 42(6): 1633–1644.

Garbey M, Bass BL, Berceli S, Collet C and Cerveri P (eds) (2014) *Computational Surgery and Dual Training: Computing, Robotics and Imaging*. Berlin: Springer-Verlag.

Haykin S (1999) *Neural Networks—A Comprehensive Foundation*, 2nd edition. Englewood Cliffs, NJ: Prentice Hall International, Inc.

Jailani R, Zakaria SH and Tokhi MO (2012) The development of quadriceps muscle model for paraplegic. *Procedia Engineering* 41: 1553–1558.

Jang JSR, Sun CT and Mizutani E (1997) *Neuro-fuzzy and soft computing*. Upper Saddle River, NJ: Prentice-Hall.

Machado JAT (2003) A probabilistic interpretation of the fractional-order differentiation. *Fractional Calculus and Applied Analysis* 6(1): 73–80.

Magin RL (2004) *Fractional Calculus in Bioengineering*. Connecticut: Begell House.

Mainardi F (2010) *Fractional Calculus and Waves in Linear Viscoelasticity. An Introduction to Mathematical Models*. London: Imperial College Press.

Malti R, Victor S and Oustaloup A (2008) Advances in system identification using fractional models. *ASME Journal of Computational and Nonlinear Dynamics* 3: 021401.

Mandic D and Chambers J (2001) *Recurrent Neural Networks for Prediction—learning algorithms, architectures and stability*. Chichester: John Wiley & Sons, Ltd.

Marquardt D (1963) An algorithm for least squares estimation of nonlinear parameters. *SIAM Journal on Applied Mathematics* 11: 431–441.

Miller KS and Ross B (1993) *An introduction to the fractional calculus and fractional differential equations*. New York: John Wiley and Sons.

Mobasser F and Hashtrudi-Zaad K (2006) A method for online estimation of human arm dynamics. In: *Proceedings of 28th annual international conference of the IEEE Engineering in Medicine and Biology Society (EMBS'06)*. pp. 2412–2416.

Nagarsheth H, Savsani P and Patel M (2008) Modeling and dynamics of human arm. In: *Proceedings of the 2008 IEEE international conference on automation science and engineering (CASE'08)*, pp. 924–928.

Nørgaard M, Ravn O, Poulsen NK and Hansen LK (2003) *Neural networks for modelling and control of dynamic systems: A practitioner's handbook*. London: Springer-Verlag.

Park S, Lim H, Kim Bs and Song Jb (2006) Development of safe mechanism for surgical robots using equilibrium point control method. In: Larsen R, Nielsen M and Sporring J (eds) *Medical Image Computing and Computer-Assisted Intervention — MICCAI 2006 (Lecture Notes in Computer Science, volume 4190)*. Berlin: Springer, pp. 570–577.

Podlubny I (1999) *Fractional differential equations: An introduction to fractional derivatives, fractional differential equations, to methods of their solution and some of their applications*. San Diego, CA: Academic Press.

Podlubny I (2002) Geometrical and physical interpretation of fractional integration and fractional differentiation. *Fractional Calculus and Applied Analysis* 5(4): 367–386.

Potkonjak V, Tzafestas S, Kostic D and Djordjevic G (2001) Human-like behavior of robot arms: General considerations and the handwriting task — Part I: Mathematical description of human-like motion: distributed positioning and virtual fatigue. *Robotics and Computer-Integrated Manufacturing* 17(4): 305–315.

Rosen J, Fuchs MB and Arcan M (1999) Performances of Hill-type and neural network muscle modelstoward a myosignal-based exoskeleton. *Computers and Biomedical Research* 32(5): 415–439.

Samko SG, Kilbas AA and Marichev OI (1993) *Fractional integrals and derivatives*. Yverdon: Gordon and Breach.

Simunic B (2003) *Model of longitudinal contractions and transverse deformations in skeletal muscles*. PhD Thesis, Faculty of Electrical Engineering, University of Ljubljana (Slovenia).

Sommacal L, Melchior P, Cabelguen JM, Oustaloup A and Ijspeert AJ (2007a) Fractional multimodels of the gastrocnemius muscle for tetanus pattern. *Advances in Fractional Calculus: Theoretical Developments and Applications in Physics and Engineering*. Berlin: Springer-Verlag, pp. 271–285.

Sommacal L, Melchior P, Dossat A, et al. (2007b) Improvement of the muscle fractional multimodel for low-rate stimulation. *Biomedical Signal Processing and Control* 2: 226–233.

Sommacal L, Melchior P, Oustaloup A, Cabelguen JM and Ijspeert AJ (2008) Fractional multi-models of the frog gastrocnemius muscle. *Journal of Vibration and Control* 14(9–10): 1415–1430.

Taïx M, Tran MT, Souères P and Guigon E (2013) Generating human-like reaching movements with a humanoid robot: A computational approach. *Journal of Computational Science* 4(4): 269–284.

Tejado I, Valério D, Pires P and Martins J (2013) Fractional order human arm dynamics with variability analyses. *Mechatronics* 23: 805–812.

Valério D, Ortigueira MD and Sá da Costa J (2008) Identifying a transfer function from a frequency response. *ASME Journal of Computational and Nonlinear Dynamics* 3(2): 021207.

Valério D and Sá da Costa J (2011) An introduction to single-input, single-output Fractional Control. *IET Control Theory and Applications* 5(8): 1033–1057.

Valério D and Sá da Costa J (2012) *An Introduction to Fractional Control*. IET.

Ventura A, Tejado I, Valério D and Martins J (2015) Direct and inverse models of human arm dynamics. In: *Proceedings of the 8th international conference on biomedical electronics and devices (BIODEVICES'15)*.

Venture G, Yamane K and Nakamura Y (2006) Identification of human musculo-tendon subject specific dynamics using musculo-skeletal computations and non linear least square. In: *Proceedings of the 1st IEEE/RAS-EMBS international conference on biomedical robotics and biomechatronics (BioRob'06)*, pp. 211–216.

Article

Fractional-order modeling of permanent magnet synchronous motor speed servo system

WeiJia Zheng[1], Ying Luo[2], YangQuan Chen[3] and YouGuo Pi[1]

Abstract

A fractional-order modeling approach for a permanent magnet synchronous motor speed servo system is proposed applying a method combining electromagnetic part modeling and mechanical part modeling. Based on the proposed fractional-order model and system identification scheme, system identification experiments are performed on the electromagnetic part and the mechanical part of the permanent magnet synchronous motor speed servo system, respectively. The fractional-order model parameters of these two parts are identified with these experimental results, and the fractional-order model of the permanent magnet synchronous motor speed servo system is integrated from these two parts. Simulations and experiments in open-loop and closed-loop are performed based on the obtained fractional-order model and integer-order model. The advantage of the proposed fractional-order model for the permanent magnet synchronous motor speed servo system is demonstrated by the simulation and experimental results.

1. Introduction

Fractional calculus has been widely studied and applied in recent years (Kilbas et al., 2006). More and more real-world systems can be precisely modeled using fractional differential equations, such as some batteries (Sabatier et al., 2006), thermal systems (Gabano and Poinot, 2011) and induction machines (Petras et al., 2009). Stability analysis of fractional systems is proposed in some literatures (Li et al., 2010; Aguila-Camacho et al., 2014), while fractional-order controllers have been designed to control real world systems (Podlubny, 1999a; Ladaci et al., 2008; Zamani et al., 2009; Luo et al., 2011; Hajiloo et al., 2012). Fractional-order system identification based on continuous-order distributions is proposed by Hartley and Lorenzo (2003), fractional-order system modeling methods for thermal system are proposed in Poinot and Trigeassou (2004) and Gabano and Poinot (2011), and a fractional-order modeling method for permanent magnet synchronous motor (PMSM) velocity servo system is studied by Yu et al. (2013). In Yu et al. (2013), the overall PMSM velocity system model is directly assumed to be a fractional-order model which is

identified using a digital simulation method. However, without full consideration of the inherent characteristics of different component mechanisms of PMSM, it is rough to identify the PMSM model as a whole.

In this paper, a fractional-order modeling approach, integrating electromagnetic part modeling and mechanical part modeling, is proposed for the PMSM speed servo system. The approach is based on the fact that the PMSM speed servo system can be divided into two parts, the electromagnetic part converting armature voltage into electromagnetic torque, and the mechanical part generating rotor rotation under the effect of electromagnetic torque. Equation (1) can be used to

[1]School of Automation Science and Engineering, South China University of Technology, China
[2]Hermes-Microvision Inc., San Jose, USA
[3]School of Engineering, University of California, USA

Corresponding author:
WeiJia Zheng, School of Automation Science and Engineering, South China University of Technology, Guangzhou, 510641, China.
Email: z.wj08@mail.scut.edu.cn

describe the electromagnetic part and equation (2) can be used to describe the mechanical part

$$U - E = U - C_e n = Ri + L\frac{d^\vartheta i}{dt^\vartheta} \qquad (1)$$

$$T - T_L = C_m(i - i_L) = \frac{GD^2}{375}\frac{d^\xi n}{dt^\xi} \qquad (2)$$

In equation (1), the U is armature voltage, E is back electromotive force, the C_e is induced electromotive force coefficient, the n is motor speed, the R is armature resistance, the i is armature current and the L is armature inductance. In equation (2), the T is electromagnetic torque, the T_L is the equivalent torque of load, the C_m is torque coefficient, the i_L is equivalent current of load and the GD^2 is flywheel inertia.

The parameters of these two parts are identified respectively and then the fractional-order mathematical model is obtained. Open-loop simulations and experiments are performed and the frequency response of the proposed models and the actual PMSM are obtained and compared. According to the obtained integer-order model and fractional-order model, three groups of PI controllers are designed for the PMSM speed servo system. PMSM speed-tracking simulations and experiments are performed using these PI controllers and the control performances are compared.

In this paper, firstly, fractional-order model structure combining an electromagnetic part and a mechanical part of a PMSM speed servo system is proposed. Secondly, a digital simulation method is applied to identify the parameters of these two parts, and the fractional-order model of PMSM speed servo system is integrated. Finally, the obtained fractional-order model is verified by open-loop frequency response tests and closed-loop speed-tracking simulations and experiments, using the PI controllers designed according to the traditional integer-order model and the proposed fractional-order model.

The rest of this paper is organized as follows, fractional-order model structure of PMSM is discussed in Section 2, time-domain identification method of fractional-order system modeling is presented in Section 3, system identification experiments are performed and the parameters of the electromagnetic part and mechanical part are identified in Section 4, open-loop simulations and experiments are performed and the frequency response of the proposed models and the actual PMSM are compared in Section 5. Three groups of PI speed controllers are designed for a PMSM speed servo system according to the integer-order model and the fractional-order model obtained in this paper. Motor speed-tracking simulations and experiments are performed using these controllers, and the deviations between the simulation results and

experimental results of these control systems are compared respectively. The conclusion is given in Section 6.

2. Fractional-order model of the PMSM speed servo system

Based on the motor unified theory, a three-phase static coordinate system can be transmitted into a two-phase rotary coordinate system after the space vector transformation. Therefore, a three-phase AC motor can be equivalent to a DC motor. Suppose that the d-axis and q-axis represent the axes in a two-phase rotary coordinate system. The direction of the d-axis is set to be the direction of the rotor flux vector and the q-axis is set to point in the vertical direction of the d-axis. Thus, the three-phase stator current of a motor can be decoupled into two DC current components, the excitation component i_d and the torque component i_q. For a PMSM, whose rotor flux is generated by a permanent magnet, the excitation component i_d is set to be zero and the torque component i_q is equivalent to the armature current of a DC motor. Then, the mathematical model of the PMSM is described by equation (3) and (4) (Chen, 2003)

$$u_q - E = u_q - C_e n = Ri_q + L\frac{di_q}{dt} \qquad (3)$$

$$T - T_L = C_m(i_q - i_L) = \frac{GD^2}{375}\frac{dn}{dt} \qquad (4)$$

The real objects are generally fractional (Nakagava and Sorimachi, 1992; Podlubny, 1999b). The real inductor behavior can be better described by a fractional-order model (Petras et al., 2009; Valsa, 2012). Since inductors are the essential components of the electromagnetic part, the model of the electromagnetic part should also be fractional. Thus, the electromagnetic part can be described as shown in equation (5), where the range of fractional order ϑ is (0, 2)

$$u_q - E = u_q - C_e n = Ri_q + L\frac{d^\vartheta i_q}{dt^\vartheta} \qquad (5)$$

The mechanical equation of the motor in equation (4) (Chen, 2003) is generated with the assumption that the moment of inertia is homogeneously distributed and physical material is an ideal block. In reality, no physical component perfectly satisfies this assumption. Thus, the mechanical part of the PMSM may also be fractional, as shown in equation (6), where the range of fractional order ξ is (0, 2)

$$T - T_L = C_m(i_q - i_L) = \frac{GD^2}{375}\frac{d^\xi n}{dt^\xi} \qquad (6)$$
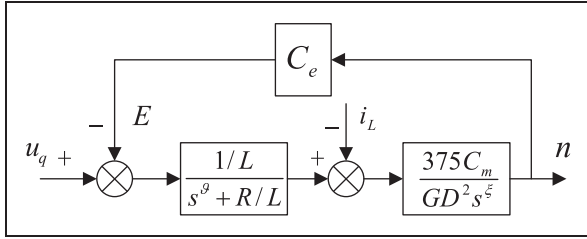
Figure 1. Fractional-order mathematical model of the PMSM.

Figure 2. Block diagram of the approximated fractional-order integrator.

Under zero initial conditions, the transfer functions of two parts are shown in equation (7) and (8)

$$G_1(s) = \frac{i_q(s)}{u_q(s) - E(s)} = \frac{1/L}{s^\vartheta + R/L} \qquad (7)$$

$$G_2(s) = \frac{n(s)}{i_q(s) - i_L(s)} = \frac{375}{GD^2} \frac{C_m}{s^\xi} \qquad (8)$$

Then, the fractional-order mathematical model of the PMSM is obtained as shown in Figure 1.

3. Time-domain identification for the fractional-order system

Theoretically, the fractional-order system is infinite-dimensional, so it is necessary to apply some special ways to study it. One of the major methods is to convert the fractional-order transfer function into an integer-order rational function using an approximation or discretization method. The integer-order approximation method is applied to approach the fractional-order system in this paper.

3.1. Approximation of fractional-order integrator

The fractional-order integrator $1/s^\xi$ can be approached by connecting an integer-order integrator and a fractional-order differentiator approximated by an Oustaloup filter (Oustaloup, 1995; Oustaloup et al., 2000) in series (Poinot and Trigeassou, 2004). Suppose that the frequency band in which the differentiator needs to be approximated is (ω_L, ω_H) and the order of the fractional-order integrator is $\xi = 1 - \gamma$, where γ is the order of the differentiator. The approximated fractional-order integrator can be described by equation (9)

$$I_\xi^*(s) = \frac{1}{s^\xi} = \frac{1}{s} \cdot s^\gamma \approx \frac{1}{s} \cdot \omega_H^{1-\xi} \prod_{t=1}^{2N+1} \frac{1 + s/w_t'}{1 + s/w_t} \prod_{t=1}^{2N+1} \frac{w_t'}{w_t} \quad (9)$$
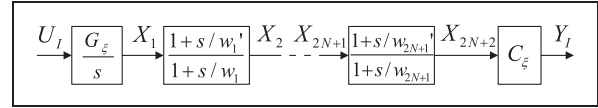
where

$$w_t' = \omega_L \left(\frac{\omega_H}{\omega_L} \right)^{\frac{t + \frac{1}{2}\xi - 1}{2N+1}} \qquad (10)$$

$$w_t = \omega_L \left(\frac{\omega_H}{\omega_L} \right)^{\frac{t - \frac{1}{2}\xi}{2N+1}} \qquad (11)$$

$2N + 1$ is the order of the filter (N is a positive integer).

Introduce two variables G_ξ and C_ξ as described by equation (12). The values of G_ξ and C_ξ guarantee that the mode of the fractional-order integrator is 1 when the angular frequency is 1 rad/s

$$G_\xi = \omega_H^{1-\xi}, \quad C_\xi = \prod_{t=1}^{2N+1} \frac{w_t'}{w_t} \qquad (12)$$

Thus, the fractional-order integrator can be described by equation (13)

$$I_\xi^*(s) = \frac{G_\xi C_\xi}{s} \prod_{t=1}^{2N+1} \frac{1 + s/w_t'}{1 + s/w_t} \qquad (13)$$

Introducing $2N + 2$ states, the block diagram of the fractional-order integrator is shown in Figure 2.

Introduce a variable α described by equation (14) (Poinot and Trigeassou, 2004)

$$\alpha = \frac{w_t}{w_t'} = \left(\frac{\omega_H}{\omega_L} \right)^{\frac{1-\xi}{2N+1}} \qquad (14)$$

Then based on Figure 2 and equation (14), the fractional-order integrator can be approximated by a state equation as in equation (15) (Poinot and Trigeassou, 2004)

$$\begin{aligned} M_I \dot{x}_I &= A_I x_I + B_I u_I \\ y_I &= C_I x_I \end{aligned} \qquad (15)$$

where M_I, A_I, B_I and C_I are described by equation (16) and (17)

$$M_I = \begin{bmatrix} 1 & 0 & \cdots & \cdots & 0 \\ -\alpha & 1 & & & \vdots \\ 0 & -\alpha & 1 & & \vdots \\ \vdots & & \ddots & \ddots & 0 \\ 0 & \cdots & 0 & -\alpha & 1 \end{bmatrix}, \quad B_I = \begin{bmatrix} G_\xi \\ 0 \\ \vdots \\ \vdots \\ 0 \end{bmatrix},$$

$$C_I = \begin{bmatrix} 0 \\ \vdots \\ \vdots \\ 0 \\ C_\xi \end{bmatrix}^T \tag{16}$$

$$A_I = \begin{bmatrix} 1 & 0 & \cdots & \cdots & 0 \\ w_1 & -w_1 & & & \vdots \\ 0 & w_2 & -w_2 & & \vdots \\ \vdots & & \ddots & \ddots & 0 \\ 0 & \cdots & 0 & w_{2N+1} & -w_{2N+1} \end{bmatrix},$$

$$x_I = \begin{bmatrix} x_1 \\ x_2 \\ \vdots \\ \vdots \\ x_{2N+2} \end{bmatrix} \tag{17}$$

The state equation can also be converted into the following form

$$\begin{aligned} \dot{x}_I &= A_I^* x_I + B_I^* u_I \\ y_I &= C_I x_I \end{aligned} \tag{18}$$

where

$$\begin{aligned} A_I^* &= M_I^{-1} A_I \\ B_I^* &= M_I^{-1} B_I \end{aligned} \tag{19}$$

Thus, the approximated system of the fractional-order integrator, $I_\xi^*(s)$, can be represented as a state space form shown in Figure 3.

3.2. Approximation of the fractional-order system

Considering the following fractional-order model

$$\frac{d^\xi y(t)}{dt^\xi} + ay(t) = bu(t) \tag{20}$$
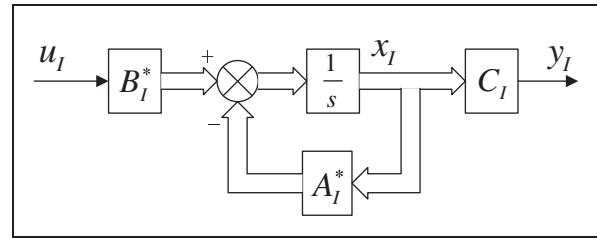
Figure 3. State space representation of the fractional-order integrator.
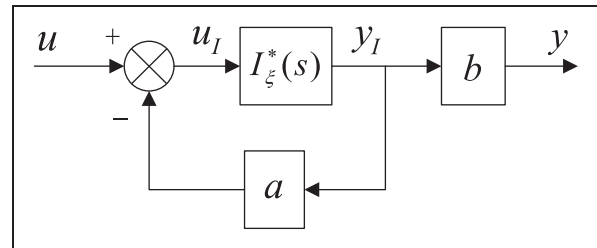

Figure 4. Structure of the fractional-order model.

the transfer function can be obtained after a Laplace transform on both sides

$$G(s) = \frac{b}{s^\xi + a} \tag{21}$$

Introduce state $x(t)$, satisfying

$$X(s) = \frac{1}{s^\xi + a} U(s) \tag{22}$$

Then the fractional-order model shown in equation (20) can be described as the following state equation

$$\begin{aligned} \frac{d^\xi x(t)}{dt^\xi} &= -ax(t) + u(t) \\ y(t) &= bx(t), \end{aligned} \tag{23}$$

with $X(0) = 0$ and $U(0) = 0$. The corresponding system structure is shown in Figure 4.

Taking the state equation of the approximated system in equation (23) into the representation of a fractional-order integrator in equation (18), yields

$$\begin{aligned} \dot{x}_I &= A_I^* x_I + B_I^* u_I = A_I^* x_I + B_I^*(u - ay_I) \\ y_I &= by_I = bC_I x_I \end{aligned} \tag{24}$$

Then the integer-order state equation of the approximated system can be obtained

$$\begin{aligned} \dot{x}_I &= (A_I^* - B_I^* C_I a) x_I + B_I^* u \\ y &= bC_I x_I \end{aligned} \tag{25}$$

Since the order of the fractional-order integrator $I_\xi^*(s)$ is determined by variable α, all the characteristics of the system model shown in equation (25) are determined by α, a and b.

3.3. Identification of the fractional-order model

Suppose that the fractional-order system to be identified is described by equation (26)

$$G(s) = \frac{b}{s^\xi + a} \tag{26}$$

Known from the previous section, the system above can be approximated by the following state equation

$$\begin{aligned}\dot{x} &= A(\theta)x + B(\theta)u \\ y &= C(\theta)x\end{aligned} \tag{27}$$

where $\theta^T = \begin{bmatrix} \alpha & a & b \end{bmatrix}$, $A(\theta) = A_I^* - B_I^* C_I a$, $B(\theta) = B_I^*$ and $C(\theta) = bC_I$.

The key issue of identification is the estimation of the fractional order ξ in equation (26). A nonlinear identification method (Poinot and Trigeassou, 2004) is applied in this paper. Suppose that K pairs of input-output sampled data (u_k, y_k) have been obtained with t as the measuring time, T_e as the sampling period ($t = KT_e$) and y_k^* as the output measurement.

Define θ as the estimation of the model parameter vector. Then based on the parameter estimation θ and input signal u_k, the output estimation $\hat{y}_k$ can be obtained from equation (27) by software simulation. The deviation between the estimated output and actual output at each sampling point can be calculated by equation (28)

$$\varepsilon_k = y_k^* - \hat{y}_k(u, \theta) \tag{28}$$

where $k = 1, 2, \ldots, K$. The sum of square deviations can be obtained as an optimizing index with the data from all the sampling points

$$J(\theta) = \sum_{k=1}^{K} \varepsilon_k^2 \tag{29}$$

The optimal value of system parameters θ_{opt} can be obtained by minimizing the index J. For this purpose, Marquardt's algorithm (Marquardt, 1963) is applied for iterative calculation to get the optimized parameters. This algorithm ensures robust convergence, even with a bad initialization of θ, in the vicinity of the global optimum (Poinot and Trigeassou, 2004).

Marquardt's algorithm estimates the parameters iteratively by

$$\theta^{i+1} = \theta^i + (J_{\theta^i}^{\prime\prime} + \lambda I)^{-1} J_{\theta^i}^{\prime} \tag{30}$$

where θ^i and θ^{i+1} represent the parameter vectors obtained after i and $i+1$ iterative calculations, λ is a positive damping factor determining the step size of the iterative algorithm, I is a unit matrix, $J_{\theta^i}^{\prime}$ and $J_{\theta^i}^{\prime\prime}$ are described as,

$$J_{\theta^i}^{\prime} = \sum_{k=1}^{K} \varepsilon_k \sigma_{y_k, \theta^i} \tag{31}$$

$$J_{\theta^i}^{\prime\prime} = \sum_{k=1}^{K} \sigma_{y_k, \theta^i} \sigma_{y_k, \theta^i}^T \tag{32}$$

where σ_{y_k, θ^i} is the output sensitivity function defined as (Poinot and Trigeassou, 2004)

$$\sigma_{y_k, \theta^i} = \left.\frac{\partial \hat{y}_k}{\partial \theta}\right|_{\theta = \theta^i}, \quad k = 1, 2, \ldots, K \tag{33}$$

Introduce the state sensitivity function defined as (Poinot and Trigeassou, 2004)

$$\sigma_{x_k, \theta^i} = \left.\frac{\partial x_k}{\partial \theta}\right|_{\theta = \theta^i}, \quad k = 1, 2, \ldots, K \tag{34}$$

Assume that there are m parameters in θ, taking the derivative of equation (27) with respect to θ_l, where θ_l represents the $l-th$ parameter in θ, yields

$$\begin{aligned}\frac{\partial \dot{x}}{\partial \theta_l} &= \dot{\sigma}_{x, \theta_l} = A(\theta)\sigma_{x, \theta_l} + \frac{\partial A(\theta)}{\partial \theta_l}x + \frac{\partial B(\theta)}{\partial \theta_l}u \\ \frac{\partial y}{\partial \theta_l} &= \sigma_{y, \theta_l} = C(\theta)\sigma_{x, \theta_l} + \frac{\partial C(\theta)}{\partial \theta_l}x\end{aligned} \tag{35}$$

where $l = 1, 2, \ldots, m$. Taking the state x and input u as inputs in equation (27), $\sigma_{x, \theta l}$ as system states and $\sigma_{y, \theta l}$ as outputs, the state equations of $\sigma_{x, \theta l}$ can be obtained

$$\begin{aligned}\dot{\sigma}_{x, \theta_l} &= A(\theta)\sigma_{x, \theta_l} + \begin{bmatrix}\frac{\partial A(\theta)}{\partial \theta_l} & \frac{\partial B(\theta)}{\partial \theta_l}\end{bmatrix} \cdot \begin{bmatrix}x \\ u\end{bmatrix} \\ \sigma_{y, \theta_l} &= C(\theta)\sigma_{x, \theta_l} + \begin{bmatrix}\frac{\partial C(\theta)}{\partial \theta_l} & 0\end{bmatrix} \cdot \begin{bmatrix}x \\ u\end{bmatrix}\end{aligned} \tag{36}$$

where $l = 1, 2, \ldots, m$. The state sensitivity function and output sensitivity function at each sampling point can be calculated by solving the state equation of each $\sigma_{x, \theta l}$ using the *lsim* function in MATLAB.

Based on the principle mentioned above, the procedure of the algorithm is summarized as follows:

1. Select a group of parameters as the estimated ones, θ.

2. Calculate the system states x and outputs $\hat{y}(u,\theta)$ based on the sampled input u_k and estimated parameters using the *lsim* function in MATLAB.
3. Calculate the sum of square deviations J and judge whether the termination requirement is satisfied. If the variation of J is smaller than a pre-set threshold, terminate the iterative calculation and then go to Step 6. Otherwise, go to step 4.
4. Calculate the output sensitivity function at each sampling point by solving the state equations (See equation (36)) of its elements using the *lsim* function in MATLAB.
5. Calculate the new parameters using equation (30) and take them as the current estimated ones. Go back to step 2.
6. Present the parameters obtained in the last loop and end the process.

The initialization of parameters is crucial for the algorithm to allow the convergence to the global optimum. In order to avoid convergence to the local optimum, a variety of initial values of parameters should be tried and checked to see whether the algorithm could give better results. Each initial value is selected from the feasible region of each parameter vector, based on the expected value range of each parameter.

Suppose that the parameter vector to be identified is $\theta = (a,b)$, for instance, where $a_{min} \le a \le a_{max}$ and $b_{min} \le b \le b_{max}$. The value ranges of a and b can be plotted as a feasible region of θ in two-dimensional space as shown in Figure 5.

The feasible region of θ is divided into several subregions. Assume that there is no more than one local optimum in each sub-region, the initial parameter vectors θ are selected from each sub-region (located at the median point of the sub-region). Then the identification algorithm calculates the optimal parameter vectors from each initial parameter vector and the best one will be selected as the global optimum.

4. Fractional-order model identification of the PMSM speed servo system

Using a method combining mechanical modeling and numerical modeling, based on the fractional-order model of the PMSM obtained in Section 2, the identification method proposed in Section 3 is applied to a numerical approximation for the system parameters. The model of the PMSM is divided into two parts, the electromagnetic part and the mechanical part. Identification experiments of these two parts are performed respectively and the fractional-order model is obtained by combining the parameters obtained in each experiment.
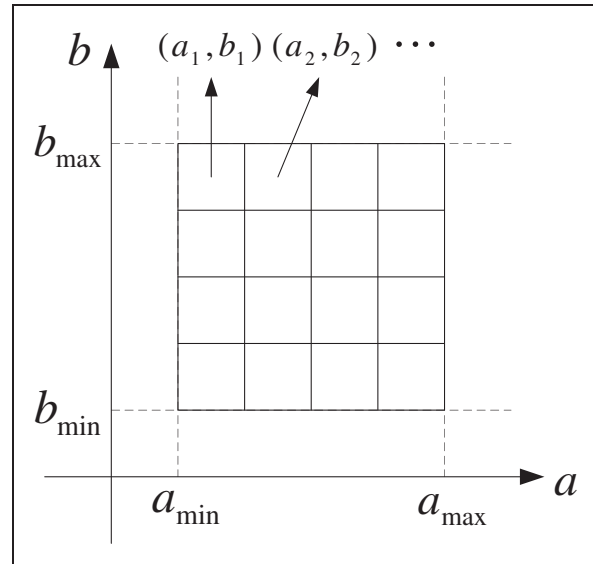

Figure 5. Selection of the initial parameters.

4.1. PMSM speed servo system platform introduction

The PMSM speed servo system platform is shown in Figure 6, where ASR is the speed controller and ACR is the current controller. Speed reference setting, speed control, current control, motor speed/angle calculation and space vector pulse width modulation (SVPWM) are all implemented in TMS320F2812 TI-digital signal processor (DSP). The details of this SVPWM control algorithm can be found in Luo et al. (2008).

The motor used in this platform is Sanyo-P10B18200BXS PMSM. The related parameters of this PMSM are listed in Table 1.

The equivalent DC motor control system of the PMSM is shown in Figure 7, where $C_v(s)$ is the speed controller, $C_i(s)$ is the current controller, K_0 is the voltage conversion factor, K_1 is the current conversion factor, K_2 is the speed conversion factor, R is the resistance, L is the inductor, C_m is the torque coefficient, GD^2 is the flywheel inertia and C_e is the induced electromotive force coefficient.

4.2. System identification excitation signal

The selection of input signal is one of the key issues affecting the identification result. Pseudo-random binary sequence (PRBS) is the most widely used as a system identification excitation signal because it can persistently excite the system to be identified with adjustable amplitude and period (Li, 1987). Besides, the PRBS can be generated simply and will not be disturbed by environmental changes. PRBS is selected to
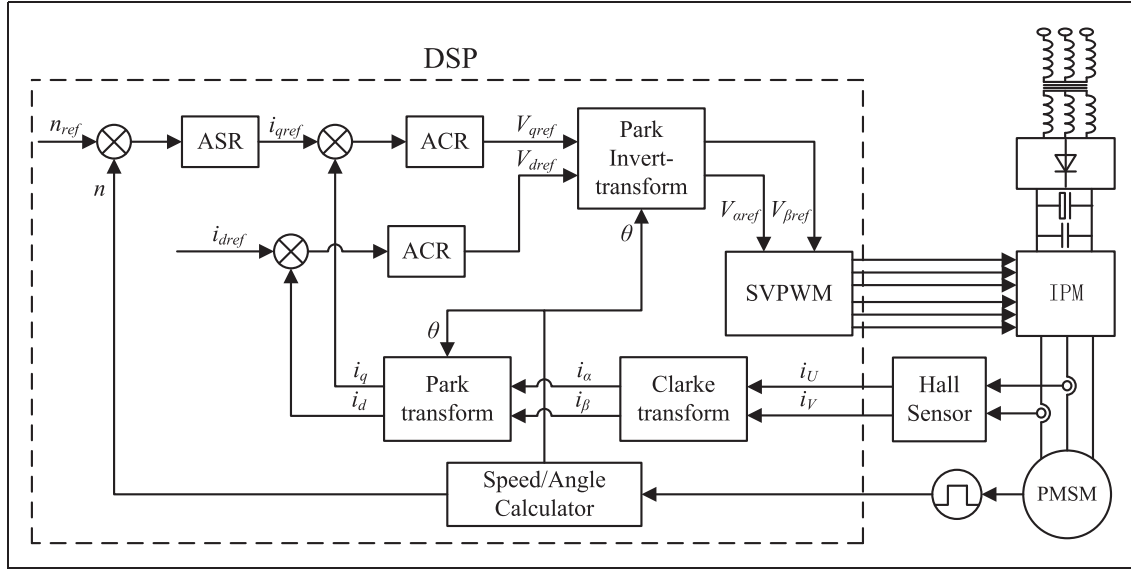
Figure 6. Space vector control system of the PMSM.

Table 1. Motor parameters.

Parameters	Symbol	Unit	Value
Rated power	P_R	kW	2.0
Rated speed	N_R	min^{-1}	2000
Rated torque	T_R	Nm	9.3
Rated current	I_R	A	9.5
Torque coefficient	C_m	Nm/A	1.32
Induced voltage coefficient	C_e	mV/min^{-1}	46.0
Phase resistance	R	Ω	0.5
Electrical time constant	t_e	ms	7.5
Mechanical time constant	t_m	ms	6.3
Number of poles	n_p	-	8
Moment of inertia	J_m	kgm^2	73.08×10^{-4}

be the input signal of the system identification in this paper.

4.3. Fractional-order model identification of the electromagnetic part

4.3.1. Model identification setup. If the motor speed n in equation (5) is zero during the sampling process, the back electromotive force will also be zero and the voltage equation can be described by equation (37)

$$u_q = Ri_q + L\frac{d^\vartheta i_q}{dt^\vartheta} \qquad (37)$$

In this way, the parameters of the electromagnetic part can be identified based on the sampled q-axis voltage and current. Therefore, the motor must be stationary

during the sampling process, which can be achieved by the magnetic positioning technique (Li and Pi, 2010).

The mathematical model of PMSM in a two-phase rotary coordinate ($d - q$ coordinate) is described as follows.

The flux equation

$$\begin{aligned} \varphi_d &= L_d i_d + \varphi_p \\ \varphi_q &= L_q i_q \end{aligned} \qquad (38)$$

the torque equation

$$T_e = 1.5n_p\big(\varphi_p i_q + (L_d - L_q)i_d i_q\big) \qquad (39)$$

and the mechanical equation

$$T_e = J\frac{d\omega}{dt} + T_L \qquad (40)$$

where φ_p is the flux of permanent magnet, i_d and i_q are an stator current components on the d- and q-axis respectively, L_d and L_q are the inductance of the PMSM on the d- and q-axis respectively, n_p is the number of pole pairs, J is the moment of inertia and T_L is the equivalent torque of the load. For a surface mounted PMSM, $L_q = L_d$, so the torque equation becomes

$$T_e = 1.5n_p\varphi_p i_q \qquad (41)$$

Based on the principle of SVPWM control (Luo et al., 2008), the direction of the d-axis is set to be the direction of the rotor flux vector and the q-axis is set at the vertical direction of the d-axis. During the rotation
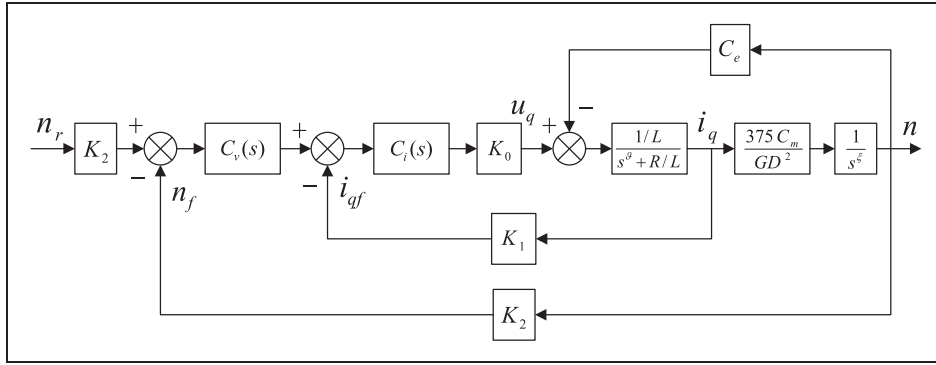
Figure 7. Equivalent DC control system of the PMSM fractional-order model.
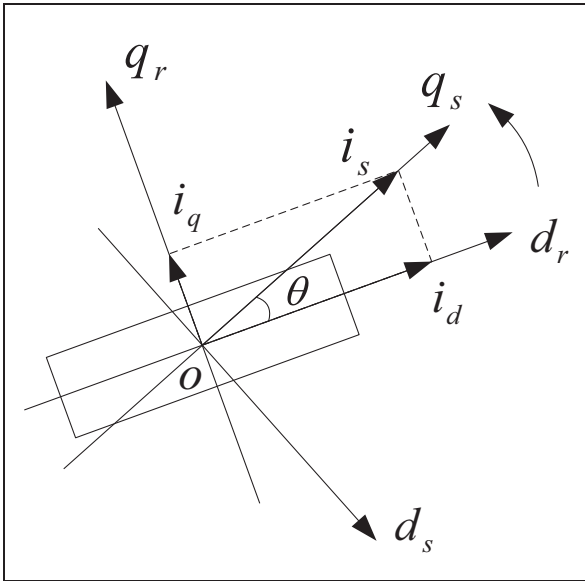

Figure 8. Decomposition of i_s.

of the rotor, the DSP calculates the rotation angle and rotor speed based on the optical encoder feedback.

Now suppose that the d-q coordinate in the DSP is fixed by the servo program, represented by the d_s-axis and the q_s-axis in Figure 8, while the "actual coordinate", synchronized with the rotor flux, is represented by the d_r-axis and the q_r-axis. Suppose that the stator coil is imported with a current vector with constant magnitude (i_s) and direction (points to the direction of the q_s-axis), as shown in Figure 8, a static circular magnetic field will be generated in the motor space.

Suppose that the rotor is originally stationary. From the actual coordinate (d_r-q_r coordinate) point of view, when the stator current is imported, it becomes

$$i_d = i_s \cos \theta$$
$$i_q = i_s \sin \theta \qquad (42)$$

Thus, without load, the mechanical equation is obtained

$$T_e = 1.5 n_p \varphi_p i_s \sin \theta = J \frac{d\omega}{dt} \qquad (43)$$

Since n_p, φ_p and i_s are constant, the direction of torque is determined by the angle, θ, between the current vector and the rotor flux. If $0 < \theta \leq \pi$, then $T_e > 0$, the rotor will rotate counterclockwise, if $-\pi \leq \theta < 0$, then $T_e < 0$, the rotor will rotate clockwise, if $\theta = 0$, then $T_e = 0$ and the rotor will not rotate.

Based on this principle, the experimental scheme can be confirmed. Before the sampling process, a current vector with constant magnitude (i_s) and direction (θ) is imported into the stator coil. Then the rotor flux direction axis (d_r-axis) will be dragged close to the current vector i_s direction axis, as shown in Figure 8. After a tiny oscillation, the rotor will eventually stop and stay at the position corresponding to the current vector, as shown in Figure 9. Then the PRBS is imported into the q_s-axis input voltage, with the d_s-axis voltage remaining at zero. The motor speed will be zero in the subsequent experiment.

The electromagnetic part is an inertia part as shown in Figure 10, under the condition that the rotor speed is always zero. In Figure 10, K_0 represents the conversion factor from the per-unit value of the q_s-axis stator voltage u_{qs} to its actual value u_q, K_1 represents the conversion factor from the actual q_s-axis current i_q to its per-unit value i_{qf} in the DSP. During the sampling process, the q_s-axis current is with open-loop control. The q_s-axis stator voltage u_{qs} and current i_{qf} are sampled respectively. The PRBS is imported into the q_s-axis stator voltage u_{qs} after the rotor stops and the q-axis current reaches a relative steady value (the current may not be strictly steady because it is achieved without current closed-loop control). The parameters of the electromagnetic part are identified applying the identification method proposed in Section 3, with the q_s-axis
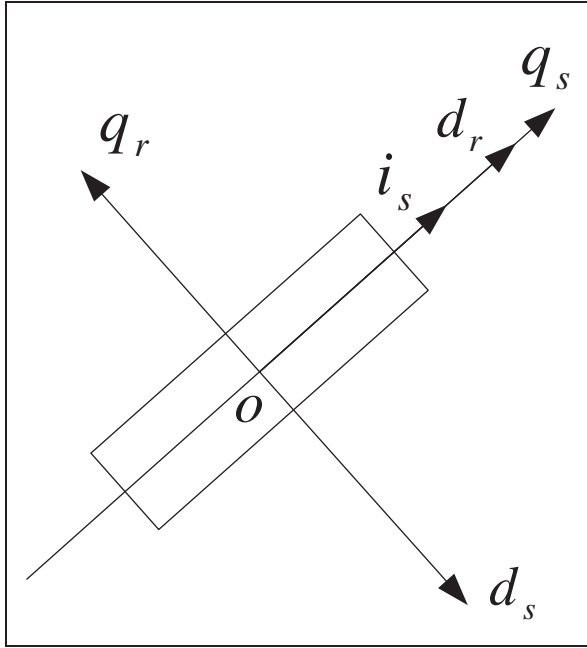
Figure 9. Positioning of the rotor flux.

stator voltage being taken as the input signal and the q_s-axis current as the output signal.

4.3.2. Identification procedure. Based on the principle mentioned in the previous section, the model identification procedure is presented as follows:

1. Disconnect the speed loop and set the rotation angle of the rotor to be a constant value. Set the q-axis input voltage to be a small constant (0.1 per unit value) and the d-axis input voltage to be zero in the servo program.
2. Sample the q-axis stator voltage and the q-axis feedback current.
3. Set the q-axis input voltage to be the PRBS and keep the d-axis input voltage as zero.
4. Applying the identification method proposed in Section 3, identify the model parameters using MATLAB software based on input-output data.

4.3.3. Identification experiment. The current conversion factor K_1 in Figure 10 can be obtained based on the design of the servo drive. The stator current of the motor is measured with a Hall sensor and then converted into the input voltage signal of the DSP's A/D conversion module. The input voltage of the DSP's A/D conversion pin is described by equation (44)

$$u_i = 1.5 + 0.025i_p \tag{44}$$
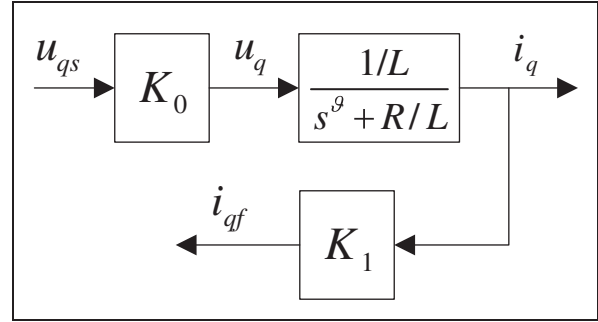
Figure 10. Block diagram of the electromagnetic part modeling.

where i_p represents the actual stator current of the motor. The input voltage range of the A/D conversion pin of DSP is $0 - 3V$, namely, $0\,V \leq u_i \leq 3\,V$. Thus

$$0 \leq 1.5 + 0.025i_p \leq 3 \tag{45}$$

The analog input voltage is then converted into digital value by the A/D conversion module in DSP. Then the per-unit value of current i_f in the DSP is calculated by equation (46)

$$i_f = \frac{2}{3}u_i - 1 \tag{46}$$

Substituting u_i with its representation shown in equation (44), it becomes

$$i_f = \frac{2}{3}(1.5 + 0.025i_p) - 1 = \frac{1}{60}i_p \tag{47}$$

Equation (47) shows the relationship between the actual stator current i_p and its per-unit value i_f in DSP. So the value of the current conversion factor is $K_1 = 1/60$. Therefore, the actual q-axis current can be obtained by

$$i_q = \frac{1}{K_1}i_{qf} = 60i_{qf} \tag{48}$$

The conversion factor K_0 can be obtained by motor experiments in open-loop. Consider the voltage equation

$$u_q = K_0 u_{qs} = Ri_q + L\frac{d^{\vartheta}i_q}{dt^{\vartheta}} + C_e n \tag{49}$$

If u_{qs} is a constant value and the motor operates with a constant load, the q-axis current and motor speed will eventually reach stable states. Therefore, the term
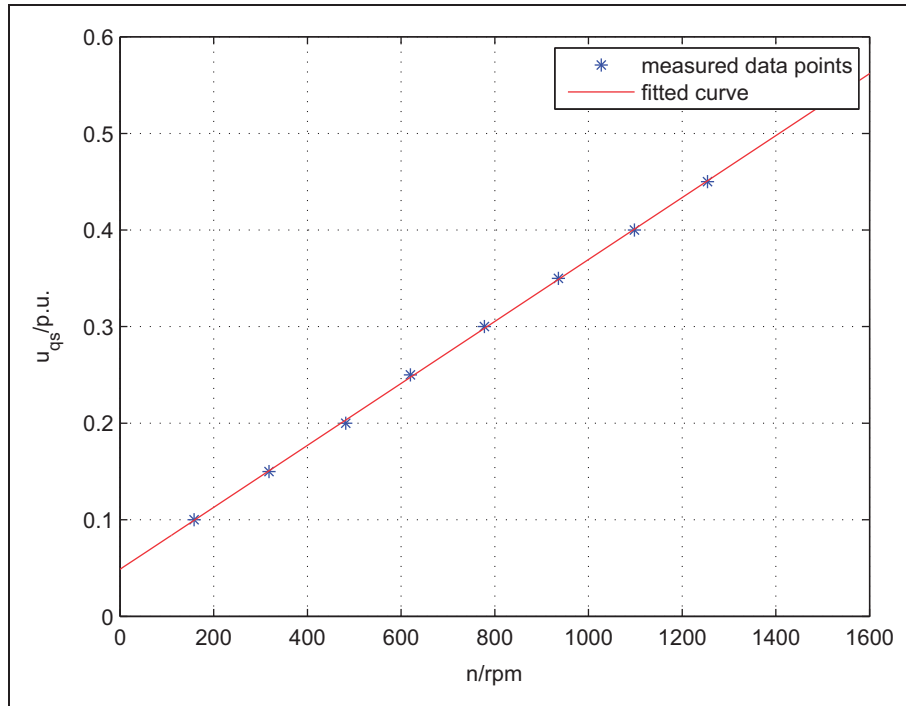
Figure 11. Quantitative relation between u_{qs} and n.

$Ri_q + L\frac{d^\vartheta i_q}{dt^\vartheta}$ can be approximated to a constant. In this way, the voltage equation can be written as

$$u_{qs} = \frac{C_e}{K_0}n + const \tag{50}$$

The value of K_0 can be calculated by measuring u_{qs} and n and confirming their quantitative relation.

Eight pairs of (u_{qs},n) are measured and plotted as data points in Figure 11. The quantitative relation between u_{qs} and n is obtained by fitting the data points using the least square method. The obtained relation can be described by equation (51), which is also plotted as a red line in Figure 11

$$u_{qs} = 0.0003207\text{n} + 0.0487 \tag{51}$$

Therefore, $\frac{C_e}{K_0} = 0.0003207$. According to the motor datasheet, $C_e = 0.046$, then it gives $K_0 = 143.41$. The actual q-axis voltage can be obtained by

$$u_q = K_0 u_{qs} = 143.41 u_{qs} \tag{52}$$

Taking u_q as the input signal and n as the output signal, the transfer function of the electromagnetic part is described by equation (53)

$$G_1(s) = \frac{i_q}{u_q} = \frac{1/L}{s^\vartheta + R/L} \tag{53}$$

For the integer-order model, the order of ϑ is 1, only the inductance L and the resistance R need to be identified. For the fractional-order model, the inductance L, the resistance R and the fractional-order ϑ need to be identified.

1024 pairs of input-output data are sampled, with the sampling period $T_s = 0.0005\,\text{s}$. The frequency band in which the filter needs to approximate the fractional operator is $(0.01\,\text{rad/s}, 10,000\,\text{rad/s})$. The order of the filter determines the accuracy of the approximated fractional operator: the higher the order, the higher the accuracy. However, the calculation time is also longer. Therefore, to balance the accuracy and efficiency, the order is set to be 9, namely, $2N+1=9$, which is time-saving and enough for precise identification.

The sampled q-axis input voltage is shown in Figure 12. The sampled q-axis current is shown in Figure 13.

The reference model of the identification method mentioned in Section 3 is described by equation (26). Taking the transfer function of the electromagnetic part (equation (53)) into account, gives $a = R/L$, $b = K_0/L$ and $\xi = \vartheta$. The order ξ is represented by variable α in the algorithm (See equation (14)). During the identification of the fractional-order model, ξ is updated in every iteration. In contrast, ξ is fixed to be 1 during the identification of the integer-order model. In order to improve the accuracy of the identification results, calculations are performed from $t = 0\,\text{s}$ to obtain the simulation outputs, but only the output data from $t = 0.1\,\text{s}$ are used in the identification algorithm. The iterative
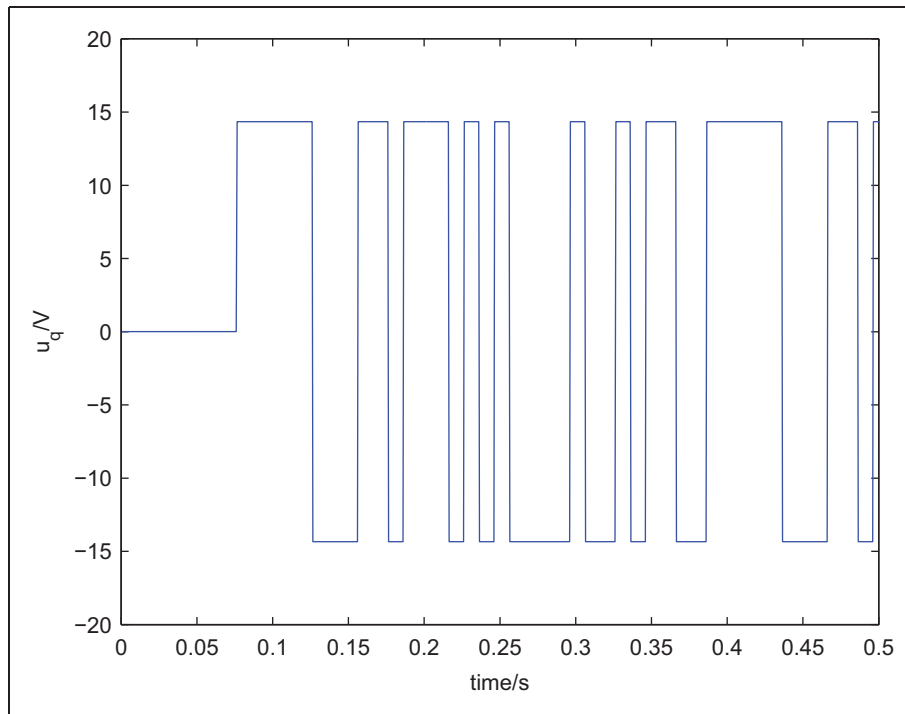
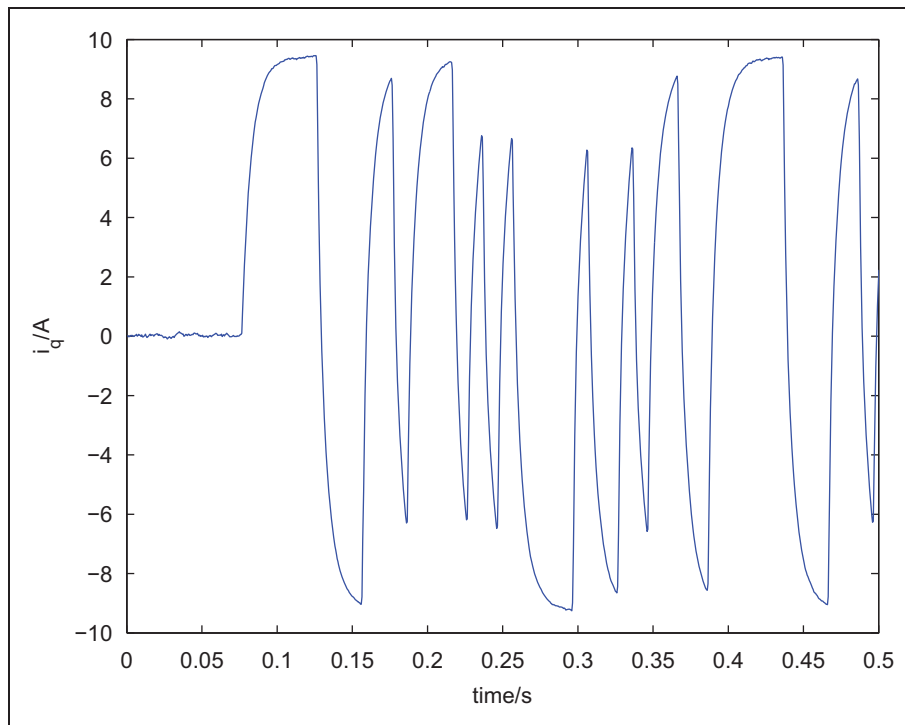**Figure 12.** The *q*-axis input voltage.
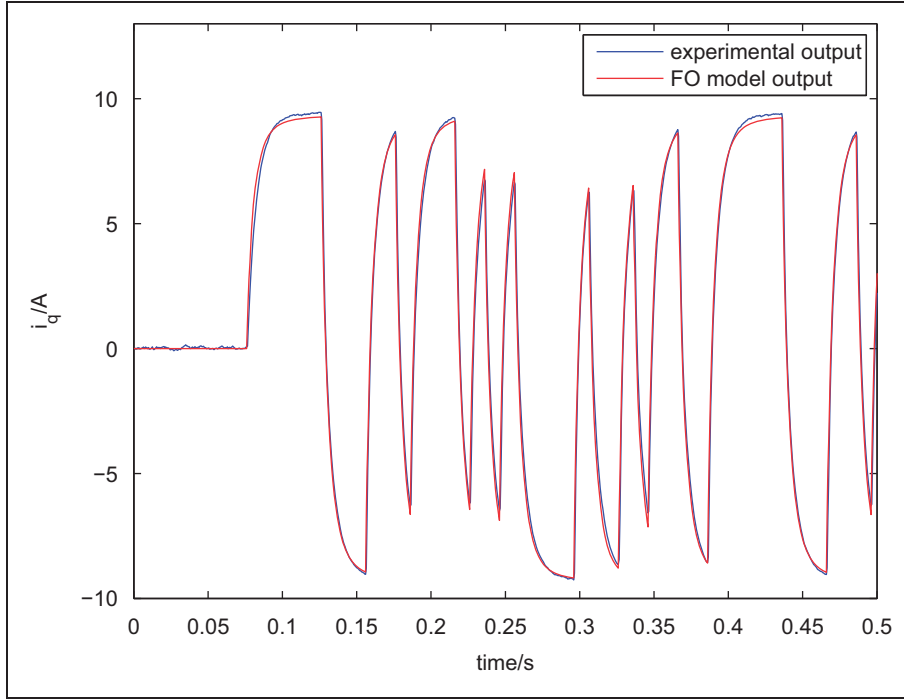

Figure 13. The *q*-axis current.

Figure 14. The estimated and actual result of the *q*-axis current for fractional-order model.

calculation will be terminated when the variation of *J* is smaller than 0.0001, which means the parameters converge to their stable values.

Using the identification method proposed in Section 3, the parameters of the fractional-order model are obtained, $\xi = 0.9081$, $a = 127.3803$ and $b = 83.6368$. The optimal sum of square deviations, *J* is 21.9403. Then it gives $\vartheta = 0.9081$, $L = 11.956$ mH and $R = 1.52$ Ω. The fractional-order model of electromagnetic part is

$$G_{1f}(s) = \frac{1/L}{s^{\vartheta} + R/L} = \frac{83.6368}{s^{0.9081} + 127.3803} \quad (54)$$

Simulation is performed based on the obtained fractional-order model of the electromagnetic part, taking the *q*-axis stator voltage samples as the input signal. The estimated result of the *q*-axis current and the actual *q*-axis current samples are showed in Figure 14, where the red curve represents the simulation output and the blue curve represents the actual output.

The parameters of the integer-order model are obtained, $a = 223.6513$ and $b = 136.4613$. The optimal sum of square deviations, *J* is 102.3944. Then it gives $L = 7.328$ mH and $R = 1.639$ Ω. The integer-order model of electromagnetic part is

$$G_{1i}(s) = \frac{1/L}{s + R/L} = \frac{136.4613}{s + 223.6513} \quad (55)$$

Simulation is performed based on the obtained integer-order model of the electromagnetic part, taking the *q*-axis stator voltage samples as the input signal. The estimated result of the *q*-axis current and the actual *q*-axis current samples are showed in Figure 15, where the red curve represents the simulation output and the blue curve represents the actual output.

Comparing Figures 14 and 15, and the sum of square deviations of two identification experiments, the conclusion is that the simulation output of the fractional-order model is closer to the experimental output than that of the integer-order model, the fitting effect of the fractional-order model is better than that of the integer-order model.

4.4. Fractional-order model identification of the mechanical part

4.4.1. Model identification setup. The block diagram of the mechanical part (marked in solid lines) is shown in Figure 16, where u_{qr} is the per-unit value of the *q*-axis stator voltage and u_q is its actual value, i_q is the *q*-axis stator current and i_{qf} is its per-unit value in DSP, and K_2 represents the conversion factor from the speed of motor *n* to its per-unit value n_f in DSP. During the experiment, the *d*-axis input voltage is zero while the *q*-axis current loop and speed loop are disconnected.

At first, the *q*-axis input voltage is set to be a constant. The *q*-axis current i_{qf1} and rotor speed n_{f1} are
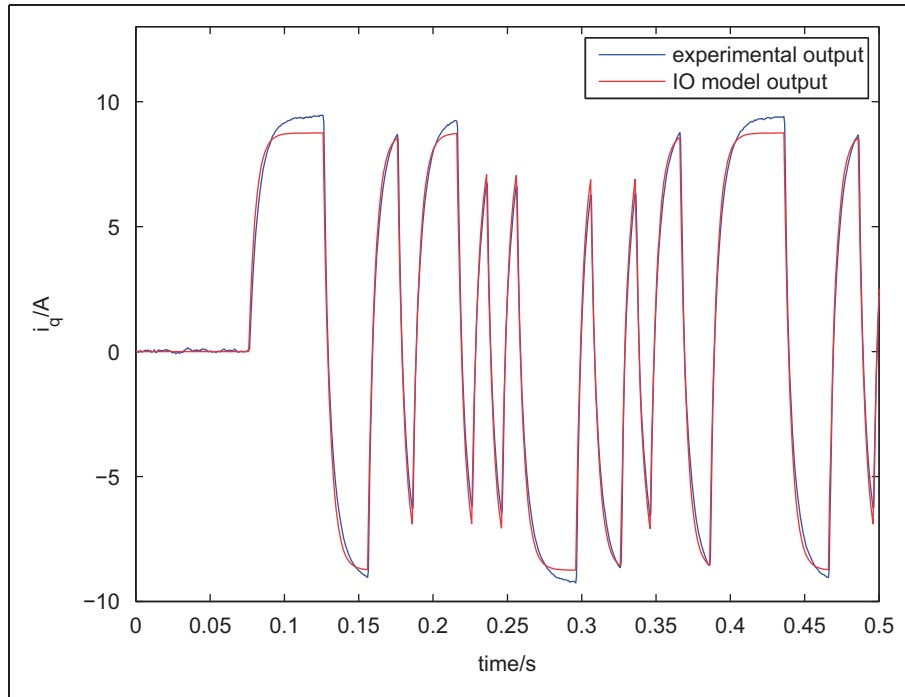
Figure 15. The estimated and actual result of the *q*-axis current for integer-order model.
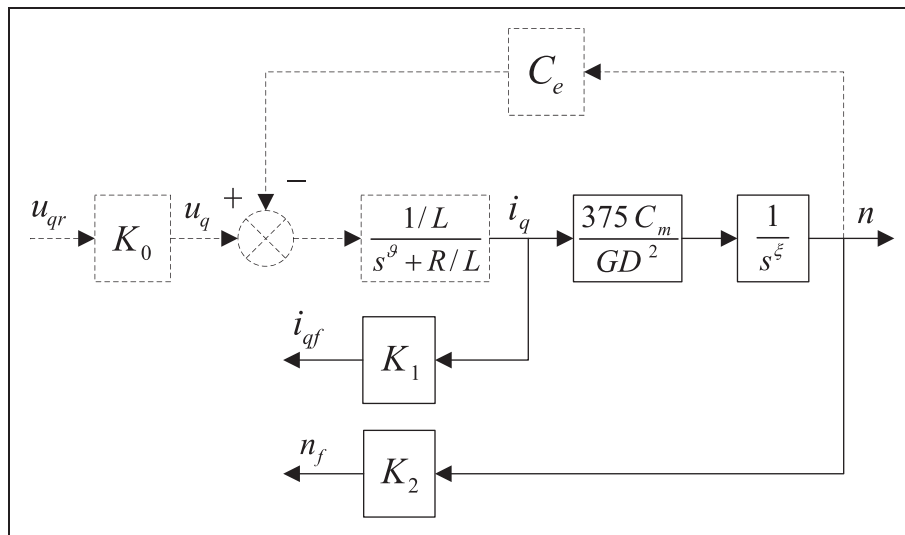

Figure 16. Block diagram of the mechanical part modeling.

sampled respectively. When the rotor speed reaches a relatively steady state (the speed may not be strictly steady because it is achieved without current and speed closed-loop control), PRBS is added into the *q*-axis input voltage. The sampled *q*-axis current can be divided into two components, one is generated by the DC component (constant) of the *q*-axis voltage, while the other is generated by the PRBS. Only the latter component is used for identification. Similarly,

the motor speed can also be divided into two components, one is generated by the DC component of the *q*-axis current (generated by the DC component of *q*-axis voltage), while the other is generated by the AC component of the *q*-axis current (generated by the PRBS). Only the latter component is used for identification. In order to obtain the components only generated by the PRBS, another process needs to be performed. The *q*-axis input voltage should be set to be constant (equal to

the value in the previous process) again. Then the q-axis current i_{qf2} and rotor speed n_{f2} are sampled respectively. This time, the q-axis current is generated by the constant q-axis voltage. The motor speed is generated by the q-axis current obtained in this process. The q-axis current, i_{qf}, only generated by the PRBS is obtained by

$$i_{qf} = i_{qf1} - i_{qf2} \tag{56}$$

The motor speed, n_f, only generated by the q-axis current generated by the PRBS is obtained by

$$n_f = n_{f1} - n_{f2} \tag{57}$$

Then the parameters of the mechanical part are identified applying the identification method proposed in Section 3, with the q-axis current i_q being taken as the input signal and the rotor speed n as the output signal.

4.4.2. Identification procedure. Based on the principle mentioned in the previous section, the experimental steps are confirmed as follows.

1. Disconnect the q-axis current loop and speed loop. Set the rotation angle of the rotor to be the value calculated based on the pulse signal transmitted by the optical encoder.
2. Set the d-axis voltage to be zero and the q-axis voltage to be a small constant (0.3 per-unit value). Sample the q-axis current and the rotor speed.
3. Perform step 2 again. When the motor current reaches a steady state, add the PRBS into the q-axis voltage.
4. Remove the DC components contained in the q-axis current by subtracting the q-axis current obtained in step 2 from that obtained in step 3. Remove the DC components contained in the motor speed by subtracting the motor speed obtained in step 2 from that obtained in step 3.
5. Applying the identification method proposed in Section 3, identify the model parameters using MATLAB software based on input-output data.

4.4.3. Identification experiment. The speed feedback coefficient K_2 can be obtained based on the motor parameters shown in Table 1. The rated motor speed is 2000 rpm, whose corresponding per-unit value in DSP is 1. Therefore, K_2, the conversion factor from actual speed value to per-unit value, is 1/2000.

Taking i_q as the input signal and n as the output signal, the transfer function of the mechanical part is described by equation (58)

$$G_2(s) = \frac{n}{i_q} = \frac{375C_m}{GD^2 s^\xi} \tag{58}$$

For the integer-order model, the order ξ is 1, only the term $\frac{375C_m}{GD^2}$ needs to be identified. For the fractional-order model, both the order ξ and the term $\frac{375C_m}{GD^2}$ need to be identified.

1024 pairs of input-output data are sampled, with the sampling period $T_s = 0.005\,\text{s}$. The frequency band in which the filter needs to approximate the fractional operator is (0.01 rad/s, 10, 000 rad/s). To balance the accuracy and efficiency, the order of the filter is also set to be 9.

The q-axis stator voltage is shown in Figure 17. The q-axis current, i_{q1}, generated by both the constant voltage and the PRBS, and i_{q2} generated only by the constant component of u_q, is shown in Figure 18.

The actual q-axis current i_q, only generated by the PRBS is obtained by equation (59)

$$i_q = i_{q1} - i_{q2} \tag{59}$$

The q-axis current i_q is shown in Figure 19.

The motor speeds n_1 generated by i_{q1}, and n_2 generated by i_{q2} are shown in Figure 20. The motor speed only generated by the AC component of the q-axis current (generated by the PRBS) is obtained by equation (60)

$$n = n_1 - n_2 \tag{60}$$

The motor speed n is shown in Figure 21.

The reference model of identification method mentioned in Section 3 is described by equation (26). Taking the transfer function of the mechanical part (equation (58)) into account, it gives $a = 0$ and $b = \frac{375C_m}{GD^2}$. The order ξ is represented by variable α in the algorithm. In the parameter vector, a is fixed to be zero. During the identification of the fractional-order model, ξ is updated in every iteration. In contrast, ξ is fixed to be 1 during the identification of the integer-order model. In order to improve the accuracy of identification results, calculations are performed from $t = 0\,\text{s}$ to obtain the simulation outputs, but only the output data from $t = 1.5\,\text{s}$ are used in the identification algorithm. The iterative calculation will be terminated when the variation of J is smaller than 0.0001.

Using the identification method proposed in Section 3, the system parameters of the fractional-order model are obtained, $\xi = 1.0463$ and $b = 1033.084$. The optimal sum of square deviations, J is 5087.6517. Then the fractional-order model of the mechanical part is

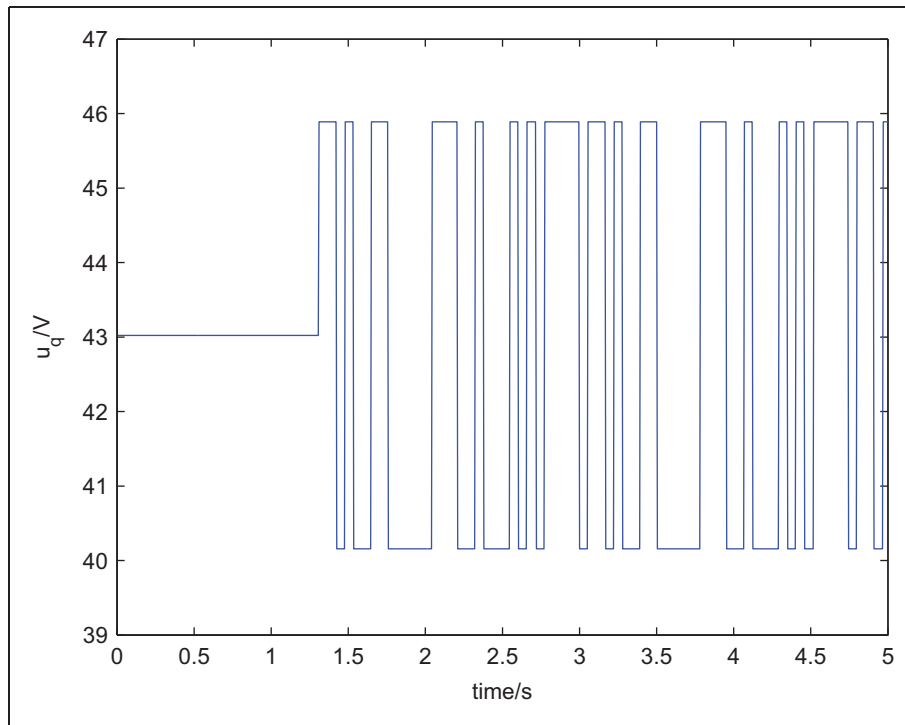$$G_{2f}(s) = \frac{375C_m}{GD^2 s^\xi} = \frac{1033.084}{s^{1.0463}} \tag{61}$$
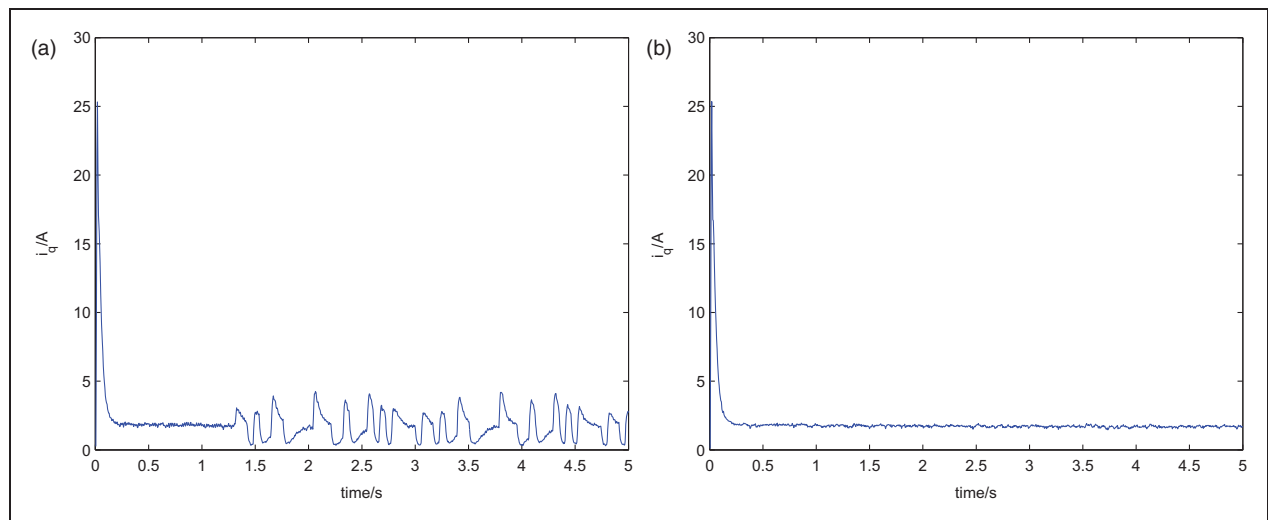
Figure 17. The *q*-axis stator voltage.

Figure 18. The *q*-axis currents, i_{q1} and i_{q2}. (a) q-axis current i_{q1}. (b) q-axis current i_{q2}.

Simulation is performed based on the obtained fractional-order model of the mechanical part, taking the *q*-axis stator current samples as the input signal. The estimated result of the motor speed and the actual motor speed samples are showed in Figure 22, where the red curve represents the simulation output and the blue curve represents the actual output.

The system parameters of the integer-order model are obtained, $b = 925.8358$. The optimal sum of square deviations, J is 15708.4198. Then the integer-order model of the mechanical part is

$$G_{2i}(s) = \frac{375 C_m}{GD^2 s} = \frac{925.8358}{s} \tag{62}$$

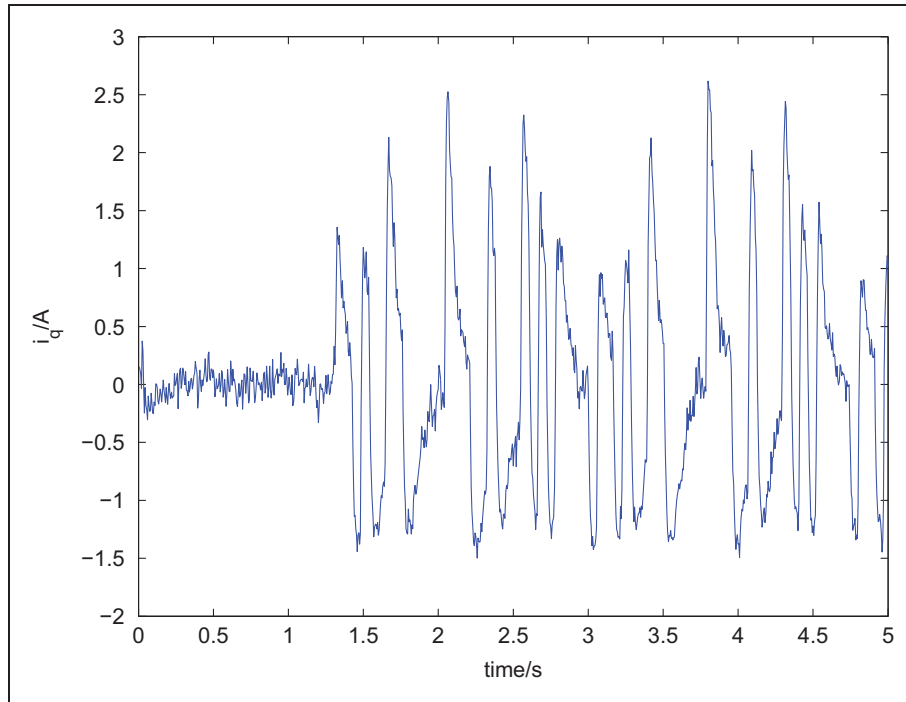Simulation is performed based on the obtained integer-order model of the mechanical part, taking the

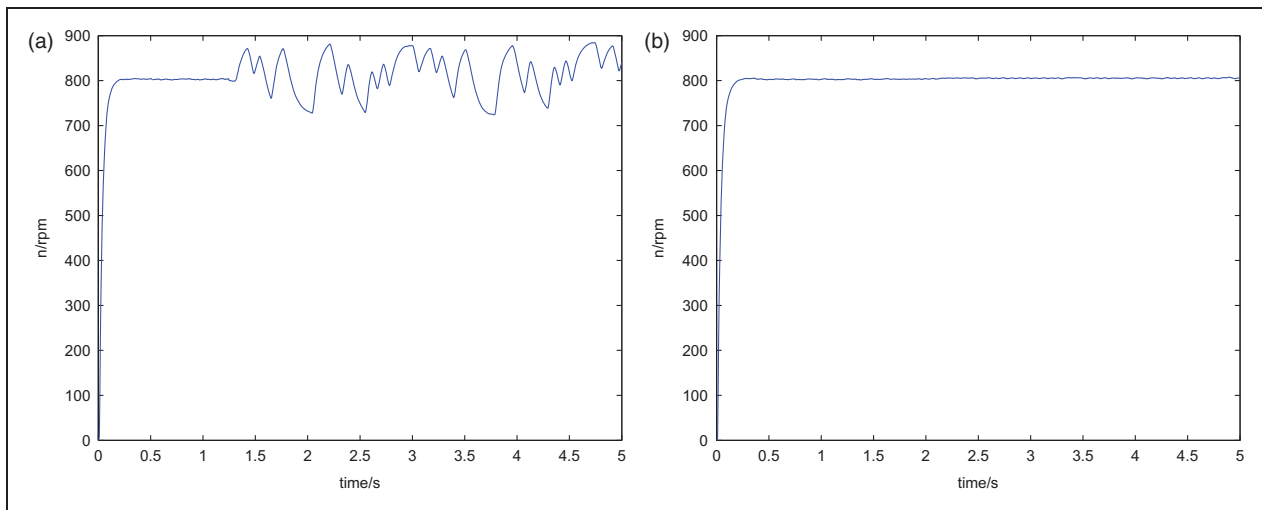**Figure 19.** The *q*-axis current, i_q.

Figure 20. Motor speeds n_1 and n_2. (a) Motor speed n_1. (b) Motor speed n_2.

q-axis stator current samples as the input signal. The estimated result of the motor speed and the actual motor speed samples are showed in Figure 23, where the red curve represents the simulation output and the blue curve represents the actual output.

Comparing Figures 22 and 23, and the sum of square deviations of two identification experiments, the conclusion is that the simulation output of the fractional-order model is closer to the experimental output than that of the integer-order model, the fitting effect of the

fractional-order model is better than that of the integer-order model.

5. Verification of the PMSM fractional-order model

5.1. Experimental platform

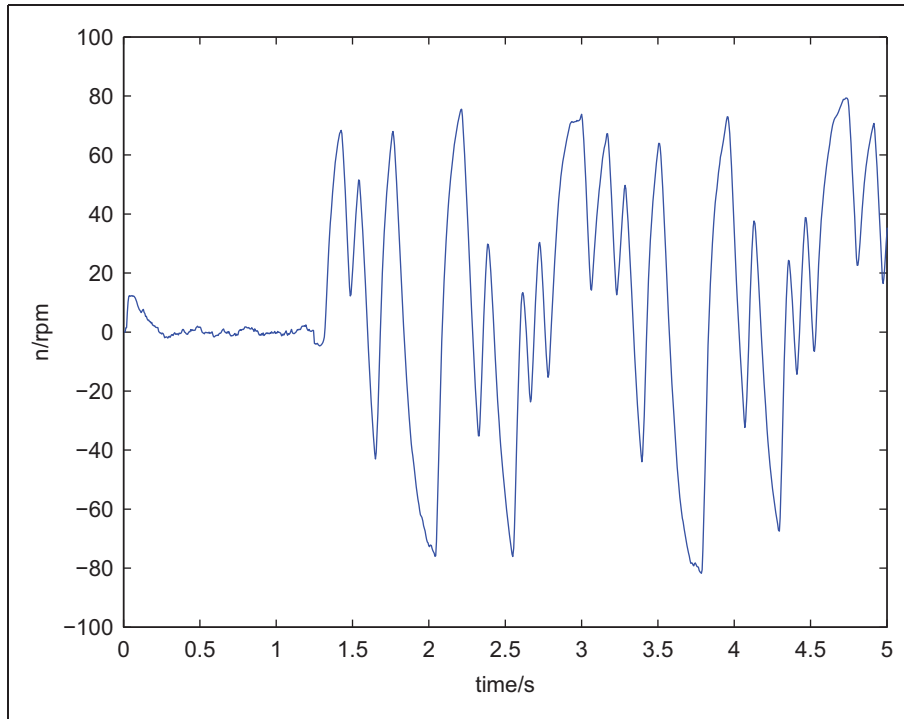The PMSM speed-control platform is shown in Figure 24. The motor to be used is the
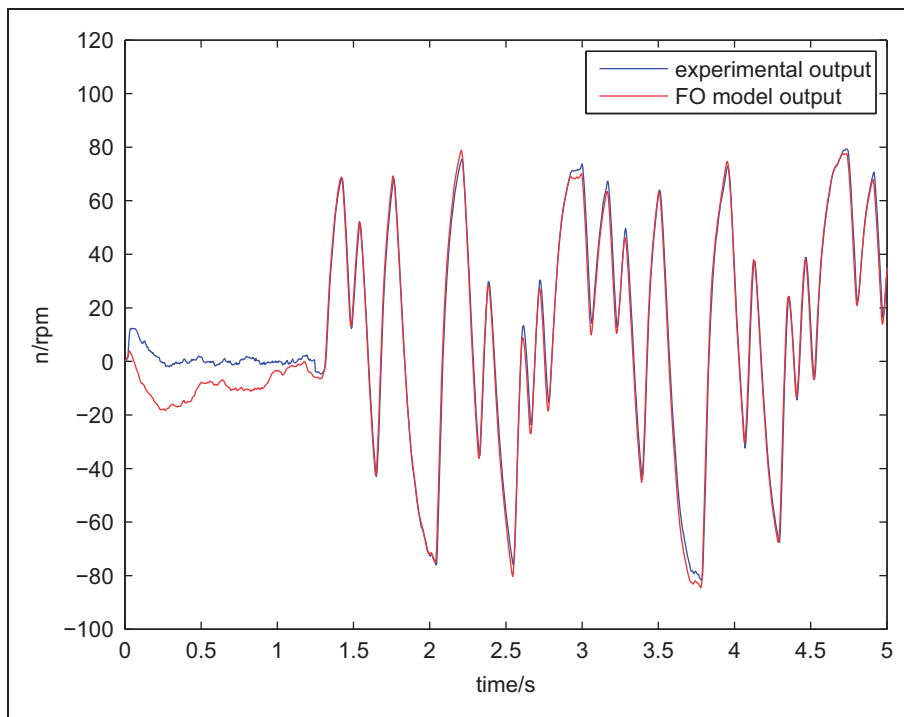
Figure 21. Motor speed *n*.

Figure 22. Estimated and actual result of the motor speed for the fractional-order model.
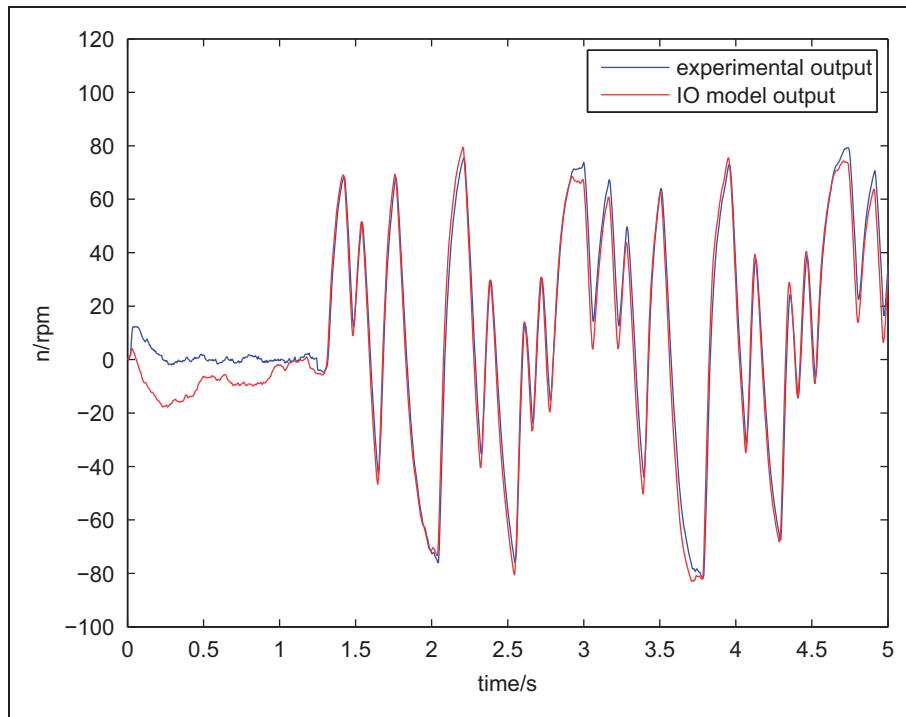
Figure 23. Estimated and actual result of the motor speed for the integer-order model.
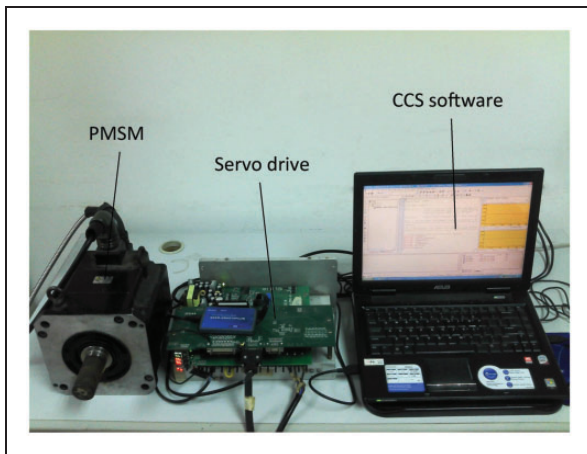

Figure 24. The PMSM speed-control platform.

Sanyo-P10B18200BXS PMSM. The servo drive is laboratory-made and the DSP used in the control board is TMS320F2812 TI-DSP. The software platform used on the PC is the Code Composer Studio (CCS) developed by Texas Instruments. The PC is connected with servo drive through an emulator, controlling the motor to operate.

5.2. Model verification setup

The deviation between the simulation output and experimental output reflects the accuracy of the mathematical

model of an actual system. Suppose that two models have been established for an actual system. Simulations and experiments are then performed based on these two models under equal conditions. If the deviation between the simulation output and experimental output of one model is smaller than that of another, it means that the former one is closer to the characteristics of the actual system. Now suppose that simulations and experiments are performed respectively, based on the integer-order model and fractional-order model of the PMSM. If the deviation between the experimental output and simulation output of the fractional-order system is smaller than that of the experimental output and simulation output of the integer-order system, it means the fractional-order model is closer to the intrinsic characteristics of the PMSM than the integer-order model. The rationality of the fractional-order model is then demonstrated. Based on this assumption, model verification experiments are performed in open-loop and closed-loop respectively.

5.3. Model verification based on open-loop response

The transfer function of the PMSM (see Figure 1) can be described by equation (63)

$$G(s) = \frac{\frac{375C_m}{GD^2L}}{s^{\vartheta+\xi} + \frac{R}{L}s^{\xi} + \frac{375C_mC_e}{GD^2L}} \tag{63}$$
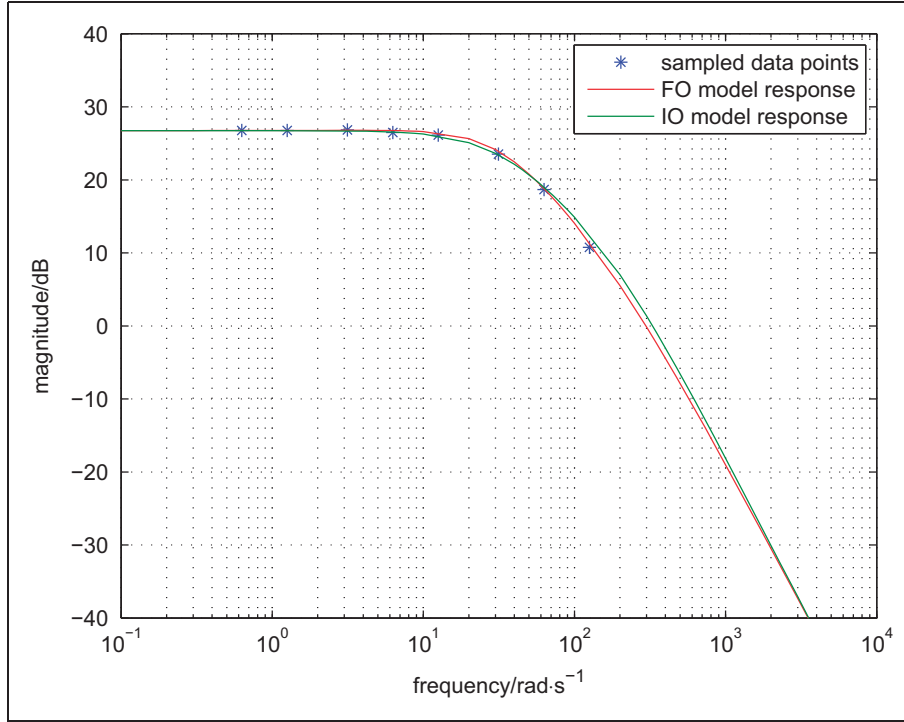
Figure 25. Magnitude-frequency characteristic.

Based on the identification results in Section 4, the fractional-order model of the PMSM is

$$G_f(s) = \frac{86405.3895}{s^{1.9544} + 127.3803s^{1.0463} + 3974.6479} \quad (64)$$

The integer-order model is

$$G_i(s) = \frac{126340.7569}{s^2 + 223.6513s + 5811.674} \quad (65)$$

Open-loop frequency response experiments are performed on the PMSM, taking u_q as input signal and n as output signal. Eight groups of (ω, A, ϕ) are measured and plotted as data points in a magnitude-frequency characteristic figure (Figure 25) and a phase-frequency characteristic figure (Figure 26).

The magnitude-frequency characteristics and phase-frequency characteristics of the fractional-order and integer-order models of PMSM are also plotted in Figures 25 and 26 respectively, where the red curves represent the characteristics of the fractional-order model and the green curves represent those of the integer-order model. Figure 25 shows that the magnitude-frequency characteristics of two models are close to each other. Figure 26 shows that the phase-frequency characteristics of two models show differences in the middle- and high-frequency range. Specifically, the characteristics of the fractional-order model is closer

to the actual characteristics of the PMSM than that of the integer-order model.

5.4. Model verification based on closed-loop response

If the current controller in Figure 7 is set to be $C_i(s) = 1$ and the speed feedback is converted into a unit feedback system, the PMSM speed-control system can be simplified as shown in Figure 27.

In Figure 27, $G_s(s)$ is the open-loop transfer function of the speed system, which can be described by equation (66)

$$G_s(s) = \frac{K_2 K_0 \frac{375 C_m}{GD^2 L}}{s^{\vartheta + \xi} + \frac{R + K_1 K_0}{L} s^{\xi} + \frac{375 C_m C_e}{GD^2 L}} \quad (66)$$

Using the parameters obtained in Section 4, the fractional-order transfer function is

$$G_{sf}(s) = \frac{6195.698}{s^{1.9544} + 327.2898s^{1.0463} + 3974.6479} \quad (67)$$

The integer-order transfer function is

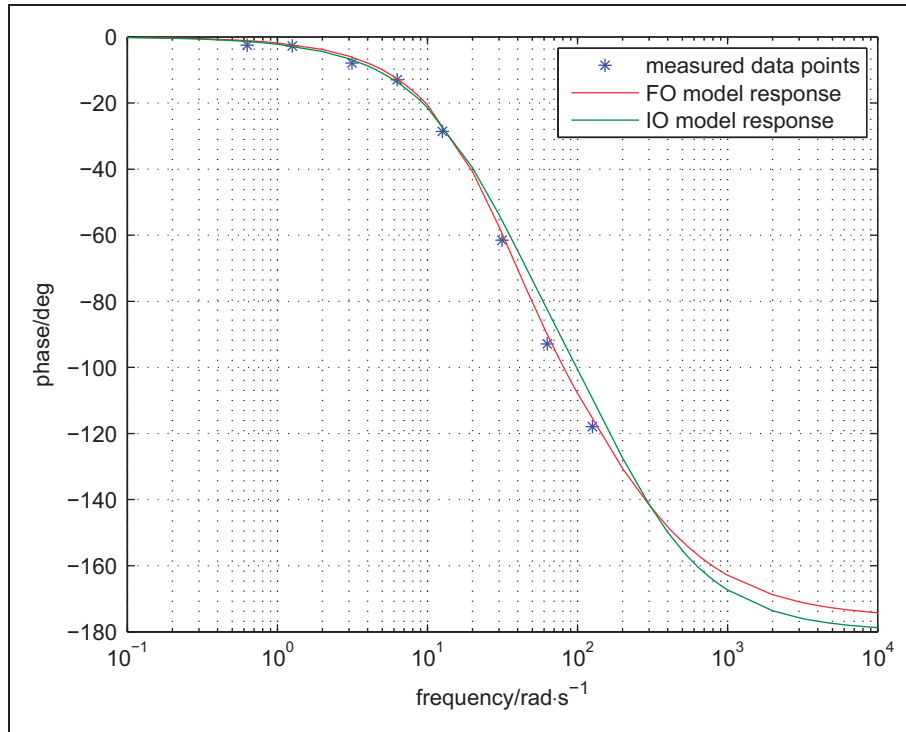$$G_{si}(s) = \frac{9059.264}{s^2 + 549.8166s + 5811.674} \quad (68)$$

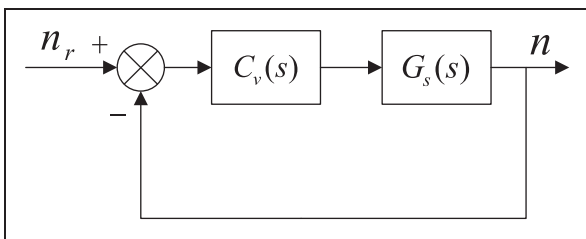**Figure 26.** Phase-frequency characteristic.

Figure 27. Simplified diagram of the PMSM speed control system.

In order to verify the proposed fractional-order model, three groups of PI controllers are designed applying the gain crossover frequency and phase margin specifications, based on the obtained fractional-order and integer-order models. Then the closed-loop speed-tracking simulations are performed, using the controllers designed for the fractional-order model to control the fractional-order model, and those for the integer-order model to control the integer-order model. Closed-loop speed-tracking experiments are also performed on the PMSM control platform using these controllers to control the PMSM. Taking the integral of absolute deviations as the criterion

$$J = \int_0^{t_s} |n_e(t) - n_s(t)| dt \qquad (69)$$

where n_e represents the experimental output, n_s represents the simulation output and t_s represents the simulation time, the simulation outputs of two models are then compared with their corresponding experimental outputs to clarify the advantage of the fractional-order model.

The PI controller has the form shown in equation (70)

$$C(s) = K_p\left(1 + \frac{K_i}{s}\right) \qquad (70)$$

The PI controller is designed based on the following gain crossover frequency and phase margin specifications (Xue at el., 2006)

$$|C(\omega_c)G(\omega_c)| = 1 \qquad (71)$$

$$Arg[C(\omega_c)G(\omega_c)] = -\pi + \varphi_m \qquad (72)$$

where ω_c represents the gain crossover frequency and φ_m represents the phase margin.

The gain and phase of the PI controller are

$$|C(\omega)| = K_p\sqrt{1 + \frac{K_i^2}{\omega^2}} \qquad (73)$$

$$Arg[C(\omega)] = -\tan^{-1}\frac{K_i}{\omega} \tag{74}$$

Assume that the plant model to be controlled has the following form

$$G(s) = \frac{c}{s^\alpha + as^\beta + b} \tag{75}$$

Then the gain and phase of this model can be obtained

$$|G(\omega)| = \frac{c}{\sqrt{A(\omega)^2 + B(\omega)^2}} \tag{76}$$

$$Arg[G(\omega)] = -\tan^{-1}\frac{B(\omega)}{A(\omega)} \tag{77}$$

where

$$A(\omega) = \omega^\alpha \cos\left(\frac{\pi}{2}\alpha\right) + a\omega^\beta \cos\left(\frac{\pi}{2}\beta\right) + b \tag{78}$$

$$B(\omega) = \omega^\alpha \sin\left(\frac{\pi}{2}\alpha\right) + a\omega^\beta \sin\left(\frac{\pi}{2}\beta\right) \tag{79}$$

Based on the gain and phase margin specifications, we get the following equations

$$K_p \sqrt{1 + \frac{K_i^2}{\omega_c^2}} \frac{c}{\sqrt{A(\omega_c)^2 + B(\omega_c)^2}} = 1 \tag{80}$$

$$-\tan^{-1}\frac{K_i}{\omega_c} - \tan^{-1}\frac{B(\omega_c)}{A(\omega_c)} = -\pi + \varphi_m \tag{81}$$

Thus, according to different gain crossover frequency and phase margin requirements, the parameters of PI controllers can be obtained by solving equations (80) and (81).

5.4.1. $\omega_c = 20$ rad/s, $\varphi_m = 75°$. Given the gain crossover frequency $\omega_c = 20$ rad/s and phase margin $\varphi_m = 75°$, $C_A(s)$ as designed for the integer-order model and $C_B(s)$ as designed for the fractional-order model are

$$C_A(s) = 1.018\left(1 + \frac{17.511}{s}\right) \tag{82}$$

$$C_B(s) = 1.045\left(1 + \frac{15.215}{s}\right) \tag{83}$$

The open-loop Bode plots of two control systems are shown in Figure 28, where the blue curve represents the characteristics of the integer-order system and the red curve represents that of the fractional-order system.

With the speed reference as 1000 rpm, the speed step response experiments are implemented on MATLAB and the PMSM speed-control platform as shown in Figure 24 using $C_A(s)$ and $C_B(s)$. The comparison between simulation output and experimental output of the integer-order control system is shown in Figure 29(a), where the red curve represents the simulation output and the blue curve represents the experimental output. The comparison between the simulation output and experimental output of the fractional-order control system is shown in Figure 29(b), where the red curve represents the simulation output and the blue curve represents the experimental output. The integral of deviation between the fractional-order system output and experimental output is 7.192, while that of the integer-order system output and experimental output is 9.839.

5.4.2. $\omega_c = 35$ rad/s, $\varphi_m = 75°$. Given the gain crossover frequency $\omega_c = 35$ rad/s and phase margin $\varphi_m = 75°$, $C_A(s)$ as designed for the integer-order model and $C_B(s)$ as designed for the fractional-order model are

$$C_A(s) = 1.823\left(1 + \frac{23.084}{s}\right) \tag{84}$$

$$C_B(s) = 1.946\left(1 + \frac{18.776}{s}\right) \tag{85}$$

The open-loop Bode plots of two control systems are shown in Figure 30, where the blue curve represents the characteristics of the integer-order system and the red curve represents that of the fractional-order system.

With the speed reference as 1000 rpm, the speed step response experiments are implemented on MATLAB and the PMSM speed-control platform using $C_A(s)$ and $C_B(s)$. The comparison between simulation output and experimental output of integer-order control system is shown in Figure 31(a), where the red curve represents the simulation output and the blue curve represents the experimental output. The comparison between simulation output and experimental output of the fractional-order control system is shown in Figure 31(b), where the red curve represents the simulation output and the blue curve represents the experimental output. The integral of deviation between the fractional-order system output and experimental output is 5.952, while that of the integer-order system output and experimental output is 12.382.
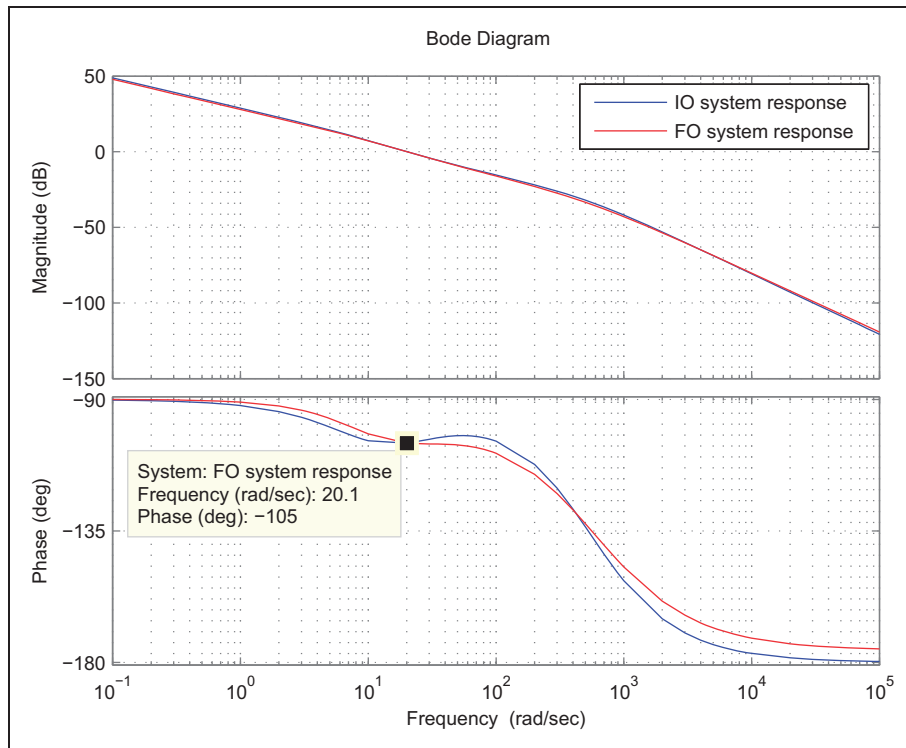
Figure 28. Open-loop Bode plots of two control systems.

5.4.3. $\omega_c = 50$ rad/s, $\varphi_m = 75°$. Given the gain cross-over frequency $\omega_c = 50$ rad/s and phase margin $\varphi_m = 75°$, $C_A(s)$ as designed for the integer-order model and $C_B(s)$ as designed for the fractional-order model are

$$C_A(s) = 2.727\left(1 + \frac{25.333}{s}\right) \qquad (86)$$

$$C_B(s) = 2.964\left(1 + \frac{19.541}{s}\right) \qquad (87)$$

The open-loop Bode plots of two control systems are shown in Figure 32, where the blue curve represents the characteristics of the integer-order system and the red curve represents that of the fractional-order system.

With the speed reference as 1000 rpm, the speed step response experiments are implemented on MATLAB and the PMSM speed-control platform using $C_A(s)$ and $C_B(s)$. The comparison between simulation output and experimental output of the integer-order control system is shown in Figure 33(a), where the red curve represents the simulation output and the blue curve represents the experimental output. The comparison between simulation output and experimental output of the fractional-order control system is

shown in Figure 33(b), where the red curve represents the simulation output and the blue curve represents the experimental output.

The integral of deviation between the fractional-order system output and experimental output is 6.31, while that of the integer-order system output and experimental output is 12.073.

5.5. Analysis of simulation and experimental results

Open-loop simulation and experimental results show that the frequency response of the fractional-order model of the PMSM is closer to the actual frequency response of the PMSM than that of the integer-order model. Speed-tracking simulation and experimental results in closed-loop using three groups of PI controllers show that the deviations between experimental outputs and simulation outputs of the fractional-order system are smaller than those between experimental outputs and simulation outputs of the integer-order system. Therefore, it is verified that the fractional-order model proposed in this paper is more accurate and closer to the true nature of the PMSM over the integer-order model.

In practical applications, the identification method proposed in this paper can be applied to
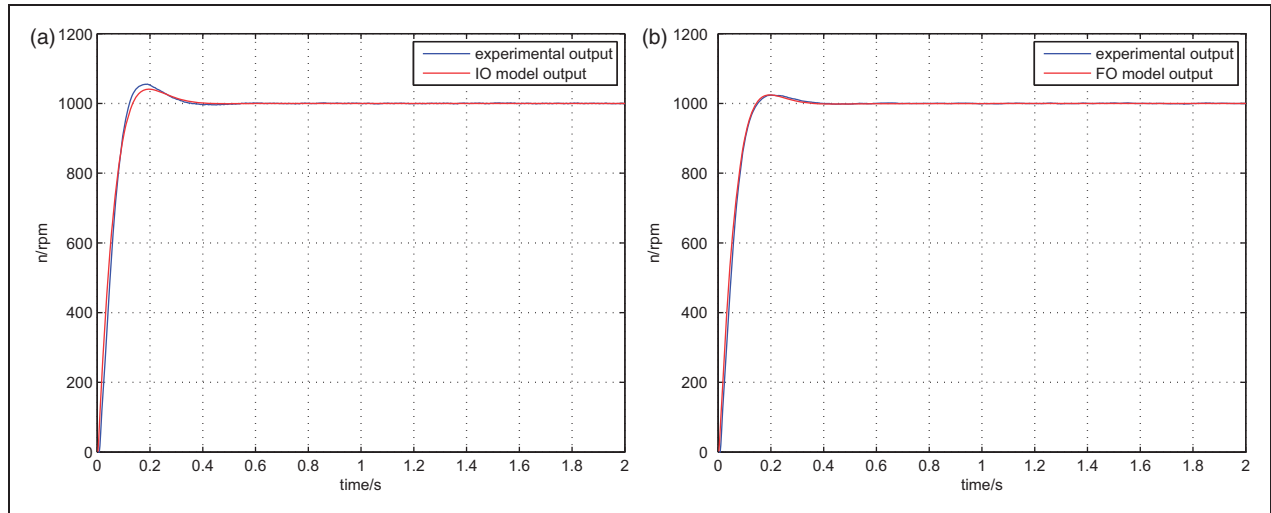
Figure 29. Speed step responses of two systems. (a) Responses of the integer-order system. (b) Responses of the fractional-order system.

Figure 30. Open-loop Bode plots of two control systems.

establish a fractional-order model of the PMSM, which is more accurate than the integer-order model. The speed controllers can be designed based on the obtained fractional-order model and then tuned based on the simulation results. Since the fractional-order model is closer to the true nature of the PMSM than the integer-order model, the actual control performance of the

controller designed based on the fractional-order model will be more satisfying and reliable.

6. Conclusion

By applying a method combining mechanical modeling and numerical modeling, fractional-order modeling of

Figure 31. Speed step responses of two systems. (a) Responses of the integer-order system. (b) Responses of the fractional-order system.
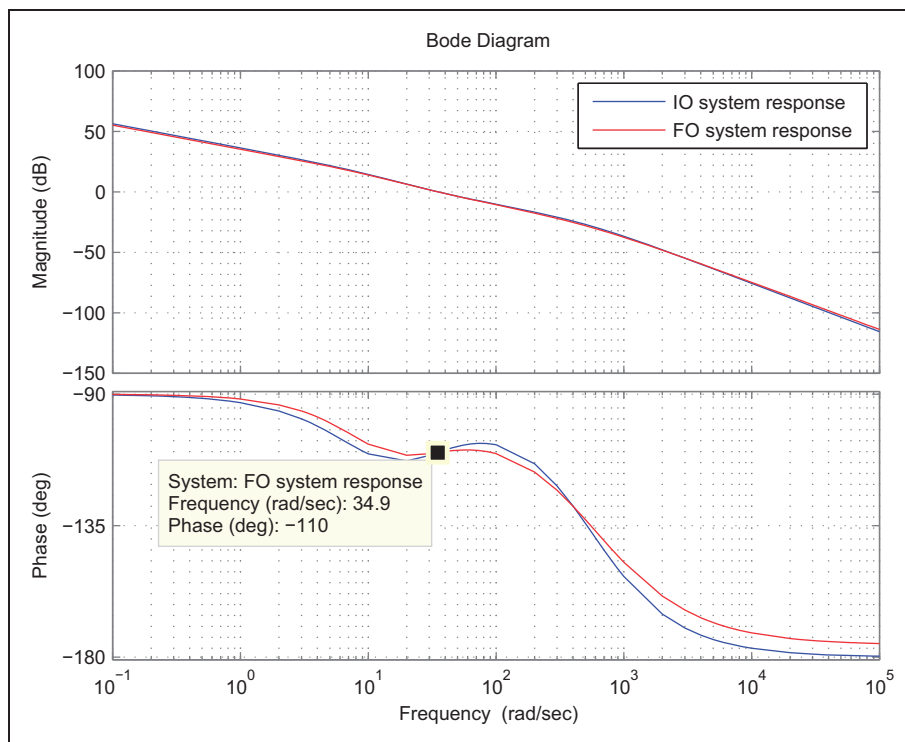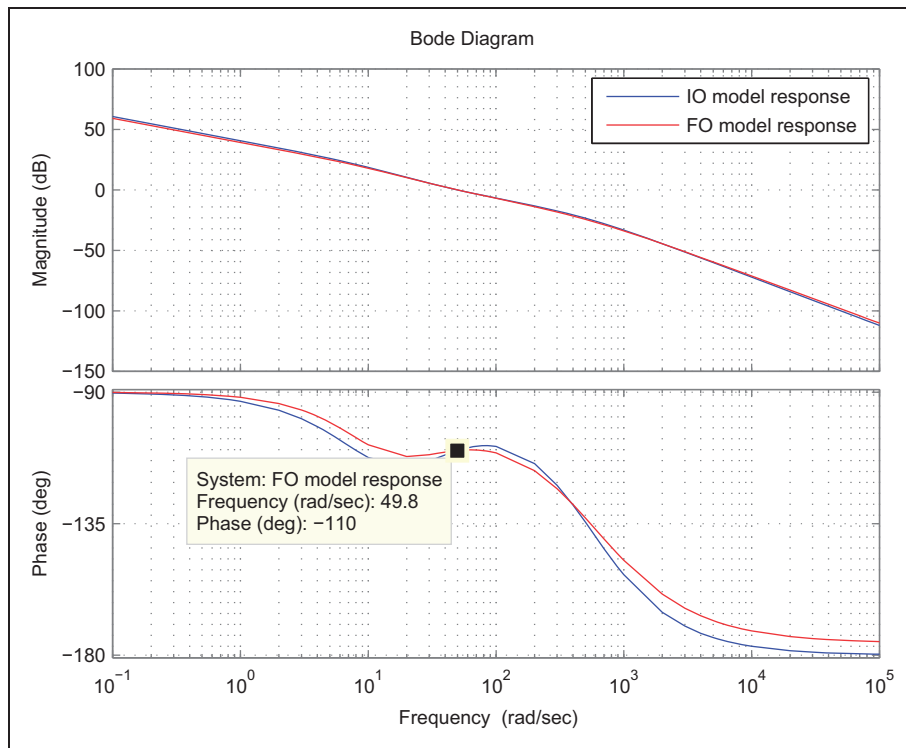

Figure 32. Open-loop Bode plots of two control systems. (a) Responses of the integer-order system. (b) Responses of the fractional-order system.

PMSM is studied. Based on the component mechanism of the PMSM, system identification experiments and parameter identification are performed on the electromagnetic part and mechanical part of the PMSM, applying the presented system identification scheme, obtaining the fractional-order and integer-order models of the PMSM. Open-loop simulations and experiments are performed, demonstrating that the frequency response of the fractional-order model of the PMSM is closer to the actual frequency response of the PMSM compared to that of the integer-order model. Three groups of PI speed controllers are
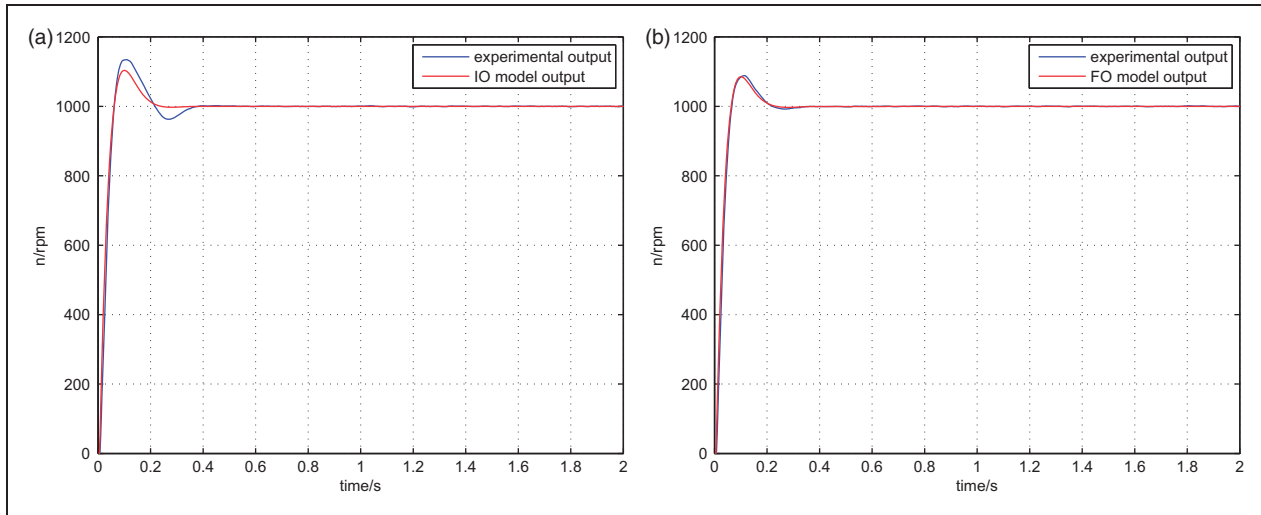
Figure 33. Speed step responses of two systems. (a) Responses of the integer-order system. (b) Responses of the fractional-order system.
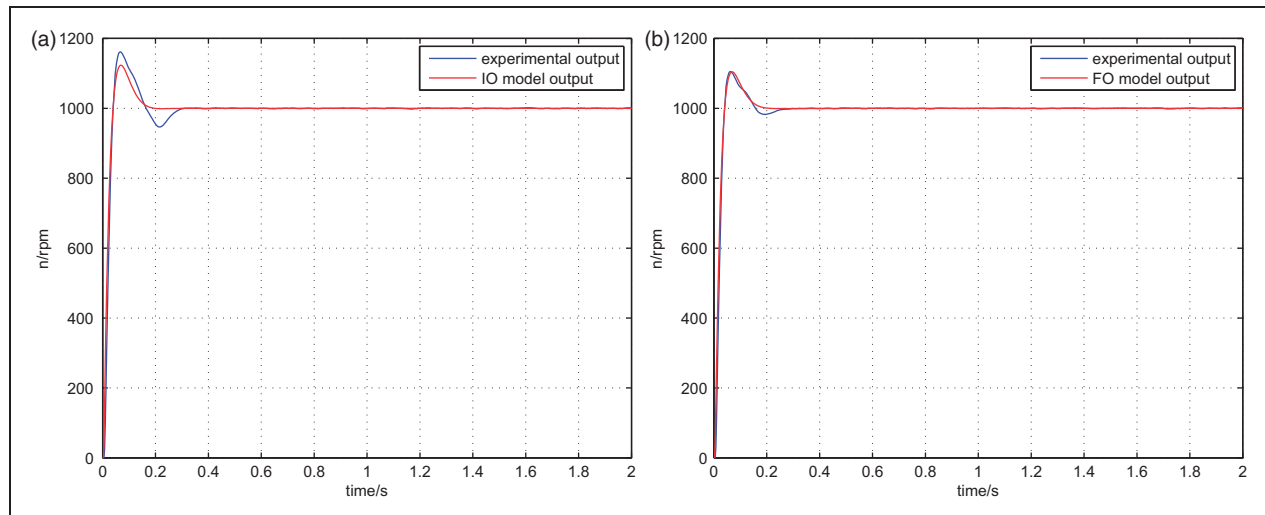
designed for the PMSM speed servo system according to the integer-order model and the fractional-order model obtained in this paper respectively. Speed-tracking simulations and experiments are performed on MATLAB and the PMSM speed-control system using these PI controllers. Simulation results and experimental results show that the deviations between experimental outputs and simulation outputs of the fractional-order system are smaller than those between experimental outputs and simulation outputs of the integer-order system, indicating that the fractional-order system model obtained in this paper is more accurate and closer to the nature of the PMSM over the traditional integer-order model. The identification method proposed in this paper can be applied to establish a fractional-order model of the PMSM. The performance of the control system designed based on this fractional-order model will be more satisfying and reliable.

Funding

References

Aguila-Camacho N, Duarte-Mermoud MA and Gallegos JA (2014) Lyapunov functions for fractional order systems. *Communications in Nonlinear Science and Numerical Simulation* 19(9): 2951–2957.

Chen BS (2003) *Electric Drive Automatic Control System: Motion Control Systems*. Beijing: China Machine Press.

Gabano JD and Poinot T (2011) Fractional modelling and identification of thermal systems. *Signal Processing* 91(3): 531–541.

Hajiloo A, Nariman-zadeh N and Moeini A (2012) Pareto optimal robust design of fractional-order PID controllers for systems with probabilistic uncertainties. *Mechatronics* 22(6): 788–801.

Hartley TT and Lorenzo CF (2003) Fractional-order system identification based on continuous-order distributions. *Signal Processing* 83(11): 2287–2300.

Kilbas AA, Srivastava HM and Trujillo JJ (2006) *Theory and Applications of Fractional Differential Equations*. Amsterdam: Elsevier Science.

Ladaci S, Loiseau JJ and Charef A (2008) Fractional order adaptive high-gain controllers for a class of linear systems. *Communications in Nonlinear Science and Numerical Simulation* 13(4): 707–714.

Li BN (1987) *Pseudo Random Signal and Related Identification*. Beijing: Science Press.

Li Y, Chen YQ and Podlubny I (2010) Stability of fractional-order nonlinear dynamic systems: Lyapunov direct method and generalized mittag-leffler stability. *Computers and Mathematics with Applications* 59(5): 1810–1821.

Li YH and Pi YG (2010) Research of the initial position based on the principle of magnetic orientation. *Electric Drive* 40(3): 28–31.

Luo Y, Chen YQ and Pi YG (2008) Authentic simulation studies of periodic adaptive learning compensation of cogging effect in PMSM position servo system. In: *Chinese control and decision conference, 2008*, Yantai, China, 2–4 July 2008, pp. 4760–4765. Yantai: IEEE.

Luo Y, Chen YQ and Pi YG (2011) Experimental study of fractional order proportional derivative controller synthesis for fractional order systems. *Mechatronics* 21(1): 204–214.

Marquardt DW (1963) An algorithm for least-squares estimation of nonlinear parameters. *Journal of Society Industrial Applied Mathematics* 11(2): 431–441.

Nakagava M and Sorimachi K (1992) Basic characteristics of a fractance device. *IEICE Transactions on Fundamentals of Electronics, Communications and Computer Sciences* E75-A(12): 1814–1818.

Oustaloup A (1995) *La Dérivation Non Entière: Théorie, Synthèse et Applications*. Paris: Editions Hermés.

Oustaloup A, François L, Benoît M, et al. (2000) Frequency-band complex noninteger differentiator: Characterization and synthesis. *IEEE Transactions on Circuits and Systems I-Fundamental Theory and Applications* 47(1): 25–39.

Petras I, Chen YQ and Coopmans C (2009) Fractional-order memristive systems. In: *IEEE conference on emerging technologies and factory automation, 2009*, Mallorca, Spain, 22–25 September 2009, pp. 1–8. IEEE.

Podlubny I (1999a) Fractional-order systems and $PI^\lambda D^\mu$ controller. *IEEE Transactions on Automatic Control* 44(1): 208–214.

Podlubny I (1999b) *Fractional Differential Equations*. San Diego: Academic Press.

Poinot T and Trigeassou JC (2004) Identification of fractional systems using an output-error technique. *Nonlinear Dynamics* 38(1–4): 133–154.

Sabatier J, Aoun M, Oustaloup A, et al. (2006) Fractional system identification for lead acid battery state of charge estimation. *Signal Processing* 86(10): 2645–2657.

Valsa J (2012) Fractional-order electrical components, networks and systems. In: *22nd international conference radioelektronika*, Brno, Czech Republic, 17–18 April 2012, pp. 1–9. IEEE.

Xue DY and Chen YQ (2007) *MATLAB Solution to Mathematical Problems in Control*. Beijing: Tsinghua University Press.

Xue DY, Zhao CY and Chen YQ (2006) Fractional order PID control of a DC-motor with elastic shaft: A case study. In: *American control conference, 2006*, Minneapolis, United States, 14–16 June 2006, pp. 3182–3187. IEEE.

Yu W, Luo Y and Pi YG (2013) Fractional order modeling and control for permanent magnet synchronous motor velocity servo system. *Mechatronics* 23(7): 813–820.

Zamani M, Karimi-Ghartemani M, Sadati N, et al. (2009) Design of a fractional order PID controller for an AVR using particle swarm optimization. *Control Engineering Practice* 17(12): 1380–1387.

Article

On comparison between iterative methods for solving nonlinear optimal control problems

JVC

Hossein Jafari[1,2], Saber Ghasempour[1] and Dumitru Baleanu[3,4]

Abstract
Recently some semi-analytical methods have been introduced for solving a class of nonlinear optimal control problems such as the Adomian decomposition method, homotopy perturbation method and modified variational iteration method. In this manuscript we compare these methods for solving a type of nonlinear optimal control problem. We prove that these methods are equivalent, which means that they use the same iterative formula to obtain the approximate/analytical solution.

1. Introduction

The theory of optimal control and its applications are now widely used in multi-disciplinary applications such as aircraft systems, biomedicine, robotics, etc. Optimal control of nonlinear systems is a challenging task which has been widely studied. It is known that a nonlinear optimal control problem (OCP) can be converted to a Hamilton–Jacobi–Bellman (HJB) partial differential equation or a nonlinear two-point boundary value problem (TPBVP). Many researchers have attempted to solve these two problems (see Diehl et al., 2005; Fakharian and Behshti, 2008; Fakharian et al., 2010; Fakharzadeh, 2012; Hämäläinen and Halme, 1976; Jajarmi et al., 2011; Manseur et al., 2005; Matinfar and Saeidy, 2014; Nik et al., 2012, and the references therein).

Several computational methods have been used for solving nonlinear OCPs. Fakharian et al. used the modified Adomian decomposition method (ADM) (Fakharian and Behshti, 2008; Fakharian et al., 2010), Saberi Nik et al. applied the homotopy perturbation method (HPM) (Nik et al., 2012), Jajarmi et al. used the series method (Jajarmi et al., 2011), Manseur et al. applied the coupled Adomian/Alienor method (Manseur et al., 2005), Fakharzadeh used differential transformation method (DTM) (Fakharzadeh, 2012)

and so on (Diehl et al., 2005; Hämäläinen and Halme, 1976).

Recently Matinfar and Saeidy presented a new technique for solving a class of nonlinear OCP (Matinfar and Saeidy, 2014), which they call the modified variational iteration method (MVIM). This method is similar to an existing method called the variational homotopy perturbation method (VHPM) (Matinfar and Ghasemi, 2010; Matinfar et al., 2010; Noor and Mohyud-Din, 2008).

In Matinfar and Saeidy, (2014) the following nonlinear OCP was considered

$$\min J = \int_{t_0}^{t_f} (x^{\mathrm{T}}(t)Qx(t) + u^{\mathrm{T}}(t)Ru(t))\mathrm{d}t$$

[1]Department of Mathematics, University of Mazandaran, Babolsar, Iran
[2]Department of Mathematical Sciences, University of South Africa, Pretoria, South Africa
[3]Department of Mathematics and Computer Science, Çankaya University, Ankara, Turkey
[4]Institute of Space Sciences, Magurele-Bucharest, Romania

Corresponding author:
Hossein Jafari, Department of Mathematics, University of Mazandaran, PO Box 47416-95447, Babolsar, Iran.
Email: jafari.ho1@gmail.com

$$s.t. \begin{cases} \dot{x} = F(t, x(t)) + G(t, x(t))u(t); & t \in [t_0, t_f] \\ x(t_0) = x_0, & x(t_f) = x_f \end{cases} \quad (1)$$

where $x \in R^n$ and $u \in R^m$ are the state and control vectors respectively, $Q \in R^{n \times n}$ and $R \in R^{m \times m}$ are positive semi-definite and positive definite matrices respectively, and x_0 and x_f are the given initial and final states at t_0 and t_f respectively. Also, F and G are continuously differentiable functions in all arguments.

According to Pontryagin's maximum principle (Pinch, 1993), and following the method presented in Jajarmi et al., (2011), they converted equation (1) into the following form of nonlinear TPBVP

$$\dot{x} = F(t, x) + G(t, x)[-R^{-1}g^T(t, x)y],$$
$$\dot{y} = -\left(Q_x + \left(\frac{\partial F(t, x)^T}{\partial x} \right) y \right.$$
$$\left. + \sum_{i=1}^{n} y_i[-R^{-1}G^T(t, x)y]^T \frac{\partial G_i}{\partial x} \right), \quad (2)$$
$$x(t_0) = x_0, \quad y(t_0) = \alpha$$

where $\alpha \in R$ is an unknown parameter which will be determined later by using boundary conditions.

Finally, they introduced an MVIM for solving equation (2).

In this paper, we prove that the ADM, the HPM and the VHPM are equivalent when used to solve nonlinear differential equations with initial or boundary conditions. *Equivalent* means these methods use the same iterative formula for solving a class of nonlinear OCP.

2. The methods

In Section 1, we saw that the nonlinear OCP (1) can be converted to a nonlinear TPBVP (2). In this section, we briefly recall the ADM, the HPM and the VHPM for solving equation (2). To convey the basic idea of the above methods, we applied these methods to the following nonlinear equation

$$L[u(t)] + R[u(t)] + N[u(t)] = g(t), \quad t > 0 \quad (3)$$

where $L = \frac{d^n}{dt^m}$, $m \in \mathbb{N}$ is a linear operator with the highest order derivative, $R[u(t)]$ (remainder linear term) is the linear differential operator of lower order than m, $N[u(t)]$ is a nonlinear operator and $g(t)$ is the source inhomogeneous term, subject to the initial conditions

$$u^{(k)}(0) = c_k, \quad k = 0, 1, 2, \ldots, m - 1 \quad (4)$$

We want to obtain a solution u of equation (3) in Hilbert space. If equation (3) does not have a unique solution, then these methods give only a solution among other possible solutions.

2.1. The ADM for solving equation (3)

For solving equation (3) using the ADM (Abbaoui and Cherruault, 1994; Adomian et al., 1996; Wazwaz, 2011), we apply $L^{-1}[.] = \frac{1}{(n-1)!} \int_0^t (t - \tau)^{n-1}[.]d\tau$ on both side of equation (3). Thus

$$u(t) = \sum_{k=0}^{m-1} c_k \frac{t^k}{k!} + L^{-1}(g(t)) - L^{-1}(R[u(t)])$$
$$- L^{-1}(N[u(t)]), \quad t > 0 \quad (5)$$

The ADM consists of the solution to equation (5) as an infinite series

$$u(x) = \sum_{i=0}^{\infty} u_i(x) \quad (6)$$

and $N(u(x))$ is also decomposed as

$$N(u(x)) = \sum_{i=0}^{\infty} A_i \quad (7)$$

where A_n, $n = 1, 2, 3, \ldots$ are called the Adomian polynomials, which are calculated by Abbaoui and Cherruault (1994), Adomian et al. (1996), and Wazwaz (2011) as

$$A_n = \frac{1}{n!} \frac{d^n}{dp^n} \left[N\left(\sum_{i=0}^{n} u_i p^i \right) \right] \Big|_{p=0} \quad (8)$$

Here p is a parameter introduced for convenience. Substituting equations (6) and (7) into equation (5) yields

$$\sum_{i=0}^{\infty} u_i(t) = \sum_{k=0}^{m-1} c_k \frac{t^k}{k!} + L^{-1}(g(t)) - L^{-1}\left(R\left[\sum_{i=0}^{\infty} u_i(t) \right] \right)$$
$$- L^{-1}\left(\sum_{i=0}^{\infty} A_i \right) \quad (9)$$

In view of the convergence of the series into equation (9), the components of the series in equation (6) are computed by following formula

$$u_0 = \sum_{k=0}^{m-1} c_k \frac{t^k}{k!} + L^{-1}(g(t))$$
$$u_{n+1} = -L^{-1}(R[u_n]) - L^{-1}(A_n), \quad n = 0, 1, 2, \ldots \quad (10)$$

When the independent variable (time) is unbounded, the series solution of equation (6) will diverge from

the true solution at larger values of time. This is where the discretization of the time axis makes itself indispensable. An estimate of local error over a particular time interval is given by Error$_l = \sum_{i=n+1}^{\infty} u_i \equiv O(\delta h^n)$.

The global error order is one integral order fewer than the corresponding local error order. It is Error$_l \equiv O(\delta\ h^{n-1})$. So it can achieve a more accurate solution and get a higher rate of convergence by increasing the number of series terms (Az-Zo'bi, 2012; Ramana and Raghu Prasad, 2014). For convergence of this method we refer to Abbaoui and Cherruault (1994), Adomian et al. (1996), and Az-Zo'bi (2012).

2.2. The HPM for solving equation (3)

The HPM was developed by combining two techniques: standard homotopy and perturbation. For solving equation (3) according to He's HPM (He, 1999), we first construct a homotopy as

$$
\mathcal{H}(v; p) = (1 - p)[L(v) - L(u_0)] + p[L(v) \\
+ R(v) + N(v) - g(t)] = 0
\tag{11}
$$

or

$$
\mathcal{H}(v; p) = L(v) - L(u_0) + pL(u_0) \\
+ p[R(v) + N(v) - g(t)] = 0
\tag{12}
$$

where $p \in [0,1]$ and u_0 is an initial guess of equation (3), which satisfies equation (4). In the HPM, a power series of p

$$
v = v_0 + v_1 p + v_2 p^2 + \cdots
\tag{13}
$$

is considered as the solution of equation (12). Substituting $p = 1$ into equation (11) gives our original equation (3). Also, as p tends to 1 in equation (13) we have

$$
u(t) = \lim_{p \to 1} v = v_0 + v_1 + v_2 + \cdots
\tag{14}
$$

Like the ADM, $N(v)$ is decomposed as

$$
N(v) = \sum_{i=0}^{\infty} p^i H_i = H_0 + pH_1 + p^2 H_2 + \cdots
\tag{15}
$$

where H_n is calculated as

$$
H_n(v_0, v_1, v_2, \ldots, v_n) = \frac{1}{n!} \frac{\partial^n}{\partial p^n} \left(N\left(\sum_{i=0}^{n} p^i v_i \right) \right) \Bigg|_{p=0}, \\
n = 0, 1, 2, \ldots
\tag{16}
$$

which a few authors call He's polynomials! It must be mentioned here that the authors of this paper have proved that He's polynomials are only Adomian polynomials (Jafari et al., 2013). Substituting equations (13) and (15) into equation (11) or (12) and arranging it according to the powers of p, we have

$$
\begin{aligned}
p^0 : \quad & L(v_0) - L(u_0) = 0 \\
p^1 : \quad & L(v_1) + L(u_0) + R(v_0) + H_0 - g(t) = 0 \\
p^2 : \quad & L(v_2) + R(v_1) + H_1 = 0, \\
& v_2^{(k)}(0) = 0, \quad k = 0, 1, 2, \ldots, m - 1 \\
& \vdots \\
p^n : \quad & L(v_n) + R(v_{n-1}) + H_{n-1} = 0, \quad v_n^{(k)}(0) = 0, \\
& n = 2, 3, \ldots
\end{aligned}
\tag{17}
$$

By solving the above equations, we obtain the components v_i, $i = 0,1,2, \ldots$ of equation (13). For convergence of this method we refer to He (1999).

2.3. The VHPM for solving equation (3)

Now we briefly describe an alternative approach of the variational iteration method (VIM) which is called MVIM (Matinfar and Saeidy, 2014) or VHPM (Matinfar and Ghasemi, 2010; Matinfar et al., 2010). This method is proposed as the coupling of the VIM and the HPM. For solving equation (3) using the VHPM, first according to He's VIM (He, 2007; Inokuti et al., 1978), a correction function for equation (3) is constructed as

$$
u_{n+1}(t) = u_n(t) + \int_0^t \lambda(\tau)\{Lu_n(\tau) + R\widetilde{u_n}(\tau) \\
+ N\widetilde{u_n}(\tau) - g(\tau)\}d\tau, \quad n \geq 0
\tag{18}
$$

where λ is a general Lagrangian multiplier, which can be identified optimally via variational theory. Here, restricted variation is applied for the nonlinear term Nu. Then we can determine λ easily. In general (Wazwaz, 2010), we have

$$
\lambda = \frac{(-1)^m}{(m-1)!}(\tau - t)^{(m-1)}
\tag{19}
$$

After finding the value of λ, unlike the VIM and similar to the HPM, we decompose the solution of equation (3) as the following series

$$
v = v_0 + v_1 p + v_2 p^2 + \cdots
\tag{20}
$$

Substituting $p = 1$ into equation (20), yields the approximate solution of equation (18). Also, the

nonlinear term is written as $N(v) = \sum_{i=0}^{\infty} H_i p^i$. Now, similar to the HPM, we have

$$\sum_{n=0}^{\infty} v_n p^n = u_0 + p \int_0^t \lambda(\tau) \left[R\left(\sum_{n=0}^{\infty} v_n p^n \right) + N\left(\sum_{n=0}^{\infty} v_n p^n \right) - g(\tau) \right] d\tau \qquad (21)$$

Finally, by sorting coefficients with respect to powers of p, we have

$$p^0: \quad v_0 = u_0$$

$$p^1: \quad v_1 = \int_0^t \lambda(\tau) [R(v_0) + H_0(v_0) - g(\tau)] d\tau$$

$$p^2: \quad v_2 = \int_0^t \lambda(\tau) [R(v_1) + H_1(v_0, v_1)] d\tau$$

$$\vdots$$

$$p^n: \quad v_n = \int_0^t \lambda(\tau) [R(v_{n-1}) + H_{n-1}(v_0, v_1, \ldots, v_{n-1})] d\tau \qquad (22)$$

which is called the VHPM using He's polynomials. For the selective zeroth approximation v_0 we used the initial values from equation (4). In the VHPM the initial approximation v_0 has been selected as

$$v_0(t) = \sum_{k=0}^{m-1} \frac{c_k}{k!} t^k \qquad (23)$$

For convergence of this method we refer to Matinfar and Ghasemi (2010).

3. Comparison between the ADM, HPM, and VHPM for solving equation (3)

As we discussed in Section 2, those methods assumed the solution of equation (3) as an infinite series, computing the components of the series by using an iterative formula. Now, we want to prove analytically that the ADM, HPM and VHPM use the same iterative formula to obtain an approximate/analytical solution of equation (3).

Definition 1. *The well-known Cauchy formula for an n-fold integral (Wazwaz, 2011)*

$$\int_a^x dx_1 \int_a^{x_1} dx_2 \ldots \int_a^{x_{n-1}} f(x_n) dx_n = \frac{1}{(n-1)!} \times \int_a^x (x-t)^{n-1} f(t) dt \qquad (24)$$

Theorem 1. *The He's polynomials equation (16) is the Adomian's polynomials equation (8).*

Proof. See Jafari et al., (2013).

Theorem 2. *The HPM for solving equation (3) is equivalent to the ADM when the homotopy $\mathcal{H}(v;p)$ is considered as equation (11).*

Proof. Applying L^{-1} to both sides of equation (17) we have

$$v_0 = \sum_{k=0}^{m-1} \frac{c_k}{k!} t^k,$$

$$v_1 = -L^{-1} R[v_0] - L^{-1} H_0 + L^{-1} g(t),$$

$$v_2 = -L^{-1} R[v_1] - L^{-1} H_1, \qquad (25)$$

$$\vdots$$

$$v_n = -L^{-1} R[v_{n-1}] - L^{-1} H_{n-1}$$

According to Theorem 1 we have $H_n = A_n$. In view of equations (9) and (13) we have

$$\lim_{p \to 1} v = \lim_{p \to 1} \sum_{i=0}^{\infty} v_i p^i = \sum_{k=0}^{m-1} \frac{c_k}{k!} t^k + L^{-1}[g(\tau)] - L^{-1} R(v_0) - L^{-1} A_0 - \cdots$$

$$= u_0 + u_1 + \cdots = \sum_{i=0}^{\infty} u_i = u$$

Theorem 3. *If we consider the homotopy $\mathcal{H}(v;p)$ as equation (21) for the VHPM. Then the VHPM is equivalent to the ADM.*

Proof. Substituting equations (13) and (15) into equation (21), we have

$$\mathcal{H}(v; p) = \sum_{n=0}^{\infty} v_n p^n - u_0 - p \int_0^t \lambda(\tau) \left[R\left(\sum_{n=0}^{\infty} v_n p^n \right) + N\left(\sum_{n=0}^{\infty} v_n p^n \right) - g(\tau) \right] d\tau = 0$$

$$\Rightarrow v_0 - u_0 + p \left[v_1 - \int_0^t \lambda(\tau) [R(v_0) + H(v_0) - g(\tau)] d\tau \right]$$

$$- \int_0^t \lambda(\tau) [R(v_n) + H_n - v_{n+1}] p^{n+1} d\tau = 0$$

By arranging the above equation according to the powers of p, we have

$$p^0: \quad v_0 - u_0 = 0$$

$$p^1: \quad v_1 - \int_0^t \lambda(\tau)[R(v_0) + H_0(v_0) - g(\tau)]d\tau = 0$$

$$p^2: \quad v_2 - \int_0^t \lambda(\tau)[R(v_1) + H_1(v_0, v_1)]d\tau = 0$$

$$\vdots$$

$$p^{n+1}: \quad v_{n+1} - \int_0^t \lambda(\tau)[R(v_n) + H_n(v_0, v_1, \ldots, v_n)]d\tau = 0,$$
$$n = 0, 1, 2, \ldots \quad (26)$$

From equation (26) we have

$$v_0 = u_0$$

$$v_1 = \int_0^t \lambda(\tau)[R(v_0) + H_0(v_0) - g(\tau)]d\tau$$

$$v_2 = \int_0^t \lambda(\tau)[R(v_1) + H_1(v_0, v_1)]d\tau$$

$$\vdots$$

$$v_{n+1} = \int_0^t \lambda(\tau)[R(v_n) + H_n(v_0, v_1, \ldots, v_n)]d\tau, \quad n = 0, 1, 2, \ldots$$
$$(27)$$

According to Theorem 1 we have $H_n = A_n$. In view of equations (19) and (23), substituting equation (27) into equation (20) leads us to

$$v = v_0 + v_1 p + v_2 p^2 + \cdots$$

$$v = \sum_{k=0}^{m-1} \frac{c_k}{k!} t^k + \left(\int_0^t \lambda(\tau)[R(v_0) + A_0 - g(\tau)]d\tau \right) p \quad (28)$$
$$+ \left(\int_0^t \lambda(\tau)[R(v_1) + A_1]d\tau \right) p^2 + \cdots$$

so

$$\lim_{p \to 1} v = \sum_{k=0}^{m-1} \frac{c_k}{k!} t^k - \int_0^t \lambda(\tau) g(\tau)d\tau$$
$$+ \left(\int_0^t \lambda(\tau)[R(v_0) + A_0]d\tau \right) \quad (29)$$
$$+ \left(\int_0^t \lambda(\tau)[R(v_1) + A_1]d\tau \right) + \cdots$$

In Jafari (2014), the first author proves that

$$\int_0^t \lambda(\tau)[.]d\tau = -L^{-1}[.] \quad (30)$$

Substituting equation (30) into equation (29) we have

$$\lim_{p \to 1} v = \sum_{k=0}^{m-1} \frac{c_k}{k!} t^k - L^{-1}[g(\tau)] - L^{-1}[R(v_0) + A_0]$$

$$- L^{-1}[R(v_1) + A_1] + \cdots$$

hence

$$\lim_{p \to 1} v = \sum_{k=0}^{m-1} \frac{c_k}{k!} t^k - L^{-1}[g(\tau)] - L^{-1}\left[\sum_{i=0}^{\infty} R(v_i) \right]$$
$$- L^{-1}\left[\sum_{i=0}^{\infty} A_i \right] = u$$

So, we prove that $\lim_{p \to 1} v = u$. In a similar way we can prove that $u = \lim_{p \to 1} v$. In view of Theorems 2 and 3 we have the following result.

Theorem 4. *Let* λ *be equation (19) and the homotopy* $\mathcal{H}(v; p)$ *be considered as equation (21). Then the VHPM for solving equation (3) is equivalent to the HPM.*

Proof. From equation (30) we have $\int_0^t \lambda(\tau)[.]d\tau = -L^{-1}[.]$ and substituting it into equation (21) we have

$$\sum_{n=0}^{\infty} v_n p^n = u_0 - pL^{-1}\left[R\left(\sum_{n=0}^{\infty} v_n p^n \right) \right.$$
$$\left. + N\left(\sum_{n=0}^{\infty} v_n p^n \right) - g(\tau) \right] \quad (31)$$

We take the limit of equation (31) as $p \to 1$ so that we have

$$u = u_0 + L^{-1}(g(t)) - L^{-1}(R[u(t)]) - L^{-1}(N[u(t)]) \quad (32)$$

Equation (32) is equivalent to equation (5). That means the VHPM for equation (3) is same as the HPM for equation (5).

Example. Consider the following type of nonlinear OCP (Fakharzadeh, 2012; Matinfar and Saeidy, 2014; Nik et al., 2012)

$$\min \quad J = \int_0^t u^2(t)dt$$
$$\text{such that} \quad \dot{x} = \frac{1}{2} x^2(t) \sin x(t) + u(t); \quad (33)$$
$$t \in [0, 1], \quad x(0) = 0, \quad x(1) = 0.5$$

Solution. It can be transformed to the following nonlinear TPBVP according to Pontryagin's maximum principle (Pinch, 1993)

$$\dot{x} = \frac{1}{2} x^2(t) \sin x(t) + u^*(t), \quad t \in [0, 1]$$

$$\dot{y} = -y(t)x(t)\sin x(t) - \frac{1}{2}y(t)x^2(t)\cos x(t), \quad t \in [0, 1]$$

$$x(0) = 0, \quad y(0) = \alpha \tag{34}$$

where the optimal control law is given by

$$u^*(t) = -\frac{1}{2}y(t)$$

To solve equation (34) we apply $L^{-1}[.] = \int_0^t [.]\mathrm{d}\tau$ on both sides of equation (34), and obtain

$$x(t) = \int_0^t \left[\frac{1}{2}x^2(t)\sin x(t) - \frac{1}{2}y(t) \right]\mathrm{d}\tau$$

$$y(t) = \alpha + \int_0^t \left[-y(t)x(t)\sin x(t) - \frac{1}{2}y(t)x^2(t)\cos x(t) \right]\mathrm{d}\tau \tag{35}$$

If we apply the ADM (Fakharian et al., 2010) or the HPM (Nik et al., 2012) to equation (35), we find same iterative formula that is given in Matinfar and Saeidy (2014) by using the VHPM.

4. Conclusions

In this paper, it has been shown that the VHPM provides exactly the same iterative formula as the ADM and HPM for solving nonlinear OCPs. It has been proved analytically that those methods, the ADM, the HPM and the VHPM, are equivalent for solving nonlinear differential equations. However the volume of calculation for the VHPM is more than for the other two methods. Specifically we show that the modified VIM or the VHPM which was recently proposed by Matinfar and Saeidy (2014) (see equation (20)) is the same as the HPM for solving integral equations or the ADM for solving differential equations.

Funding

References

Abbaoui K and Cherruault Y (1994) Convergence of Adomian's method applied to differential equations. *Computers & Mathematics with Applications* 28(5): 103–109.

Adomian G, Cherruault Y and Abbaoui K (1996) A nonperturbative analytical solution of immune response with time-delays and possible generalization. *Mathematical and Computer Modelling* 24(10): 89–96.

Az-Zo'bi E (2012) *Convergence and Stability of Modified Adomian Decomposition Method.* Germany: Lambert Academic Publishing.

Diehl M, Bock HG and Schloder JP (2005) A real-time iteration scheme for nonlinear optimization in optimal feedback control. *Carbohydrate Polymers* 43(5): 1714–1736.

Fakharian A and Behshti M (2008) Solving linear and nonlinear optimal control problem using modified Adomian decomposition method. *Journal of Computer and Robotics* 1(1): 1–8.

Fakharian A, Beheshti M and Davari A (2010) Solving the Hamilton–Jacobi–Bellman equation using Adomian decomposition method. *International Journal of Computer Mathematics* 87(12): 2769–2785.

Fakharzadeh A (2012) Solving a class of nonlinear optimal control problems by differential transformation method. *Journal of Mathematics and Computer Science* 5(3): 146–152.

Hämäläinen RP and Halme A (1976) A solution of nonlinear TPBVP's occurring in optimal control. *Automatica* 12(5): 403–415.

He JH (1999) Homotopy perturbation technique. *Computer Methods in Applied Mechanics and Engineering* 178(3–4): 257–262.

He JH (2007) Variational iteration method—some recent results and new interpretations. *Journal of Computational and Applied Mathematics* 207(1): 3–17.

Inokuti M, Sekine H and Mura T (1978) General use of the Lagrange multiplier in nonlinear mathematical physics. In: *IUTAM symposium* (ed S Nemat-Nasser), Evanston, USA, 11–13 September 1978, pp. 156–162. Oxford: Pergamon Press.

Jafari H (2014) A comparison between the variational iteration method and the successive approximations method. *Applied Mathematics Letters* 32: 1–5.

Jafari H, Ghasempour S and Khalique C (2013) A comparison between Adomian's polynomials and He's polynomials for nonlinear functional equations. *Mathematical Problems in Engineering* 2013: 943232.

Jajarmi A, Pariz N, Effati S and Vahidian Kamyad A (2011) Solving infinite horizon nonlinear optimal control problems using an extended modal series method. *Journal of Zhejiang University, Science, C* 12(8): 667–677.

Manseur S, Attalah K and Cherruault Y (2005) Optimal control of chemotherapy of HIV model using the coupled Adomian/Alienor methods. *Kybernetes* 34(7–8): 1200–1210.

Matinfar M and Ghasemi M (2010) Variational homotopy perturbation method for the Zakharove-Kuznetsov equations. *Journal of Mathematics and Statistics* 6(4): 425–430.

Matinfar M, Raeisi Z and Mahdavi M (2010) Variational homotopy perturbation method for the Fisher's equation. *International Journal of Nonlinear Science* 9(3): 374–378.

Matinfar M and Saeidy M (2014) A new analytical method for solving a class of nonlinear optimal control problems. *Optimal Control Applications and Methods* 35(3): 286–302.

Nik HS, Effati S and Shirazian M (2012) An approximate-analytical solution for the Hamilton–Jacobi–Bellman equation via homotopy perturbation method. *Applied Mathematical Modelling* 36(11): 5614–5623.

Noor MA and Mohyud-Din ST (2008) Variational homotopy perturbation method for solving higher dimensional initial

boundary value problems. *Mathematical Problems in Engineering* 2008: 1–11.

Pinch E (1993) *Optimal Control and the Calculus of Variations*. Oxford: Oxford University Press.

Ramana P and Raghu Prasad B (2014) Modified Adomian decomposition method for Van der Pol equations. *International Journal of Non-Linear Mechanics* 65: 121–132.

Wazwaz AM (2010) The variational iteration method for solving linear and nonlinear Volterra integral and integro-differential equations. *International Journal of Computer Mathematics* 87(5): 1131–1141.

Wazwaz AM (2011) *Linear and Nonlinear Integral Equations: Methods and Applications*. Higher Education Press.

A highly accurate collocation algorithm for 1 + 1 and 2 + 1 fractional percolation equations

Ali H Bhrawy

Abstract

This paper reports two successive spectral collocation methods, that enable easy and highly accuracy discretization, for 1 + 1 and 2 + 1 fractional percolation equations (FPEs). The first step depends mainly on the shifted Legendre Gauss–Lobatto collocation method for spatial discretization. An expansion in a series of shifted Legendre polynomials for the approximate solution and its spatial derivatives occurring in the FPE is investigated. In addition, the Legendre-Gauss–Lobatto quadrature rule is established to treat the boundary conditions. Thereby, the expansion coefficients are then determined by reducing the FPE with its boundary conditions to a system of ordinary differential equations for these coefficients. The second step is to propose the shifted Chebyshev Gauss–Radau collocation scheme, for temporal discretization, to reduce such a system to a system of algebraic equations, which is far easier to solve. The proposed collocation scheme, both in temporal and spatial discretizations, is successfully extended to the numerical solution of two-dimensional FPEs. An upper bound of the absolute error is obtained of the approximate solution for the two-dimensional case. Convergence properties of the method are discussed through numerical examples. Several numerical examples with comparisons are reported to highlight the high accuracy of the present method over other numerical techniques.

1. Introduction

Spectral methods (Heinrichs, 1989; Canuto et al., 2006; Doha et al., 2014b; Eslahchi et al., 2014; Kayedi-Bardeh et al., 2014; Khalil and Khan, 2014; Abdelkawy et al., 2015a) are often efficient and highly accurate schemes when compared with local methods. The speed of convergence is one of the great advantages of spectral approximations. The spectral collocation method is a specific type of spectral method that is more applicable and widely used to solve almost all types of differential equations (Bhrawy, 2014; Doha et al., 2014a; Bhrawy and Zaky, 2015b). In pseudo-spectral techniques for partial differential equations, the boundary conditions play a much more crucial role than for ordinary differential equations, and it becomes important to decide whether to satisfy the related conditions implicitly, in the

formulation of the collocation scheme, or to investigate the related conditions as additional constraints. The boundary conditions were treated implicitly in some recent pseudo-spectral approximations (Bhrawy, 2014; Doha et al., 2014a).

The development and analysis of fractional calculus began in recent decades, when the fractional differential equation emerged as a tool for the description of

Department of Mathematics, Faculty of Science, Beni-Suef University, Egypt

Received: 23 February 2015; accepted: 16 June 2015

Corresponding author:
Ali H Bhrawy, Department of Mathematics, Faculty of Science, Beni-Suef University, Beni-Suef 62511, Egypt.
Email: alibhrawy@yahoo.co.uk

phenomena in nature. Fractional differential equations (Giona and Roman, 1992; Kirchner et al., 2000; Magin, 2006; Li and Deng, 2007; Garrappa and Popolizio, 2011; Alipour et al., 2012; Baleanu et al., 2012; Machado et al., 2013; Rostamy et al., 2013) are used to model many phenomena in several fields (Pooseh et al., 2013; Dehghan et al., 2014; Lazo and Torres, 2014; Pinto and Carvalho, 2015; Raja and Chaudhary, 2015; Xu et al., 2015). Numerical techniques are widely used by scientists and engineers to solve fractional PDEs. A major advantage of numerical techniques is that a numerical solution can be obtained even when a problem has no analytical solution. In some cases, PDEs of fractional order can be solved analytically, where finding their solutions in the general case is hard and limited to the linear one. Therefore, there has been a growing interest in recent decades in developing numerical methods for solving FDEs. Several numerical treatments based on the improvement of finite difference schemes for FDEs are given in Meerschaert and Tadjeran (2006), Ding et al. (2010) and Wang and Du (2014). Also, efficient spectral algorithms (He, 1998; Chou et al., 2006; Chen et al., 2011b; Doha et al., 2011; Doha et al., 2012; Chen et al., 2013; Bhrawy, 2014; Bhrawy et al., 2015a; Chen et al., 2014; Irandoust-Pakchin et al., 2014; Abdelkawy et al., 2015b; Ezz-Eldien et al., 2015) have been designed and developed for solving different kinds of fractional differential equation.

Percolation flow problems (Chou et al., 2006) have been discussed in many fields including groundwater dynamics, seepage hydraulics, and fluid dynamics in porous media. He (1998) introduced analytical solutions for fractional percolation equations (FPEs) by using the variational iteration method. Fractional derivatives are becoming widely used and accepted in models of percolation flow problems. Recently, three advanced implicit finite difference methods have been investigated in Chen et al. (2011b, 2013, 2014) to discretize the numerical solutions of FPEs in one- and two-dimensional spaces. Along the same line of thought, Chen et al. (2011b) proposed a new implicit finite difference scheme for solving the $1+1$ FPE. A developed numerical algorithm has been achieved and analyzed by Chen et al. (2013), for solving the $2+1$ FPE. Several authors have also improved and developed efficient numerical methods for approximating the solution of other similar fractional PDEs (Chen et al., 2011a; Al-Khaled and Alquran, 2014; Irandoust-Pakchin et al., 2014; Mohebbi et al., 2014; Bhrawy and Zaky, 2015a; Bhrawy et al., 2015a, 2015b).

The main aim of the present paper is to propose a numerical method that improves the accuracy of the numerical solutions of FPEs in one- and two-dimensional space. The main advantage of the present method is that it proposes a collocation scheme for both temporal and spatial discretizations. Firstly, the shifted Legendre Gauss–Lobatto collocation (SL-GL-C) is proposed, with a suitable modification for treating the boundary conditions, for spatial discretization. This treatment, for the conditions, improves the accuracy of the scheme greatly. Therefore, the FPE with its boundary conditions is reduced to a system of ordinary differential equations (SODEs) subject to a vector of initial values. Secondly, the SC-GR-C is then investigated for temporal discretization, which is more reasonable for solving initial value problems. Thereby, the problem is reduced to a system of algebraic equations which makes it far easier to solve. In addition, this algorithm is developed for the numerical solution of FPEs in two dimensions. An upper bound of the absolute error is obtained for the approximate solution for the two-dimensional case. Finally, several numerical examples with comparisons highlighting the high accuracy and effectiveness of the present method are included. By choosing relatively limited Legendre Gauss–Lobatto and Chebyshev Gauss–Radau collocation nodes, we are able to obtain highly accurate solutions, confirming the applicability and high accuracy of the proposed method over other numerical schemes in the literature.

This article is organized as follows. Section 2 presents some fractional calculus preliminaries, and shifted Legendre and shifted Chebyshev polynomials. Spectral approximation schemes of $1+1$ and $2+1$ FPEs based on a combination of SL-GL-C and SC-GR-C methods are presented in Sections 3 and 4, respectively. Numerical results are introduced in Section 5. Finally, we end the paper with some concluding remarks.

2. Preliminaries and notation

This section presents several useful fractional definitions, and shifted Legendre and shifted Chebyshev polynomials.

2.1. Fractional calculus

There are many definitions of the fractional-order derivative, which are not necessarily equivalent to each other (Miller and Ross, 1993; Kayedi-Bardeh et al., 2014; Ezz-Eldien et al., 2015; Jafari and Tajadodi, 2015). Riemann–Liouville and Caputo fractional definitions are the two most popular definitions from all the other definitions of fractional calculus which have been introduced recently.

Definition 2.1. The Riemann–Liouville fractional integral of order $v \geq 0$ is obtained from

$$J^v f(x) = \frac{1}{\Gamma(v)} \int_0^x (x - \zeta)^{v-1} f(\zeta) \, d\zeta, \quad v > 0, \quad x > 0,$$

$$J^0 f(x) = f(x) \tag{1}$$

where

$$\Gamma(v) = \int_0^\infty x^{v-1} e^{-x} \, dx \tag{2}$$

is the gamma function.

The fractional operator J^v satisfies

$$J^v J^\mu f(x) = J^{v+\mu} f(x),$$
$$J^v J^\mu f(x) = J^\mu J^v f(x), \tag{3}$$
$$J^v x^\beta = \frac{\Gamma(\beta + 1)}{\Gamma(\beta + 1 + v)} x^{\beta+v}$$

The Riemann–Liouville fractional derivative of order μ satisfies

$$D^\mu f(x) = \frac{d^n}{x^n} (J^{n-\mu} f(x)) \tag{4}$$

where $n - 1 < \mu \leq n$, $n \in N$ and n is the smallest integer greater than μ.

Lemma 2.1. *If $n - 1 < \mu \leq n$, $n \in N$, then*

$$D^\mu J^\mu f(x) = f(x),$$
$$J^\mu D^\mu f(x) = f(x) - \sum_{j=0}^{n-1} f^{(j)}(0^+) \frac{x^j}{j!}, \quad x > 0 \tag{5}$$

2.2. Shifted Legendre Gauss–Lobatto interpolation

In this subsection, we recall some approximation results for the shifted Legendre Gauss–Lobatto (SL-GL) interpolation, which play important roles in the proposed collocation scheme. The Legendre polynomials $P_k(x)$ $(k = 0, 1 \ldots)$ satisfy the following Rodrigue's formula

$$P_k(x) = \frac{(-1)^k}{2^k k!} D^k ((1 - x^2)^k) \tag{6}$$

also we recall that $P_k(x)$ is a polynomial of degree k. Accordingly, $P_k^{(p)}(x)$ (the pth derivative of $P_k(x)$) is given by

$$P_k^{(p)}(x) = \sum_{\substack{i=0 (i+k=\text{even})}}^{k-p} C_p(k, i) P_i(x) \tag{7}$$

where

$$C_p(k, i) = \frac{2^{p-1}(2i + 1)\Gamma(\frac{p+k-i}{2})\Gamma(\frac{p+k+i+1}{2})}{\Gamma(p)\Gamma(\frac{2-p+k-i}{2})\Gamma(\frac{3-p+k+i}{2})}$$

Next, denoting by $\|u\|$ and (u, v) the norm and inner product of space $L^2[-1, 1]$. The set of $P_k(x)$ is a complete orthogonal system in $L^2[-1, 1]$, namely

$$(P_j(x), P_k(x)) = \int_{-1}^1 P_j(x) P_k(x) \, dx = h_k \delta_{jk} \tag{8}$$

where $h_i = \frac{2}{2i+1}$ and δ_{jk} is the Dirac function. Thus for any $v \in L^2[-1, 1]$

$$v(x) = \sum_{i=0}^\infty a_i P_i(x), \quad a_i = \frac{1}{h_i} \int_{-1}^1 v(x) P_i(x) dx \tag{9}$$

For any positive integer N, let $S_N[-1, 1]$ be the set of all polynomials of degree at most N, due to the L-GL quadrature. Thus, for any $\phi \in S_{2N-1}[-1, 1]$ we obtain

$$\int_{-1}^1 \phi(x) dx = \sum_{i=0}^N \varpi_{N,i} \phi(x_{N,i}) \tag{10}$$

where $x_{N,i}$ $(0 \leq i \leq N)$ and $\varpi_{N,i}$ $(0 \leq i \leq N)$ are the nodes and Christoffel numbers of the L-GL interpolation on the interval $[-1, 1]$, respectively. Now, it is quite useful in the sequel to define the following norm and discrete inner product

$$\|u\|_N = (u, v)_N^{\frac{1}{2}}, \quad (u, v)_N = \sum_{j=0}^N u(x_{N,j}) v(x_{N,j}) \varpi_{N,j} \tag{11}$$

Let us denote by $P_{L,i}(x)$ the shifted Legendre polynomials which are defined on the interval $[0, L]$. These polynomials can be generated from the following recurrence relation

$$(j + 1)P_{L,j+1}(x) = (2j + 1)$$
$$\times \left(\frac{2x}{L} - 1\right) P_{L,j}(x) - j P_{L,j-1}(x), \quad j = 1, 2, \ldots \tag{12}$$

The analytical form of $P_{L,i}(x)$ can be written as

$$P_{L,i}(x) = \sum_{k=0}^{i} (-1)^{i+k} \frac{(i+k)!}{(i-k)! \, (k!)^2 \, L^k} \, x^k \qquad (13)$$

The Riemann–Liouville fractional integration of $P_{L,i}(x)$ may be obtained from

$$J^{\nu} P_{L,i}(x) = \sum_{k=0}^{i} (-1)^{k+i} \frac{(k+i)!}{(-k+i)! \, (k!)^2 \, t^k} \, J^{\nu} x^k$$

$$= \sum_{k=0}^{i} (-1)^{k+i} \frac{(k+i)! \, k!}{(-k+i)! \, (k!)^2 \, t^k \, \Gamma(k+\nu+1)}$$

$$\times x^{k+\nu}, \quad i = 0, 1, \ldots, N \qquad (14)$$

where $P_{L,i}(0) = (-1)^i$.

The orthogonality condition is

$$\int_0^L P_{L,j}(x) P_{L,k}(x) w_L(x) dx = h_k^L \delta_{jk} \qquad (15)$$

where $w_L(x) = 1$ and $h_k^L = \frac{L}{2k+1}$.

If a function $u(t) \in L^2[0,L]$, then one can express it by means of $P_{L,i}(t)$ as

$$u(t) = \sum_{i=0}^{\infty} c_i P_{L,i}(t)$$

where c_i is given by

$$c_i = \frac{1}{h_i^L} \int_0^L u(t) P_{L,i}(t) x, \quad i = 0, 1, 2, \ldots \qquad (16)$$

In the approximation, $u(x)$ may be expanded as

$$u_N(t) \simeq \sum_{i=0}^{N} c_i P_{L,i}(t) \qquad (17)$$

2.3. Shifted Chebyshev Gauss–Radau interpolation

The Chebyshev polynomials are defined on the interval $[-1,1]$, by

$$T_k(t) = \cos(k \arccos(t)), \quad k \geq 0 \qquad (18)$$

Also

$$T_k(\pm 1) = (\pm 1)^k, \quad T_k(-t) = (-1)^k T_k(t) \qquad (19)$$

Let $w^c(t) = \frac{1}{\sqrt{1-t^2}}$, then we introduce the following norm and inner product of the the weighted space $L^2_{w^c}[-1, 1]$ as

$$\|u\|_{w^c} = (u,u)_{w^c}^{\frac{1}{2}}, \qquad (u,v)_{w^c} = \int_{-1}^{1} u(t) \, v(t) w^c(t) dt \qquad (20)$$

The set of Chebyshev polynomials satisfies

$$\|T_k\|_{w^c}^2 = h_k^c$$

$$= \begin{cases} \frac{\varsigma_k}{2}\pi, & k = j, \\ 0, & k \neq j, \end{cases} \qquad \varsigma_0 = 2, \quad \varsigma_k = 1, \quad k \geq 1 \qquad (21)$$

Now, we introduce the following norm and discrete inner product

$$\|u\|_{w^c} = (u,u)_{w^c}^{\frac{1}{2}}, \qquad (u,v)_{w^c} = \sum_{j=0}^{N} u(t_{N,j}) \, v(t_{N,j}) \, \varpi_{N,j}^c \qquad (22)$$

Let us denote by $T_{T,n}(t)$ the shifted Chebyshev polynomials which are defined on the interval $[0,T]$. The analytical form of $T_{T,n}(t)$ is obtained from

$$T_{T,n}(t) = n \sum_{k=0}^{n} (-1)^{n-k} \frac{(n+k-1)! \, 2^{2k}}{(n-k)! \, (2k)! \, T^k} \, t^k \qquad (23)$$

where $T_{T,n}(0) = (-1)^n$ and $T_{T,n}(T) = 1$.

The orthogonality condition is

$$\int_0^L T_{T,m}(t) T_{T,n}(x) w_T(x) \, dx = \delta_{mn} \, {}^c h_n^T \qquad (24)$$

where $w_T(t) = \frac{1}{\sqrt{Tt-t^2}}$ and ${}^c h_n^T = \frac{c_n}{2}\pi$, with $c_0 = 2$, $c_i = 1$, and $i \geq 1$.

As in the previous subsection, if $u(t) \in L^2_{w_T(t)}[0, T]$, then one can express it by means of $T_{T,i}(t)$ as

$$u(t) = \sum_{j=0}^{\infty} a_j T_{T,j}(t) \qquad (25)$$

where

$$a_j = \frac{1}{{}^c h_j^T} \int_0^T u(t) T_{T,j}(t) w_T(t) dt, \quad j = 0, 1, 2, \ldots \qquad (26)$$

3. One-dimensional space fractional percolation equation

This section outlines the key aspects of discretization for the numerical solution of the one-dimensional FPE using a new spectral technique.

Consider the following $1+1$ FPE

$$\partial_t u(x,t) = \partial_x^{v_1}\Big(g_1(x)\partial_x^{v_2}u(x,t)\Big) + f(x,t),$$
$$\times (x,t) \in [0,L] \times [0,T] \tag{27}$$

subject to

$$u(x,0) = g_2(x), \quad x \in [0,L] \tag{28}$$

and

$$u(0,t) = g_3(t), \quad u(L,t) = g_4(t), \quad t \in [0,T] \tag{29}$$

where v_1 and v_2 $(0 < v_1, v_2 < 1)$ are the fractional orders, and $f(x,t)$, $g_1(x)$, $g_2(x)$, $g_3(t)$ and $g_4(t)$ are given functions. We discretize equation (27) for the spatial variable x by the SL-GL-C method. While the SC-GR-C method is applied to discretize the resulting SODEs in time advance.

3.1. SL-GL-C scheme for the space variable

We first propose the SL-GL-C method to transform the $1+1$ FPE into SODEs. To this end, we approximate the spatial variable using the SL-GL-C method at some nodes. The nodes are the set of points in a specified domain. To acquire high accuracy, the choice of nodes is usually related to some Gaussian integration formula, see Canuto et al. (2006) for more details. The collocation points are taken to be the SL-GL quadrature nodes which we denote by $x_{N,i}^L$.

Equation (27) may be restated as

$$\partial_t u(x,t) = g_5(x)\partial_x^{v_2}u(x,t) + g_1(x)\partial_x^{v_1}\Big(\partial_x^{v_2}u(x,t)\Big) + f(x,t),$$
$$0 < v_1, v_2 < 1, (x,t) \in [0,L] \times [0,T] \tag{30}$$

where $g_5(x) = \partial_x^{v_1}g_1(x)$.

Now, we present the main steps of applying the SL-GL-C scheme to solve the FPE. Let the approximate solution of equation (27) be

$$u_N(x,t) = \sum_{j=0}^N a_j(t)P_{L,j}(x) \tag{31}$$

the unknown coefficients $a_j(t)$ may be approximated by

$$a_j(t) = \frac{1}{h_j^L}\sum_{i=0}^N P_{L,j}(x_{N,i}^L)\varpi_{N,i}^L u(x_{N,i}^L, t) \tag{32}$$

Accordingly, the approximate solution (31) may be expanded to

$$u_N(x,t) = \sum_{i=0}^N \Big(\sum_{j=0}^N \frac{1}{h_j^L}P_{L,j}(x_{N,i}^L)P_{L,j}(x)\varpi_{N,i}^L\Big)u(x_{N,i}^L, t) \tag{33}$$

where $\varpi_{N,j}^L$ $(0 \le j \le N)$ are the weights of the SL-GL quadrature on $[0,L]$.

The fractional derivative of the approximate solution $u_N(x,t)$ is then estimated as

$$\partial_x^{v_2}u_N(x,t) = \sum_{i=0}^N \Big(\sum_{j=0}^N \frac{1}{h_j^L}P_{L,j}(x_{N,i}^L)\partial_x^{v_2}(P_{L,j}(x))\varpi_{N,i}^L\Big)$$
$$u(x_{N,i}^L, t), \tag{34}$$

For $0 < v_2 < 1$, the Riemann–Liouville fractional derivative is

$$\partial_x^{v_2}x^k = \frac{1}{\Gamma(1-v_2)}\partial_x\Big(\int_0^x \frac{\chi^k}{(x-\chi)^{v_2}}\,d\chi\Big) = \frac{x^{k-v_2}\Gamma(1+k)}{\Gamma(1+k-v_2)} \tag{35}$$

thus

$$\partial_x^{v_2}P_{L,i}(x) = P_{L,i}^{(v_2)}(x)$$
$$= \sum_{k=0}^i (-1)^{i+k}\frac{(k+i)!\Gamma(k+1)}{(i-k)!(k!)^2\Gamma(1+k-v_2)L^k}x^{k-v_2} \tag{36}$$

Consequently

$$\partial_x^{v_2}u_N(x,t) = \sum_{i=0}^N \Big(\sum_{j=0}^N \frac{1}{h_j^L}P_{L,j}(x_{N,i}^L)P_{L,i}^{(v_2)}(x)\varpi_{N,i}^L\Big)u(x_{N,i}^L, t) \tag{37}$$

Similarly, we obtain

$$\partial_x^{v_1}\Big(\partial_x^{v_2}u_N(x,t)\Big)$$
$$= \sum_{i=0}^N \Big(\sum_{j=0}^N \frac{1}{h_j^L}P_{L,j}(x_{N,i}^L)\partial_x^{v_1}(P_{L,i}^{(v_2)}(x))\varpi_{N,i}^L\Big)u(x_{N,i}^L, t)$$
$$= \sum_{i=0}^N \Big(\sum_{j=0}^N \frac{1}{h_j^L}P_{L,j}(x_{N,i}^L)(P_{L,i}^{(v_1+v_2)}(x))\varpi_{N,i}^L\Big)u(x_{N,i}^L, t) \tag{38}$$

The fractional derivative of the numerical solution $u_N(x,t)$ is then computed at the collocation points as

$$\left(\partial_x^{v_2} u_N(x,t)\right)_{x=x_{N_n}^L} = \sum_{i=0}^{N} \gamma_{n,i} u_i(t), \quad n = 1, 2, \ldots, N-1,$$

(39)

$$\left(\partial_x^{v_1}\left(\partial_x^{v_2} u_N(x,t)\right)\right)_{x=x_{N_n}^L} = \sum_{i=0}^{N} \varepsilon_{n,i} u_i(t), \quad n = 1, 2, \ldots, N-1$$

(40)

where

$$u_i(t) = u_N(x_{N,i}^L, t),$$

$$\gamma_{n,i} = \sum_{j=0}^{N} \frac{\varpi_{N,i}^L}{h_j^L} P_{L,j}(x_{N,i}^L)\left(P_{L,j}^{(v_2)}(x)\right)_{x=x_{N_n}^L},$$

$$\varepsilon_{n,i} = \sum_{j=0}^{N} \frac{\varpi_{N,i}^L}{h_j^L} P_{L,j}(x_{N,i}^L)\left(P_{L,i}^{(v_1+v_2)}(x)\right)_{x=x_{N_n}^L}$$

Since the approximate solution and its derivatives in equations (33)–(40) do not satisfy the FPE (27) exactly, we enforce the approximate solution and its derivatives to satisfy it exactly at the chosen collocation points, by making the residuals equal to zero. In addition, the boundary conditions (29) will be satisfied at the two nodes 0 and L. Thus, we ensure that the boundary conditions are satisfied without adding additional equations. Therefore, adopting equations (30)–(40), enables one to write equation (27) in the form

$$\dot{u}_n(t) = g_5(x_{N,n}^L)\left(\sum_{i=1}^{N-1} \gamma_{n,i} u_i(t) + \gamma_{n,0} u_0(t) + \gamma_{n,N} u_N(t)\right)$$

$$+ f(x_{N,n}^L, t) + g_1(x)\left(\sum_{i=1}^{N-1} \varepsilon_{n,i} u_i(t) + \varepsilon_{n,0} u_0(t)\right.$$

$$\left. + \varepsilon_{n,N} u_N(t)\right)$$

(41)

Obviously, the problem (27)–(29) is equivalent to the following SODEs

$$\dot{u}_n(t) = g_5(x_{N,n}^L)\left(\sum_{i=1}^{N-1} \gamma_{n,i} u_i(t) + \gamma_{n,0} g_3(t) + \gamma_{n,N} g_4(t)\right)$$

$$+ f(x_{N,n}^L, t) + g_1(x)\left(\sum_{i=1}^{N-1} \varepsilon_{n,i} u_i(t) + \varepsilon_{n,0} g_3(t)\right.$$

$$\left. + \varepsilon_{n,N} g_4(t)\right), \quad n = 1, \ldots, N-1$$

(42)

subject to the initial values

$$u_n(0) = g_2(x_{N,n}^L), \quad n = 1, \ldots, N-1 \qquad (43)$$

We can reformulate the previous equations in matrix form as

$$\begin{pmatrix} \dot{u}_1(t) \\ \dot{u}_2(t) \\ \cdots \\ \cdots \\ \cdots \\ \dot{u}_{N-2}(t) \\ \dot{u}_{N-1}(t) \end{pmatrix} = \begin{pmatrix} F_1(t, u_1(t), u_2(t), \ldots, u_{N-1}(t)) \\ F_2(t, u_1(t), u_2(t), \ldots, u_{N-1}(t)) \\ \cdots \\ \cdots \\ \cdots \\ F_{N-2}(t, u_1(t), u_2(t), \ldots, u_{N-1}(t)) \\ F_{N-1}(t, u_1(t), u_2(t), \ldots, u_{N-1}(t)) \end{pmatrix}$$

(44)

subject to a vector of initial values

$$\begin{pmatrix} u_1(0) \\ u_2(0) \\ \cdots \\ \cdots \\ \cdots \\ u_{N-2}(0) \\ u_{N-1}(0) \end{pmatrix} = \begin{pmatrix} g_2(x_{N,1}^L) \\ g_2(x_{N,2}^L) \\ \cdots \\ \cdots \\ \cdots \\ g_2(x_{N,N-2}^L) \\ g_2(x_{N,N-1}^L) \end{pmatrix}$$

(45)

where

$$F_n(t, u_1(t), u_2(t), \ldots, u_{N-1}(t))$$

$$= g_5(x_{N,n}^L)\left(\sum_{i=1}^{N-1} \gamma_{n,i} u_i(t) + \gamma_{n,0} g_3(t) + \gamma_{n,N} g_4(t)\right)$$

$$+ f(x_{N,n}^L, t) + g_1(x)\left(\sum_{i=1}^{N-1} \varepsilon_{n,i} u_i(t) + \varepsilon_{n,0} g_3(t) + \varepsilon_{n,N} g_4(t)\right)$$

(46)

3.2. SC-GR-C scheme for the time variable

The second step of our algorithm is to propose an efficient collocation scheme to approximate the solution of the following SODEs

$$\begin{pmatrix} \dot{u}_1(t) \\ \dot{u}_2(t) \\ \cdots \\ \cdots \\ \cdots \\ \dot{u}_{N-2}(t) \\ \dot{u}_{N-1}(t) \end{pmatrix} = \begin{pmatrix} F_1(t, u_1(t), u_2(t), \ldots, u_{N-1}(t)) \\ F_2(t, u_1(t), u_2(t), \ldots, u_{N-1}(t)) \\ \cdots \\ \cdots \\ \cdots \\ F_{N-2}(t, u_1(t), u_2(t), \ldots, u_{N-1}(t)) \\ F_{N-1}(t, u_1(t), u_2(t), \ldots, u_{N-1}(t)) \end{pmatrix}$$

(47)

subject to the initial values

$$
\begin{pmatrix}
u_1(0) \\
u_2(0) \\
\dots \\
\dots \\
\dots \\
u_{N-2}(0) \\
u_{N-1}(0)
\end{pmatrix}
=
\begin{pmatrix}
g_2(x_{N,1}^L) \\
g_2(x_{N,2}^L) \\
\dots \\
\dots \\
\dots \\
g_2(x_{N,N-2}^L) \\
g_2(x_{N,N-1}^L)
\end{pmatrix}
\tag{48}
$$

In order to approximate the solution of the previous system, we use the SC-GR-C method to deal with the temporal variable t. We choose the approximate solution of the form

$$
u_{n,M}(t) = \sum_{j=0}^{M} a_{n,j} T_{T,j}(t), \quad n = 1, \dots, N-1
\tag{49}
$$

Furthermore, the approximation of the time derivative can be computed as

$$
\partial_t u_{n,M}(t) = \sum_{j=0}^{M} a_{n,j} \partial_t(T_{T,j}(t)) = \sum_{j=0}^{M} a_{n,j} T_{T,j}^{(1)}(t),
$$
$$
n = 1, \dots, N-1
\tag{50}
$$

where $T_{T,k}^{(1)}(t)$ represents the first time derivative of the shifted Chebyshev polynomials, which can be easily evaluated at any point $t_{K,s}^T$ (shifted Chebyshev Gauss–Radau points).

Therefore, adopting equations (49)–(50) enables one to write equations (47)–(48) in the form

$$
\begin{pmatrix}
\sum_{j=0}^{M} a_{1,j} T_{T,j}(0) \\
\sum_{j=0}^{M} a_{2,j} T_{T,j}(0) \\
\dots \\
\dots \\
\dots \\
\sum_{j=0}^{M} a_{N-2,j} T_{T,j}(0) \\
\sum_{j=0}^{M} a_{N-1,j} T_{T,j}(0)
\end{pmatrix}
=
\begin{pmatrix}
g_2(x_{N,1}^L) \\
g_2(x_{N,2}^L) \\
\dots \\
\dots \\
\dots \\
g_2(x_{N,N-2}^L) \\
g_2(x_{N,N-1}^L)
\end{pmatrix}
\tag{52}
$$

In the proposed technique, the residual of equation (51) has to be enforced to zero at $M \times (N-1)$ collocation points. In other words, we have to collocate equation (51) at the $M \times (N-1)$ shifted Chebyshev Gauss–Radau collocation nodes, which immediately yields

$$
\sum_{j=0}^{M} a_{n,j} T_{T,j}^{(1)}(t_{M,s}^T) = F_n\left(t_{M,s}^T, \sum_{j=0}^{M} a_{1,j} T_{T,j}(t_{M,s}^T), \dots, \right.
$$
$$
\left. \times \sum_{j=0}^{M} a_{N-1,j} T_{T,j}(t_{M,s}^T)\right),
$$
$$
n = 1, \dots, N-1, \quad s = 1, \dots, M
\tag{53}
$$

In virtue of equation (52), we get

$$
\sum_{j=0}^{M} a_{n,j} T_{T,j}(0) = \tau_n, \quad n = 1, \dots, N-1
\tag{54}
$$

$$
\begin{pmatrix}
\sum_{j=0}^{M} a_{1,j} T_{T,j}^{(1)}(t) \\
\sum_{j=0}^{M} a_{2,j} T_{T,j}^{(1)}(t) \\
\dots \\
\dots \\
\dots \\
\sum_{j=0}^{M} a_{N-2,j} T_{T,j}^{(1)}(t) \\
\sum_{j=0}^{M} a_{N-1,j} T_{T,j}^{(1)}(t)
\end{pmatrix}
=
\begin{pmatrix}
F_1\left(t, \sum_{j=0}^{M} a_{1,j} T_{T,j}(t), \dots, \sum_{j=0}^{M} a_{N-1,j} T_{T,j}(t)\right) \\
F_2\left(t, \sum_{j=0}^{M} a_{1,j} T_{T,j}(t), \dots, \sum_{j=0}^{M} a_{N-1,j} T_{T,j}(t)\right) \\
\dots \\
\dots \\
\dots \\
F_{N-2}\left(t, \sum_{j=0}^{M} a_{1,j} T_{T,j}(t), \dots, \sum_{j=0}^{M} a_{N-1,j} T_{T,j}(t)\right) \\
F_{N-1}\left(t, \sum_{j=0}^{M} a_{1,j} T_{T,j}(t), \dots, \sum_{j=0}^{M} a_{N-1,j} T_{T,j}(t)\right)
\end{pmatrix},
\tag{51}
$$

The set of previous equations is equivalent to a system of $(N-1) \times (M+1)$ algebraic equations in the unknowns $a_{i,j}$, $i=1,\ldots,N-1$; $j=0,\ldots,M$

$$
\begin{pmatrix}
\kappa_{1,0} & \cdots & \kappa_{1,M} \\
\kappa_{2,0} & \cdots & \kappa_{2,M} \\
\cdots & \ddots & \cdots \\
\cdots & \ddots & \cdots \\
\cdots & \ddots & \cdots \\
\kappa_{N-2,0} & \cdots & \kappa_{N-2,M} \\
\kappa_{N-1,0} & \cdots & \kappa_{N-1,M}
\end{pmatrix}
=
\begin{pmatrix}
\xi_{1,0} & \cdots & \xi_{1,M} \\
\xi_{2,0} & \cdots & \xi_{2,M} \\
\cdots & \ddots & \cdots \\
\cdots & \ddots & \cdots \\
\cdots & \ddots & \cdots \\
\xi_{N-2,0} & \cdots & \xi_{N-2,M} \\
\xi_{N-1,0} & \cdots & \xi_{N-1,M}
\end{pmatrix}
\tag{55}
$$

where

$$
\kappa_{n,s} =
\begin{cases}
\displaystyle\sum_{j=0}^{M} a_{n,j} T_{T,j}(0), & s=0, \quad n=1,\ldots,N-1, \\
\displaystyle\sum_{j=0}^{M} a_{n,j} T_{T,j}^{(1)}(t_{M,s}^{T}), & n=1,\ldots,N-1, \quad s=1,\ldots,M
\end{cases}
\tag{56}
$$

and

$$
\xi_{l,m} =
\begin{cases}
\tau_n, & s=0, \quad n=1,\ldots,N-1, \\
F_n\Big(t_{M,s}^{T}, \displaystyle\sum_{j=0}^{M} a_{1,j} T_{T,j}(t_{M,s}^{T}), \ldots, \displaystyle\sum_{j=0}^{M} a_{N-1,j} T_{T,j}(t_{M,s}^{T})\Big), & n=1,\ldots,N-1, \quad s=1,\ldots,M
\end{cases}
\tag{57}
$$

The system of algebraic equations can be solved using Newton's iterative method. After the coefficients $a_{i,j}$ are determined, the approximate solution $u_{N,M}(x,t)$ can be computed at any value of (x,t) in the given domain from

$$
u_{N,M}(x,t) = \sum_{k=0}^{M} \sum_{i=0}^{N} \sum_{j=0}^{N} a_{i,k} \left(\frac{P_{L,j}(x_{N,i}^{L}) \varpi_{N,i}^{L}}{h_j^{L}} \right) P_{L,j}(x) T_{T,k}(t)
\tag{58}
$$

4. Two-dimensional space fractional percolation equations

In this section, we develop the algorithm for one-dimensional FPEs to handle the following two-dimensional space FPE

$$
\partial_t u(x,y,t) = \partial_x^{v_1}\Big(g_1(x,y)\partial_x^{v_2} u(x,y,t)\Big) + \partial_y^{v_3}\Big(g_2(x,y)\partial_y^{v_4} u(x,y,t)\Big) + f(x,y,t),
$$

$$
0 < v_1,\, v_2,\, v_3,\, v_4 < 1,\ (x,y,t) \in [0,L_1] \times [0,L_2] \times [0,T]
\tag{59}
$$

with the initial condition

$$
u(x,y,0) = g_3(x,y), \quad (x,y) \in [0,L_1] \times [0,L_2]
\tag{60}
$$

and four boundary conditions

$$
\begin{aligned}
&u(0,y,t) = g_4(y,t), \quad u(L_1,y,t) = g_5(y,t), \\
&\quad (y,t) \in [0,L_2] \times [0,T], \\
&u(x,0,t) = g_6(x,t), u(x,L_2,t) = g_7(x,t) \\
&\quad (x,t) \in [0,L_1] \times [0,T]
\end{aligned}
\tag{61}
$$

4.1. SL-GL-C scheme for the space variable

The SL-GL-C method will be extended to reduce the solution of the previous FPE into SODEs. Let us expand the dependent variable in the form

$$
u_{N,M}(x,y,t) = \sum_{j=0}^{M} \sum_{i=0}^{N} a_{i,j}(t) P_{L_1,i}(x) P_{L_2,j}(y)
\tag{62}
$$

The coefficients $a_{i,j}(t)$ can be approximated by

$$
\begin{aligned}
a_{i,j}(t) = \frac{1}{h_i^{L_1} h_j^{L_2}} \sum_{l=0}^{N} \sum_{k=0}^{M} \Big(&P_{L_2,j}(y_{M,k}^{L_2}) \varpi_{M,k}^{L_2} P_{L_1,i}(x_{N,l}^{L_1}) \varpi_{N,l}^{L_1} \Big) \\
&\times u(x_{N,l}^{L_1}, y_{M,k}^{L_2}, t)
\end{aligned}
\tag{63}
$$

Hence we can rewrite $u_{N,M}(x,y,t)$ as

$$
\begin{aligned}
u_{N,M}(x,y,t) = \sum_{j=0}^{M} \sum_{i=0}^{N} \sum_{l=0}^{N} \sum_{k=0}^{M} \\
\times \frac{\Big(P_{L_2,j}(y_{M,k}^{L_2}) \varpi_{M,k}^{L_2} P_{L_1,i}(x_{N,l}^{L_1}) \varpi_{N,l}^{L_1} \Big)}{h_i^{L_1} h_j^{L_2}} \\
\times P_{L_1,i}(x) P_{L_2,j}(y) u_{l,k}(t)
\end{aligned}
\tag{64}
$$

where $u_{N,M}(x_{N,n}, y_{M,m}, t) = u_{n,m}(t)$.

Similarly to equations (34)–(38), we compute the fractional spatial partial derivatives as

$$
\partial_x^{v_2} u(x,y,t)
$$
$$
= \sum_{l=0}^{N} \sum_{k=0}^{M} \sum_{j=0}^{M} \sum_{i=0}^{N} \frac{\left(P_{L_2,j}(y_{M,k}^{L_2}) \varpi_{M,k}^{L_2} P_{L_1,i}(x_{N,l}^{L_1}) \varpi_{N,l}^{L_1} \right)}{h_i^{L_1} h_j^{L_2}}
$$
$$
\times P_{L_1,i}^{(v_2)}(x) P_{L_2,j}(y)\, u_{l,k}(t), \tag{65}
$$

$$
\partial_y^{v_4} u(x,y,t)
$$
$$
= \sum_{l=0}^{N} \sum_{k=0}^{M} \sum_{j=0}^{M} \sum_{i=0}^{N} \frac{\left(P_{L_2,j}(y_{M,k}^{L_2}) \varpi_{M,k}^{L_2} P_{L_1,i}(x_{N,l}^{L_1}) \varpi_{N,l}^{L_1} \right)}{h_i^{L_1} h_j^{L_2}}
$$
$$
\times P_{L_2,j}^{(v_4)}(y) P_{L_1,i}(x)\, u_{l,k}(t), \tag{66}
$$

$$
\partial_x^{v_1}\left(\partial_x^{v_2} u(x,y,t) \right)
$$
$$
= \sum_{l=0}^{N} \sum_{k=0}^{M} \sum_{j=0}^{M} \sum_{i=0}^{N} \frac{\left(P_{L_2,j}(y_{M,k}^{L_2}) \varpi_{M,k}^{L_2} P_{L_1,i}(x_{N,l}^{L_1}) \varpi_{N,l}^{L_1} \right)}{h_i^{L_1} h_j^{L_2}}
$$
$$
\times P_{L_1,i}^{(v_1+v_2)}(x) P_{L_2,j}(y)\, u_{l,k}(t), \tag{67}
$$

$$
\partial_y^{v_3}\left(\partial_y^{v_4} u(x,y,t) \right)
$$
$$
= \sum_{l=0}^{N} \sum_{k=0}^{M} \sum_{j=0}^{M} \sum_{i=0}^{N} \frac{\left(P_{L_2,j}(y_{M,k}^{L_2}) \varpi_{M,k}^{L_2} P_{L_1,i}(x_{N,l}^{L_1}) \varpi_{N,l}^{L_1} \right)}{h_i^{L_1} h_j^{L_2}}
$$
$$
\times P_{L_2,j}^{(v_3+v_4)}(y) P_{L_1,i}(x)\, u_{l,k}(t) \tag{68}
$$

The previous fractional derivatives can be evaluated at the SL-GL interpolation nodes for $n = 1, 2, \ldots, N-1$, $m = 1, 2, \ldots, M-1$, as follows

$$
\left(\partial_x^{v_2} u(x,y,t) \right)_{y=y_{M,m}^{L_2}}^{x=x_{N,n}^{L_1},} = \sum_{l=0}^{N} \sum_{k=0}^{M} \rho_{l,k}^{n,m} u_{l,k}(t) \tag{69}
$$

$$
\left(\partial_x^{v_1}\left(\partial_x^{v_2} u(x,y,t) \right) \right)_{y=y_{M,m}^{L_2}}^{x=x_{N,n}^{L_1},} = \sum_{l=0}^{N} \sum_{k=0}^{M} \sigma_{l,k}^{n,m} u_{l,k}(t) \tag{70}
$$

$$
\left(\partial_y^{v_4} u(x,y,t) \right)_{y=y_{M,m}^{L_2}}^{x=x_{N,n}^{L_1},} = \sum_{l=0}^{N} \sum_{k=0}^{M} \lambda_{l,k}^{n,m} u_{l,k}(t) \tag{71}
$$

$$
\left(\partial_y^{v_3}\left(\partial_y^{v_4} u(x,y,t) \right) \right)_{y=y_{M,m}^{L_2}}^{x=x_{N,n}^{L_1},} = \sum_{l=0}^{N} \sum_{k=0}^{M} \mu_{l,k}^{n,m} u_{l,k}(t) \tag{72}
$$

where

$$
\rho_{l,k}^{n,m} = \sum_{i=0}^{N} \sum_{j=0}^{M} \frac{\left(P_{L_2,j}(y_{M,k}^{L_2}) \varpi_{M,k}^{L_2} P_{L_1,i}(x_{N,l}^{L_1}) \varpi_{N,l}^{L_1} \right)}{h_i^{L_1} h_j^{L_2}}
$$
$$
\times \left(P_{L_1,i}^{(v_2)}(x) \right)_{x=x_{N,n}^{L_1}} P_{L_2,j}(y_{M,m}^{L_2}) \tag{73}
$$

$$
\sigma_{l,k}^{n,m} = \sum_{i=0}^{N} \sum_{j=0}^{M} \frac{\left(P_{L_2,j}(y_{M,k}^{L_2}) \varpi_{M,k}^{L_2} P_{L_1,i}(x_{N,l}^{L_1}) \varpi_{N,l}^{L_1} \right)}{h_i^{L_1} h_j^{L_2}}
$$
$$
\times \left(P_{L_1,i}^{(v_1+v_2)}(x) \right)_{x=x_{N,n}^{L_1}} P_{L_2,j}(y_{M,m}^{L_2}), \tag{74}
$$

$$
\lambda_{l,k}^{n,m} = \sum_{i=0}^{N} \sum_{j=0}^{M} \frac{\left(P_{L_2,j}(y_{M,k}^{L_2}) \varpi_{M,k}^{L_2} P_{L_1,i}(x_{N,l}^{L_1}) \varpi_{N,l}^{L_1} \right)}{h_i^{L_1} h_j^{L_2}}
$$
$$
\times \left(P_{L_2,j}^{(v_4)}(y) \right)_{y=y_{M,m}^{L_2}} P_{L_1,i}(x_{N,n}^{L_1}), \tag{75}
$$

$$
\mu_{l,k}^{n,m} = \sum_{i=0}^{N} \sum_{j=0}^{M} \frac{\left(P_{L_2,j}(y_{M,k}^{L_2}) \varpi_{M,k}^{L_2} P_{L_1,i}(x_{N,l}^{L_1}) \varpi_{N,l}^{L_1} \right)}{h_i^{L_1} h_j^{L_2}}
$$
$$
\times \left(P_{L_2,j}^{(v_3+v_4)}(y) \right)_{y=y_{M,m}^{L_2}} P_{L_1,i}(x_{N,n}^{L_1}) \tag{76}
$$

In the proposed SL-GL-C method, the residual of equation (59) is set to zero at $(N-1) \times (M-1)$ SL-GL points. Moreover, the values of $u_{0,k}(t)$, $u_{N,k}(t)$, $u_{l,0}(t)$ and $u_{l,N}(t)$ can be given by

$$
u_{0,k}(t) = g_7(y_{M,k}^{L_2}, t), \quad u_{N,k}(t) = g_8(y_{M,k}^{L_2}, t), \quad k = 0, \ldots, M,
$$
$$
u_{l,0}(t) = g_9(x_{N,l}^{L_1}, t), \quad u_{l,N}(t) = g_{10}(x_{N,l}^{L_1}, t), \quad l = 0, \ldots, N \tag{77}
$$

the combination of equations (64)–(77), with equations (59)–(61) leads us to the $(N-1) \times (M-1)$ SODEs

$$
\dot{u}_{n,m}(t) = g_8(x_{N,n}^{L_1}, y_{M,m}^{L_2}) \sum_{l=0}^{N} \sum_{k=0}^{M} \rho_{l,k}^{n,m} u_{l,k}(t) + g_1(x_{N,n}^{L_1}, y_{M,m}^{L_2})
$$
$$
\times \sum_{l=0}^{N} \sum_{k=0}^{M} \sigma_{l,k}^{n,m} u_{l,k}(t) + g_9(x_{N,n}^{L_1}, y_{M,m}^{L_2})
$$
$$
\times \sum_{l=0}^{N} \sum_{k=0}^{M} \lambda_{l,k}^{n,m} u_{l,k}(t) + g_2(x_{N,n}^{L_1}, y_{M,m}^{L_2})
$$
$$
\times \sum_{l=0}^{N} \sum_{k=0}^{M} \mu_{l,k}^{n,m} u_{l,k}(t) + f(x_{N,n}^{L_1}, y_{M,m}^{L_2}, t),
$$
$$
n = 1, \ldots, N-1, \quad m = 1, \ldots, M-1 \tag{78}
$$

subject to the initial conditions

$$u_{n,m}(0) = g_3(x_{N,n}^{L_1}, y_{M,m}^{L_2}) = g_3^{n,m}, \quad n = 1, \ldots, N-1,$$
$$m = 1, \ldots, M-1$$

(79)

where

$$g_8(x_{N,n}^{L_1}, y_{M,m}^{L_2}) = \left(\partial_x^{\nu_1} g_1(x,y) \right)_{y=y_{M,m}^{L_2}}^{x=x_{N,n}^{L_1}},$$
$$g_9(x_{N,n}^{L_1}, y_{M,m}^{L_2}) = \left(\partial_y^{\nu_3} g_2(x,y) \right)_{y=y_{M,m}^{L_2}}^{x=x_{N,n}^{L_1}}$$

(80)

Finally, we can rearrange equations (78)–(79) to their matrix formulation

$$\times \sum_{l=0}^{N} \sum_{k=0}^{M} \sigma_{l,k}^{n,m} u_{l,k}(t) + g_9(x_{N,n}^{L_1}, y_{M,m}^{L_2}) \sum_{l=0}^{N} \sum_{k=0}^{M} \lambda_{l,k}^{n,m} u_{l,k}(t)$$
$$+ g_2(x_{N,n}^{L_1}, y_{M,m}^{L_2}) \sum_{l=0}^{N} \sum_{k=0}^{M} \mu_{l,k}^{n,m} u_{l,k}(t) + f(x_{N,n}^{L_1}, y_{M,m}^{L_2}, t),$$
$$n = 1, \ldots, N-1, \quad m = 1, \ldots, M-1 \quad (83)$$

4.2. SC-GR-C scheme for the time variable

We are interested in using the SC-GR-C method to transform the SODEs (81) subject to equation (82) into a system of algebraic equations. To this end, we approximate the time variable using the following approximation

$$
\begin{pmatrix}
\dot{u}_{1,1}(t) & \cdots & \dot{u}_{1,M-1}(t) \\
\dot{u}_{2,1}(t) & \vdots & \dot{u}_{2,M-1}(t) \\
\cdots & \ddots & \cdots \\
\cdots & \ddots & \cdots \\
\cdots & \ddots & \cdots \\
\dot{u}_{N-2,1}(t) & \vdots & \dot{u}_{N-2,M-1}(t) \\
\dot{u}_{N-1,1}(t) & \cdots & \dot{u}_{N-1,M-1}(t)
\end{pmatrix}
=
\begin{pmatrix}
H_{1,1}(t,u_1,\ldots,u_{N-1}) & \cdots & H_{1,M-1}(t,u_1,\ldots,u_{N-1}) \\
H_{2,1}(t,u_1,\ldots,u_{N-1}) & \vdots & H_{2,M-1}(t,u_1,\ldots,u_{N-1}) \\
\cdots & \ddots & \cdots \\
\cdots & \ddots & \cdots \\
\cdots & \ddots & \cdots \\
H_{N-2,1}(t,u_1,\ldots,u_{N-1}) & \vdots & H_{N-2,M-1}(t,u_1,\ldots,u_{N-1}) \\
H_{N-1,1}(t,u_1,\ldots,u_{N-1}) & \cdots & H_{N-1,M-1}(t,u_1,\ldots,u_{N-1})
\end{pmatrix}
$$

(81)

$$
\begin{pmatrix}
u_{1,1}(0) & \cdots & u_{1,M-1}(0) \\
u_{2,1}(0) & \vdots & u_{2,M-1}(0) \\
\cdots & \ddots & \cdots \\
\cdots & \ddots & \cdots \\
\cdots & \ddots & \cdots \\
u_{N-2,1}(0) & \vdots & u_{N-2,M-1}(0) \\
u_{N-1,1}(0) & \cdots & u_{N-1,M-1}(0)
\end{pmatrix}
=
\begin{pmatrix}
g_3^{1,1} & \cdots & g_3^{1,M-1} \\
g_3^{2,1} & \vdots & g_3^{2,M-1} \\
\cdots & \ddots & \cdots \\
\cdots & \ddots & \cdots \\
\cdots & \ddots & \cdots \\
g_3^{N-2,1} & \vdots & g_3^{N-2,M-1} \\
g_3^{N-1,1} & \cdots & g_3^{N-1,M-1}
\end{pmatrix}
$$

(82)

where

$$H_{n,m}(t, u_{1,1}, \ldots, u_{N-1,M-1})$$
$$= g_8(x_{N,n}^{L_1}, y_{M,m}^{L_2}) \times \sum_{l=0}^{N} \sum_{k=0}^{M} \rho_{l,k}^{n,m} u_{l,k}(t) + g_1(x_{N,n}^{L_1}, y_{M,m}^{L_2})$$

$$u_{n,m,K}(t) = \sum_{k=0}^{K} a_k^{n,m} T_{T,k}(t), \quad n = 1, \ldots, N-1,$$
$$m = 1, \ldots, M-1$$

(84)

This allows us to immediately obtain the time derivative of the approximate solution in the form

$$\partial_t u_{n,m}(t) = \sum_{k=0}^{K} a_k^{n,m} \partial_t (T_{T,k}(t)) = \sum_{k=0}^{K} a_k^{n,m} T_{T,k}^{(1)}(t),$$

$$n = 1, \ldots, N-1, \quad m = 1, \ldots, M-1 \qquad (85)$$

Combining equations (81)–(85), enables us to write

$$
\begin{pmatrix}
\sum_{k=0}^{K} a_k^{1,1} T_{T,k}^{(1)}(t) & \cdots & \sum_{k=0}^{K} a_k^{1,M-1} T_{T,k}^{(1)}(t) \\
\sum_{k=0}^{K} a_k^{2,1} T_{T,k}^{(1)}(t) & \vdots & \sum_{k=0}^{K} a_k^{2,M-1} T_{T,k}^{(1)}(t) \\
\cdots & \ddots & \cdots \\
\cdots & \ddots & \cdots \\
\cdots & \ddots & \cdots \\
\sum_{k=0}^{K} a_k^{N-2,1} T_{T,k}^{(1)}(t) & \vdots & \sum_{k=0}^{K} a_k^{N-2,M-1} T_{T,k}^{(1)}(t) \\
\sum_{k=0}^{K} a_k^{N-1,1} T_{T,k}^{(1)}(t) & \cdots & \sum_{k=0}^{K} a_k^{N-1,M-1} T_{T,k}^{(1)}(t)
\end{pmatrix}
=
\begin{pmatrix}
\eta_{1,1}(t) & \cdots & \eta_{1,M-1}(t) \\
\eta_{2,1}(t) & \cdots & \eta_{2,M-1}(t) \\
\cdots & \ddots & \cdots \\
\cdots & \ddots & \cdots \\
\cdots & \ddots & \cdots \\
\eta_{N-2,1}(t) & \cdots & \eta_{N-2,M-1}(t) \\
\eta_{N-1,1}(t) & \cdots & \eta_{N-1,M-1}(t)
\end{pmatrix},
\qquad (86)
$$

$$
\begin{pmatrix}
\sum_{k=0}^{K} a_k^{1,1} T_{T,k}(0) & \cdots & \sum_{k=0}^{K} a_k^{1,M-1} T_{T,k}(0) \\
\sum_{k=0}^{K} a_k^{2,1} T_{T,k}(0) & \cdots & \sum_{k=0}^{K} a_k^{2,M-1} T_{T,k}(0) \\
\cdots & \ddots & \cdots \\
\cdots & \ddots & \cdots \\
\cdots & \ddots & \cdots \\
\sum_{k=0}^{K} a_k^{N-2,1} T_{T,k}(0) & \cdots & \sum_{k=0}^{K} a_k^{N-2,M-1} T_{T,k}(0) \\
\sum_{k=0}^{K} a_k^{N-1,1} T_{T,k}(0) & \cdots & \sum_{k=0}^{K} a_k^{N-1,M-1} T_{T,k}(0)
\end{pmatrix}
=
\begin{pmatrix}
g_3^{1,1} & \cdots & g_3^{1,M-1} \\
g_3^{2,1} & \vdots & g_3^{2,M-1} \\
\cdots & \ddots & \cdots \\
\cdots & \ddots & \cdots \\
\cdots & \ddots & \cdots \\
g_3^{N-2,1} & \vdots & g_3^{N-2,M-1} \\
g_3^{N-1,1} & \cdots & g_3^{N-1,M-1}
\end{pmatrix}
\qquad (87)
$$

where $\eta_{n,m}(t) = H_{n,m}\left(t, \sum_{k=0}^{K} a_k^{1,1} T_{T,k}(t), \ldots, \sum_{k=0}^{K} a_k^{N-1,M-1} T_{T,k}(t)\right)$.

In the proposed method, the residual of equation (86) is set to be zero at $K \times (N-1) \times (M-1)$ collocation points.

$$\sum_{k=0}^{K} a_k^{n,m} T_{T,k}^{(1)}(t_{K,s}^T) = \eta_{n,m}(t_{K,s}^T), \quad n = 1, \ldots, N-1,$$

$$m = 1, \ldots, M-1, \quad s = 1, \ldots, K \qquad (88)$$

according to initial conditions, we have another $(N-1) \times (M-1)$ algebraic equations

$$\sum_{k=0}^{K} a_k^{n,m} T_{T,k}(0) = g_3^{n,m}, \quad n = 1, \ldots, N-1,$$

$$m = 1, \ldots, M-1 \qquad (89)$$

Finally, we can merge the previous equations (88) and (89) in the following matrix system form

$$\Omega = \Psi \qquad (90)$$

where

$$
\Omega = \begin{pmatrix}
\begin{pmatrix} \mathfrak{J}_0^{1,1} \\ \mathfrak{J}_1^{1,1} \\ \cdots \\ \cdots \\ \mathfrak{J}_{K-1}^{1,1} \\ \mathfrak{J}_K^{1,1} \end{pmatrix} &
\begin{pmatrix} \mathfrak{J}_0^{1,2} \\ \mathfrak{J}_1^{1,2} \\ \cdots \\ \cdots \\ \mathfrak{J}_{K-1}^{1,2} \\ \mathfrak{J}_K^{1,2} \end{pmatrix} & \cdots &
\begin{pmatrix} \mathfrak{J}_0^{1,M-2} \\ \mathfrak{J}_1^{1,M-2} \\ \cdots \\ \cdots \\ \mathfrak{J}_{K-1}^{1,M-2} \\ \mathfrak{J}_K^{1,M-2} \end{pmatrix} &
\begin{pmatrix} \mathfrak{J}_0^{1,M-1} \\ \mathfrak{J}_1^{1,M-1} \\ \cdots \\ \cdots \\ \mathfrak{J}_{K-1}^{1,M-1} \\ \mathfrak{J}_K^{1,M-1} \end{pmatrix} \\
\cdots & \cdots & \ddots & \cdots & \cdots \\
\cdots & \cdots & \ddots & \cdots & \cdots \\
\cdots & \cdots & \ddots & \cdots & \cdots \\
\begin{pmatrix} \mathfrak{J}_0^{N-1,1} \\ \mathfrak{J}_1^{N-1,1} \\ \cdots \\ \cdots \\ \mathfrak{J}_{K-1}^{N-1,1} \\ \mathfrak{J}_K^{N-1,1} \end{pmatrix} &
\begin{pmatrix} \mathfrak{J}_0^{N-1,2} \\ \mathfrak{J}_1^{N-1,2} \\ \cdots \\ \cdots \\ \mathfrak{J}_{K-1}^{N-1,2} \\ \mathfrak{J}_K^{N-1,2} \end{pmatrix} & \cdots &
\begin{pmatrix} \mathfrak{J}_0^{N-1,M-2} \\ \mathfrak{J}_1^{N-1,M-2} \\ \cdots \\ \cdots \\ \mathfrak{J}_{K-1}^{N-1,M-2} \\ \mathfrak{J}_K^{N-1,M-2} \end{pmatrix} &
\begin{pmatrix} \mathfrak{J}_0^{N-1,M-1} \\ \mathfrak{J}_1^{N-1,M-1} \\ \cdots \\ \cdots \\ \mathfrak{J}_{K-1}^{N-1,M-1} \\ \mathfrak{J}_K^{N-1,M-1} \end{pmatrix}
\end{pmatrix}, \tag{91}
$$

$$
\Psi = \begin{pmatrix}
\begin{pmatrix} \mathfrak{R}_0^{1,1} \\ \mathfrak{R}_1^{1,1} \\ \cdots \\ \cdots \\ \mathfrak{R}_{K-1}^{1,1} \\ \mathfrak{R}_K^{1,1} \end{pmatrix} &
\begin{pmatrix} \mathfrak{R}_0^{1,2} \\ \mathfrak{R}_1^{1,2} \\ \cdots \\ \cdots \\ \mathfrak{R}_{K-1}^{1,2} \\ \mathfrak{R}_K^{1,2} \end{pmatrix} & \cdots &
\begin{pmatrix} \mathfrak{R}_0^{1,M-2} \\ \mathfrak{R}_1^{1,M-2} \\ \cdots \\ \cdots \\ \mathfrak{R}_{K-1}^{1,M-2} \\ \mathfrak{R}_K^{1,M-2} \end{pmatrix} &
\begin{pmatrix} \mathfrak{R}_0^{1,M-1} \\ \mathfrak{R}_1^{1,M-1} \\ \cdots \\ \cdots \\ \mathfrak{R}_{K-1}^{1,M-1} \\ \mathfrak{R}_K^{1,M-1} \end{pmatrix} \\
\cdots & \cdots & \ddots & \cdots & \cdots \\
\cdots & \cdots & \ddots & \cdots & \cdots \\
\cdots & \cdots & \ddots & \cdots & \cdots \\
\begin{pmatrix} \mathfrak{R}_0^{N-1,1} \\ \mathfrak{R}_1^{N-1,1} \\ \cdots \\ \cdots \\ \mathfrak{R}_{K-1}^{N-1,1} \\ \mathfrak{R}_K^{N-1,1} \end{pmatrix} &
\begin{pmatrix} \mathfrak{R}_0^{N-1,2} \\ \mathfrak{R}_1^{N-1,2} \\ \cdots \\ \cdots \\ \mathfrak{R}_{K-1}^{N-1,2} \\ \mathfrak{R}_K^{N-1,2} \end{pmatrix} & \cdots &
\begin{pmatrix} \mathfrak{R}_0^{N-1,M-2} \\ \mathfrak{R}_1^{N-1,M-2} \\ \cdots \\ \cdots \\ \mathfrak{R}_{K-1}^{N-1,M-2} \\ \mathfrak{R}_K^{N-1,M-2} \end{pmatrix} &
\begin{pmatrix} \mathfrak{R}_0^{N-1,M-1} \\ \mathfrak{R}_1^{N-1,M-1} \\ \cdots \\ \cdots \\ \mathfrak{R}_{K-1}^{N-1,M-1} \\ \mathfrak{R}_K^{N-1,M-1} \end{pmatrix}
\end{pmatrix}, \tag{92}
$$

$$
\mathfrak{J}_s^{n,m} = \begin{cases} \sum\limits_{k=0}^{K} a_k^{n,m} T_{T,k}(0), & s=0, \quad n=1,\dots,N-1, \quad m=1,\dots,M-1, \\ \sum\limits_{k=0}^{K} a_k^{n,m} T_{T,k}^{(1)}(t_{K,s}^T), & n=1,\dots,N-1, \quad m=1,\dots,M-1, \quad s=1,\dots,K \end{cases} \tag{93}
$$

and

$$
\xi_{l,m} = \begin{cases} g_3^{n,m}, & s=0, \quad n=1,\dots,N-1, \quad m=1,\dots,M-1; \\ \eta_{n,m}(t_{K,s}^T), & n=1,\dots,N-1, \quad m=1,\dots,M-1, \quad s=1,\dots,K \end{cases} \tag{94}
$$

Finally, from equations (91)–(94), we get a system of $(N-1) \times (M-1) \times (K+1)$ algebraic equations. This system can be solved by any iteration technique. Then, the approximate solution $u_{N,M,K}(x,y,t)$ can be evaluated as

$$u_{N,M,K}(x,y,t)$$

$$= \sum_{r=0}^{K} \sum_{j=0}^{M} \sum_{i=0}^{N} \sum_{l=0}^{N} \sum_{k=0}^{M} a_r^{l,k} \frac{\left(P_{L_2,j}(y_{M,k}^{L_2}) \varpi_{M,k}^{L_2} P_{L_1,i}(x_{N,l}^{L_1}) \varpi_{N,l}^{L_1} \right)}{h_i^{L_1} h_j^{L_2}}$$

$$\times P_{L_1,i}(x) P_{L_2,j}(y) T_{T,r}(t) \tag{95}$$

4.3. Error bound

In this subsection, we present an analytic expression for the error norm of the best approximation for a smooth function $u(x,y,t) \in \Omega \equiv [0,L_1] \times [0,L_2] \times [0,T]$ by its expansion

$$u_{N,M,K}(x,y,t) = \sum_{k=0}^{K} \sum_{i=0}^{N} \sum_{j=0}^{M} \pi_{i,j,k} P_{L_1,i}(x) P_{L_2,j}(y) T_{T,k}(t) \tag{96}$$

where

$$\pi_{i,j,k} = \sum_{l=0}^{N} \sum_{r=0}^{M} a_k^{l,r} \frac{\left(P_{L_2,j}(y_{M,r}^{L_2}) \varpi_{M,r}^{L_2} P_{L_1,i}(x_{N,l}^{L_1}) \varpi_{N,l}^{L_1} \right)}{\hbar_i \hbar_j} \tag{97}$$

at any value of (x,y,t) in the given domain. Here we provide an upper bound on the error expected in our approximations in the two-dimensional case and for the one-dimensional case we refer the reader to Bhrawy and Zaky (2015a).

Let us first consider the space

$$\Pi^{N,M,K} = \mathrm{span}\{P_{L_1,i}(x) P_{L_2,j}(y) T_{T,k}(t), \ i = 0, 1, \ldots, N,$$
$$j = 0, 1, \ldots, M, \ k = 0, 1, \ldots, K\}$$

In the following analysis it will always be assumed that $u_{N,M,K}(x,y,t) \in {}^{N,M,K}$ is the best approximation of $u(x,y,t)$, then by the definition of the best approximation, we have

$$\forall \ v_{N,M,K}(x,y,t) \in \Pi^{N,M,K},$$
$$\left\| u(x,y,t) - u_{N,M,K}(x,y,t) \right\|_{\infty} \le \left\| u(x,y,t) \right.$$
$$\left. - v_{N,M,K}(x,y,t) \right\|_{\infty} \tag{98}$$

It turns out that the previous inequality is also true if $v_{N,M,K}(x,y,t)$ denotes the interpolating polynomial for

$u(x,y,t)$ at points $(x_{N,i}^{L_1}, y_{M,j}^{L_2}, t_{K,k}^T)$, where $t_{K,k}^T$, $(0 \le k \le K)$ are the shifted Chebyshev Gauss–Radau points and $x_{N,i}^{L_1}$, $(0 \le i \le N)$ and $y_{M,j}^{L_2}$, $(0 \le j \le M)$ are the shifted Legendre Gauss–Lobatto collocation points. Then by similar procedures to those in Bhrawy and Zaky (2015a), we can write

$$u(x,y,t) - v_{N,M,K}(x,y,t) = \frac{\partial^{N+1} u(\epsilon_1, y, t)}{\partial x^{N+1}(N+1)!} \prod_{i=0}^{N} (x - x_{N,i}^{L_1})$$

$$+ \frac{\partial^{M+1} u(x, \epsilon_2, t)}{\partial y^{M+1}(M+1)!} \prod_{j=0}^{M} (y - y_{M,j}^{L_2})$$

$$+ \frac{\partial^{K+1} u(x, y, \epsilon_3)}{\partial t^{K+1}(K+1)!} \prod_{k=0}^{K} (t - t_{K,k}^T)$$

$$- \frac{\partial^{N+M+K+3} u(\epsilon_1', \epsilon_2', \epsilon_3')}{\partial x^{N+1} \partial y^{M+1} \partial t^{K+1} (M+1)!(N+1)!(K+1)!}$$

$$\times \prod_{i=0}^{N} (x - x_{N,i}^{L_1}) \prod_{j=0}^{M} (y - y_{M,j}^{L_2}) \prod_{k=0}^{K} (t - t_{K,k}^T) \tag{99}$$

where $\varepsilon_1, \ \varepsilon_1' \in [0, L_1]$, $\varepsilon_2, \ \varepsilon_2' \in [0, L_2]$ and $\varepsilon_3, \ \varepsilon_3' \in [0, T]$, and thereby we obtain that

$$\left\| u(x,y,t) - v_{N,M,K}(x,y,t) \right\|_{\infty}$$

$$\le \max_{(x,y,t) \in \Omega} \left| \frac{\partial^{N+1} u(\epsilon_1, y, t)}{\partial x^{N+1}} \right| \frac{\left\| \prod_{i=0}^{N} (x - x_{N,i}^{L_1}) \right\|_{\infty}}{(N+1)!}$$

$$+ \max_{(x,y,t) \in \Omega} \left| \frac{\partial^{M+1} u(x, \epsilon_2, t)}{\partial y^{M+1}} \right| \frac{\left\| \prod_{j=0}^{M} (y - y_{M,j}^{L_2}) \right\|_{\infty}}{M+1)!}$$

$$+ \max_{(x,y,t) \in \Omega} \left| \frac{\partial^{K+1} u(x, y, \epsilon_3)}{\partial t^{K+1}} \right| \frac{\left\| \prod_{k=0}^{K} (t - t_{K,k}^T) \right\|_{\infty}}{(K+1)!}$$

$$+ \max_{(x,y,t) \in \Omega} \left| \frac{\partial^{N+M+K+3} u(\varepsilon_1', \varepsilon_2', \varepsilon_3')}{\partial x^{N+1} \partial y^{M+1} \partial t^{K+1}} \right|$$

$$\times \frac{\left\| \prod_{i=0}^{N} (x - x_{N,i}^{L_1}) \right\|_{\infty} \left\| \prod_{j=0}^{M} (y - y_{M,j}^{L_2}) \right\|_{\infty} \left\| \prod_{k=0}^{K} (t - t_{K,k}^T) \right\|_{\infty}}{(K+1)!(N+1)!(M+1)!} \tag{100}$$

Since $u(x,y,t)$ is a smooth function on Ω, then there exists the constants C_1, C_2, C_3 and C_4, such that

$$\max_{(x,y,t) \in \Omega} \left| \frac{\partial^{N+1} u(x,y,t)}{\partial x^{N+1}} \right| \le C_1,$$

$$\max_{(x,y,t) \in \Omega} \left| \frac{\partial^{M+1} u(x,y,t)}{\partial y^{M+1}} \right| \le C_2,$$

$$\max_{(x,y,t)\in\Omega}\left|\frac{\partial^{K+1}u(x,y,t)}{\partial t^{K+1}}\right|\le C_3,$$

$$\max_{(x,y,t)\in\Omega}\left|\frac{\partial^{N+M+K+3}u(x,t)}{\partial x^{N+1}\partial y^{M+1}\partial t^{K+1}}\right|\le C_4 \tag{101}$$

Here, we try to reduce the error in the polynomial approximation by minimizing the factor $\left\|\prod_{i=0}^{N}(x-x_{N,i}^{L_1})\right\|_\infty$. Let us use the one-to-one mapping $x=\frac{L_1}{2}(z+1)$ between the intervals $[-1,1]$ and $[0,L_1]$ to deduce that

$$\begin{aligned}
&\min_{x_{N,i}^{L_1}\in[0,L_1]}\max_{0\le x\le L_1}\left|\prod_{i=0}^{N}(x-x_{N,i}^{L_1})\right|\\
&=\min_{z_i\in[-1,1]}\max_{-1\le z\le1}\left|\prod_{i=0}^{N}\frac{L_1}{2}(z-z_i)\right|\\
&=\left(\frac{L_1}{2}\right)^{N+1}\min_{z_i\in[-1,1]}\max_{-1\le z\le1}\left|\prod_{i=0}^{N}(z-z_i)\right|\\
&=\left(\frac{L_1}{2}\right)^{N+1}\max_{-1\le z\le1}\left|\frac{P_{N+1}(z)}{\kappa_N}\right|
\end{aligned} \tag{102}$$

where $\kappa_N=\frac{(2N)!}{2^N(N!)^2}$ is the leading coefficient of $P_{N+1}(z)$ and z_i are the Legendre Gauss–Lobatto collocation points. It is a well-known fact (Canuto et al., 2006), that the Legendre and Chebyshev polynomials satisfy

$$\max_{-1\le z\le1}\left|P_{N+1}(z)\right|\le1 \quad \text{and} \quad \max_{-1\le z\le1}\left|T_{K+1}(z)\right|\le1$$

We can obtain

$$\left\|\prod_{i=0}^{N}(x-x_{N,i}^{L_1})\right\|_\infty\le\frac{(L_1/2)^{N+1}}{\kappa_N} \tag{103}$$

Also we can obtain

$$\left\|\prod_{k=0}^{K}(t-t_{K,k}^{T})\right\|_\infty\le\frac{(T/2)^{K+1}}{\kappa_K'} \tag{104}$$

where $\kappa_K'=2^K$ is the leading coefficient of $T_{K+1}(z)$.

Combining equations (100), (101), (103) and (104), yields

$$\begin{aligned}
\|u(x,y,t)-u_{N,M,K}(x,y,t)\|_\infty\le{}&C_1'\frac{(L_1/2)^{N+1}}{\kappa_N(N+1)!}\\
&+C_2'\frac{(L_2/2)^{M+1}}{\kappa_M(M+1)!}+C_3'\frac{(T/2)^{K+1}}{\kappa_K'(K+1)!}
\end{aligned}$$

$$+C_4'\frac{(L_1/2)^{N+1}(L_2/2)^{M+1}(T/2)^{K+1}}{\kappa_N\kappa_M\kappa_K'(N+1)!(M+1)!(K+1)!} \tag{105}$$

Hence, an upper bound of the absolute error is obtained for the approximate solutions. The convergence of the proposed method depends basically on the above error bound.

5. Numerical results and comparisons

After the construction of the spectral collocation methods, we now carry out some numerical examples of $1+1$ and $2+1$ FPEs to study the performance of the methods, which are discussed and developed in the current paper, and to compare our results with those proposed in Chen et al. (2011b, 2013, 2014). We divide this section into two main parts. In the first one, we introduce two examples of $1+1$ FPEs. Then, we deal with three numerical examples of $2+1$ FPEs in the second part.

5.1. Examples for one-dimensional space fractional percolation equations

Example 1. *Let us start with the following FPE (Chen et al., 2011b)*

$$\begin{aligned}
\partial_t u(x,t)={}&\partial_x\left((30-x^2)\partial_x^{0.5}u(x,t)\right)\\
&-\frac{e^{-t}(45\sqrt{x}-3.5x^{2.5})\Gamma(3)}{\Gamma(2.5)}\\
&-e^{-t}x^2,\ (x,t)\in[0,1]\times[0,1]
\end{aligned} \tag{106}$$

subject to

$$\begin{aligned}
u(x,0)=x^2,\quad x\in[0,1],\quad u(0,t)=0,\\
u(1,t)=e^{-t},\quad t\in[0,1]
\end{aligned} \tag{107}$$

The exact solution is $u(x,t)=e^{-t}x^2$.

Recently, Chen et al. (2011b) introduced approximate solutions to the previous problem with various choices of N and M using a novel implicit finite difference (NIFD) method. Now, we list in Table 1 a comparison based on the maximum absolute error (M_E) between the numerical method introduced in Chen et al. (2011b), and our results with choices of N and M, which are less than those in Chen et al. (2011b). We observe that the error, using the present method, decays exponentially with an increase in the collocation nodes N,M. In Table 2, we see the high accuracy of the present method based on absolute error at $N=M=12$.

A space–time graph of the error function between the exact and approximate solutions at $N=12$, is sketched in Figure 1. In addition, to confirm the high

Table 1. Comparing M_E of the proposed method with the NIFD (Chen et al., 2011b) method for problem (106).

N = M	SL-GL-C Method			NIFD (Chen et al., 2011b)	
	4	8	12	40	80
M_E	1.24×10^{-5}	1.94×10^{-11}	6.66×10^{-16}	1.52×10^{-7}	7.68×10^{-8}

Table 2. Absolute error at $N = M = 12$ and various choices of (x,t) for problem (106).

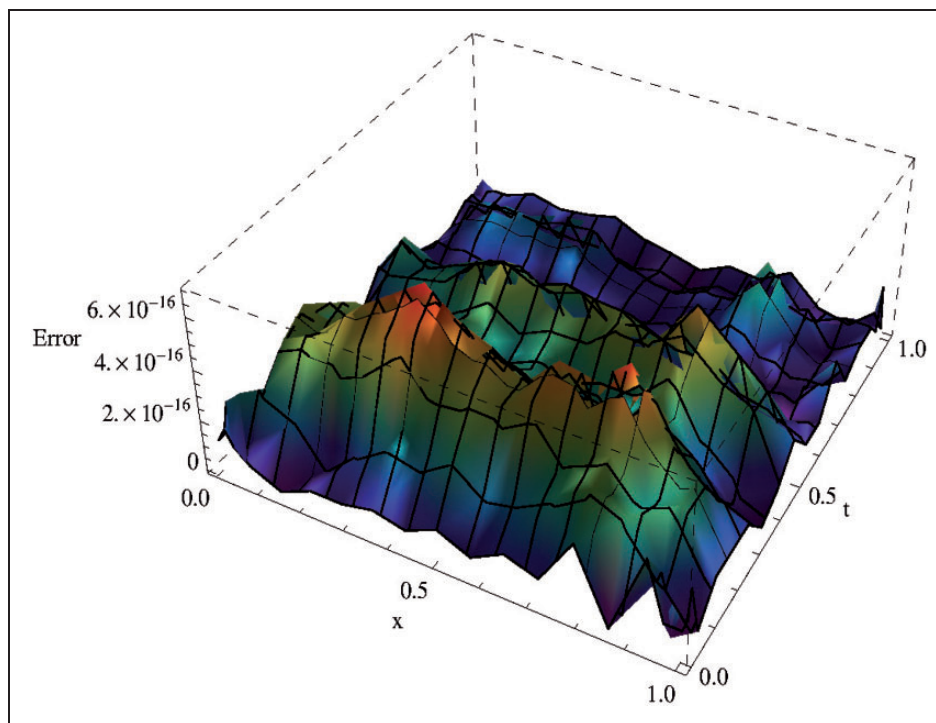| x	t	E(x,t)	x	t	E(x,t)	x	t	E(x,t)
0.1	0.1	3.33×10^{-16}	0.1	0.5	3.05×10^{-16}	0.1	1	1.11×10^{-16}
0.2		2.22×10^{-16}	0.2		3.33×10^{-16}	0.2		1.11×10^{-16}
0.3		3.05×10^{-16}	0.3		4.44×10^{-16}	0.3		1.38×10^{-16}
0.4		4.16×10^{-16}	0.4		5.13×10^{-16}	0.4		1.38×10^{-16}
0.5		3.33×10^{-16}	0.5		5.07×10^{-16}	0.5		5.89×10^{-17}
0.6		3.54×10^{-16}	0.6		4.61×10^{-16}	0.6		8.50×10^{-17}
0.7		3.05×10^{-16}	0.7		3.89×10^{-16}	0.7		1.04×10^{-16}
0.8		3.33×10^{-16}	0.8		5.27×10^{-16}	0.8		1.39×10^{-16}
0.9		1.67×10^{-16}	0.9		3.33×10^{-16}	0.9		0
1		1.11×10^{-16}	1		2.22×10^{-16}	1		1.11×10^{-16}

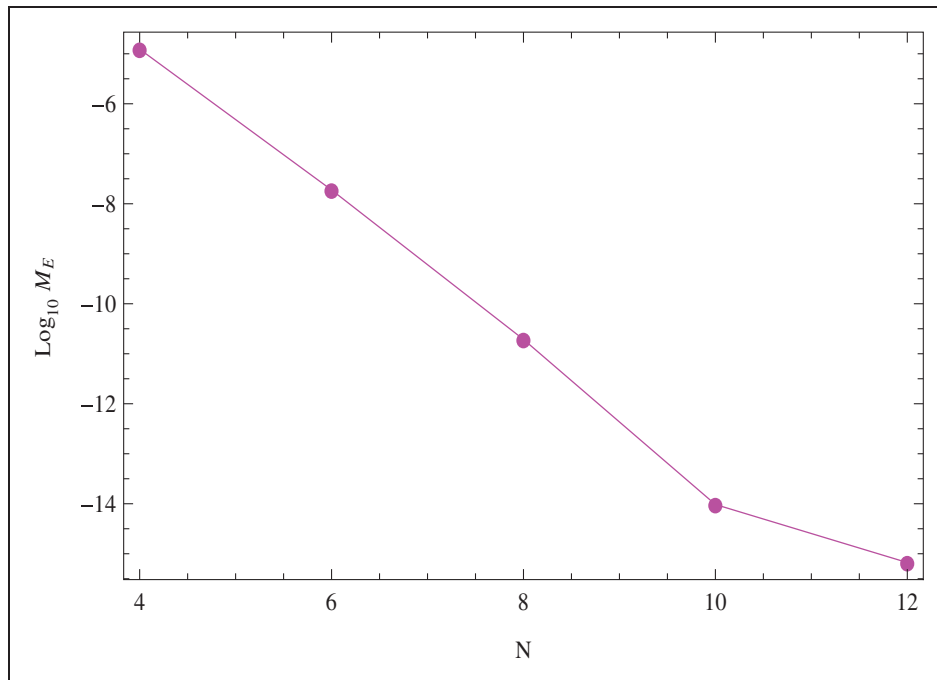**Figure 1.** Absolute error of problem (106).

Figure 2. Convergence of problem (106).

Table 3. Comparing M_E of the proposed method and the NIFD (Chen et al., 2011b) method for problem (108).

	SL-GL-C Method			NIFD (Chen et al., 2011b)	
$N = M$	6	10	14	40	80
M_E	1.77×10^{-8}	8.55×10^{-15}	6.66×10^{-16}	7.55×10^{-4}	3.82×10^{-4}

accuracy and convergence of the present scheme, in Figure 2, we plot the logarithmic graph of M_E($\log_{10}$ M_E) at various values of $N(N = M)$, which shows that the proposed method provides an accurate approximation and yields exponential convergence rates.

Example 2. *Consider the following FPE (Chen et al., 2011b)*

$$\partial_t u(x,t) = \partial_x^{0.9}\left(\partial_x^{0.8} u(x,t)\right) - e^{-t}\left(x^2 + \frac{\Gamma(0.3)}{\Gamma(1.3)} x^{0.3}\right),$$

$$(x,t) \in [0,1] \times [0,1]$$

$$(108)$$

subject to

$$u(x,0) = x^2, \quad x \in [0,1], \quad u(0,t) = 0,$$
$$u(1,t) = e^{-t}, \quad t \in [0,1]$$

$$(109)$$

The exact solution is $u(x,t) = e^{-t} x^2$.

In Table 3, the numerical results based on M_E, obtained using the proposed algorithm, are compared with those presented by the NIFD method (Chen et al., 2011b). From this table, we observe that the proposed method is more accurate than the NIFD method (Chen et al., 2011b). A comparison of the x-directional curves of the exact solution and the numerical solution at $t = 0.1$, 0.5, 0.9 is shown in Figure 3. Meanwhile, the absolute error in the x-directional and at time value $t = 0$ and $N = M = 14$, is plotted in Figure 4. In Figure 5, we sketch the logarithmic graph of M_E ($\log_{10} M_E$) at various values of $N(N = M)$ to demonstrate the convergence of the present method.

5.2. Examples for two-dimensional space fractional percolation equations

Example 3. *Consider the two-dimensional FPE (Chen et al., 2013)*

$$\partial_t u(x,y,t) = \partial_x^{\beta_1}\left((2 - x^2)\partial_x^{\alpha_1} u(x,y,t)\right) + \partial_y^{\beta_2}$$
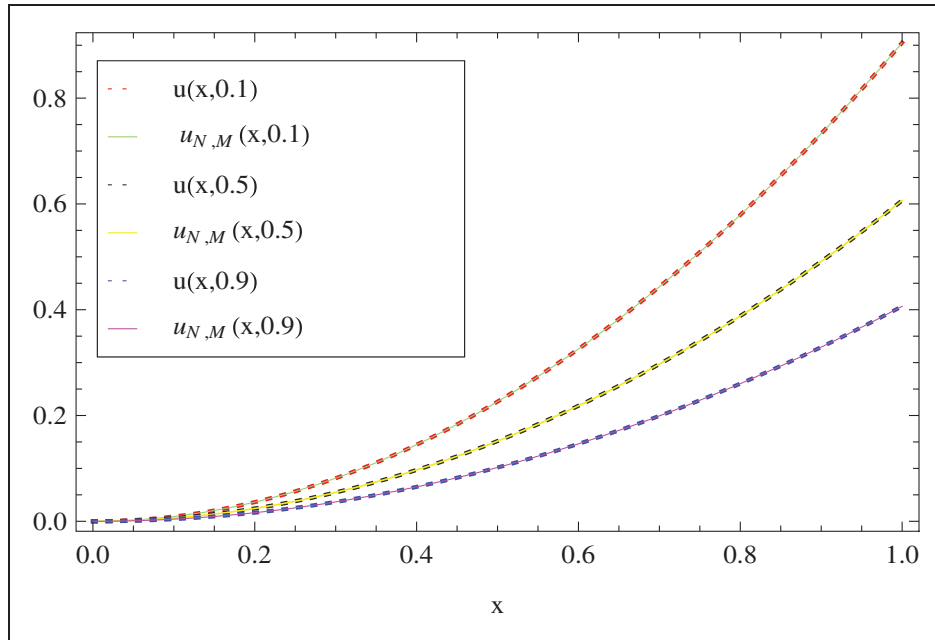
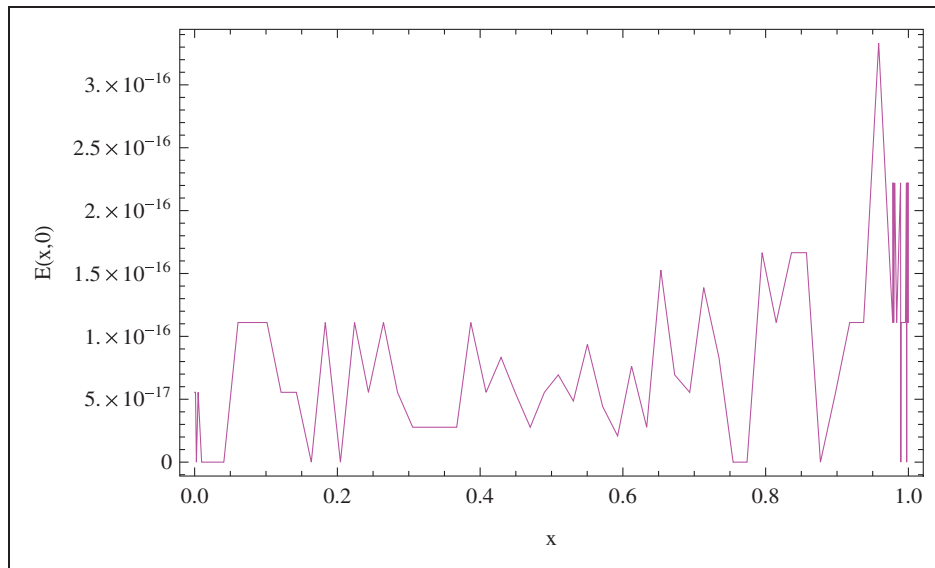**Figure 3.** *x*-Directional curves of the approximate and exact solutions of problem (108) at $N=M=14$.

Figure 4. Absolute error of problem (108) at $t=0$ and $N=M=14$.

$$\left((2 - y^2)\partial_y^{\alpha_2} u(x, y, t) \right) - e^{-t} x^2 y^2$$
$$- e^{-t} y^2 \frac{\Gamma(3)}{\Gamma(3 - \alpha_1)} \left(\frac{2\Gamma(3 - \alpha_1)}{\Gamma(3 - \alpha_1 - \beta_1)} x^{2 - \alpha_1 - \beta_1} \right.$$
$$\left. - \frac{2\Gamma(5 - \alpha_1)}{\Gamma(5 - \alpha_1 - \beta_1)} x^{4 - \alpha_1 - \beta_1} \right)$$

$$- e^{-t} x^2 \frac{\Gamma(3)}{\Gamma(3 - \alpha_2)} \left(\frac{2\Gamma(3 - \alpha_2)}{\Gamma(3 - \alpha_2 - \beta_2)} y^{2 - \alpha_2 - \beta_2} \right.$$
$$\left. - \frac{2\Gamma(5 - \alpha_2)}{\Gamma(5 - \alpha_2 - \beta_2)} y^{4 - \alpha_2 - \beta_2} \right),$$
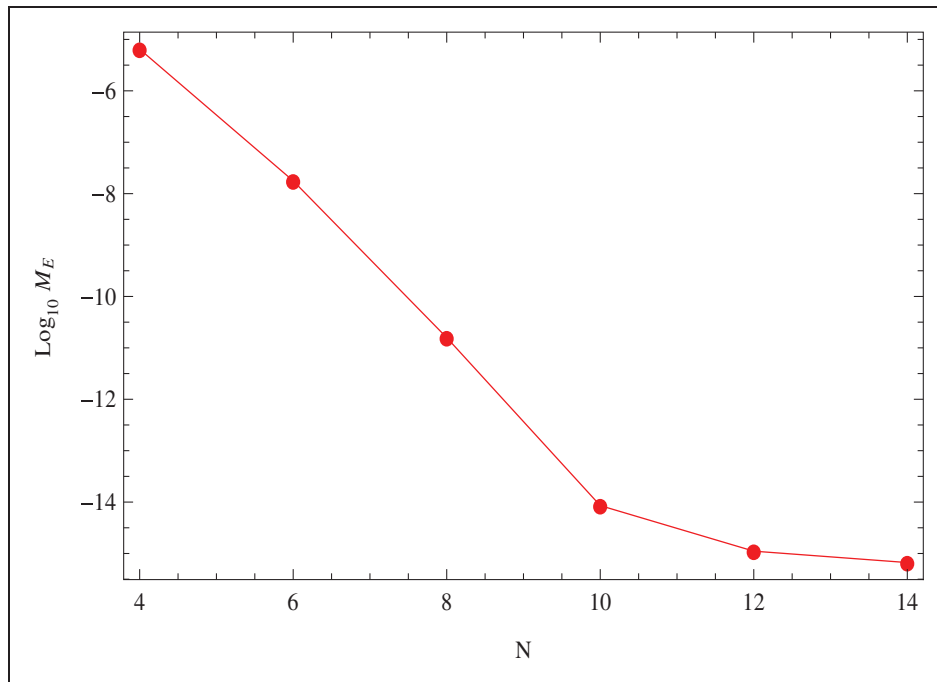$$\times (x, y, t) \in [0, 1] \times [0, 1] \times [0, 1] \qquad (110)$$

Figure 5. Convergence of problem (108).

Table 4. Comparing M_E of the proposed method and the NIFD (Chen et al., 2013) method for problem (110) at $\alpha_1 = 0.5$, $\beta_1 = 1$, $\alpha_2 = 0.5$ and $\beta_2 = 1$.

	SL-GL-C Method			NIFD (Chen et al., 2013)	
$N = M = K$	4	6	8	80	160
M_E	2.94×10^{-6}	6.38×10^{-9}	1.44×10^{-11}	–	–
M_E (at $t=1$)	6.00×10^{-6}	1.57×10^{-8}	6.82×10^{-12}	1.17×10^{-3}	5.92×10^{-4}

subject to the initial condition

$$u(x, y, 0) = x^2 y^2, \quad (x, y) \in [0, 1] \times [0, 1] \quad (111)$$

and the boundary conditions

$$u(0, y, t) = 0, \quad u(1, y, t) = e^{-t}y^2, \quad (y, t) \in [0, 1] \times [0, 1],$$
$$u(x, 0, t) = 0, \quad u(x, 1, t) = e^{-t}x^2, \quad (x, t) \in [0, 1] \times [0, 1] \quad (112)$$

The exact solution is $u(x,t) = e^{-t} x^2, y^2$.

In spite of using small values of N, M and K, we obtain highly accurate solutions to this problem using the present method. In Table 4, we present the maximum absolute error (M_E at $t=1$) obtained by our method, at different values of N, M and K, along with a comparison with the results given by using the

implicit finite difference method (Chen et al., 2013), at the special values $\alpha_1 = 0.5$, $\beta_1 = 1$, $\alpha_2 = 0.5$ and $\beta_2 = 1$. In Table 5, we list the absolute error at $N = M = K = 8$ for problem (110), where $\alpha_1 = 0.5$, $\beta_1 = 1$, $\alpha_2 = 0.5$ and $\beta_2 = 1$. We also plot the space graph of absolute error in Figure 6, with the parameter values listed in its caption. In order to demonstrate the exponential convergence of the method, in Figure 7, we sketch the logarithmic graphs of M_E at various values of $N(N = M = K)$.

Example 4. *Consider the two-dimensional FPE (Chen et al., 2014)*

$$\partial_t u(x, y, t) = \partial_x \left(\frac{\Gamma(3 - v_1)(3 - 2x)}{2} \partial_x^{v_1} u(x, y, t) \right)$$
$$+ \partial_y \left(\frac{\Gamma(4 - v_2)(4 - y)}{6} \partial_y^{v_2} u(x, y, t) \right)$$

Table 5. Absolute error for problem (110) with $\alpha_1 = 0.5$, $\beta_1 = 1$, $\alpha_2 = 0.5$, $\beta_2 = 1$ at $N = M = K = 8$.

| x	y	t	E(x,y,t)	x	y	t	E(x,y,t)	x	y	t	E(x,y,t)
0	0.5	0.1	1.60×10^{-13}	0	0.5	0.5	3.31×10^{-13}	0	0.5	1	6.05×10^{-13}
0.1			2.84×10^{-13}	0.1			8.05×10^{-13}	0.1			5.40×10^{-13}
0.2			2.62×10^{-13}	0.2			1.18×10^{-12}	0.2			8.12×10^{-13}
0.3			6.44×10^{-14}	0.3			1.44×10^{-12}	0.3			1.43×10^{-12}
0.4			1.02×10^{-13}	0.4			1.99×10^{-12}	0.4			1.36×10^{-12}
0.5			4.63×10^{-13}	0.5			2.30×10^{-12}	0.5			1.30×10^{-12}
0.6			1.04×10^{-12}	0.6			2.23×10^{-12}	0.6			1.37×10^{-12}
0.7			1.51×10^{-12}	0.7			2.17×10^{-12}	0.7			2.16×10^{-13}
0.8			1.83×10^{-12}	0.8			1.75×10^{-12}	0.8			2.24×10^{-12}
0.9			2.24×10^{-12}	0.9			4.12×10^{-13}	0.9			2.36×10^{-12}
1			1.60×10^{-13}	1			3.31×10^{-13}	1			6.05×10^{-13}
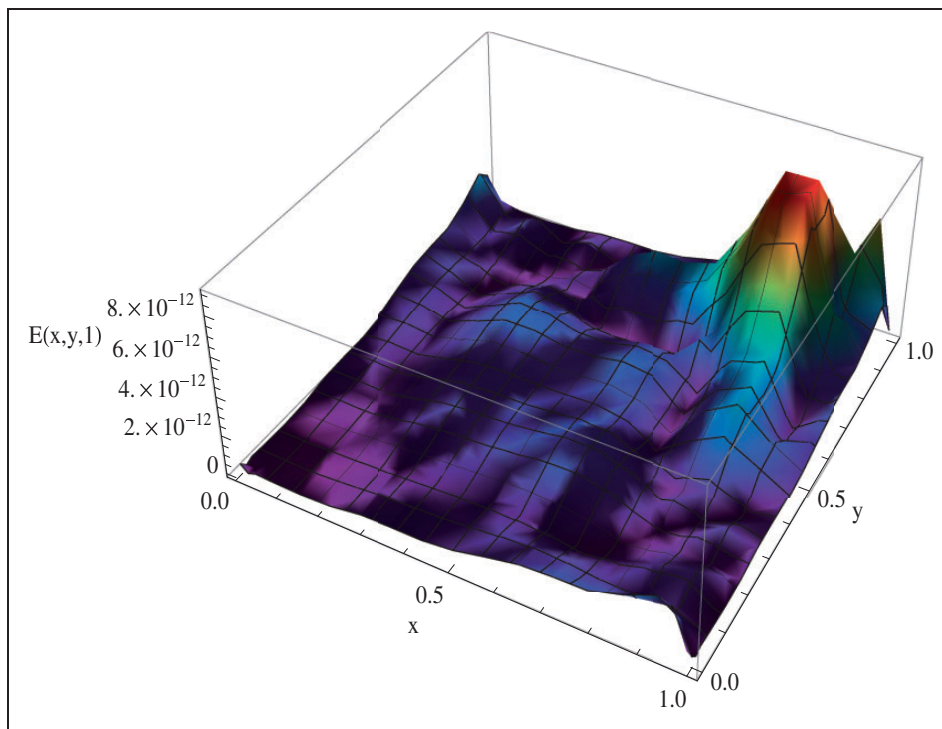
Figure 6. The space graph of the absolute error for problem (110) at $\alpha_1 = 0.5$, $\beta_1 = 1$, $\alpha_2 = 0.5$, $\beta_2 = 1$ and $N = M = K = 8$.

$$-e^{-t}x^2y^3 + e^{-t}x^2y^{2-\nu_2}((\nu_2 - 3)(4 - y) + y)$$
$$+ e^{-t}x^{1-\nu_1}y^3((\nu_1 - 2)(3 - 2x) + 2x),$$
$$(x, y, t) \in [0, 1] \times [0, 1] \times [0, 1] \qquad (113)$$

subject to

$$u(x, y, 0) = x^2y^3, \quad (x, y) \in [0, 1] \times [0, 1] \qquad (114)$$

and

$$u(0, y, t) = 0, \quad u(1, y, t) = e^{-t}y^3, \quad (y, t) \in [0, 1] \times [0, 1],$$
$$u(x, 0, t) = 0, \quad u(x, 1, t) = e^{-t}x^2, \quad (x, t) \in [0, 1] \times [0, 1] \qquad (115)$$

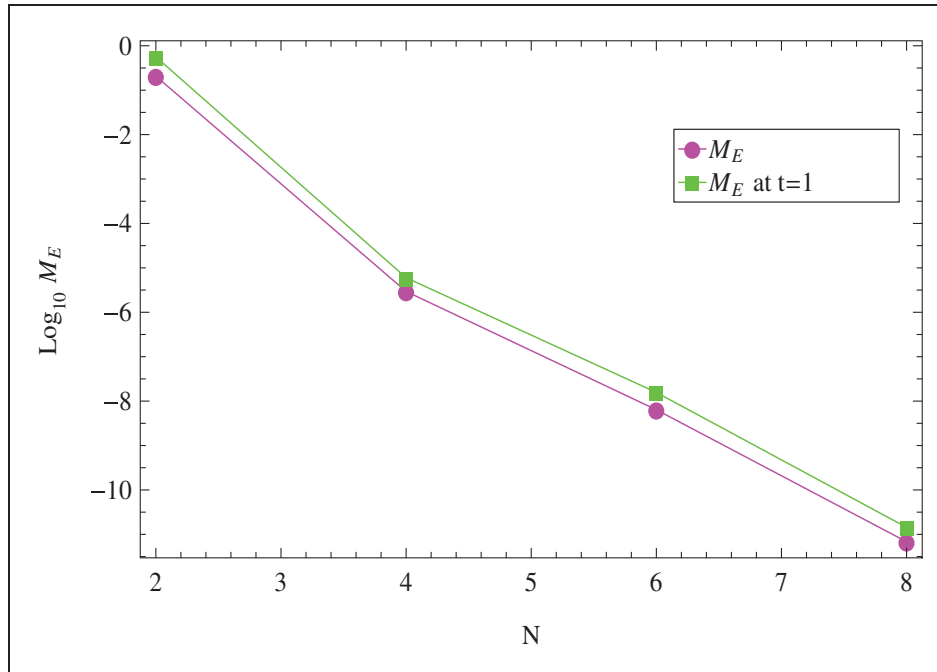The exact solution of equation (113) is $u(x,y,t) = e^{-t} x^2 y^3$.

Figure 7. Convergence of problem (110).

Table 6. Comparing M_E of the proposed method and IDM (Chen et al., 2014) for problem (113).

$N=M=k$	SL-GL-C Method			IDM (Chen et al., 2014)	
	4	6	8	80	160
M_E	5.04×10^{-6}	9.82×10^{-9}	1.19×10^{-11}	–	–
M_E (at $t=1$)	5.90×10^{-6}	1.67×10^{-8}	1.48×10^{-11}	2.07×10^{-3}	1.06×10^{-3}

In order to show that our method is more accurate than the implicit difference method (IDM) (Chen et al., 2014), in Table 6 the numerical results for M_E using the proposed algorithm are compared with those presented by the IDM (Chen et al., 2014). From this table, we observe that the proposed method is more accurate than the IDM (Chen et al., 2014).

Example 5. *Finally, consider the two-dimensional FPE*

$$\partial_t u(x,y,t) = \partial_x^{0.8}\left(\partial_x^{0.7} u(x,y,t)\right) + \partial_y^{0.9}\left(\partial_y^{0.6} u(x,y,t)\right)$$
$$- e^{-t}x^2 y^2 - \frac{\Gamma(3)}{\Gamma(1.5)}e^{-t}x^{0.5}y^2 -$$
$$\frac{\Gamma(3)}{\Gamma(1.5)}e^{-t}x^2 y^{0.5}, \quad (x,y,t) \in [0,1]$$
$$\times [0,1] \times [0,1]$$

$$(116)$$

Table 7. Maximum absolute error for problem (116).

$N=M=K$	4	6	8
M_E	3.11×10^{-6}	6.57×10^{-9}	7.83×10^{-12}
M_E (at $t=1$)	5.78×10^{-6}	1.59×10^{-8}	1.44×10^{-11}

subject to the initial condition

$$u(x,y,0) = x^2 y^2, \quad (x,y) \in [0,1] \times [0,1] \qquad (117)$$

and the boundary conditions

$$u(0,y,t) = 0, \quad u(1,y,t) = e^{-t}y^2, \quad (y,t) \in [0,1] \times [0,1],$$
$$u(x,0,t) = 0, \quad u(x,1,t) = e^{-t}x^2, \quad (x,t) \in [0,1] \times [0,1]$$

$$(118)$$

The exact solution of equation (116) is $u(x,y,t) = e^{-t}\,x^2 y^2$.
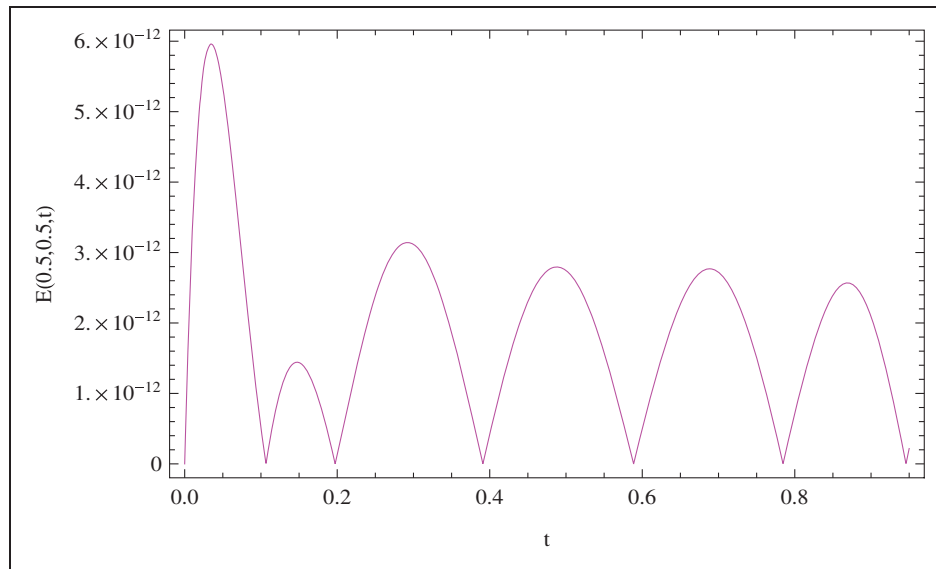
Figure 8. *t*-Directional curve of the absolute error of problem (116) at $x = y = 0.5$ and $N = M = K = 8$.

Table 7 lists the M_E of $u(x,y,t)$ for problem (116) with various choices of N, M, and K. The numerical results presented in this table show that the results are very accurate for small values of N, M and K. Figure 8 demonstrates that the absolute error $E(x,y,t)$ is very small for even the small number of grid points taken.

6. Conclusion

As one of the few articles dealing with FPEs, we have proposed and developed a spectral collocation method to obtain accurate numerical solutions for one- and two-dimensional FPEs. The core of the proposed method was to discretize the FPE in the spatial direction by the SL-GL-C method, along with a new treatment for the subjected conditions, to create SODEs of the unknown coefficients of spectral expansion in the time direction. An efficient numerical integration process for SODEs was investigated based on the SC-GR-C method. The proposed method has been successfully applied to numerically solve one- and two-dimensional FPEs. The main advantage of the present approach is, by adding a few terms of the shifted SL-GL and SC-GR collocation nodes, a highly accurate solution of the problem can be obtained. Comparison between our approximate solutions and the approximate solutions achieved by other methods were presented to demonstrate the high accuracy and validity of our method.

References

Abdelkawy M, Ahmed EA and Sanchez P (2015a) newblock A method based on Legendre pseudo-spectral approximations for solving inverse problems of parabolic types equations. *Mathematical Sciences Letters* 4(1): 81–90.

Abdelkawy MA, Ezz-Eldien SS and Amim AZM (2015b) A Jacobi spectral collocation scheme for solving Abel's integral equations. *Progress in Fractional Differentiation and Applications* 1(3): 1–14.

Al-Khaled K and Alquran M (2014) An approximate solution for a fractional model of generalized Harry Dym equation. *Mathematical Sciences* 8(4): 125–130.

Alipour M, Rostamy D and Baleanu D (2012) Solving multi-dimensional FOCPs with inequality constraint by BPs operational matrices. *Journal of Vibration and Control* 19(16): 2523–2540.

Baleanu D, Diethelm K, Scalas E and Trujillo JJ (2012) *Fractional Calculus Models and Numerical Methods*. New York: World Scientific Publishing Company.

Bhrawy A (2014) An efficient Jacobi pseudospectral approximation for nonlinear complex generalized Zakharov system. *Applied Mathematics and Computation* 247: 30–46.

Bhrawy A, Doha E, Baleanu D and Ezz-Eldien S (2015a) A spectral tau algorithm based on Jacobi operational matrix for numerical solution of time fractional diffusion-wave equations. *Journal of Computational Physics* 293: 142–156.

Bhrawy A and Zaky M (2015a) A method based on the Jacobi tau approximation for solving multi-term time–space fractional partial differential equations. *Journal of Computational Physics* 281: 876–895.

Bhrawy A and Zaky M (2015b) Numerical simulation for two-dimensional variable-order fractional nonlinear cable equation. *Nonlinear Dynamics* 80(1): 101–116.

Bhrawy A, Zaky M and Machado JT (2015b) Efficient Legendre spectral tau algorithm for solving the two-sided space–time Caputo fractional advection–dispersion equation. *Journal of Vibration and Control*. Epub ahead of print 22 January 2015. DOI: 10.1177/1077546314566835.

Canuto C, Hussaini MY, Quarteroni A and Zang TA (2006) *Spectral Methods: Fundamentals in Single Domains*. New York: Springer-Verlag.

Chen CM, Liu F, Anh V and Turner I (2011a) Numerical simulation for the variable-order Galilei invariant advection diffusion equation with a nonlinear source term. *Applied Mathematics and Computation* 217(12): 5729–5742.

Chen S, Liu F and Anh V (2011b) A novel implicit finite difference method for the one-dimensional fractional percolation equation. *Numerical Algorithms* 56(4): 517–535.

Chen S, Liu F and Burrage K (2014) Numerical simulation of a new two-dimensional variable-order fractional percolation equation in non-homogeneous porous media. *Computers & Mathematics with Applications* 68(12): 2133–2141.

Chen S, Liu F, Turner I and Anh V (2013) An implicit numerical method for the two-dimensional fractional percolation equation. *Applied Mathematics and Computation* 219(9): 4322–4331.

Chou H, Lee B and Chen C (2006) The transient infiltration process for seepage flow from cracks. *Advances in Subsurface Flow and Transport: Eastern and Western Approaches III*. Eos Trans. AGU, Western Pacific Meeting, 2006.

Dehghan M, Hamedi EA and Khosravian-Arab H (2014) A numerical scheme for the solution of a class of fractional variational and optimal control problems using the modified Jacobi polynomials. *Journal of Vibration and Control*. Epub ahead of print 3 September 2014. DOI: 10.1177/1077546314543727.

Ding Z, Xiao A and Li M (2010) Weighted finite difference methods for a class of space fractional partial differential equations with variable coefficients. *Journal of Computational and Applied Mathematics* 233(8): 1905–1914.

Doha E, Bhrawy A, Abdelkawy M and Van Gorder RA (2014a) Jacobi–Gauss–Lobatto collocation method for the numerical solution of $1+1$ nonlinear Schrödinger equations. *Journal of Computational Physics* 261: 244–255.

Doha E, Bhrawy A, Baleanu D and Hafez R (2014b) A new Jacobi rational–Gauss collocation method for numerical solution of generalized pantograph equations. *Applied Numerical Mathematics* 77: 43–54.

Doha E, Bhrawy A and Ezz-Eldien S (2011) Efficient Chebyshev spectral methods for solving multi-term fractional orders differential equations. *Applied Mathematical Modelling* 35(12): 5662–5672.

Doha E, Bhrawy A and Ezz-Eldien S (2012) A new Jacobi operational matrix: An application for solving fractional differential equations. *Applied Mathematical Modelling* 36(10): 4931–4943.

Eslahchi M, Dehghan M and Parvizi M (2014) Application of the collocation method for solving nonlinear fractional integro-differential equations. *Journal of Computational and Applied Mathematics* 257: 105–128.

Ezz-Eldien S, Doha E, Baleanu D and Bhrawy A (2015) A numerical approach based on Legendre orthonormal polynomials for numerical solutions of fractional optimal control problems. *Journal of Vibration and Control*. Epub ahead of print 3 March 2015. DOI: 10.1177/1077546315573916.

Garrappa R and Popolizio M (2011) On the use of matrix functions for fractional partial differential equations. *Mathematics and Computers in Simulation* 81(5): 1045–1056.

Giona M and Roman HE (1992) Fractional diffusion equation for transport phenomena in random media. *Physica A: Statistical Mechanics and its Applications* 185(1): 87–97.

He JH (1998) Approximate analytical solution for seepage flow with fractional derivatives in porous media. *Computer Methods in Applied Mechanics and Engineering* 167(1): 57–68.

Heinrichs W (1989) Spectral methods with sparse matrices. *Numerische Mathematik* 56(1): 25–41.

Irandoust-Pakchin S, Dehghan M, Abdi-Mazraeh S and Lakestani M (2014) Numerical solution for a class of fractional convection–diffusion equations using the flatlet oblique multiwavelets. *Journal of Vibration and Control* 20(6): 913–924.

Jafari H and Tajadodi H (2015) Numerical solutions of the fractional advection-dispersion equation. *Progress in Fractional Differentiation and Applications* 1(1): 37–45.

Kayedi-Bardeh A, Eslahchi M and Dehghan M (2014) A method for obtaining the operational matrix of fractional Jacobi functions and applications. *Journal of Vibration and Control* 20(5): 736–748.

Khalil H and Khan RA (2014) A new method based on Legendre polynomials for solutions of the fractional two-dimensional heat conduction equation. *Computers & Mathematics with Applications* 67(10): 1938–1953.

Kirchner JW, Feng X and Neal C (2000) Fractal stream chemistry and its implications for contaminant transport in catchments. *Nature* 403(6769): 524–527.

Lazo MJ and Torres DF (2014) The Legendre condition of the fractional calculus of variations. *Optimization* 63(8): 1157–1165.

Li C and Deng W (2007) Remarks on fractional derivatives. *Applied Mathematics and Computation* 187(2): 777–784.

Machado JT, Galhano AM and Trujillo JJ (2013) Science metrics on fractional calculus development since 1966. *Fractional Calculus and Applied Analysis* 16(2): 479–500.

Magin RL (2006) *Fractional Calculus in Bioengineering*. West Redding: Begell House Publishers.

Meerschaert MM and Tadjeran C (2006) Finite difference approximations for two-sided space-fractional partial differential equations. *Applied Numerical Mathematics* 56(1): 80–90.

Miller KS and Ross B (1993) *An Introduction to the Fractional Calculus and Fractional Differential Equations*. New York: John Wiley & Sons.

Mohebbi A, Abbaszadeh M and Dehghan M (2014) High-order difference scheme for the solution of linear time fractional Klein–Gordon equations. *Numerical Methods for Partial Differential Equations* 30(4): 1234–1253.

Pinto CMA and Carvalho RM (2015) Fractional modeling of typical stages in HIV epidemics with drug-resistance. *Progress in Fractional Differentiation and Applications* 1(2): 111–122.

Pooseh S, Almeida R and Torres DF (2013) A discrete time method to the first variation of fractional order variational functionals. *Central European Journal of Physics* 11(10): 1262–1267.

Raja MAZ and Chaudhary NI (2015) Two-stage fractional least mean square identification algorithm for parameter estimation of CARMA systems. *Signal Processing* 107: 327–339.

Rostamy D, Alipour M, Jafari H and Baleanu D (2013) Solving multi-term orders fractional differential equations by operational matrices of BPs with convergence analysis. *Romanian Reports in Physics* 65(2): 334–349.

Wang H and Du N (2014) Fast alternating-direction finite difference methods for three-dimensional space-fractional diffusion equations. *Journal of Computational Physics* 258: 305–318.

Xu Q, Hesthaven JS and Chen F (2015) A parareal method for time-fractional differential equations. *Journal of Computational Physics* 293: 173–183.